Mirror and Triplet spectroscopy in the fp shell with SeGA and GRETINA

Thomas William Henry

Ph.D.

University of York

Department of Physics

September 2015

Abstract

In this thesis, data relevant to isospin-non conserving effects in the fp shell are presented. The data are interpreted in terms of the shell model and use empirically derived isospin non-conserving terms. Understanding the empirically derived isospin-non conserving terms is the main motivation for this research. The $J = 2$ anomaly is a term that has been introduced into shell model calculations to reproduce mirror energy difference (MED) data in the $f_{\frac{7}{2}}$ shell.

The first of the two experiments in this thesis examines the $T_z = -\frac{3}{2}$ nucleus ^{51}Co. Excited states were identified through gamma ray spectroscopy with SeGA at the NSCL facility using the A1900+S800 setup. The transitions were identified using mirror symmetry arguments. The results show that the $f_{\frac{7}{2}}$ MED calculation approach is still accurate when the states relevant to the MED are unbound to proton emission in the negative T_z nucleus.

A second experiment is presented which is the main focus of this thesis. The experimental setup was much the same except for higher mass beams and GRETINA was used in place of SeGA. The experiment used a ^{66}As beam, and isotonic contaminants of ^{65}Ge and ^{64}Ga to populate excited states in fp shell nuclei. Results and discussion are presented for the following nuclide and pairs of mirror nuclei: ^{62}Ga; ^{63}Ge and ^{63}Ga; ^{65}As and ^{65}Ge.

The conclusions drawn from the results of these two experiments are as follows:

- No additional isospin non-conserving effects are observed when states in one of the mirror nuclei are as much as 1.5 MeV unbound to proton emission.
- The $A = 63$ MED show that one of the expected terms (V_{cr}) does not function in the upper-fp shell.
- The implication from the presented data is that states in ^{65}As undergo proton emission.
- A study of triplet energy difference (TED) systematics is presented along side data from ^{62}Ga to produce a new candidate for the anomalous $T = 1$, 2^+ state in ^{62}Ga.

Contents

List of Figures

List of Tables

Acknowledgements

There are many people that need to be thanked.

Firstly I'd like to thank my family, all of them, for their continued support during what might have seemed like an unusual way to spend four years.

Thanks Mike for being a great supervisor and setting me loose with science to think about and data to analyse, I don't think I would have enjoyed it so much without you. Thanks also to Paul, the countless hours you spent discussing the experiment with me helped me to limp over the finish line.

You can learn a lot from teachers, but you can probably learn more from Phil and James' arguments. Listening to them debate all forms of nuclear physics was the best introduction to a PhD I could have received. Thank you Jack, for being the source/target of so many of my arguments.

I thrived on the support of the post grads *et al.* In addition to those already mentioned my thanks to Gemma, Matt, Su, and all those who answered our rally cry (pub!).

Finally, thank you to my army of proof readers and those who gave me advice and help, particularly Matt and Phil.

Declaration

This thesis has been submitted for the degree of Doctor of Philosophy, in accordance with the regulations of the University of York. The work described herein has not been submitted for any other degree or qualification. All work was carried out under the supervision of Prof. M. A. Bentley. Experimental work was undertaken in collaboration with National Superconducting Cyclotron Laboratory of Michigan State University, the Lawrence Berkeley National Laboratory, and many others. In particular the relevant calibrations to resolve beams of ^{54}Ni, ^{53}Co, ^{54}Fe and subsequent recoils were performed by Dr Paul J. Davies, as was final preparation of Figures relevant to ^{62}Ga. All other work is my own.

Signed

Thomas William Henry

Chapter 1

Introduction

The nuclear force can be treated as charge symmetric (neutron-neutron and proton-proton forces having the same strength) and charge independent (neutron-proton forces having the same strength as the average of neutron-neutron and proton-proton forces). However the proton-proton (pp), neutron-proton (np), and neutron-neutron (nn) scattering lengths differ: $a_{np} = -23.5 \pm 0.8$ fm, $a_{pp} = -17.3 \pm 0.4$ fm, and $a_{nn} = -18.9 \pm 0.4$ fm (after being corrected for electromagnetic effects) [1, 2]. Scattering lengths are proportional to the interaction strengths. The discrepancy demonstrates that the nuclear force is neither charge symmetric nor charge independent. This symmetry breaking effect is small compared to the absolute values and accordingly in the shell model one treats the nuclear interaction as charge symmetric with charge symmetry breaking effects (i.e. the Coulomb force) introduced as perturbations.

As a metric the energy difference between isobaric analogue states is used (which are described in Chapter 2). This metric is compared to the difference predicted using nuclear wavefunctions and electromagnetic interactions which therefore gives an insight into the nuclear wavefunction. Early work used Coulomb displacement energies, comparing the absolute binding energy for neighbouring pairs of isobaric nuclei. This approach aimed to use basic models such as those developed by H.A. Bethe [3] to calculate the charge radius of the nucleus. Direct measurements of the charge radius contradicted these calculations, with the models underestimating the Coulomb displacement energy by about 7% [4]. This is known as the Nolen-Schiffer anomaly and was the first example of a significant deviation from the understood isospin breaking effects.

In 2001 Cameron *et al.* described the $A = 49$ mirror energy difference (MED) in terms of nucleon alignment [5]. It was noted that a large change in rotational frequency was coincident with a large MED. The authors interpreted this as a smaller overlap of proton-proton pairs in the new rotational configuration. Further work was carried out to reproduce the MED with the cranked shell model [6], however, approaches like this were unable to reproduce more than general trends. It was not until Coulomb matrix elements (CME) were introduced to large scale shell model calculations that it was possible to reproduce the MED accurately [7]. It was found that CME calculated from a harmonic oscillator basis were not accurate at low spin and empirical ones were used based on a fit to the $A = 42$ data.

Coulomb matrix elements extracted from fits to data will include all isospin non-conserving (INC) effects. Some INC terms are expected, such as the Coulomb effect. Work was undertaken

to quantify and account for these effects by creating matrix elements by Zuker *et. al.* [8] and Williams *et. al.* [9]. Zuker *et. al.* noted that these "isospin non-conserving forces" are dominated by the $J = 0$ and $J = 2$ couplings. That is, considering two nucleons in the $f_{\frac{7}{2}}$ shell that can couple to $J = 0, 2, 4,$ or 6 it was deduced that $J = 0$ and $J = 2$ couplings require an additional matrix element in shell model calculations. To account for the disparity between theoretical and experimental MED and triplet energy differences (TED) two approaches were employed: 1) the MED was corrected by a 100 keV isovector matrix element on $J = 2$ pairings; 2) the TED was corrected by a 100 keV isotensor matrix element on $J = 0$ pairings. Williams *et. al.* used multiple methods to extract isovector matrix elements from the available data in the $f_{\frac{7}{2}}$ shell. This rigorous demonstration of the need for additional INC matrix elements spawned the search for effective isovector and isotensor interactions to be applied in addition to a Coulomb interaction. As the isovector problem can be accounted for with $J = 2$ couplings this problem has since become known as the "$J = 2$ anomaly".

In 2007 Bentley and Lenzi gave a detailed description of Coulomb energy differences in the shell model including details on smaller monopole shifts that had previously been overlooked [10]. This detailed approach and all the available data clearly show that the $J = 2$ anomaly is a real effect within the effective interaction of the $f_{\frac{7}{2}}$ orbital. Future research into the $J = 2$ anomaly has several clear goals:

- Gather more data in the $f_{\frac{7}{2}}$ shell where the theoretical approach is well established. Accessing more exotic nuclei and higher spin states will both confirm the extent to which INC matrix elements are needed and help in further quantifying the effect.
- Investigate different regions of the nuclear chart to determine if INC effects are an artifact of the $f_{\frac{7}{2}}$ shell, an artifact of the shell model approach, or a reflection of a physical effect not normally included in our models.
- Understand the origin of the $J = 2$ anomaly.

The work presented in this thesis is motivated by these goals. Two experiments are presented: the first revealing data on excited states in the exotic $f_{\frac{7}{2}}$ nucleus, ^{51}Co. All of the observed states are above the proton separation energy. Any effects introduced by being above the proton separation energy are not included in the shell model calculations calculations used to interpret the results. Despite being above threshold the MED is well described by shell model calculations. The second experiment pushes into the upper-fp shell in order to acquire data on excited states. This allowed a systematic look at the upper-fp shell as has been performed in the $f_{\frac{7}{2}}$ shell. Results on ^{63}Ge and ^{63}Ga are interpreted in terms of MED, however complications prevented more than tentative assignments; direct knockout reactions to ^{65}As and ^{65}Ge yielded unexpected results which are interpreted in terms of proton decay of ^{65}As; and ^{62}Ga is populated in direct and indirect reactions. For ^{62}Ga the TED systematics, reaction models, and shell model structure calculations were used as a guide to understanding the populated states. All experiments were performed at NSCL [11] using the A1900+S800 [12, 13] setup, one with the Gamma Ray Energy Tracking In-Beam Nuclear Array, GRETINA [14], the other with the Segmented Germanium Array SeGA [15].

Two-neutron knockout was heavily relied upon for the work in this thesis, being the main reaction mechanism to populate ^{51}Co and ^{62}Ga. Attempts were made to estimate the relative

population of states in daughter nuclei from two-neutron knockout using wavefunction overlap between relevant states in the parent nuclei, and all states in the daughter nuclei, and Eikonal reaction theory. The wavefunction overlap was calculated using the shell model, and due to the large valence space in the upper-fp shell the calculations were heavily truncated, and as such this was used as a guide.

Chapter 2

Theory

2.1 Isospin

The concept of isospin, first put forward by Heisenberg in 1932 [16], is a framework in which the proton and neutron are considered projections of the same particle: the nucleon. For nuclei T is used, for nucleons t to denote the isospin quantum number. T_z is used to denote the projection of isospin for nuclei and t_z for the projection of isospin for nucleons. Each nucleon is given an isospin of $t = \frac{1}{2}$. The proton is assigned a projection of $t_z = -\frac{1}{2}$ and the neutron is assigned a projection of $t_z = +\frac{1}{2}$ [17]. When constructing a nucleus within this framework the projections add, such that:

$$T_z = \frac{N - Z}{2}, \vec{T} = \sum \vec{t} \tag{2.1}$$

where N is the number of neutrons and Z is the number of protons. Therefore, states in a nucleus can have any value of isospin so long as $T \geq T_z$. This principle is demonstrated in Figure 2.1 which shows allowed states across sets of nuclei of the same mass and differing T_z (isobaric multiplets) [18]. In this Figure each circle represents a set of states. When examining states of a certain T, in the absence of all isospin non-conserving effects (i.e. the Coulomb force), the n^{th} state of a certain J^π will be identical in structure regardless of T_z.

When one considers a triplet of $T = 1$ states, some of the proton-proton interactions in the $T_z = -1$ nucleus are swapped for neutron-neutron interactions in the $T_z = +1$ nucleus and *vice versa*, and these will also be swapped for neutron-proton interactions in the $T_z = 0$ nucleus. The three versions of this state are known as isobaric analogue states (IAS) (as are the same versions of states in mirror nuclei). In the absence of any isospin non-conserving (INC) effects the nuclear interaction is referred to as isoscalar. In this extreme, IAS have no difference in structure or excitation energy. For this case two statements are true:

- The nuclear force is charge independent as described by Equation 2.2.
- The nuclear force is charge Symmetric as described by Equation 2.3.

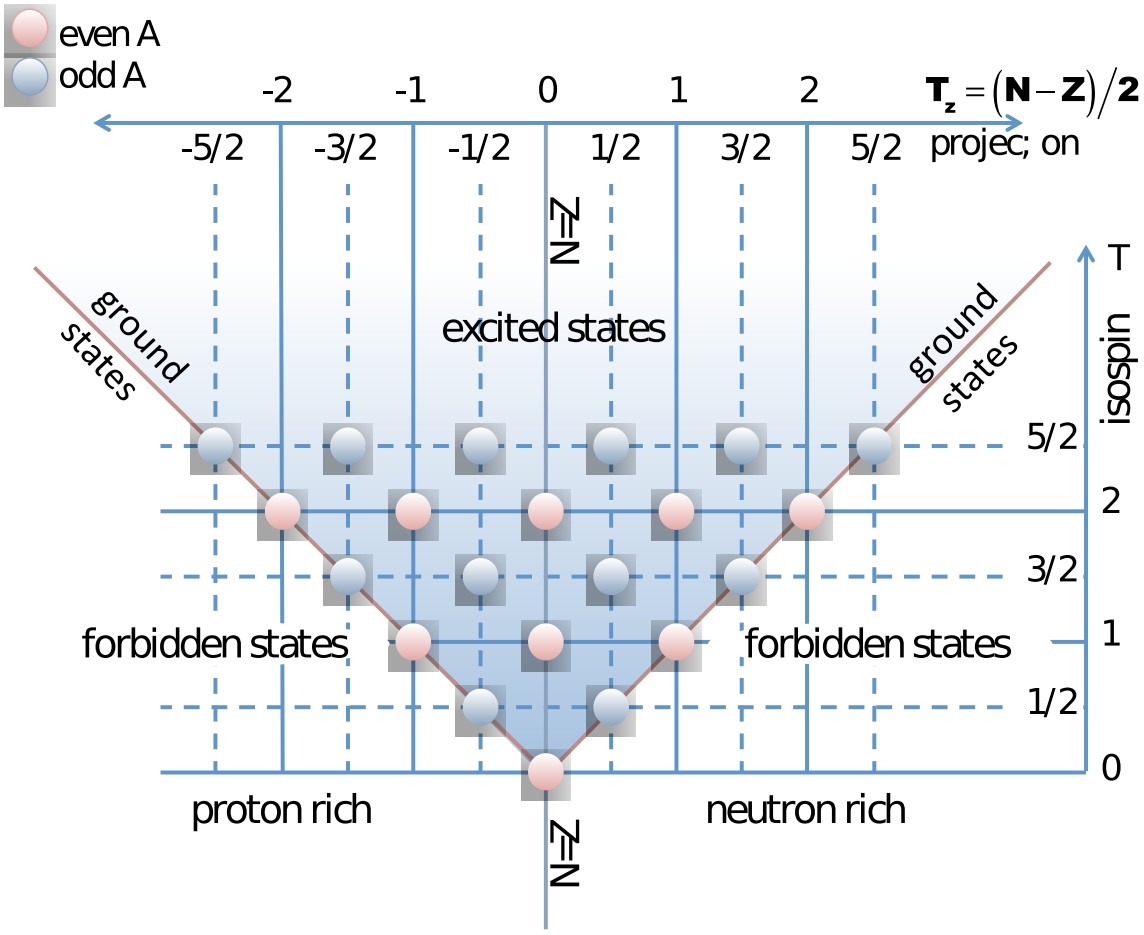

Figure 2.1: This Figure shows allowed states in terms of T, and T_z. Sets of states in nuclei are represented by circles. Any circle on a red line would be expected to be a ground state, states below this line are forbidden and those above are excited states. Generally states of higher T are many MeV higher in excitation energy than the ($T = T_z$) ground state. The exception to this are odd-odd $T_z = 0$ nuclei, where the $T = 1$ states are so low in energy that they often become the ground state [18].

$$V_{np} = \frac{V_{pp} + V_{nn}}{2} \tag{2.2}$$

$$V_{pp} = V_{nn} \tag{2.3}$$

where V_{pp} is the proton-proton interaction, V_{nn} is the neutron-neutron interaction, and V_{np} is the neutron-proton interaction.

INC effects can be categorised as isovector effects, $V_{isovector}$, which are described by equation 2.4 or isotensor and take the form of $V_{isotensor}$ which is described in equation 2.5.

$$V_{isovector} = V_{pp} - V_{nn} \tag{2.4}$$

$$V_{isotensor} = V_{pp} + V_{nn} - 2V_{np} \tag{2.5}$$

As discussed in Chapter 1, IAS are not perfectly symmetric due to the Coulomb interaction. Other INC effects also break charge symmetry and these are discussed in Section 2.3.2. INC effects are generally small compared to the nuclear isoscalar interaction and are treated as perturbations. To quantify INC effects one can use the mirror energy difference (MED) described in Equation 2.6. The MED is sensitive to isovector effects, probing the difference in the *pp* and *nn* interactions in the nuclear medium. The MED is defined as:

$$MED = E_{J,\pi}^{T_z=-n} - E_{J,\pi}^{T_z=n}, \tag{2.6}$$

where $E_{J,\pi}^{T_z=n}$ is the excitation energy of a state with a total angular momentum of J and a parity of π in nuclei of $T_z = n, -n$. One plots the MED against J, as in Figure 2.2 where the $A = 51$ system is compared to theoretical predictions [19].

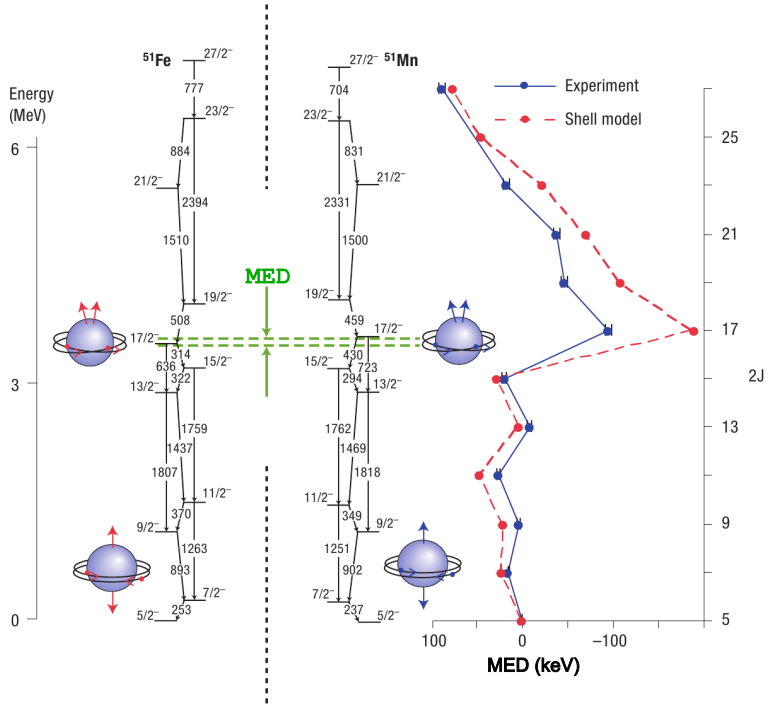

Figure 2.2: The experimental (blue) and theoretical (red) MED alongside level scheme for the $A = 51$ system. The green dashed line demonstrates the MED for the $\frac{17}{2}^-$ state. The diagrams set against the level scheme depict alignment of the valence nucleons, the cause of the MED. Edited from Reference [19] such that naming conventions are in line with this thesis.

When examining $T = 1$ triplets one can also examine the triplet energy difference (TED), defined as:

$$TED = Ex_{J,\pi}^{T_z=-1} + Ex_{J,\pi}^{T_z=1} - 2Ex_{J,\pi}^{T_z=0}. \tag{2.7}$$

The TED is sensitive to isotensor effects and can be seen as probing the strength of the np interaction compared to the average of the pp and nn interactions.

In a TED the excitation energy is taken relative to the lowest energy $T = 1$ state. This is important in the case of the $T_z = 0$ nucleus where the ground state is often of a $T = 0$ configuration. Consequently TED centred on odd-odd nuclei are more accessible experimentally. Odd-odd $T_z = 0$ systems normally have $T = 1$ ground states, which makes these nuclei the only known case where the ground state of a nucleus does not have $T = |T_z|$. States with $T > T_z$ are normally many MeV higher in excitation energy.

The TED is normally plotted against spin such as in Figure 2.3 taken from [20]. In this Figure the experimental TED is plotted for the $A = 54$ and $A = 42$ systems and shown in comparison with several calculations. For triplet systems centred on odd-odd nuclei the TED will always be negative. The TED is negative because the energy of the $T = 1$, $J^\pi = 2^+$ is always higher in the $T_z = 0$ nucleus than the average energy in the other two nuclei due to the Coulomb force. The reason for higher energies for IAS in $T = 1$, $T_z = 0$ nuclei is discussed further in Section 2.1.1. Calculations show that the nuclear and Coulomb interactions are not enough to replicate the TED and an additional INC component is needed. The approach used here is discussed further in section 2.3.3.

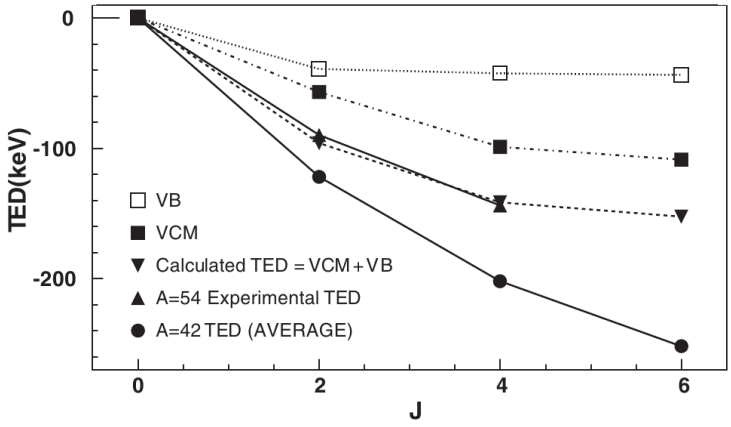

Figure 2.3: This figure shows experimental data for the $A = 42$ and $A = 54$ experimental TED, as well as shell model calculations with an empirically found term to reproduce them. In this figure the empirical term is denoted by VB, the coulomb multipole term denoted with VCM [20]. More detail is given on the Coulomb multipole and additional empirical terms in section 2.3.2.

2.1.1 Pairing, Isospin and TEDs

In analogy to Cooper pairs in superconductivity, Bohr, Mottelson and Pines used pairing to explain the difference in energy of the first excited states between odd and even A nuclei [21]. Here pairs of like nucleons are viewed as being in time reversed orbits. This work was comparing pairs of

like nucleons (pp or nn pairs). In the case of nuclei with the same or similar numbers of protons and neutrons np pairing can be considered [22]. In analogy to the deuteron, there are two possible pairing channels: $T = 0$ (isoscalar), and $T = 1$ (isovector). In this instance isovector refers to anti-aligned pairs which is the equivalent alignment to the pp or nn channel.

It is possible to count the types of pairs in a nucleus using a simple model based on the group SO(5) that considers a single J orbital [23]. It is noted that this model predicts the same pairing behaviour as large scale shell model calculations which consider many more effects. Using this model there are simple analytical formulae to predict the number of pp, nn and isovector np pairs in $|T_z| < 1$ nuclei as presented by Engel, Langanke and Vogel [24].

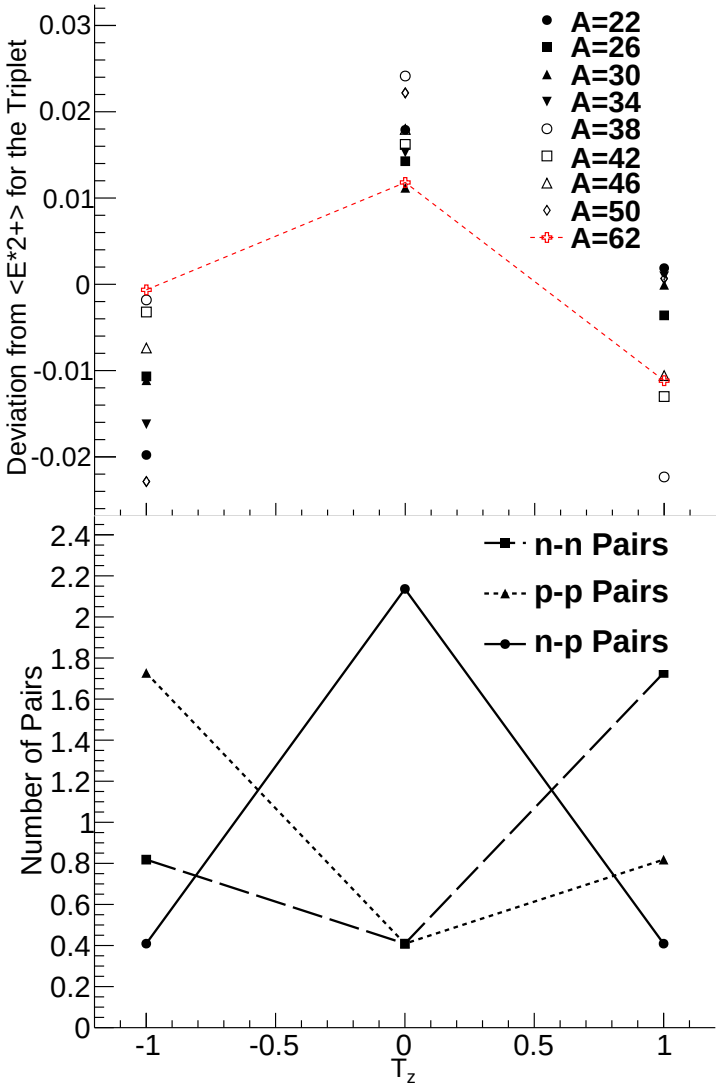

Figure 2.4: This Figure depicts energies of $T = 1$, 2^+ states for $A = 4n + 2$ systems (where the $N = Z$ nucleus is odd-odd). The top panel shows how the energy of each 2^+ state deviates from the average energy of the 2^+ states in that triplet (denoted by $< E * 2+ >$ in the Figure) for each triplet up to $A = 62$. For comparison the lower panel gives the predicted average number of nn, pp, and np pairs in the $A = 62$ system using the equations presented in [24].

The calculation displayed in the lower panel of Figure 2.4 is a typical result from this model. The predicted behaviour is an affinity towards *np* pairing in the $N = Z$ nucleus, *pp* pairing in the $T_z = -1$ nucleus, and *nn* pairing in the $T_z = 1$ nucleus. This trend is not specific to a particular state in the nucleus, but is considered as a rough approximation of the wavefunction based on the available pairs. It is reasonable to expect that excited-yrast states will have a similar number of pairs, but coupled to higher spin. Comparing yrast $J = 0$ and $J = 2$ states (as an MED does) the average geometric separation between all pairs of nucleons will be reduced in the $J = 2$ state (see Figure 2.11 for details). When the two nucleons are *pp* pairs the closer overlap results in a less bound $J = 0$ state relative to the $J = 2$ state. A lower relative binding energy for a $J = 2$ state to the ground state gives it a lower excitation energy. As there are predicted to be more *pp* pairs in $|T_z| = 1$ nuclei compared to $T_Z = 0$ nuclei, the IAS in $T_z = 0$ nuclei always have higher excitation energy. This effect is observed in the upper panel of Figure 2.4. The difference in excitation energy of $|T_z| = 1$ nuclei is largely influenced by monopole effects, which will cancel out in a TED (assuming there is no large change in valence space across a triplet). As explained in section 2.3.3 it is worth again noting that in shell model calculations the TED is underestimated by a factor of approximately 2 hence the corrections that are explained in Section 2.3.3.

2.2 Shell model

The shell model is a mean field approach developed to understand magic numbers. The magic numbers being the numbers of protons or neutrons at which nuclei exhibit stronger binding and additional stability. For a realistic nuclear potential a Woods-Saxon potential can be used of the form:

$$V(r) = \frac{-V_0}{1 + e^{\frac{r - R_0}{a}}} \tag{2.8}$$

where $R_0 = 1.25A^{\frac{1}{3}}$ fm, and V_0 and a are empirically derived values of approximately 57 MeV and 0.65 fm respectively. This function is shown in Figure 2.5. However often a simple harmonic oscillator potential is used for simplicity.

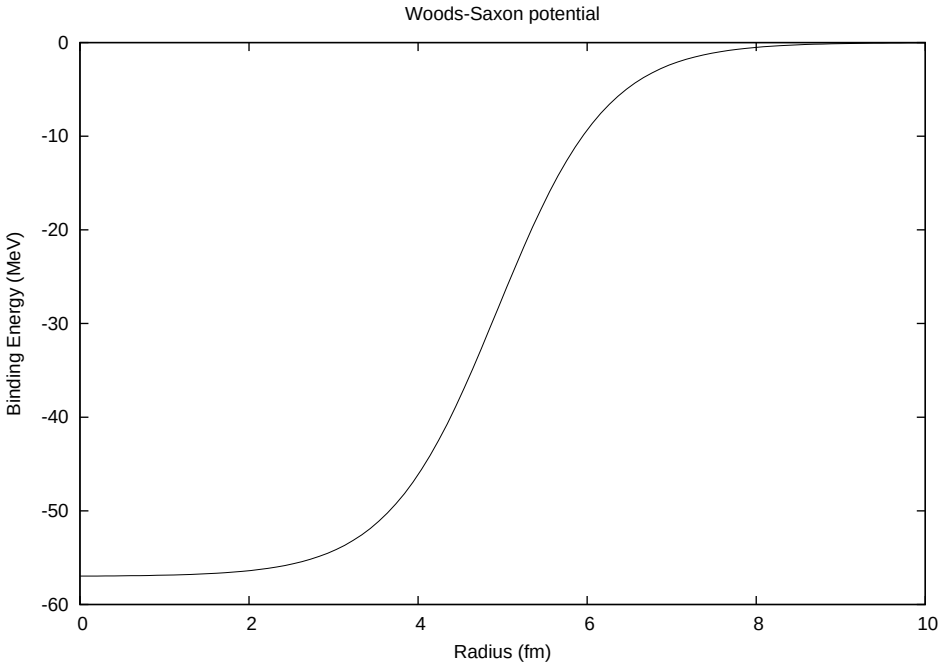

Figure 2.5: A Woods-Saxon potential plotted using Equation 2.8, with $V_0 = 57$ MeV and $a = 0.65$ fm for an $A = 62$ nucleus.

In 1963 Maria Goepart-Meyer and Johannes Hans Daniel Jensen shared a Nobel prize for the introduction of a spin-orbit term which lowers the energy of a state if the spin of the nucleon is aligned with the spin of the eigenstate. One also includes an l^2 term to account for the change in binding energy from the angular momentum of nucleons. The potential used now takes the form of Equation 2.9.

$$V(r) = \frac{1}{2}m\omega^2 r + V_{ll}l^2 - V_{ls}(r)l.s. \tag{2.9}$$

This potential accurately reproduces the magic numbers 2, 8, 20, 28, 50, 82 and 126. Solving the Schröedinger Equation with this potential produces the single particle levels shown in Figure 2.6.

So far in this description only the net attractive potential between the nucleons has been considered. One also has to consider interactions between nucleons. To consider the interactions between nucleons one can consider a Hamiltonian of the form

$$H = H_0 + H_{res}, \tag{2.10}$$

where H_0 contains the mean attractive potential from equation 2.9. The residual interaction, H_{res}, accounts for all of the effects which are not dealt with by the mean field interaction. This

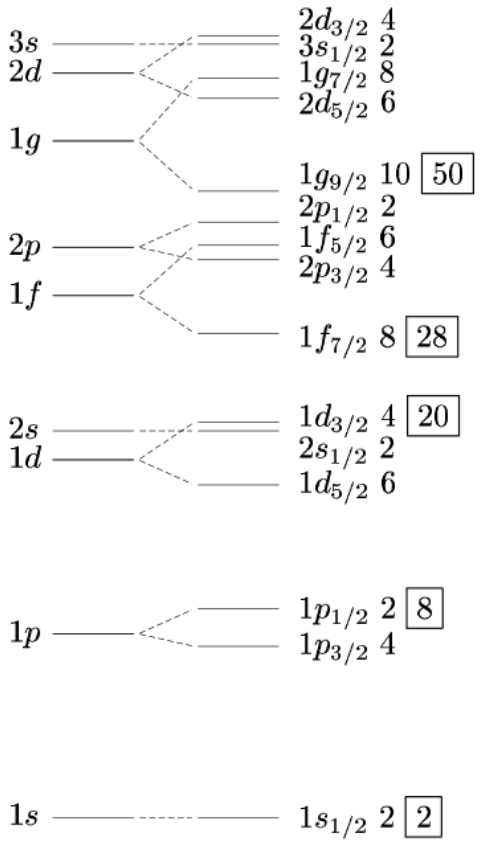

Figure 2.6: A representation of the degeneracy of basis states in the nuclear shell model found by solving the Schröedinger equation with angular momentum effects and a spin-orbit interaction. Spectroscopic notation has been used. The numbers in boxes represent the number of nucleons taken to fill the nucleus to that point (assuming no excitation), while the numbers immediately to the left of those are the degeneracy of the associated basis state.

includes accounting for the coupling of pairs of nucleons by a series of two-body matrix elements. These matrix elements can be determined phenomenologically from nuclear data, however there are different methods and approaches to doing so. As such, for a calculation in a given region there is often more than one interaction that can be used.

2.3 Shell Model Calculations

Shell model calculations start off with the calculated single particle levels from H_0. Basis states are constructed based around all possible configurations of nucleons in the single particle levels, H_{res} is then used to consider the interaction of nucleons that occupy these states. The calculation varies the wavefunction until the energy has hit a minimum. A matrix can be used to represent the wavefunction with a row for each way the nucleons can couple to create the states of interest in the valence space chosen. In order to find the minimum energy the matrix must be inverted.

To invert the matrix with all of the available shells and nucleons is in most cases too compu-

tationally intensive. Calculations where this approach is used, referred to as no-core calculations, are computationally unfeasible for systems containing more than 12 or 13 nucleons. In order to perform calculations in heavier systems, one considers only those nucleons which contribute significantly to the states of interest. By defining a core, and a number of nucleons that can be excited into specific shells it is possible to truncate this valence space. In this view the nucleus is in three parts. This is shown in Figure 2.7.

1. Core of non-interacting nucleons: these nucleons cannot be excited to other single particle levels and are not considered by the residual interaction. They can be considered as generating the potential that the rest of the nucleons occupy.

2. Valence nucleons: these are the nucleons that are considered by the residual interaction and how they couple will determine the properties of the nucleus.

3. Valence space: this defines the space the valence nucleons can move in and how they can couple.

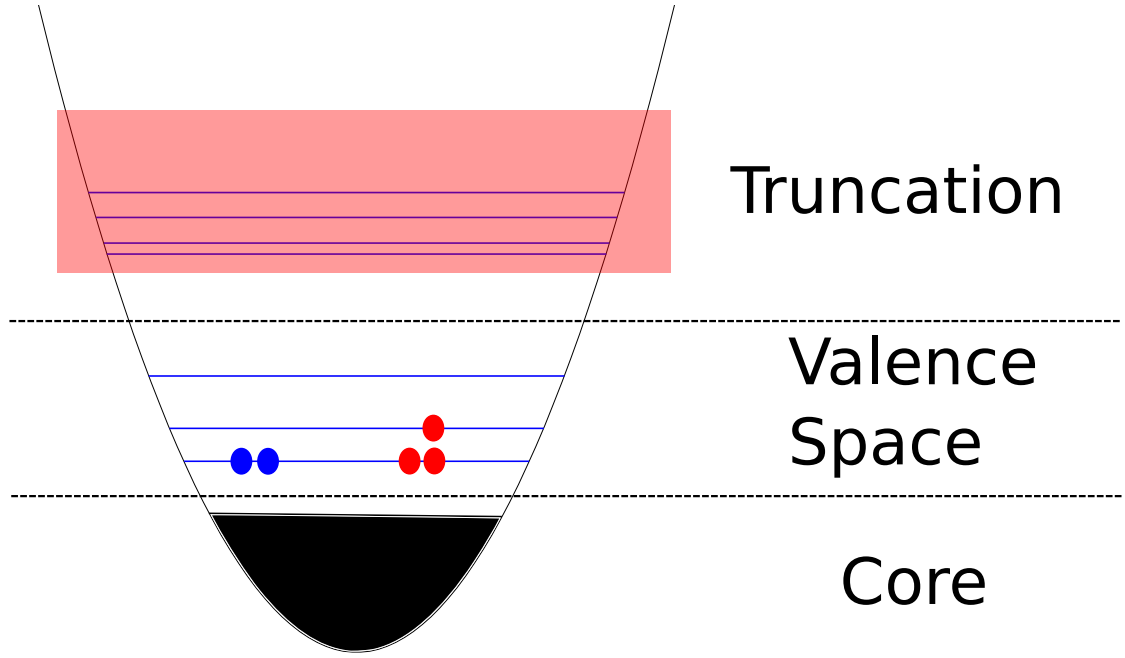

Figure 2.7: A schematic representation of the ingredients of a shell model calculation. The harmonic oscillator potential is filled with an inert core. Some valence single particle levels are shown filled with fermions of two types, denoted by different colours. Some single particle levels, those in the truncation region, have been shaded red denoting that they are not included in the calculation.

Even with truncation it can still be too computationally difficult to calculate a result. The maximum size of a calculation can be increased by using an iterative method such as the Lanczos method [25].

If the truncation is too severe the states calculated will not have realistic wavefunctions, and the binding energy will be higher. If the ideal wavefunction has been achieved then reducing the truncation will have no effect to the result of the calculation. Once a state is at the lowest energy

solution it is referred to as converged. A converged calculation will not necessarily accurately reproduce experimental data, it is merely the correct result for that interaction and valence space. It is possible to confirm a calculation has converged by slowly increasing the space it is performed in and ensuring the binding energies do not change. This principle is demonstrated in Refs [26–29].

2.3.1 The upper fp-shell

The full fp shell stretches from the doubly magic ^{40}Ca to ^{80}Zr where the $g_{\frac{9}{2}}$ orbital begins. This is not a major shell closure. However the full fp shell including the $g_{\frac{9}{2}}$ orbital is far too large to be considered. Additionally, there are currently no shell model interactions capable of interpreting a coupling between the $f_{\frac{7}{2}}$ and $g_{\frac{9}{2}}$ orbitals. Due to this large valence space, it is possible that the truncation required will prevent an accurate result. Figure 2.8 demonstrates the size of the fp shell space based on Reference [30].

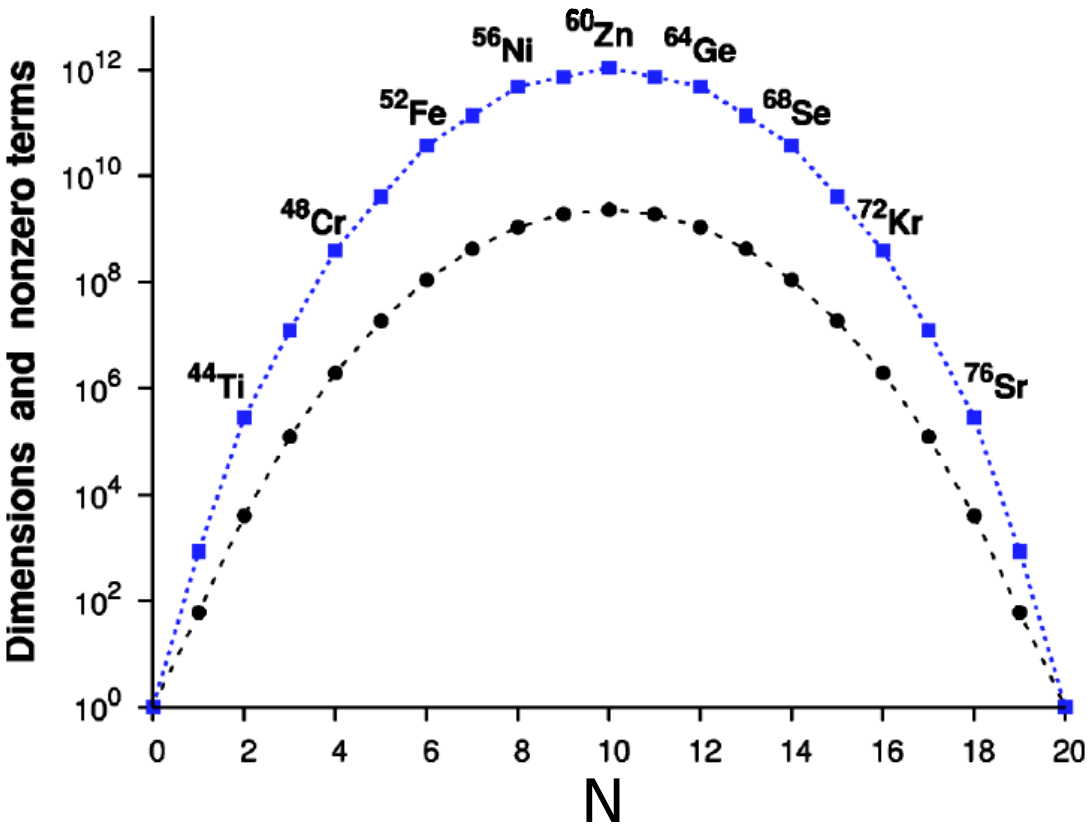

Figure 2.8: Dimensions of calculations (circles) and number of non-zero matrix elements (squares) in a shell model calculation for $T_z = 0$ fp-shell nuclei as a function of the number of valence nucleons in the calculation (N). This assumes that there is no truncation. Based on Reference [30].

There are several interactions that can be used in this region. For the work presented in this thesis the relevant ones are KB3G [31], GXPF1a [32], and LNPS [33]. GXPF1a and KB3G use a ^{40}Ca core and include the $f_{\frac{7}{2}}$, $p_{\frac{3}{2}}$, $f_{\frac{5}{2}}$, and $p_{\frac{1}{2}}$ orbitals. In principle LNPS calculations can be

run including all of the mentioned orbitals and the $g_{\frac{9}{2}}$. It is worth noting that despite the large number of valence shells available in LNPS there are no interactions between the $g_{\frac{9}{2}}$ and the $f_{\frac{7}{2}}$ orbitals so one of these must be closed [34]. Each of the mentioned interactions has been derived in a slightly different way:

- KB3G has single particle energies that have been taken by examining the ^{41}Ca spectrum, with matrix elements taken from a realistic interaction derived from nucleon-nucleon interactions.
- GXPF1a started as a realistic interaction derived from nucleon-nucleon interactions, and then the matrix elements were allowed to vary to fit to 669 energy level data from masses between $A = 47$ and $A = 66$.
- LNPS is a realistic interaction derived from nucleon-nucleon interactions, but with single particle energies that have been allowed to vary to fit to experimental data.

2.3.2 MED Calculations within the shell model

MED depend entirely on isovector interactions as an isoscalar nuclear interaction will always give an MED of zero. This provides an opportunity to further develop smaller isovector effects not often considered in shell model calculations. These INC terms are small enough that they can be considered perturbations of the main isoscalar interaction, meaning that including these terms has a small effect on the wavefunctions, the MED being one of the only observable differences as it is mostly dependent on the valence nuclei. It is worth noting that for the work presented in this thesis this approach was not used. Instead isospin non-conserving terms were added to the main interactions. The four main terms that are considered in shell model MED calculations are V_{CM}, V_{lls}, V_{Cr}, and V_B. These are described in the following sections.

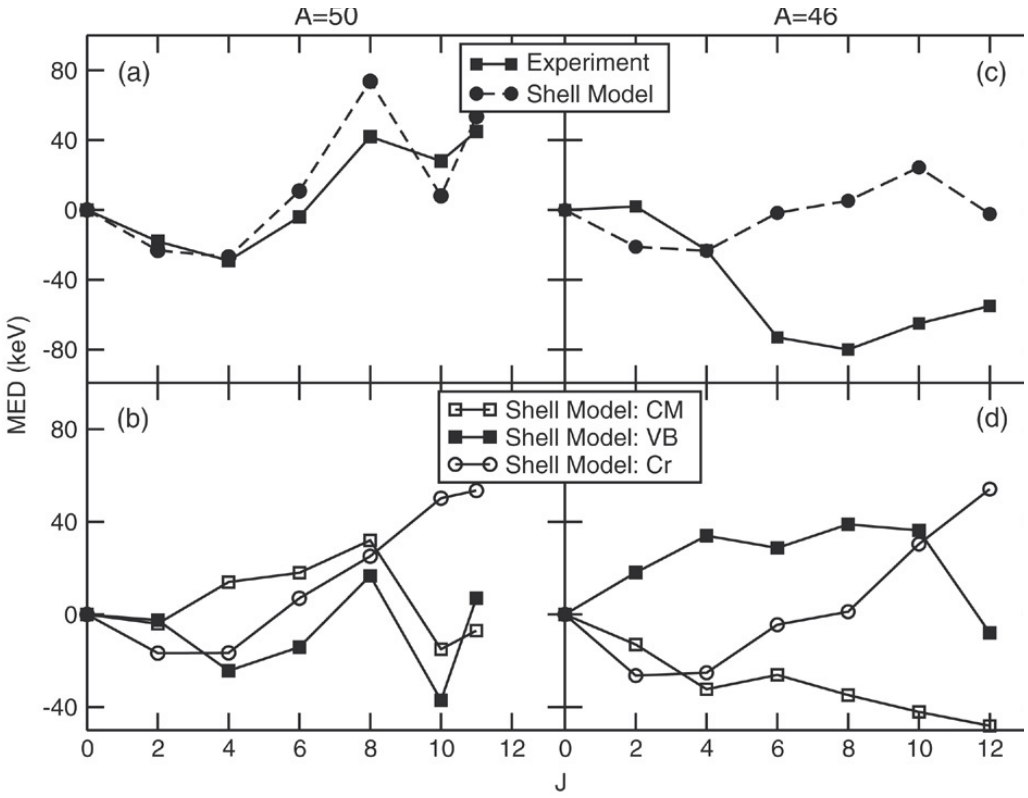

Figure 2.9: Shell model calculations and experimental data for $A = 50$ and $A = 46$ systems. The upper panels ((a) and (c)) show the experimental MED and results from the shell model calculation. The lower panels ((b) and (d)) show the breakdown of the terms included in the calculations: V_{CM}, V_{cr} and V_B terms. A full description of these terms is included in Sections 2.3.2.3, 2.3.2.2, and 2.3.2.1. Taken from Reference [10]

Figure 2.9 is provided as an example of MED calculations using V_{CM}, V_B, and V_{Cr}. Taken from Reference [10], it shows the experimental and theoretical mirror energy difference for the $A = 50$ and $A = 46$ mirror nuclei. The $A = 50$ calculations will be used as an example in the coming sections as the $A = 46$ calculations fail completely to reproduce the experimental trends. This is explained in Reference [10] in terms of the wavefunction coupling to a $T = 0$ core which is not accounted for in the MED calculations. The following sections will explain the individual terms in this example.

2.3.2.1 $\mathbf{V_{CM}}$

V_{CM} is the Coulomb multipole component. This accounts for the different Coulomb interactions between different *pp* couplings. In the $f_{\frac{7}{2}}$ shell two protons can couple to $J = 0, 2, 4$ or 6, it is expected that two protons at higher spin will have a lower average geometric overlap and thus a smaller repulsion. The calculated spatial overlap of two protons is shown in Figure 2.11 for pure $f_{\frac{7}{2}}$ couplings.

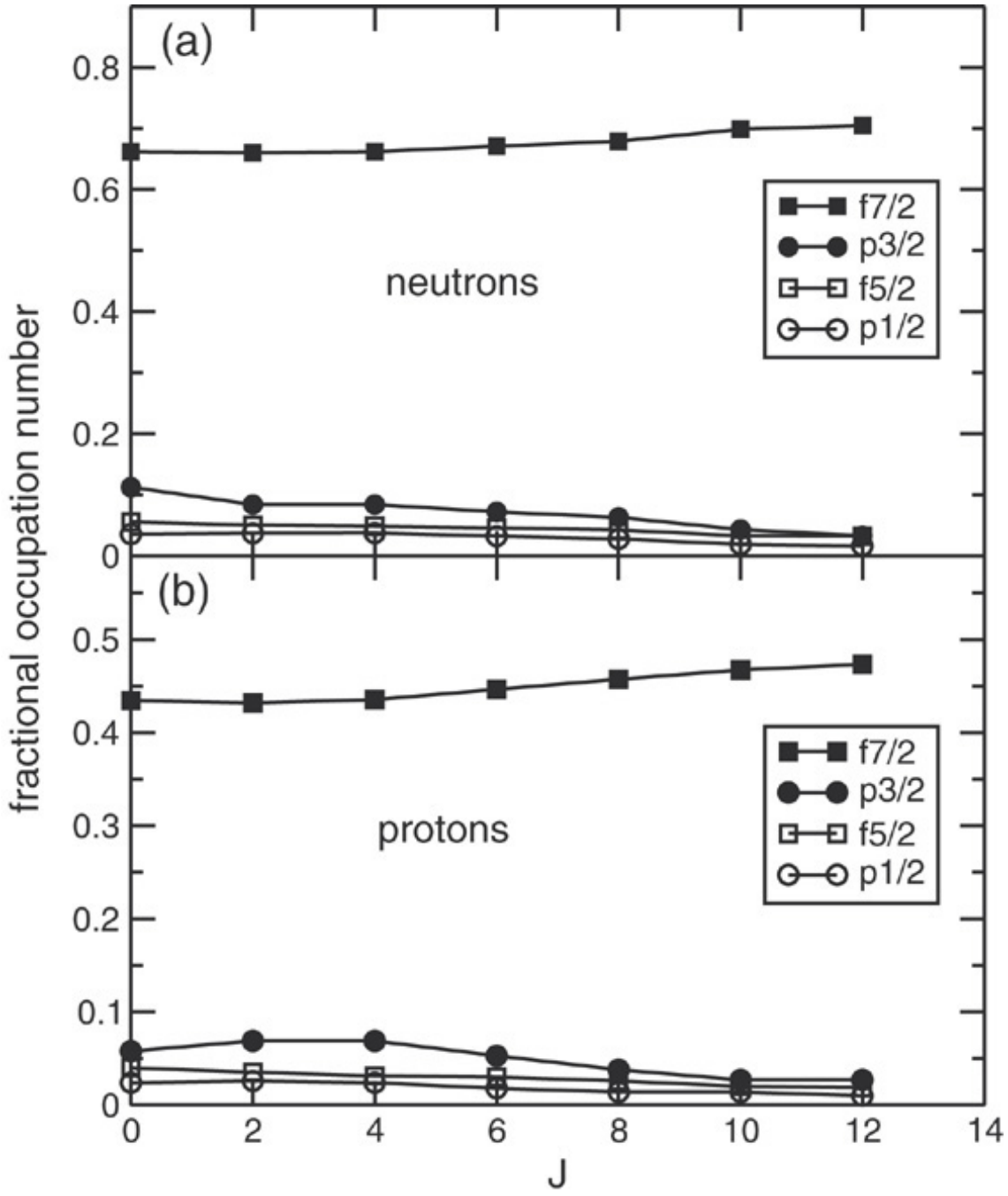

Figure 2.10: Calculated Proton and neutron shell occupancies for $T_z = \frac{1}{2}$, $A = 50$ mirror nuclei. Data to create this Figure was taken from the same calculations used to calculate the MED shown in Figure 2.9. Taken from Reference [10].

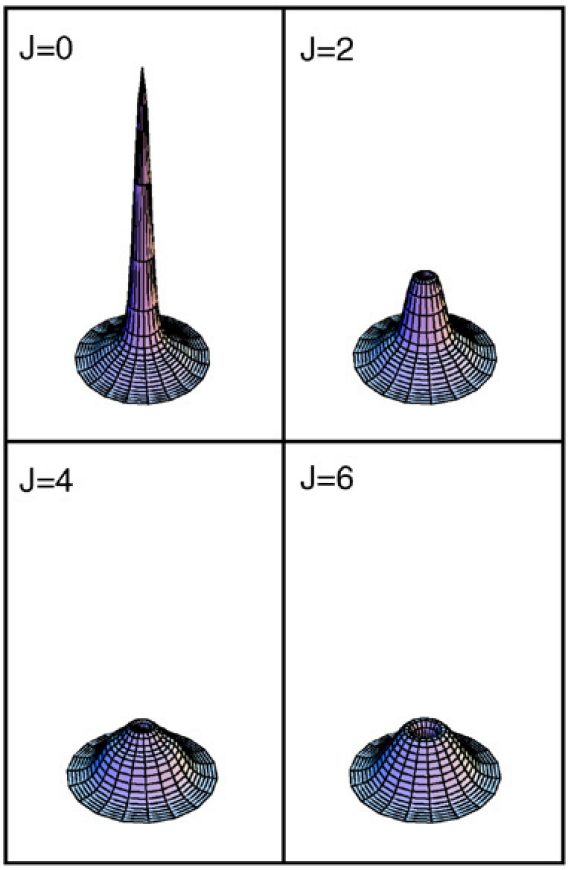

Figure 2.11: This is a plot of the calculated average radial separation, r, of two $f_{\frac{7}{2}}$ protons. The centre of each shape corresponds to $r = 0$ and r increases radially outwards. The amplitude is proportional to the overlap between the two nucleons. It can be seen that lower J has a larger concentration at $r = 0$ compared to higher J. These plots show that at higher J, the protons have a larger average geometric separation [19].

The absolute Coulomb energy of the nucleus will not contribute to the MED, as the MED is normalised to ground states. Only these contributions from the re-coupling of protons will have an effect. A proton pair coupled to high J (e.g. for a high spin state) has less Coulomb repulsion than a proton pair coupled to low J (e.g. the ground state). Consequently the excitation energy will be lowered compared with the case where two neutrons are acting instead. From Equation 2.6, one would expect a negative MED for the case of two active protons, for example in the $A = 42$ case.

The Coulomb contribution to the MED is calculated by running a calculation with a Coulomb interaction added to the interaction for protons in both nuclei. This component shows the difference in Coulomb energy from the protons recoupling from their ground state configuration to the state of interest as described. In the example given by Figure 2.9 the V_{CM} term increases slowly with spin before changing rapidly above the 8^+ state. This is explained by the nature of the wavefunctions of these states: as the band terminating state is approached, the wavefunctions become dominated more by individual configurations. Thus the changes in MED become more pronounced as the MED is sensitive to individual particle alignments.

2.3.2.2 $\mathbf{V_{lls}}$

V_{lls} consists of two terms combined: V_{ls} and V_{ll}, which are both single particle effects applied directly to the single particle levels of an interaction. V_{ls} is a magnetic spin-orbit component. Introduced in Reference [35], it was used to explain the ^{7}Be-^{7}Li MED in Reference [36]. V_{ll} represents the Coulomb energy in a proton orbital due to repulsion from the core. Refs. [10, 27] present the following equation, quantifying the effect after treating the nucleus as a charged sphere.

$$E_{ls} \simeq (g_s - g_l)\frac{1}{2m_N^2c^2}\left(-\frac{Ze^2}{R_C^3} < \vec{l}\cdot\vec{s} >\right), \tag{2.11}$$

where g_s and g_l are spin and orbit gyromagnetic factors. The free values of gyromagnetic factors can be used and are listed in Table 2.1. m_N and r_C are the nuclear mass and radius. For orbits where $j = l + s$ then $< \vec{l}\cdot\vec{s} >= \frac{l}{2}$; for orbits where $j = l - s$ then $< \vec{l}\cdot\vec{s} >= -\frac{l+1}{2}$

$$E_{ll} = \frac{-4.5Z_{cs}^{\frac{13}{12}}\left[2l(l+1) - N(N+3)\right]}{A^{\frac{1}{3}}\left(N + \frac{3}{2}\right)}keV \tag{2.12}$$

V_{ll} is an effect applied to the proton orbitals. It accounts for the change in energy of the orbital from the overlap of that orbital with the core. Using the Coulomb potential in an oscillator form and the potential for a charged sphere Duflo and Zuker [37] demonstrated that:

	Proton	Neutron
Spin	5.586	-3.828
Orbit	1	0

Table 2.1: Free values of the gyromagnetic factors

2.3.2.3 $\mathbf{V_{cr}}$ [37]

The V_{cr} term accounts for changing nuclear radii and deformation effects. Different nuclear orbitals have different average radii. Therefore as well as accounting for the single particle effects such as V_{ll} one must also account for the bulk radius change of the nucleus. While performing calculations with valence nucleons in the $f_{\frac{7}{2}}$ shell, this is achieved by tracking the occupancy of the $p_{\frac{3}{2}}$ orbital. V_{cr} is calculated using Equation 2.13.

$$V_{cr} = 2T\alpha_r \left(\frac{m_\pi(g.s.) + m_\nu(g.s.)}{2} - \frac{m_\pi(J) + m_\nu(J)}{2} \right) \tag{2.13}$$

where T is the isospin of the state, m_π and m_ν are the proton and neutron occupancies of either the ground state ($g.s.$) or the state of interest (J). α_r is a constant deduced from $A = 41$ data to be 200 keV.

This component has been used in the $f_{\frac{7}{2}}$ shell. In this case the occupation of the $p_{\frac{3}{2}}$ orbital would also be considered to increase with deformation; it is possible then that the V_{cr} term is accounting for deformation effects. Understanding how to apply the V_{cr} term in the upper fp-shell is a current research goal.

In Figure 2.9 the V_{cr} term varies slowly across the rotational band, as would be expected (as the states should have very similar structure and occupancy of the $p_{\frac{3}{2}}$ orbital). It is noteworthy that this term becomes one of the largest at higher spin. It can be further seen from Figure 2.10 that the variation in V_{cr} comes from the slow average occupancy decrease of the $p_{\frac{3}{2}}$ orbital. The empirically deduced value of α_r is large enough to precipitate such a small change into a tangible effect.

2.3.2.4 $\mathbf{V_b}$

However, analysis performed using the terms discussed above were not able to fully recreate MED or TED in the $f_{\frac{7}{2}}$ region [9]. To account for this A.P Zuker *et. al.* suggested the use of an additional matrix element [8]. For the MED a 100 keV isovector matrix element was added to $J = 2$ $f_{\frac{7}{2}}$ couplings for protons. For the TED a 100 keV isotensor matrix element was added to $J = 0$ $f_{\frac{7}{2}}$ couplings. These numbers were gathered empirically by observing the MED and TED in $A = 42$ and $A = 54$ systems (i.e. two nucleons or two-nucleon holes in the $f_{\frac{7}{2}}$ shell).

In the original work on V_b the data were confined to the $f_{\frac{7}{2}}$ region and the correction was only applied to $(f_{\frac{7}{2}})^2$, $J = 2$ couplings. As data are extended into the upper-fp region the approach has been extended to apply V_b to all $(l)^2$, $J = 2$ configurations, where l is a shell of any angular momentum, by Lenzi *et. al.* [34]. However in the data presented here the V_b term is only applied to the $f_{\frac{7}{2}}$ single particle level.

In the example given by Figure 2.9, for the same reason as for the V_{CM} term, the behaviour of the V_b term becomes more pronounced beyond the 8^+ state. Figure 2.10 can be used to understand the behaviour of the V_b term. The V_b term only effects $(f_{\frac{7}{2}})^2$ couplings; Figure 2.10 shows the average $f_{\frac{7}{2}}$ occupancy does not change significantly, showing that this effect is sensitive to the individual particle alignments.

2.3.3 TED Calculations within the shell model

Triplet energy differences are not sensitive to monopole effects such as single particle energy level changes [10]. This is because monopole terms depend only on average particle occupancy of single particle levels which are symmetric across the IAS, so cancel out in the TED. As such the only effect normally considered is the Coulomb multipole term V_{CM}. V_{CM} alone however has been found to consistently underestimate the magnitude of the TED by approximately a factor of 2 [20]. To compensate for this, an analogous term to the previously discussed V_b is used, however now an isotensor term is used affecting $J = 0$ couplings [20] rather than an isovector term affecting $J = 2$ couplings.

2.4 Reaction model calculations

All experiments discussed in this thesis, regardless of reaction, utilised beams produced via the projectile fragmentation technique (explained in Chapter 3). Among the reactions used are knockout, nucleon removal, and fragmentation. This section explains these reactions and how they are used.

The projectile fragmentation experimental technique was used in this thesis and is discussed in detail in Chapter 3. For this experimental technique, beams impinge on low mass and thin targets at energies typically between 0.08 GeV/nucleon and 1 GeV/nucleon. Beams before the target will be referred to as the projectile and beams after a target will be referred to as recoils. At these high energies the Coulomb barrier is negligible and a range of impact parameters and reactions are observed. For low impact parameter collisions many nucleons can be removed. This leaves a lower mass nucleus to continue through the separator (fragmentation) or the target nucleus can also be broken up (spallation). In peripheral or grazing reactions a process known as knockout happens. In the case of one or two nucleons being removed from a nucleus the reaction is generally considered a knockout reaction. With more (3-5) nucleon removal the process is seen as being a combination of knockout and fragmentation [38].

2.4.1 Knockout

Knockout reactions are direct reactions, meaning that the initial and final states are linked by some direct process. If the process is sufficiently well understood it is possible to predict the final states populated from an initial state.

In knockout the probability of populating specific states in a recoil is related to the spectroscopic factor between the (initial) state of the projectile and that of the recoil (final), and the probability of removing a nucleon from the shell required to populate that state. The cross section to individual states can be calculated using the formalism presented by E.C Simpson and J.A Tostevin [39]. It is shown here as equation 2.14 for one-neutron knockout.

$$\sigma = \sum_{nlj} \left[\frac{A}{A-1} \right] C^2S(J^\pi, nlj)\sigma_{sp}(nlj, S_N^{eff}), \tag{2.14}$$

where A is the mass of the projectile nucleus, C^2S is a shell model spectroscopic factor, nlj are

the quantum numbers of the removed nucleon, and S_N^{eff} is the separation energy for the removed nucleon. The spectroscopic factor is the likelihood that all but one of the nucleons in the initial state will arrange themselves in the same configuration as the final state [40]. It is given as a value between 0 and 1, the more similar the two states are the higher, and thus the higher the cross section, or transition rate in analogy to Fermi's golden rule. The spectroscopic factor accounts for the valence orbital from which the nucleon is removed. Two processes are considered: stripping and elastic breakup. In stripping reactions the removed nucleon excites the target. In elastic breakup the nucleon is removed after interacting with the target but the target remains in its ground state. For inelastic breakup the removed nucleon continues in the beam direction. The contributions from stripping and elastic breakup are not separable experimentally, so the theoretical cross sections are summed.

Eikonal reaction theory is used to evaluate an expression for the single particle effects. It is assumed that the energy of the reaction is much larger than the interaction between target and projectile. Expressions can then be reached using scattering matrices. The scattering matrices are obtained using density folding potentials, and the target and removed nucleons are assumed to have a Gaussian density profile. The density of the projectile is found using Hartree-Fock calculations that have been constrained to reproduce the experimentally known separation energy. This formalism and the calculations have also been extended to two nucleon knockout [41, 42].

2.5 Other reaction and population mechanisms

The work presented in this thesis relies on the knockout and fragmentation mechanisms. Knockout is an excellent tool for studies such as this due to its selective nature and ability to reach states very close to the proton drip line. This section will concentrate on other reaction mechanisms which are relevant to this thesis. The reaction mechanisms presented will be used to explain other experiments that have populated the nuclei presented in this thesis.

2.5.1 Fusion Evaporation

In fusion evaporation reactions the target and projectile fuse to form a compound nucleus with a composite mass of the sum of the component masses. The compound nucleus is generally created in a very high energy and high spin state owing to the energy. In the de-excitation of the compound nucleus particle emission competes with gamma decay. At higher energies the particle emission mode tends to dominate, allowing the energies of a reaction to be tuned for a specific reaction channel. After particle emission, gamma decay will occur as the nucleus is left in an excited state. Figure 2.12 demonstrates a possible decay path and the tendency of the nucleus to decay through yrast states.

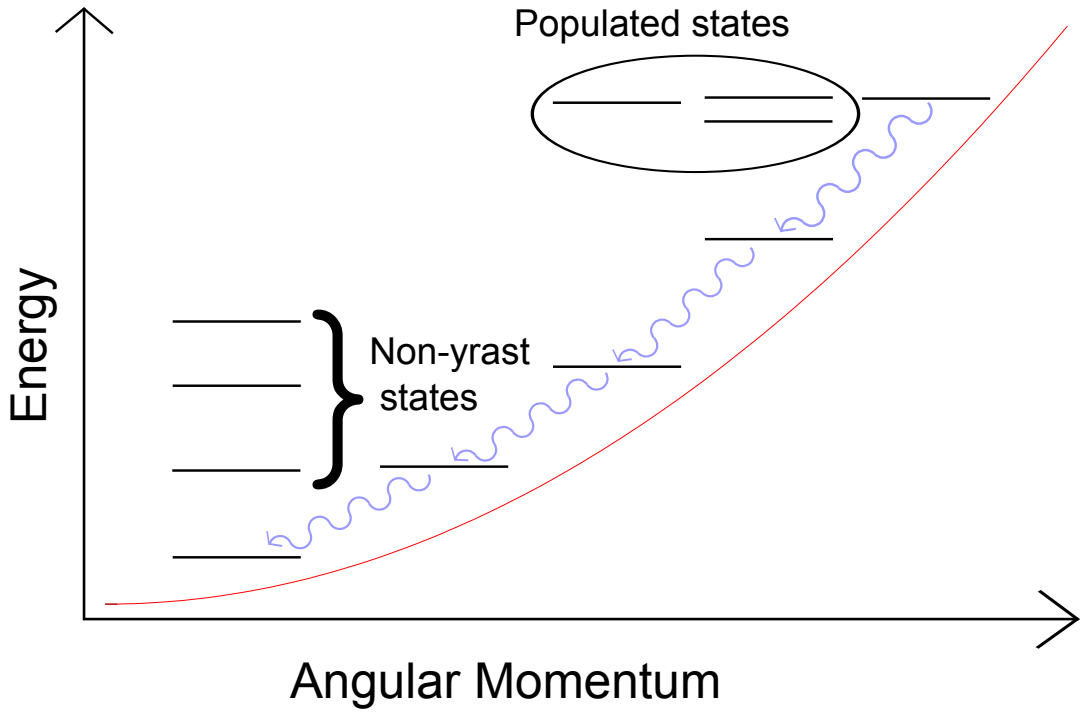

Figure 2.12: This figure gives an example of how states can be populated by fusion evaporation reactions. The (circled) populated states tend to decay towards the yrast states, and then decay through them. The red line denotes an energy proportional to angular momentum squared and the blue arrows denote possible gamma ray transitions through the yrast band.

2.5.2 β-decay

While analysis of data from β-decay is not presented in this thesis, recent relevant work has used it as a population mechanism [43]. A brief discussion of β-decay is presented here to inform subsequent discussion in Chapter 7.

In accordance with Fermi's golden rule the β decay rate in seconds is

$$\lambda = \frac{g^2 m^5 c^4}{2\pi^3 \hbar^7} |M_{fi}|^2 f, \tag{2.15}$$

where g is the Fermi coupling constant, m is the mass of the nucleus, $|M_{fi}|$ is a matrix element coupling the initial and final states, and f is a Fermi function to account for the Coulomb interaction between nucleus and emitted particle. By considering $FT_{\frac{1}{2}}$ one considers a constant that depends only on the wavefunction overlap, and can be used to identify the spin of states populated in the decay. $FT_{\frac{1}{2}}$ is calculated using Equation 2.16.

$$FT_{\frac{1}{2}} = \frac{1.386\pi^3\hbar^7}{g^2 m^5 c^4 |M_{fi}|^2} \tag{2.16}$$

A value of g of 1.4×10^{-62} Jm^{-3} has been deduced from mirror nuclei, where the matrix element

for the decay should be identical.

The selection rules for allowed β-decay allow for a change in angular momentum of 0 or 1 between the initial and final states, but for no change in parity. β decay is either a Fermi or Gamow-Teller transition. Allowed Fermi decay will have $\Delta J = 0$, allowed Gamow-Teller transitions will have $\Delta J = 0, \pm 1$. Allowed Fermi decay does not change the spin of any nucleon and thus conserves isospin to keep the wavefunction anti-symmetric, Gamow-Teller transitions may change isospin with $\Delta T = 0, \pm 1$. Decays that do not obey these rules are hindered, but a wide range of forbidden decays are observed when the $T_{\frac{1}{2}}$ of allowed transitions is sufficiently long that forbidden transitions can compete.

2.5.3 Coulomb Excitation

A brief description of Coulomb excitation is included here as it is suggested as possible further experimentation following the work in this thesis. Coulomb Excitation, as the name suggests, is the use of the Coulomb interaction to excite the nucleus via the exchange of virtual photons. The matrix elements for this are the same as those for gamma decay. The cross section to individual states is dependent on the energy of the reaction. At lower energy it is more likely to reach multi-step excitations to populate high spin states, while at higher energy it is more likely to populate fewer excited states directly. As with electromagnetic (gamma) decay, electric quadrupole and magnetic dipole transitions are dominant. Coulomb excitation with exotic nuclei can only be performed in inverse kinematics as the short half lifes prevent the use of an exotic target.

Chapter 3

Experimental Setup

Gamma ray spectroscopy is one of the cornerstones of experimental nuclear physics. This technique has provided vital information on the nature of excited states, from stable nuclei to those at the extremes of spin, isospin and mass. There are several experimental techniques and types of reactions that can be employed to access these excited states; for example: fusion-evaporation reactions with recoil decay tagging, or Coulomb excitation reactions with radioactive ion beams. All methods share the same common requirements: a reaction suitable for populating the states of interest, identification of incoming and outgoing reaction products, and the detection of radiation from the decay of excited states. This Chapter briefly outlines the detector systems employed in the experimental work for this thesis.

3.1 The National Superconducting Cyclotron Lab

The National Superconducting Cyclotron Lab (NSCL) provides beams of exotic nuclei via projectile fragmentation. This method allows for the study of very short-lived nuclei as they can be produced and transported to an experimental setup in less than 1 μ second. The A1900 Separator is used to purify secondary beams so they contain nuclides of interest separated by time-of-flight (ToF), which are identified event-by-event. Purified secondary beams can then be delivered to a range of experimental setups. The present work only concerns the S800 experimental setup at NSCL, the S800 is a magnetic spectrograph. Reactions with the radioactive fragment happen at the target position surrounded by a gamma ray detection array. Then the reaction products are transported around a 120° bend and are identified event-by-event. With this setup, reactions can be performed with both incoming and outgoing particles identified.

Two experiments are considered in this thesis, each use the same A1900-S800 setup but differ in the gamma ray detection array and magnetic settings used. The aim of both experiments was to perform mirrored reactions. The first used a primary beam of ^{58}Ni and two magnet settings to produce mirrored A1900 beams: ^{54}Ni and ^{54}Fe with contaminants beam of ^{53}Co from the ^{54}Ni setting; the Segmented Germanium Array (SeGA) was used to detect gamma rays at the target position of the S800. The second experiment used a primary beam of ^{78}Kr with the A1900 set to accept ^{66}As. As the beam through the A1900 was $N = Z$ only one magnet setting was required. Contaminant beams of ^{65}Ge and ^{64}Ga were also utilised for the analysis. In the second experiment

Primary and secondary beams				
Experiment	Primary beam	Energy	Secondary beam	Useful Contaminent
1	^{58}Ni	160 A MeV	^{54}Ni ^{54}Fe	^{53}Co
2	^{78}Kr	150 A MeV	^{66}As	^{65}Ge, ^{64}Ga

Table 3.1: A summary of the primary and secondary beams used in the experiments presented by this thesis.

the Gamma Ray Energy Tracking In beam Nuclear Array (GRETINA) was used (see Chapter 4) to detect gamma rays at the target position of the S800.

3.2 The coupled cyclotron facility

The coupled cyclotron facility [11] (CCF) provided the primary beams for the experiments, the layout of which can be seen in Figure 3.1. The first cyclotron, the K500, accelerates the primary beams to an energy of around 10 A MeV. After this the ions can be fully ionised and injected into the second cyclotron, the K1200. The K1200 generally accelerates beams to between 100 and 160 A MeV. The energies of the beams used are given in Table 3.1.

3.3 A1900 Seperator

The A1900 separator [13] is a magnetic separator designed to purify secondary beams so that they mostly contain nuclei of interest. Nuclei are separated and identified by time-of-flight (ToF) such that they can be identified event-by-event. The layout of the A1900 is shown in Figure 3.1.

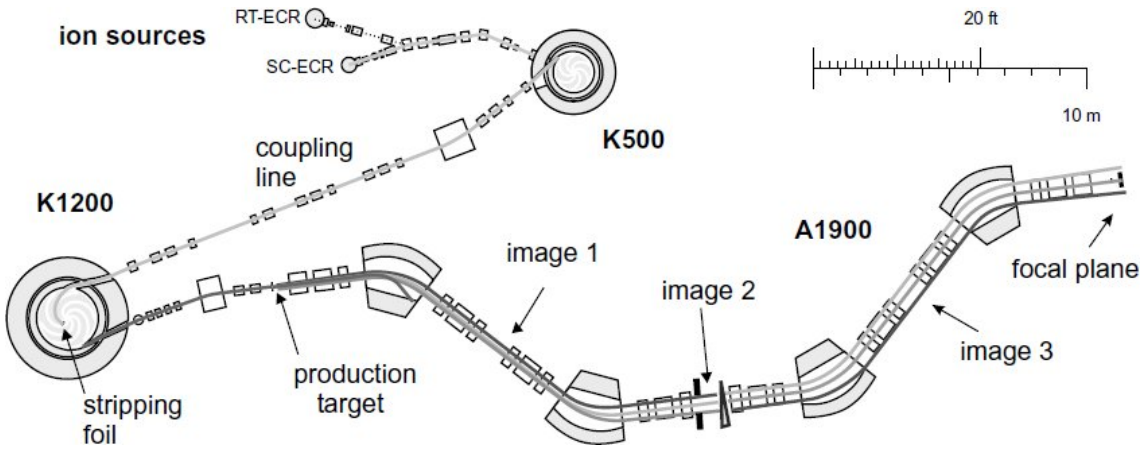

Figure 3.1: A schematic diagram of the A1900 and coupled cyclotron facility. Beams are accelerated by the K500 and K1200 cyclotrons, undergo reactions at the production target then are separated in the A1900 separator.

The A1900 separates nuclei according to their $B\rho$,

$$B\rho = \frac{mv}{q} \tag{3.1}$$

where B is the magnetic field strength, ρ is the radius of the path of the particles in the field B, v their velocity, q their charge, and m their mass. Time difference is measured between two plastic scintillator signals, one at the extended focal plane of the A1900 (the *xfp* scintillator) and one at the object position of the S800 (the *obj* scintillator). The signals from the scintillators are only used to produce a time relative to the *E1* scintillator that sits at the end of the S800 focal plane.

Beams from the CCF are fragmented at the entrance of the A1900 using a thick ^{9}Be target. Nuclides of different mass and atomic charge take different paths through the A1900. The paths shown in Figure 3.1 demonstrate how some nuclides do not make it through the separator. They have a charge to mass ratio such that they are deflected from the ideal flight path (through the slits) by the magnets. The slits at "image 2" can be moved to restrict the nuclides that are accepted, and the momentum spread of the beam. Image 2 contains a wedge that acts as an optical component to the beam. It increases the momentum separation between beams of different Z. The wedge can be constructed such that the A1900 runs in an achromatic mode. In this mode the position separation between nuclides is increased so as to improve the selectivity. The primary target thickness and reaction used introduces a momentum spread of the secondary beams. The first experiment used an 850 mg/cm^2 ^{9}Be target, and the second a 650 mg/cm^2 ^{9}Be target. Nuclides were identified by the time it takes them to traverse the separator as their paths are governed by their $B\rho$.

3.4 S800

Between the A1900 and S800 there is a transfer hall containing two scintillators, the *xfp* and *obj* scintillators. The difference in time of the signal from these scintillators is used to identify the nuclei from the A1900. The focal plane of the S800 contains further detectors which are described in this Section. They are: two cathode ray drift counters (CRDCs), an ion chamber, and *E1*, *E2*, and *E3* scintillators. All of the scintillator time signals are measured relative to the signal from the *E1* scintillator.

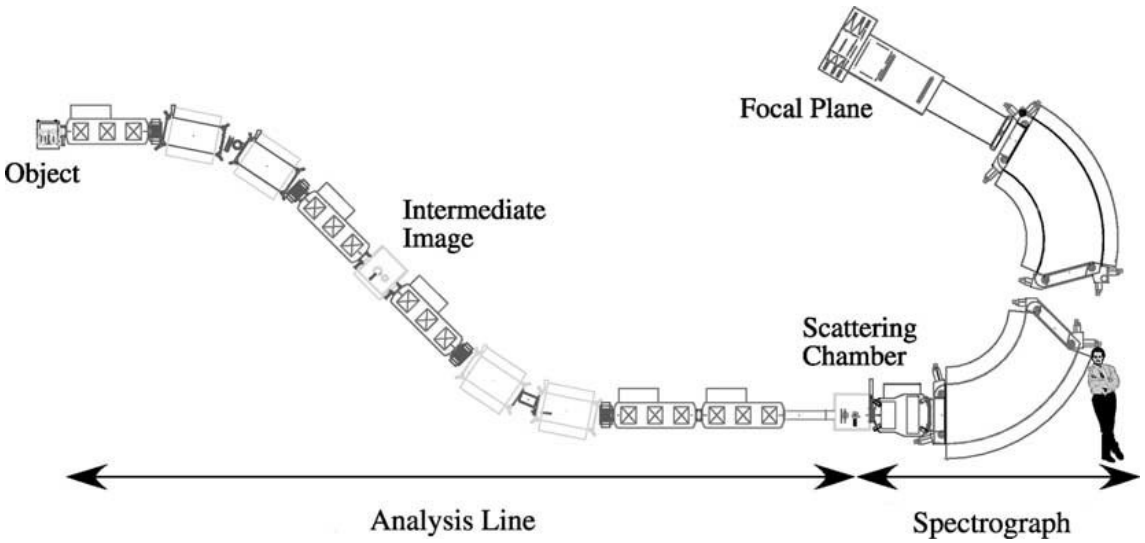

Figure 3.2: A schematic diagram of the S800 taken from reference [12]. Secondary beams enter at the "object" position from the transfer hall and are guided through the S800 to the Focal Plane. A person is depicted in the lower right hand corner for scale.

The S800 is a magnetic spectrograph [12], consisting of two dipole magnets. An ionisation chamber is located at the focal point. The ionisation chamber is used to measure the Z of nuclei and the ToF between the the *obj* scintillator and *E1* scintillator is used to measure the charge to mass ratio. These measurements have to be corrected for the angles at which the nuclei enter the relevant detectors as different momenta appear in different parts of the focal plane for the same nuclide. Angles are calculated using the two cathode readout drift chambers (CRDCs) which form part of the focal plane detector setup along with the *E1* scintillator and ionisation chamber [44]. This setup is shown in Figure 3.2 and the focal plane in more detail in Figure 3.3

The angle of the beam at the focal plane is used to correct for differences in paths nuclei can take through it. Longer paths take more time to traverse the separator which leads to the ToF separation between different charge to mass ratios becoming blurred. A similar effect is observed for the measured Ion chamber energy: the longer the path taken through it is the more energy is deposited. Thus both Ion Chamber energy and ToF must be corrected to account for the paths taken by nuclei. To perform the path correction angles are gathered from positions measured by each of the CRDCs at the focal plane. From this the dispersive angle at the focal plane (afp) can be calculated using:

$$afp = \tan^{-1}\left(\frac{x_2 - x1}{d}\right) \tag{3.2}$$

where x_2 is the position in CRDC2 and x_1 the position in CRDC1 in the dispersive direction, and d the distance between the CRDCs (1073mm). In addition to measuring angles at the focal plane it is possible to calculate the angles at the target position. The fringing fields around the magnets cause aberrations so calculating the angles is performed by producing an inverse map. The inverse map relates positions and angles at the focal plane to angles at the target for a specific

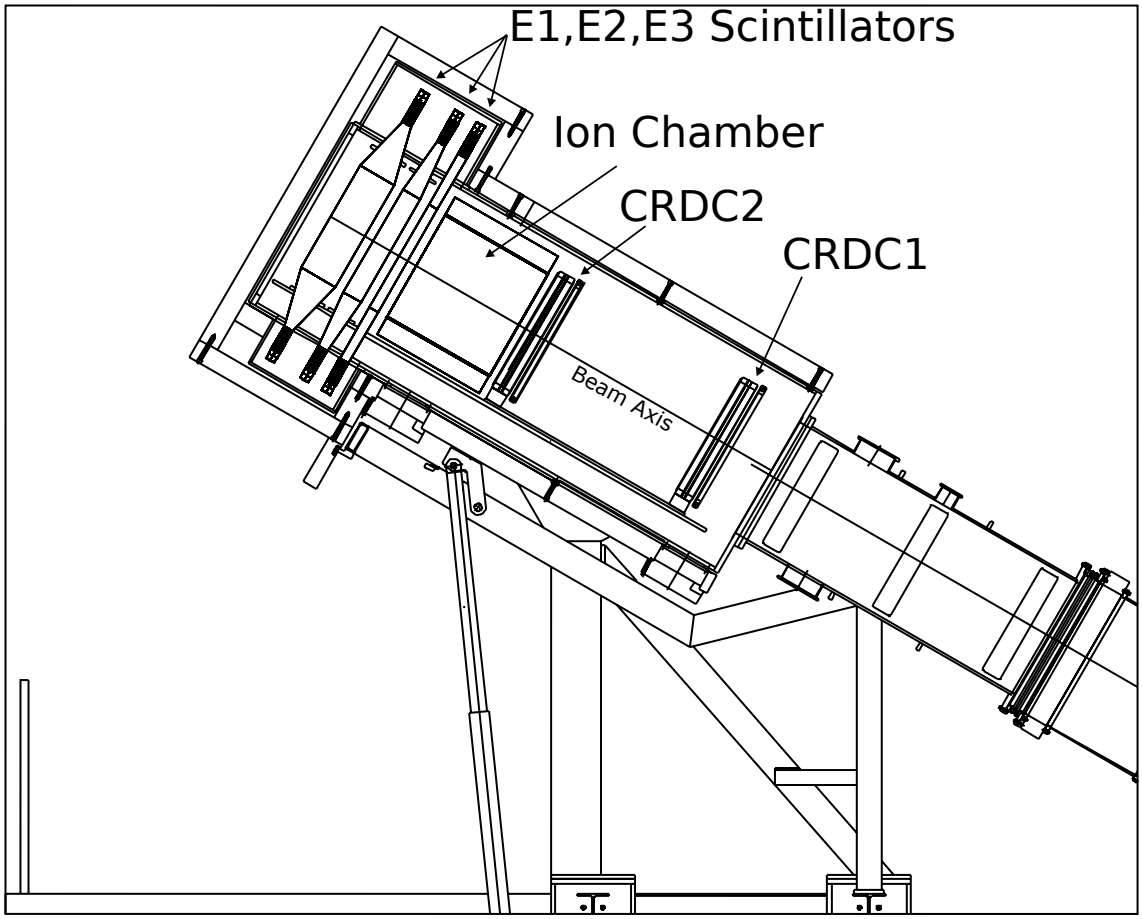

Figure 3.3: Diagram of the S800 focal plane setup taken from references [15,44]. The beam travels along the labelled "beam axis" through the CRDCs, Ion Chamber, and scintillators. The first scintillator from the beam direction is the *E1* scintillator used for the timing in this analysis.

nucleus [45]. It is produced using the COSY code [46]. The angles at the target position are used to aid the Doppler correction of gamma rays, as the relevant angle is that between the nucleus and the gamma ray.

The CRDCs are position sensitive. They are 30 cm by 59 cm and 1.5 cm deep. They are filled with a mix of 80% CF_4 and 20% C_4H_{10} at 140 Torr. Incident beam particles ionise the gas and the electrons travel through the applied electric field to an anode wire. Townsend avalanching occurs as the electrons move to the wire whereby more gas is ionized by the already moving electrons, resulting in a larger current. Located very close to the anode wire are 224 cathode pads which are 2.54 mm thick. These pads register the induced charge from the electrons moving to the anode. The position in the dispersive plane is ascertained by a centre of gravity fit to the cathodes that registered a signal for each event. For the position in the non-dispersive plane the drift time can be used. As the drift time is on the order of 20 μs this limits the rate data can be acquired to around 5 kHz in the S800.

The ionisation chamber is able to measure the Z of nuclei as the energy deposited by ions is

proportional to the Z. This effect is shown by the Bethe-Bloch formula in Equation 3.3.

$$-\frac{dE}{dx} \propto \frac{\rho Z^2}{\beta^2} \tag{3.3}$$

where β is the velocity of the ion as a fraction of the speed of light in a vacuum, and ρ is the density of the material. The ion chamber has the same vertical and horizontal dimensions as the CRDCs, and is 41 cm deep. It is filled with P10 gas (90% argon and 10% methane) which is typically kept at 300 Torr. The operating principles of the detector are similar to the CRDCs, except that instead of ascertaining the position of the ions they detect the energy deposited. In order to reduce the capacitance and thus the electronic noise (from Johnson-Nyquist theory), the anode is split into 16 separate sections which have lower capacitance and the signals from these are summed.

3.5 Gamma ray spectroscopy

Gamma ray spectroscopy is performed to gain high precision information on energies of excited states, hence insight into the structure of nuclei produced. To gain the most information from this technique a gamma ray detector array with a high resolving power (RP) [47] is required. The resolving power is a measure of the ability of a spectrometer to resolve individual gamma rays in a spectrum, as given in Equations 3.5 and 3.4.

$$R = 0.76\left(\frac{SE}{\delta E}\right)P/T \tag{3.4}$$

$$RP = exp\left(\frac{ln(N_0/N)}{1 - ln(\epsilon)/ln(R)}\right) \tag{3.5}$$

where P/T is the peak to total, or size of the peak compared to the background in a spectrum and δE is the energy resolution, SE is the energy spacing of the transitions being resolved, ϵ is the detection efficiency for the peak being resolved, N_0 is the total number of gamma events, and N is the number of counts required in a peak for it to be resolved. To optimise the array one can considering N_0 and N to be constants. To improve the array one must increase either the resolution or efficiency. Due to their high resolution, Hyper-Pure Germanium (HPGe) detectors are often used to maximise resolving power. Scintillating materials such as lanthanum bromide and sodium iodide can also be used but offer worse resolution. Silicon crystals can not currently be grown large enough to have a high efficiency.

Figure 3.4 shows the mass attenuation coefficient (which is proportional to probability) for photo-electric interactions, Compton scattering, and pair production inside germanium. At low energies it is more likely that gamma rays will interact via a photoelectric event and deposit their entire energy in the crystal. Full energy deposition is the ideal situation as none of the photon energy escapes and contributes to background, leading to a very clean spectrum. The gamma rays of interest to the present work are of higher energy however. They are in the region in which Compton scattering is the dominant interaction process. In order to maximise the detection efficiency for the scattered photon, larger detectors are required. However large detectors cause

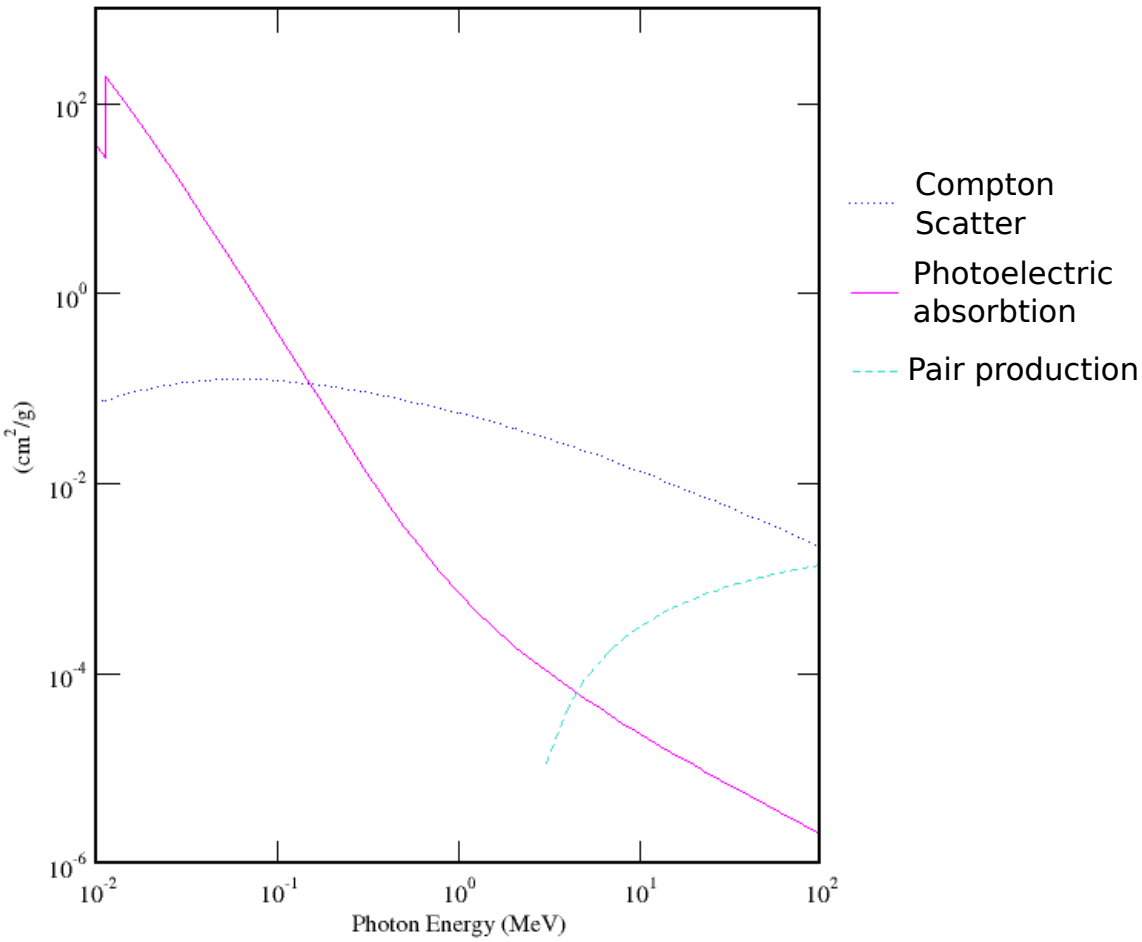

Figure 3.4: The photon mass attenuation coefficient (which is proportional to interaction probability) as a function of photon energy for photoelectric absorption, Compton scatter and Pair production. Adapted from Reference [48].

problems for Doppler correction.

Gamma ray spectroscopy at the beam velocities described here (relativistic gamma ray spectroscopy) additionally requires the energy of observed gamma rays to be Doppler corrected. The formula for doing this is shown in Equation 3.6.

$$E^{\gamma}_{nuc} = E^{\gamma}_{lab}(1 - \beta cos(\theta))\gamma. \tag{3.6}$$

$$\tag{3.7}$$

$$\gamma = \frac{1}{\sqrt{1-\beta^2}} \tag{3.8}$$

where E^{γ}_{nuc} and E^{γ}_{lab} are the energies of the gamma ray in the nuclear and lab frame respectively, γ is the Lorentz gamma factor, θ is the azimuthal angle from the beam direction measured in the

lab frame, and β is the beam velocity as a fraction of the speed of light in a vacuum. Typical values of β for the work described in this thesis vary between 0.3 to 0.4. Uncertainty in the Doppler correction effectively worsens the resolution of a detector, so knowing θ to high precision is of great importance. In order to attain a higher precision in θ the contacts on HPGe crystals can be segmented. Segmentation allows one to deduce where a gamma ray interacted within the detector volume and get a better estimate of θ. Section 3.5.1 and Chapter 4 contain detailed information on how this is applied to these arrays.

A longer nuclear half life will prevent an accurate Doppler correction as decays will happen downstream of the target position rather than at the target position. As decays occur downstream the measured θ will become wrong, preventing an accurate Doppler correction. With the beam velocities used here any state with a half life longer than around 15 ps will not Doppler correct properly. Typically excited nuclear states have half lifes on the order of a few pico seconds but range to years. The lifetimes of excited states can be described from the following equation, derived from Fermi's golden rule.

$$\lambda(\sigma L) = \frac{2(L+1)}{\hbar\epsilon_0 L[2(L+1)!!]^2}\left(\frac{E_\gamma}{\hbar c}\right)^{2L+1} B(\sigma L) \tag{3.9}$$

where L is the multipolarity of the decay, E_γ is the gamma ray energy, and ϵ_0 is the permeability of free space. $B(\sigma L)$ is the transition matrix element squared and describes how similar the initial and final states are.

3.5.1 SeGA

The SeGA [49] (SEgmented Germanium Array) system is one of the gamma ray detection arrays available at NSCL. It consists of 18 electrically segmented HPGe semi-conducting detectors, and is used for the detection of prompt gamma rays at the target position of the S800. In order to increase solid angle coverage the detectors are arranged as shown in Figure 3.5. In other arrays to get a lower error in θ the flat end of a cylindrical detector (which has a smaller area) would be facing the target. Here the segmentation allows a high resolution in θ regardless of the geometry. A side-on configuration is used to give a larger solid angle and hence larger efficiency. The detectors are arranged in two rings, one at 37 degrees with 7 detectors and one at 90 degrees with 10 detectors. This is known as the classic SeGA configuration and is shown in Figure 3.5. The detectors are located 24.2 cm from the target. The classic SeGA configuration is optimised for Doppler boosted gamma rays which are more forwards focused, with some allowances for the space available at the target position.

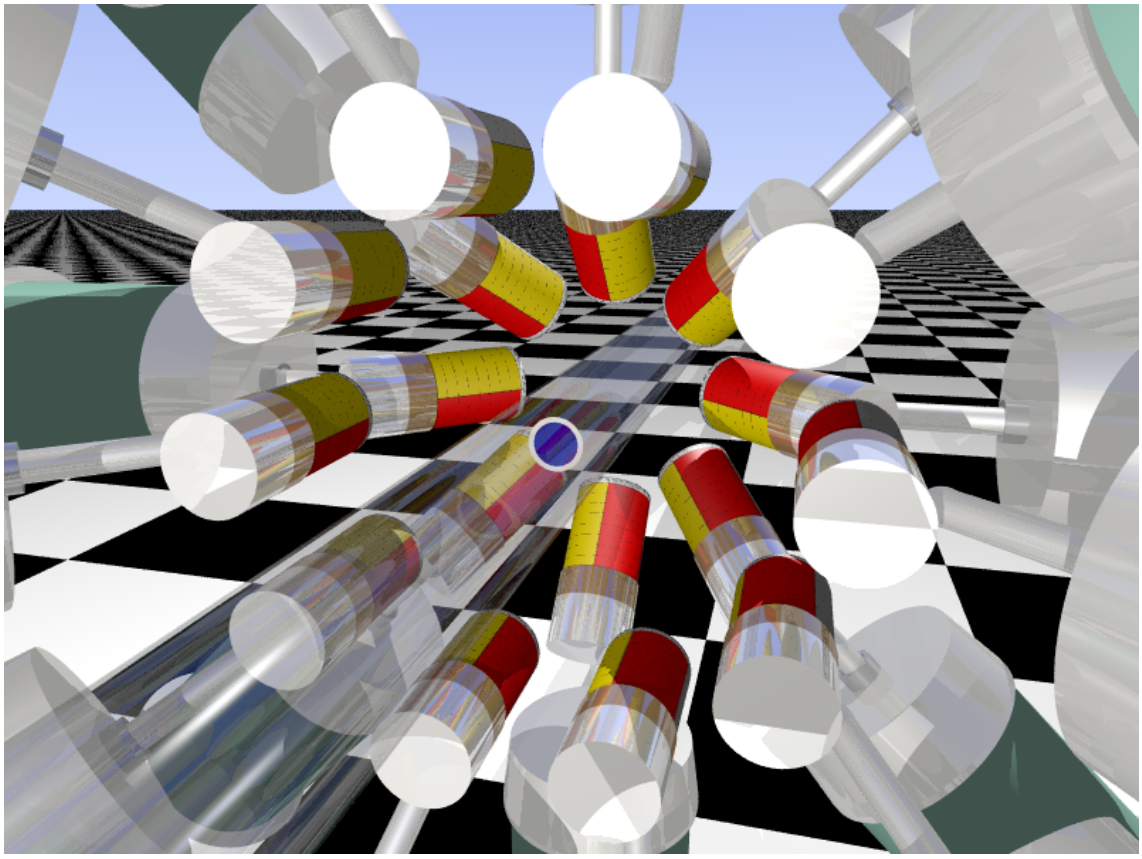

Figure 3.5: The SeGA array and target position viewed from upstream. Taken from Reference [15]. The red and yellow volumes are germanium crystals with the lines on them representing the segmentation of the array. The blue circle is the target.

Each SeGA detector consists of a coaxial germanium crystals with a 70 mm diameter and 80 mm in length. The segmentation of the cathodes is shown in Figure 3.6. Each crystal has 8 longitudinal segments and four axial for a total of 32 segments.

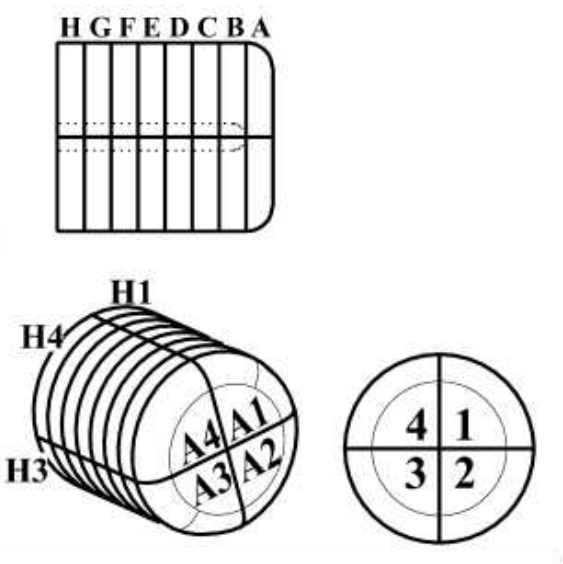

Figure 3.6: A diagram of the segmentation of the germanium crystals from SeGA detectors taken from ref [50]. There are seven axial segments and four radial.

The energy of gamma rays is taken from the central contact, with the segmented cathodes used to deduce a hit pattern [50]. When a gamma ray enters the detector it may scatter several times. While this will not effect the energy measured from the anode it will produce signals in several cathodes. The flow chart in Figure 3.7 is used to decide which cathode signal refers to the first interaction point (which is used to determine θ for Doppler correction)

An addback correction is also applied, whereby signals detected in adjacent detectors are summed with the highest energy interaction point from both used for the Doppler correction. As we are not expecting high multiplicity data this greatly reduces the Compton background. This is shown in detail in Chapter 5.

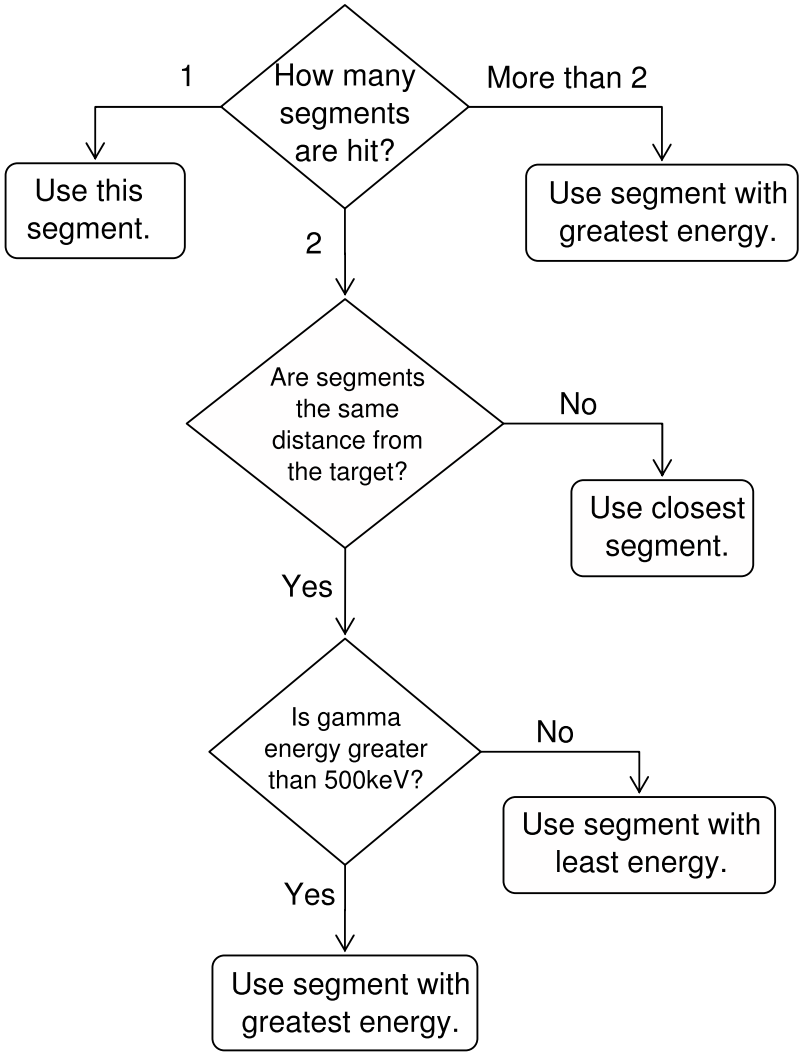

Figure 3.7: The process by which the first gamma ray interaction point in SeGA is decided for use in Doppler correction. This process has been developed to correctly identify the first interaction point with the highest probability.

Chapter 4

GRETINA

The experiment presented in this thesis using GRETINA was one of the first in a campaign to couple GRETINA to the A1900+S800 setup at MSU.

GRETINA (Gamma ray energy tracking in-beam nuclear array) is the first implementation of GRETA (the Gamma ray energy tracking array). GRETA, once constructed, will be a 4π array of large volume HPGe crystals capable of tracking the interactions of gamma rays within it. Tracking gamma ray interactions enables GRETA to use Compton reconstruction and accurate Doppler correction. This helps reconstruct Compton background, making a full GRETA on the order of 1000 times more powerful than current arrays [47].

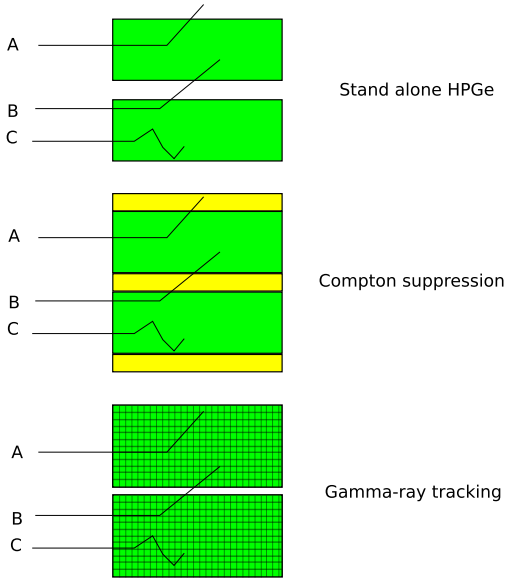

Figure 4.1: A schematic illustrating the effects of Compton scattering and ways of suppressing it. The green volumes are HPGe, the yellow volumes are scintillating material, and grey lines represent segmented detectors.

Figure 4.1 is a schematic illustrating Compton-scattering events between detectors. The advantage of Compton suppression over unsuppressed HPGe is the ability to veto Compton events that have scattered into surrounding scintillating material. This removes almost all of the Compton background. However, it results in an efficiency loss compared to having a larger volume HPGe detector. GRETA was designed for high-spin experiments, where many gamma rays need to be resolved in coincidence. Large detectors are not good for resolving many gamma rays as it is impossible to deconvolve the Compton scatter from multiple simultaneous events. To gain a higher efficiency than Compton suppressed arrays but maintain the ability to resolve high multiplicity events the idea of a germanium shell able to track gamma rays was put forward [47].

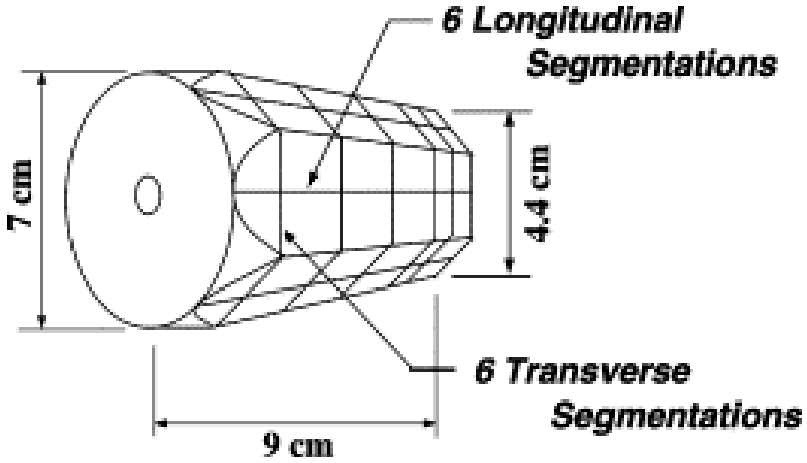

Figure 4.2: A diagram showing the size and segmentation of the GRETINA crystals, taken from [51]. There are six axial and six radial segments. Including the anode, 37 signals are read from each crystal.

GRETINA only has a solid angle coverage of $\approx 1\pi$ and therefore lower efficiency than some existing HPGe arrays [52]. However, it has finer position resolution so is ideal for relativistic gamma ray spectroscopy. The existing HPGe array at NSCl SeGA has an efficiency of around 3% at 1.3 MeV. GRETINA has an efficiency of around 6.6% at 1.3 MeV, and the improved resolution in θ dramatically improves Doppler correction and therefore improves the effective resolution for in-beam data.

The GRETINA crystals are tapered and hexagonal, as shown in Figure 4.2, to better aid with tessellation, with each crystal containing six longitudinal and six transverse segments for a total of 36 segments. The crystals are arranged in seven cryostats of four crystals each, for a total of 28 crystals. For the work presented in this thesis the crystal arrangement was closely packed downstream, in a similar configuration to that depicted in Figure 4.3. This configuration gives a higher efficiency for Lorentz-boosted gamma rays, most of which will be emitted forwards.

4.1 Signal Decomposition

In order to Compton track the data the position of all gamma ray interaction points must be known. In fact, a position resolution of around 2 mm is required, which is smaller than the size of the segments. To achieve sub-segment resolution pulse-shape analysis has to be performed to

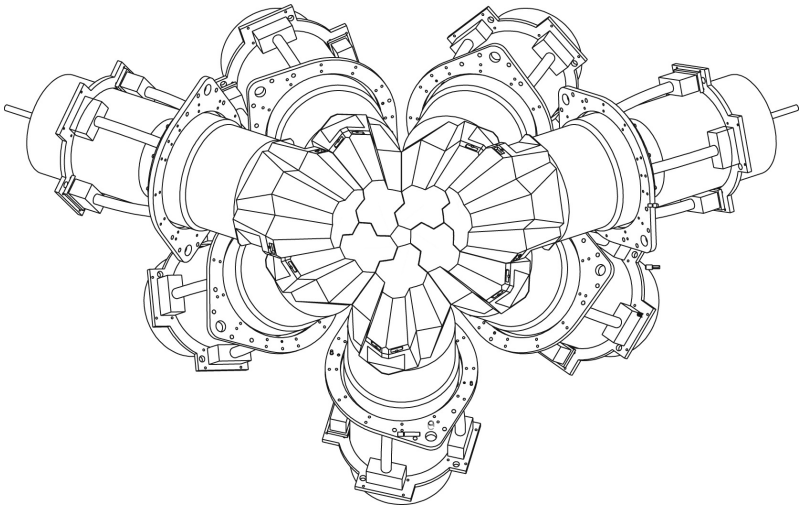

Figure 4.3: Schematic diagram showing a possible GRETINA configuration taken from [14].

analyse "image charge". Image charge is induced charge from the movement of electrons and holes on the contacts surrounding the one closest to the interaction point. The general principle is to have a series of example pulses that can be fitted to ones taken during an experiment. This should determine the number of gamma ray interaction points, their positions, and the energy deposited at each. This effect is shown in Figure 4.4 with signals collected from an interaction at a known position.

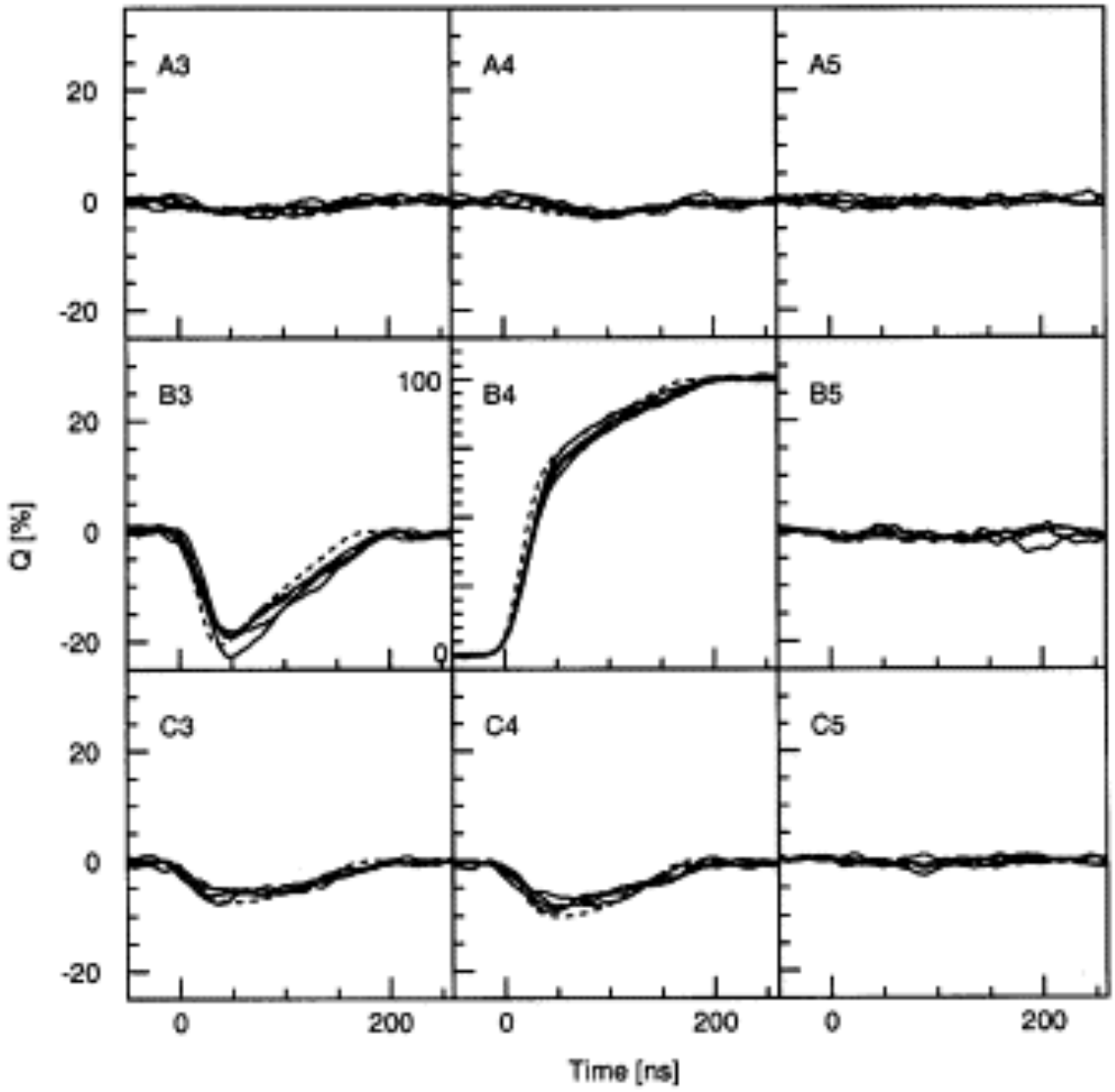

Figure 4.4: An example of signals collected from a GRETINA crystal using a collimated source. Each panel is the signal read from a different cathode, letters represent radial segments and numbers axial. The interactions are assumed close to segment B4 where most of the signal is collected and 4.5 mm away from segment C4 and 1.5 mm away from segment B3. The dashed lines show calculated signals, these signals have been corrected for cross talk effects [53].

The general approach [51] is to simulate the electrical signals that would be collected in each contact from interactions at every point in the crystal (in practice a 1 mm grid is used). However, simulation cannot account for cross talk between electrical components. In this context cross talk refers to the capacitive coupling between contacts as well as the coupling between closely placed electronics within the pre-amplifier. The cross-talk effects look very similar to the image charge and are very sensitive to small changes in each detector. To have a basis that accounts for the cross talk the following steps are taken:

- Calculate an electric field for each crystal based on geometry, impurities and bias voltage for each crystal.
- Calculate the charge collected on each pad for a charge at each point across the crystal.
- Fit these calculated signals to known signals taken with a ^{60}Co source to take into account cross talk.

The effect of the cross talk correction is shown in Figure 4.5, it is clear that this is a significant step in the decomposition process. It has been reported in reference [51] that imperfect basis simulation can cause the decomposition routine to split interaction points. An effect of this is that the energies of reconstructed gamma rays do not appear to be reliable, even though the use of pencil beams has shown that the reconstructed positions are. To counter this the energies for events are taken from the central contact of the crystal, rather than the segmented pads. To get interaction energies when there is more than one in the crystal, the crystal energy is split by ratio of the energies measured in the segments.

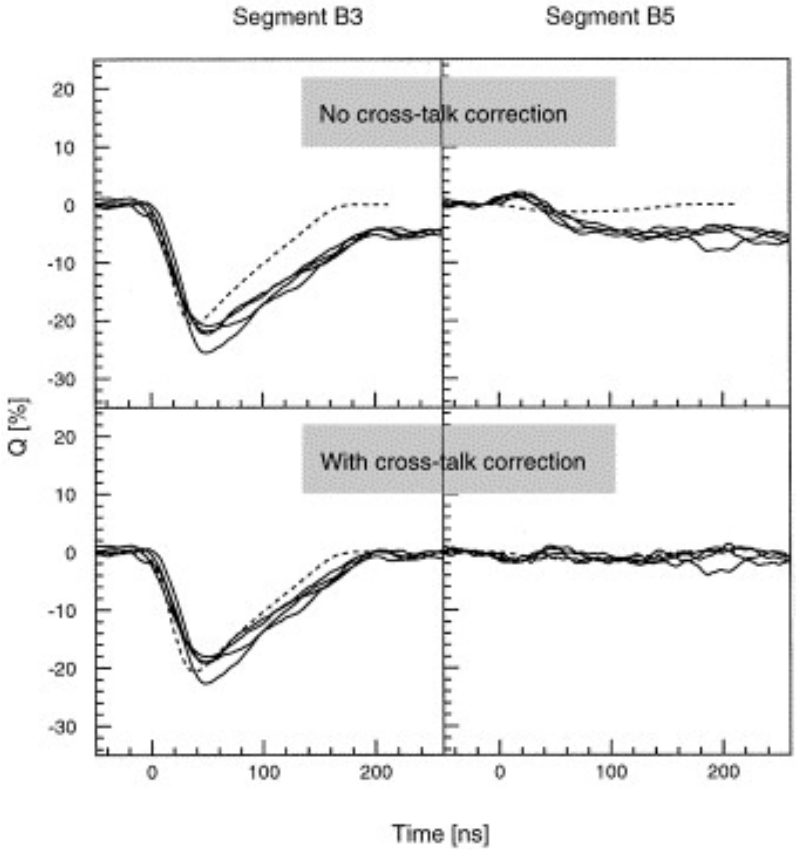

Figure 4.5: The signals of segments B3 and B5 are shown before and after cross talk corrections are applied. The signals are the same as those shown in Figure 4.4. Taken from [53].

4.2 Compton tracking

Once the three-dimensional position of every interaction point has been determined by the signal decomposition, they need to be clustered into events from individual gamma rays. Compton tracking is used to assess how good the clustering is [54].

Compton tracking works by assigning each cluster a figure of merit (FoM) based on how closely its interaction points fit to the Compton scatter formula:

$$E_{\gamma}^{''} = \frac{0.511}{1 + \frac{0.511}{E_{\gamma}} - \cos(\theta_c)}, \tag{4.1}$$

where $E_{\gamma}^{''}$ and E_{γ} are the energies of the scattered and incident gamma rays in MeV, and θ_c is the angle between them. The gamma rays are assumed to have originated in the centre of GRETINA. The best fit to this equation is found choosing a sequence of interaction points with the lowest FoM. The figure of merit defined as:

$$\mathrm{FoM}_n = \frac{\theta_{mn} - \theta_{cn}}{\Delta\theta} \tag{4.2}$$

$$\mathrm{FoM} = \left(\frac{1}{N-1}\right) \sum \mathrm{FoM}_n, \tag{4.3}$$

where FoM_n is the FoM for the n^{th} scatter out of N scatters, θ_{mn} is the measured angle between incident and outgoing gamma rays, θ_{cn} is the predicted Compton angle based on Equation 4.1, and $\Delta\theta$ is the combined error from the position. The error from energy not considered as it is much smaller. The full Compton-tracking process is described below.

1. The interaction points are assigned polar co-ordinates.
2. The points are ordered by θ, and sorted through to find any that are within the clustering angle (25 degrees is the angle used in the presented analysis).
3. A FoM is calculated for each ordering of the interaction points, the order with the lowest FoM is kept.
4. If the FoM is greater than 1.0 it is assumed that the clustering is incorrect and an attempt is made to change the clustering to get a better FoM. The cluster can be split, add to another, or both split with some interactions reclustered with another event.
5. Events with one interaction point are assumed to be photoelectric events. These events are initially given a FoM of 0.
6. Photoelectric events that happen deeper than 90% of their interaction length +0.5 cm are vetoed as they are most likely Compton scatter that has not been fully captured.

As alluded to in the previous section, the decomposition does not always provide perfect set of interaction points, in which case the Compton tracking will not be perfect. The range of FoM observed is attributed to the position resolution of GRETINA. Figure 4.6 shows the range of FoM.

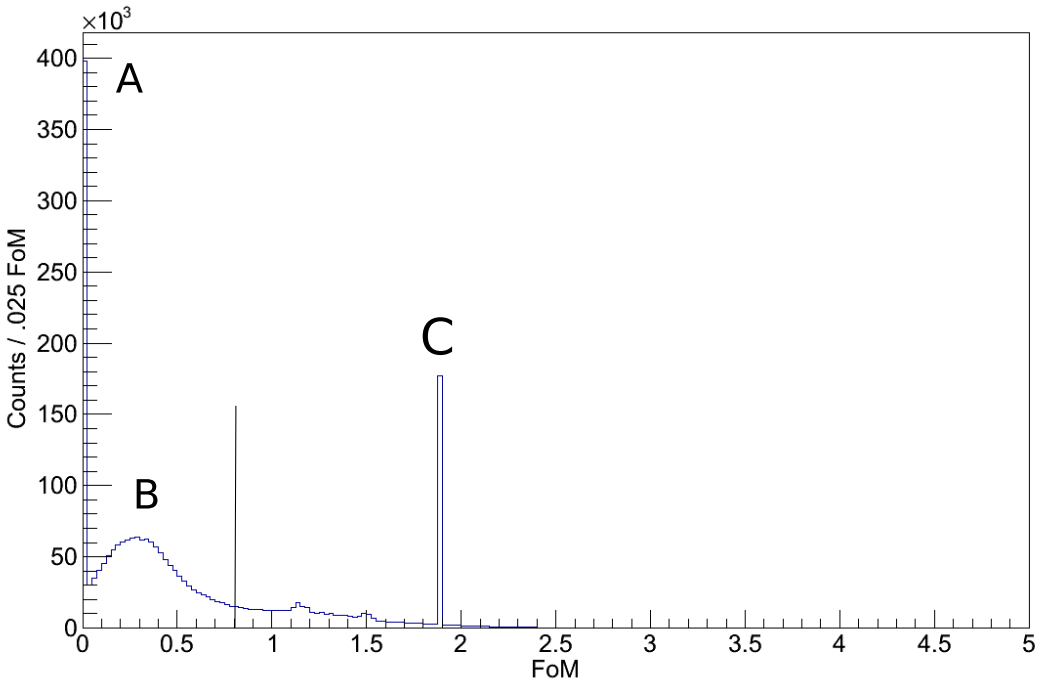

Figure 4.6: The FoM for fully tracked data taken with a ^{152}Eu source. The first bin, labelled A, mostly corresponds to events with only one interaction point, hence a FoM of 0. The hump around B is the majority of the good data, these have non-zero FoM due to the position resolution of GRETINA. The large peak labelled C corresponds to photoelectric events that happen too deep into the crystal and are most likely scatter (see step 6 above). The line at 0.8 is the cut applied to the FoM, those with a lower FoM are deemed to be good events.

The effect of this FoM cut to a spectrum is demonstrated in Figure 4.7. The upper panel (A) shows a spectrum taken with a ^{152}Eu source, the red data have the FoM cut applied and the blue do not. When the FoM cut is applied there is a loss of data, but a higher peak to background ratio. The lower panel of Figure 4.7 shows the 244 keV peak from the decay of ^{152}Eu from the same data in the upper panel. This closer look demonstrates the higher peak to background once the FoM cut is applied.

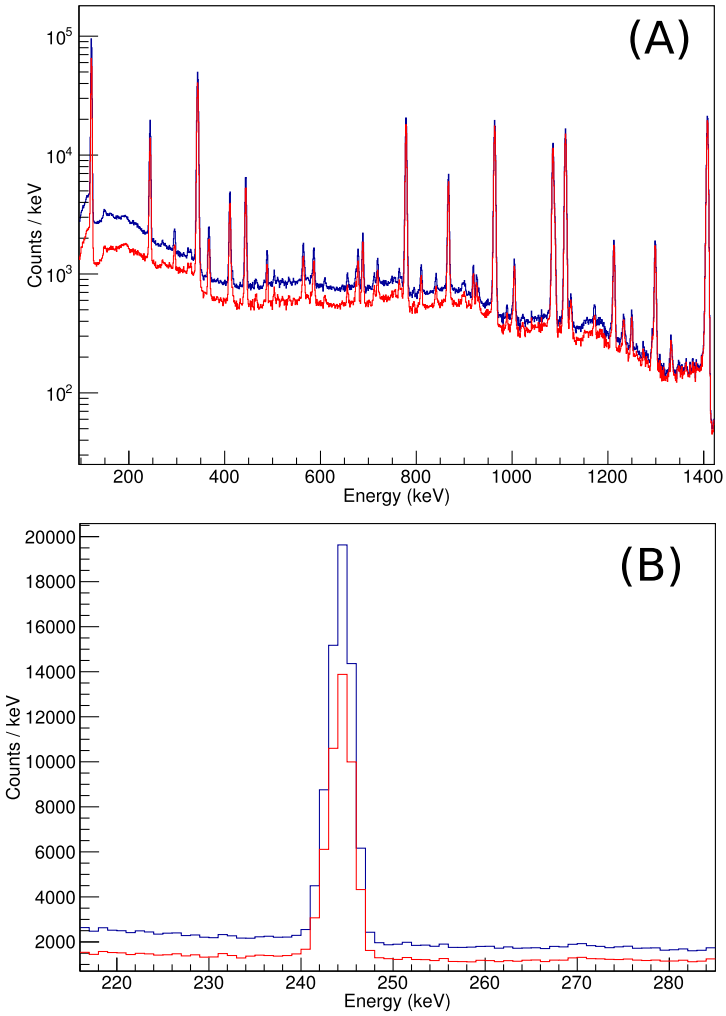

Figure 4.7: Gamma ray spectra taken with a ^{152}Eu source at the centre of GRETINA. The upper panel shows the full calibration spectra, the lower panel is zoomed in to just the 244 keV peak. The red spectrum has had the FoM cut applied and the blue has not, see text for details.

4.3 Efficiency of GRETINA

The efficiency of GRETINA was measured before the experimental run described in Chapter 6 using ^{152}Eu and ^{226}Ra sources placed at the centre of the array. The measured efficiency is shown in Figure 4.8. The efficiency of GRETINA was calculated and shown in two different modes: mode 1, wherein the data were fully tracked and the FoM cut shown in Figure 4.6 was used; mode 2 the individual GRETINA crystals were treated as separate detector and no clustering was done. In the latter case an add back routine was also used to reduce the Compton background. The clustering and tracking process did not always find a good solution and consequently there was an efficiency loss in the clustering routine. This loss was recouped at energies where Compton scatter is the dominant process and the tracking process provides a higher efficiency.

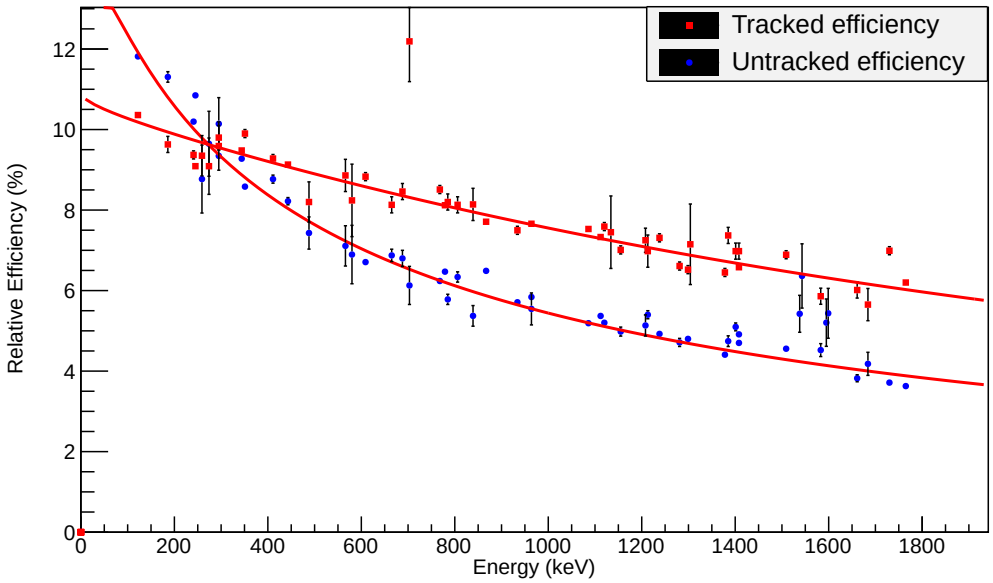

Figure 4.8: Efficiency curves for GRETINA calculated from a ^{152}Eu spectrum taken with the source at the centre of GRETINA. Mode 1 (red) is in red and Mode 2 in (blue).

Data	A	B	C
Tracked	12.1 ± 844	0 (fixed)	0 (fixed)
Untracked	2.389 ± .02	0 (fixed)	0 (fixed)

Table 4.1: The fit parameters for tracked and untracked efficiency curves in GRETINA, part one.

The efficiency curves have been fit with the following equation where E is the energy in MeV:

$$\text{Efficiency} = e^{([A+Bx+Cx^2]^{-G}+[D+Ey+Fy^2]^{-G})^{-1/G}}. \tag{4.4}$$

$$x = log\left(\frac{E}{100}\right) \tag{4.5}$$

$$y = log\left(\frac{E}{1000}\right) \tag{4.6}$$

It is clear from the error on paramater A that the standard efficiency curve is not a good fit to the tracked data. At energies lower than the crossover point (where the tracked and untracked

D	E	F	G
1.694 ± .001	-.546 ± .002	-0.0826 ± 0.001	11.7 ± 160
2.136 ± 0.005	-0.517 ± 0.006	-0.06 ± 0.01	6.76 ± 0.4

Table 4.2: The fit parameters for tracked and untracked efficiency curves in GRETINA, part two.

A	B	C
7.9 ± 0.4	-117 ± 5	0.810± .007

Table 4.3: The fit parameters for the efficiency of SeGA, fitted with equation 4.7.

data cross over) the shape of the tracked efficiency curve is unusual. The exact shape is not exactly known. For the analysis in this thesis the tracked efficiency curve is only used for energies above 300 keV, for which a first order polynomial fit is used.

Unfortunately, for in-beam data it is not possible to use the tracked efficiency for two reasons:

1. The clustering process assumes that gamma rays originate from the centre of GRETINA. As the position sensitivity of GRETINA is around 2 mm [14] it stands to reason that a gamma ray that has come from a position different to the centre of GRETINA by more than 2 mm will have a FoM that is measurably larger. A larger FoM means the event may not be clustered properly and may be cut out in subsequent analysis. Only events that originate more than 2 mm from the centre of GRETINA are susceptible to this effect. At $\frac{1}{3}$ of the speed of light in a vacuum 2 mm corresponds to about 20 ps. So beyond around 20 ps the longer the half life of the state the less likely gamma rays from the decay of the state, or from subsequent decays will be measured with the correct efficiency.

2. The efficiency of the clustering routine may change with the multiplicity of events. So for nuclei that emit large chains of multiple gamma rays a different efficiency is observed to those that emit one or two gamma rays. This means that a calibration curve from a calibration source may produce different results to the efficiency for in-beam data. A further, similar concern is the effect of bremsstrahlung which is not present when using a calibration source. Bremsstrahlung may increase the multiplicity of events when beam is used.

In the subsequent analysis in this thesis, where efficiency is required, the untracked data is used. If a comparison is now made to the efficiency of SeGA (shown in Figure 4.9) it is clear that for SeGA a much steeper drop off with energy and lower overall efficiency is presented.

$$\text{Efficiency} = A(E_\gamma - B)^{-C}. \tag{4.7}$$

The SeGA efficiency curve has been fit to with Equation 4.7, the parameters from the fit are in Table 4.3.

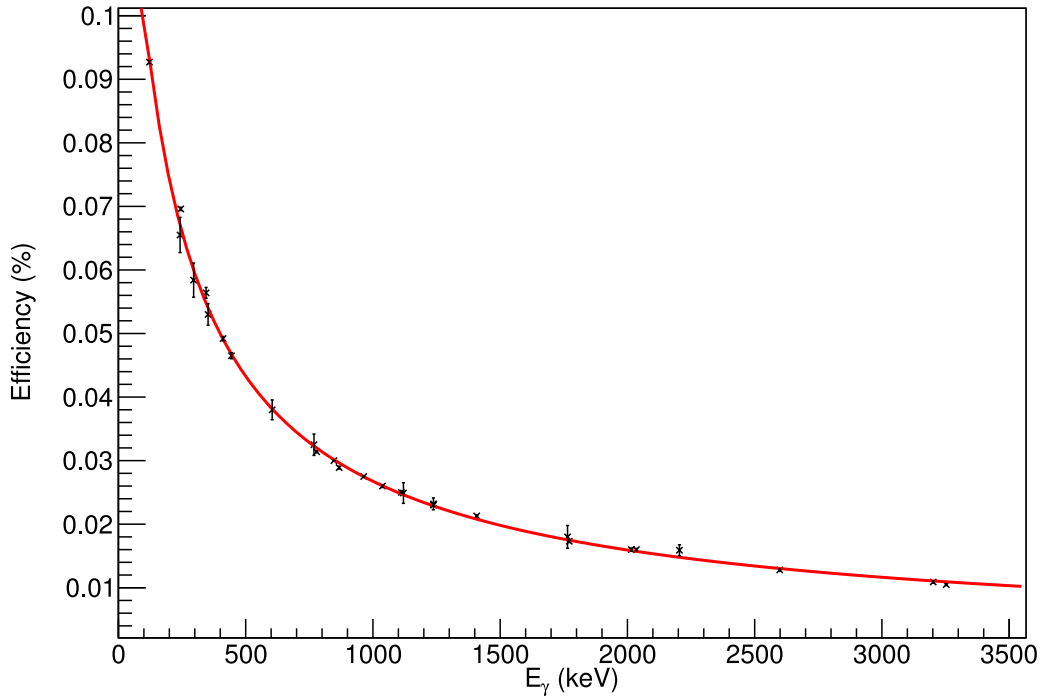

Figure 4.9: Efficiency curve for SeGA calculated from ^{152}Eu spectrum with the source at the centre of SeGA. Prepared by S. Milne.

Chapter 5

SeGA Analysis and results

The aim of the first experiment was to perform mirrored knockout reactions. Mirrored reactions are pairs of reactions where the parent and daughter nuclei are mirror nuclei. To investigate these reactions it was necessary to run with two settings: a ^{54}Ni beam to populate new states in exotic nuclei, and an ^{54}Fe beam (mirror of ^{54}Ni) to populate IAS in the stable counterparts. The work presented in this Chapter was published in reference [55]. The analysis was performed using the GrROOT software [56].

5.1 Secondary beams

The secondary beams are identified by plotting the time signals of the xfp and obj scintillators relative to the *E1* scintillator as described in Section 3.3. The A1900 was first tuned for ^{54}Ni and the particle ID is shown in Figure 5.1. Different nuclides are observed along diagonal lines which are labelled. This reaction setting was run for approximately 78 hours.

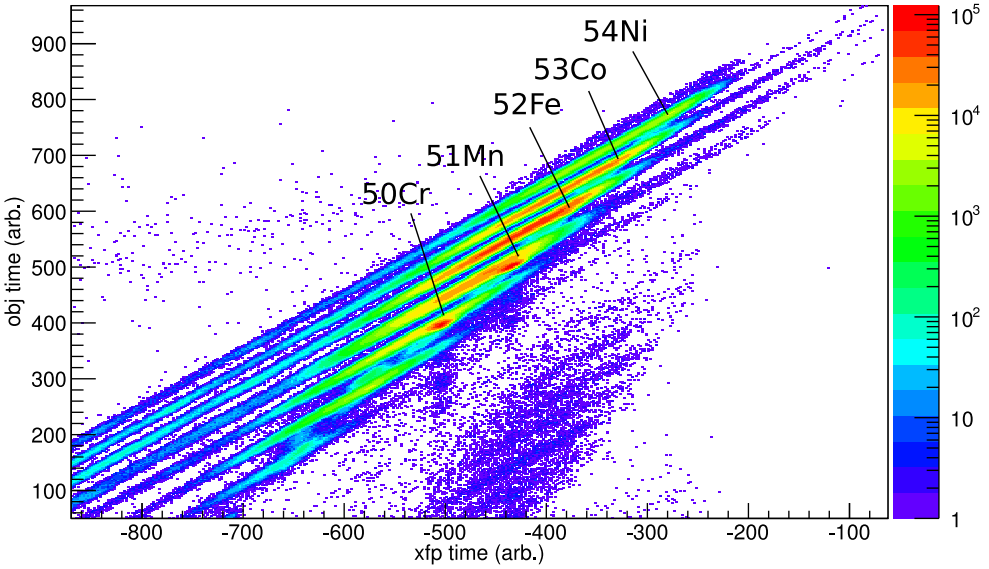

Figure 5.1: The particle ID of incoming beams is shown with the A1900 tuned to produce ^{54}Ni. The contaminants are labelled. The spectrum was created by plotting the timing signals from the *xfp* and *obj* scintillators relative to the *E1* scintillator.

In order to perform mirrored reactions the setup was also used to produce a ^{54}Fe beam. This is curious as it is a rare case of projectile fragmentation being used to produce a stable beam. Due to the higher cross section enough data were gathered after running for less than 1 hour [57]. The particle ID is shown in Figure A.1 in Appendix A.

5.2 Secondary reaction

Reactions from the secondary beams were identified in the S800. Gating on an incident beam allowed for unambiguous identification of recoils from the reaction. Figure 5.2 depicts fragmentation of fragmentation from the ^{54}Fe beam, with the loci labelled. These plots were produced using a software gate on the secondary beam particle ID to isolate individual nuclides. Each locus in Figures 5.2 and A.3 is a different nuclide identified by charge and mass as described in Chapter 3. The red lines denote nuclides of the same z and the black lines denote nuclei of the same T_z. Although the S800 beam blocker was tuned to not let through unreacted beam, ^{54}Fe in this case, some will make it through. This was due to the momentum spread of the beam and possibly variation in the charge state of the beam. Consequently, the ^{54}Fe in this particle ID plot corresponds to the tail of the momentum distribution for the reaction. Particle identification plots such as this from the ^{54}Ni and ^{53}Co beams are shown in Appendix A, with the beam nuclei and either ^{51}Co or ^{51}Cr labelled in each case.

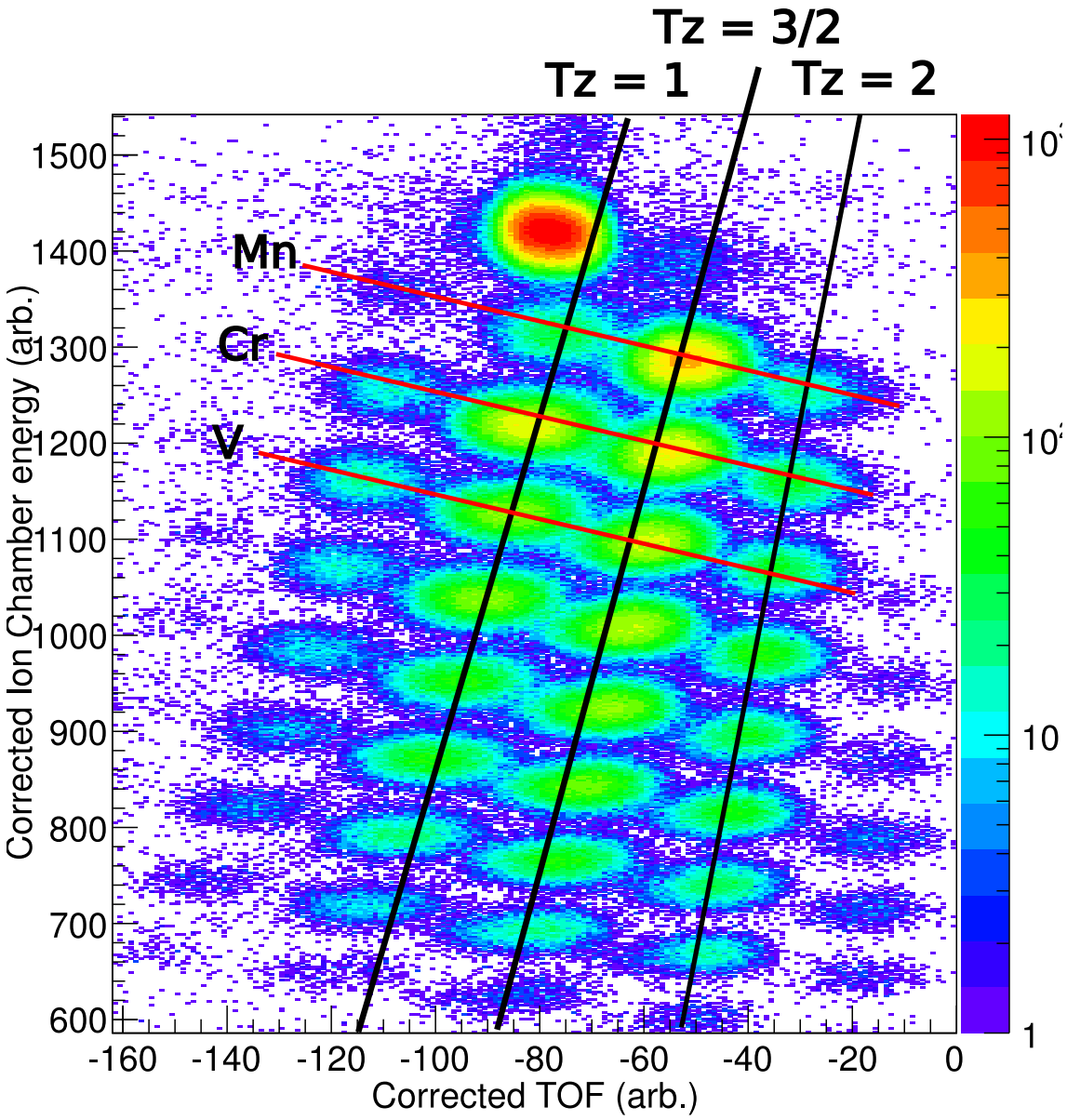

Figure 5.2: Particle identification after fragmentation of ^{54}Fe in the S800. The spectrum was created by selecting the ^{54}Fe data from plots such as Figure 5.1. See text for details.

5.3 Gamma ray calibration

Gamma ray spectra were produced by gating on both a secondary beam and recoil from a secondary reaction. In order to resolve peaks the spectra had to be Doppler corrected using Equation 3.6. The main features of these spectra are the bremsstrahlung continuum, the peaks, and the Compton background. Figure 5.3 shows a Doppler corrected ^{52}Fe spectrum, with the only peak corresponds to the 2^+ to ground state transition.

The bremmstrahlung background was reduced by applying a timing gate. The time of signals

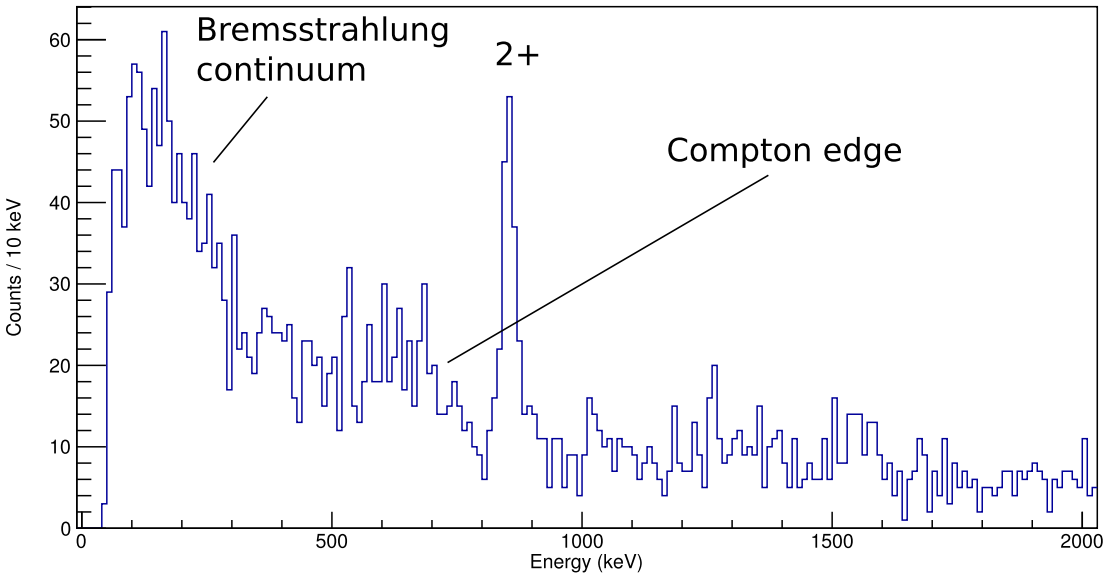

Figure 5.3: Doppler corrected ^{52}Fe gamma ray spectrum with the main features labelled. The spectrum was created by selecting ^{54}Fe beam data in the A1900 and ^{52}Fe data from the S800 detectors.

from SeGA was measured relative to the signal the beam produced in the *E1* scintillator using a time analogue converter (TAC), the distribution of which is shown in Figure 5.4. The black lines represent a cut that was applied to reduce the bremmstrahlung background. Figure 5.5 shows the same gamma ray spectrum as in Figure 5.3 with the gate applied. The reduction in the low energy background is clear.

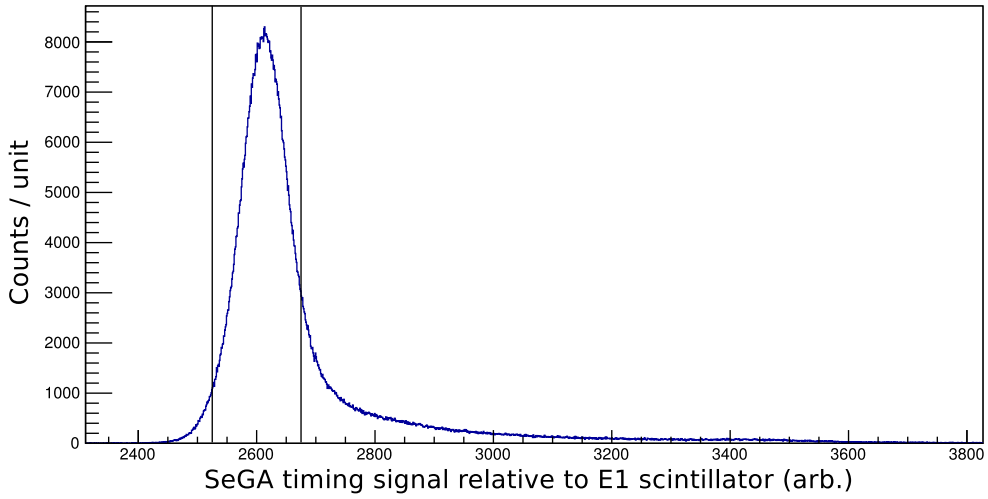

Figure 5.4: Timing signals from the SeGA array measured relative to signals in the *E1* scintillator. The black lines represent the cut used to reduce the bremsstrahlung background.

By calibrating using short-lived nuclear states (< 10 ps) it is calculated that the state decays before it effectively leaves the target. (Target thickness ≈ 1 mm, and the beam velocity of ap-

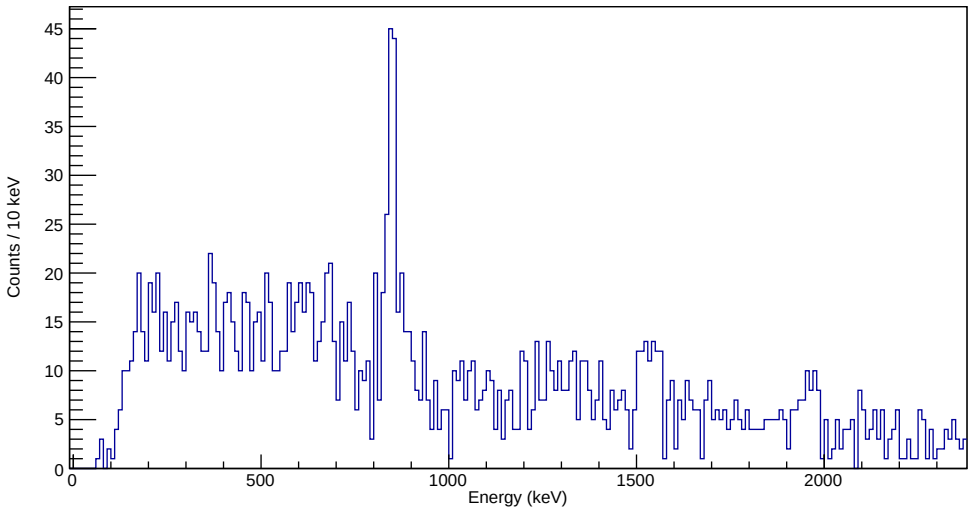

Figure 5.5: Doppler corrected ^{52}Fe gamma ray spectrum produced as in Figure 5.3 with a timing gate applied.

proximately 0.1 $^{\text{mm}}/_{\text{ps}}$). In order to fully Doppler correct spectra, the beam velocity at an effective target position (ETP) was determined. The ETP was used to account for the target not being perfectly centred in the array and long-lived states which mostly decayed downstream of the target. As SeGA was configured into two rings with different θ an incorrect Doppler correction would lead to the same peak in each ring appearing to have different energy. While there are an infinite number of combinations of ETP and β that would make the peaks in both detectors align, only one solution aligned the peaks to the correct energy. To find the ETP that corresponds to the physical target position (at the centre of SeGA) the β and ETP were varied for known transitions from states with short half lifes. For this approach to work the transitions chosen must have decayed before the nucleus had left the target. States with half lifes < 5 ps were chosen, as the target thickness was ≈ 1 mm and the beam velocity was approximately 0.1 $^{\text{mm}}/_{\text{ps}}$. This approach allowed for deduction of the physical target position. Unknown states were then assumed to have promptly decayed, and only β was varied to align them in the two rings of SeGA.

1. The energy of a peak was measured in each ring of detectors separately.
2. The lab energy of these peaks was calculated for each detector ring.
3. For a range of β values:
   - The energy of both peaks was calculated with a range of ETP.
   - The energy in both detectors was recorded for all values of β and ETP.
4. This data was plotted for all values where the peaks had the same energy in both detectors.
5. For known decays:
   - The data points were selected that produced the correct energy, in order to find the ETP for a transition of that lifetime.

6. For unknown decays:

   - An ETP was assumed which was appropriate for prompt decays, unless a longer lifetime was expected, to find an ideal β for the analysis of this nucleus.

An example of this analysis is depicted in Figure 5.6 for the 850 keV transition from the first excited 2^+ in ^{52}Fe to the ground state ($T_{\frac{1}{2}} = 7.8$ ps), for solutions where peaks in both rings of SeGA have the same energy are shown. The X and Y axes show the β and ETP used, and the Z axis shows the energy of the peaks. This 850 keV peak was used to deduce an ETP of 0.1 mm for that decay, as shown in Figure 5.6. From this analysis it was determined that the effective target position for prompt decays is -0.02 mm.

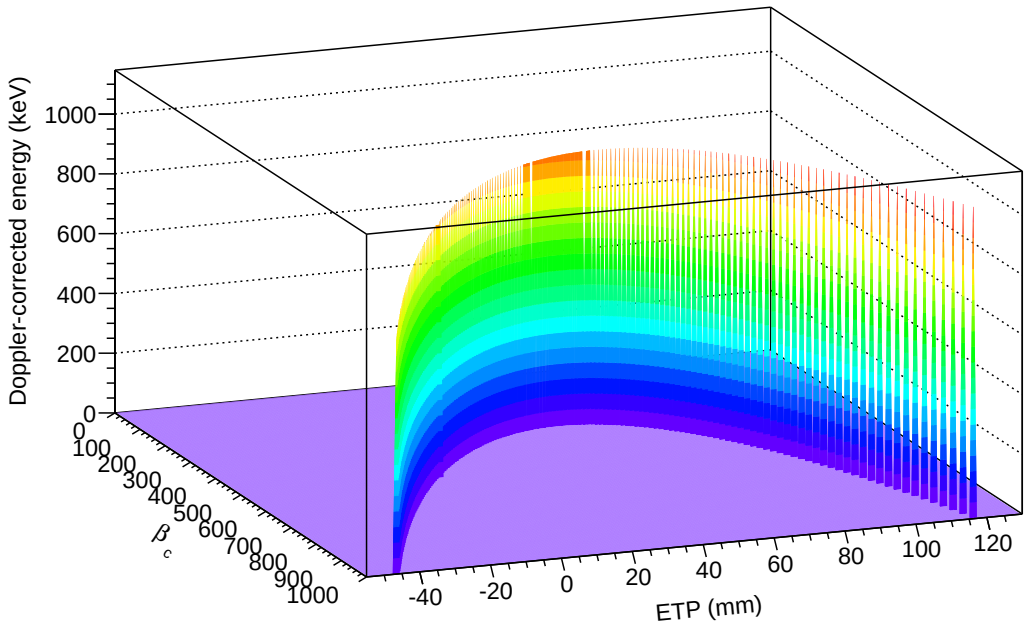

Figure 5.6: The results from the algorithm in appendix B. β_c is proportional to β such that $\beta = 0.301 + 0.0001\beta_c$, ETP is the effective target position, and the Doppler corrected energy is the energy that gets the peaks to line up from the two rings of SeGA.

5.4 Indirect mirrored reactions to the $A = 51$ system

The data presented in the following Sections represents the only spectroscopy of excited states in ^{51}Co. The level scheme was deduced by comparing to known states in ^{51}Cr.

Mirrored reaction mechanisms were used to populate ^{51}Co and ^{51}Cr from ^{54}Ni and ^{54}Fe beams. The reactions used were 1p2n removal and 2p1n removal, which are not necessarily direct reactions [38]. There are still limits on the spins of states that can be populated due to the available angular momentum from removal of the corresponding nucleons. The unit of angular momentum limit means that population of a similar range of states may be expected. Figure 5.7 shows the

gamma ray spectra resulting from these mirrored reactions. Two peaks are observed in each spectrum in ^{51}Cr that have the same energies as the previously observed decays from the first excited $^{11}/_{2}-$ and $^{13}/_{2}-$ states and are labelled as such. The newly observed peaks in ^{51}Co are assigned as the mirrors of the known $^{11}/_{2}-$ and $^{13}/_{2}-$ states in ^{51}Cr, giving these states energies of 1129(5) keV and 1495(7) keV.

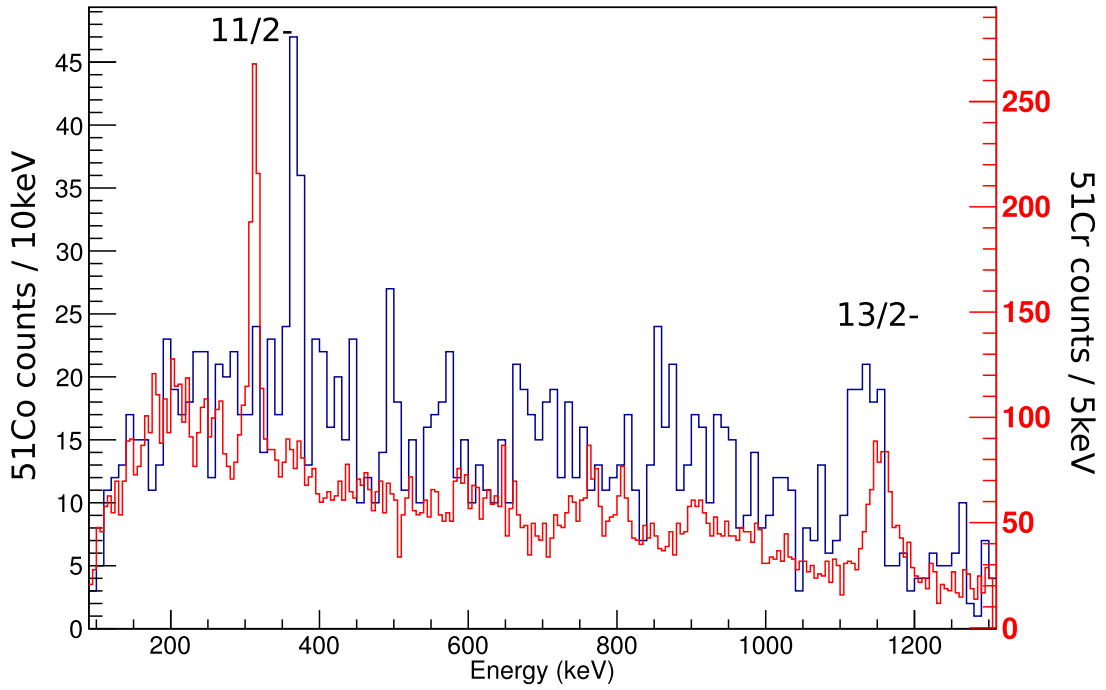

Figure 5.7: Gamma ray spectrum from ^{51}Co (blue) and ^{51}Cr (red) populated via mirrored reaction mechanisms. These spectra were obtained by gating on ^{54}Ni and ^{54}Fe beams through the A1900 then ^{51}Co and ^{51}C recoils in the S800, timing cuts have been applied to the spectra as described by Figure 5.4

5.5 Using two-nucleon knockout to access ^{51} Co

To investigate the level scheme of ^{51}Co to higher spin, two-neutron knockout from ^{53}Co was used. Using conservation of angular momentum and the Pauli-exclusion principle it was possible to consider the spectrum of excited states it was possible to populate. As previously discussed in Chapter 2 two-neutron knockout conserves spin. Two $f_{\frac{7}{2}}$ nucleons can couple to $J = 0, 2, 4,$ or 6, as ^{53}Co has a ground state spin of $J^{\pi} = \frac{7}{2}^{-}$. This allowed a maximum spin to be populated of $J^{\pi} = \frac{19}{2}^{-}$.

Gamma rays from the two-neutron knockout populating ^{51}Co and 2p1n removal populating ^{51}Cr are shown in Figure 5.8. By comparing the spectrum to the known states in the mirror nucleus a level scheme was formulated. Taking the 366 keV peaks and 1129 keV peaks as assigned from the mirrored reactions there is still a missing transition at 1495 keV that was not observed in

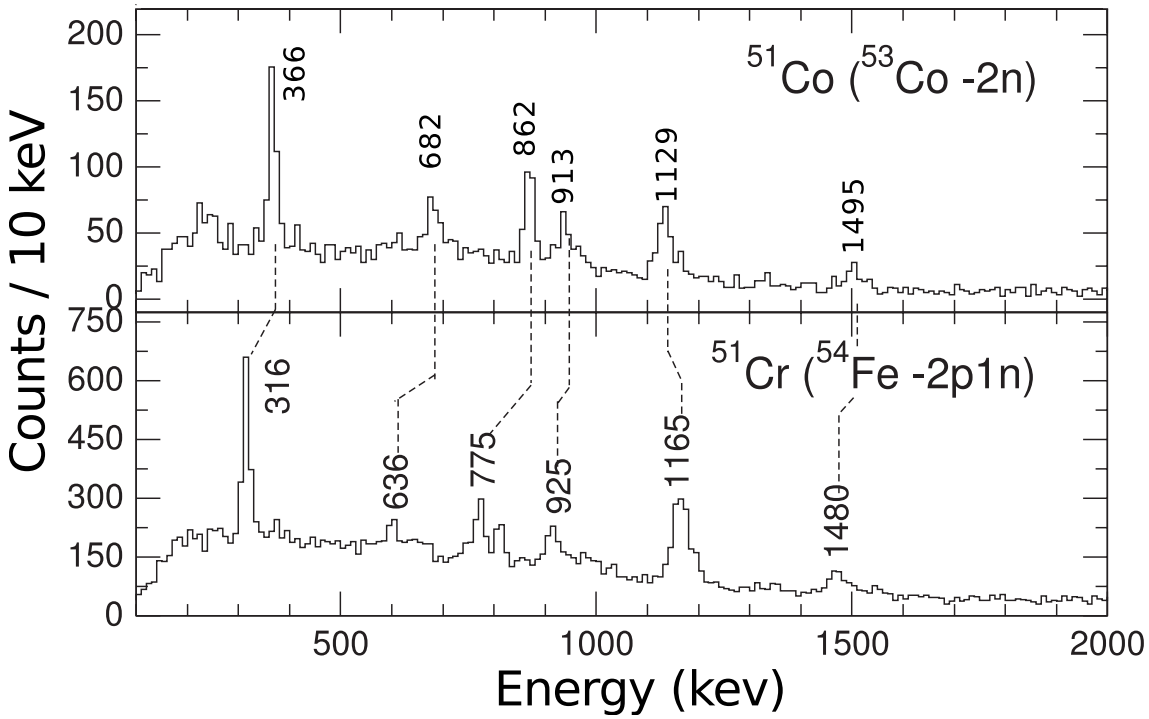

Figure 5.8: Gamma rays in ^{51}Co populated by two-neutron knockout. These gamma rays are compared to known states in ^{51}Cr which in this case has been populated by 2p1n removal. The spectra were obtained by gating on ^{53}Co and ^{54}Fe beams through the A1900 then ^{51}Co and ^{51}C recoils in the S800, timing cuts have been applied to the spectra as described by Figure 5.4. Gamma rays from ^{51}Cr have been labelled with literature values. Adapted from reference [55].

the mirror spectra. It is assumed that the 1495 keV transition was not observed in the mirrored reaction due to the low statistics and low efficiency of SeGA at such high energy. However, in the 2n channel the 1495 keV peak is observed. To aid in the assignment of the remaining peaks to a position in the level scheme it was assumed that they all decay from yrast states.

The assumption that yrast states are predominantly populated is supported by reaction cross section calculations, wherein one neutron evaporation is not energetically favourable from ^{52}Co; consequently this can be considered a direct reaction. Using spectroscopic factors and the Eikonal reaction theory discussed in Chapter 2 the cross section to individual states was calculated. These calculations were performed by Dr Ed Simpson. Calculations of the wavefunction overlap were performed using NUSHELLX and the KB3G interaction. The calculations are shown in Figure 5.9 and were used as a guide to the analysis in assuming all peaks decay from members of the yrast band. To order the remaining peaks into the yrast band they were efficiency corrected using the efficiency curve in Figure 4.9. The energy of each peak was found in the lab frame and the efficiency found for that peak at its lab frame energy. Additionally, the efficiency of each detector was altered for its opening angle in the nuclear frame, using Equation 5.1. The peaks were then ordered into the yrast band by their Doppler corrected area, and are shown in the level scheme in Figure 5.10.

Peak Energy	Relative intensity	J of parent state
365.9	11363 (931)	$^{11}/_{2}$
682	3679 (809)	$(^{19}/_{2})$
862	13654 (989)	$(^{15}/_{2})$
922	2858 (2653)	$^{13}/_{2}$
953	9168 (998)	$(^{17}/_{2})$
1129	17208 (1821)	$^{9}/_{2}$
1495	*	

Table 5.1: Relative intensity of peaks observed from the decay of excited states in ^{51}Co.* As the 1495 keV peak was particularly weak it could not be resolved in both rings, and intensity for this transition in Figure 5.10 is estimated.

$$\theta_{nuclear} = \cos^{-1}\left[\frac{\beta - \cos(\theta_{lab})}{\beta\cos(\theta_{lab}) - 1}\right]. \tag{5.1}$$

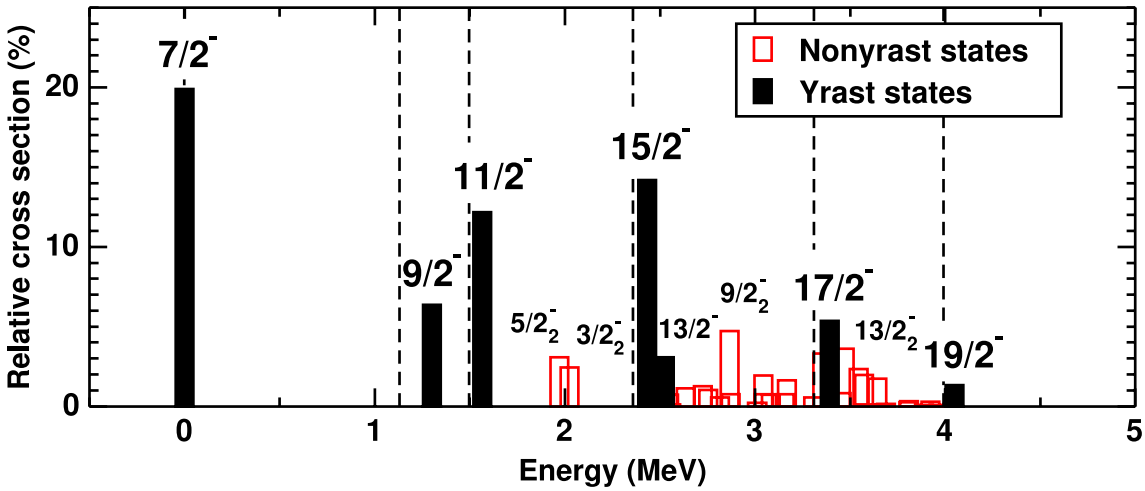

Figure 5.9: Calculated relative population of states in ^{51}Co from two-neutron knockout. The calculations give an indication that mostly yrast states should be populated, see text for details. Taken from reference [55].

5.5.1 The $^{15}/_{2}^{-}$ state

In ^{51}Cr the $^{15}/_{2}^{-}$ state has a 45.8 ps half life ($T_{1/2}$). From the arguments of wavefunction symmetry presented in Chapter 2, it is expected that the $^{15}/_{2}^{-}$ state in ^{51}Co will have a long $T_{1/2}$. This presents a problem for the analysis so far, as a long $T_{1/2}$ will change the ETP. Hence the method presented will settle on an incorrect energy on the assumption that the transition is prompt. Fortunately a method was pioneered by Dr. J. Brown in Reference [58] to determine the correct ETP, and β to use in Doppler correction, which allows for calculation of the energy of the state. Using Equation 3.9 and assuming the $B(E2)$ for decays from IAS will be identical it was possible to relate the $T_{1/2}$ to the energy of an unknown gamma ray, assuming its mirror transition is known. In our case this relation is as follows:

$$T_{1/2} = \left(\frac{775.4}{E^{\gamma}}\right)^{5} 45.8 \text{ ps}, \tag{5.2}$$

where E^{γ} is the energy inferred for the transition from the $^{15}/_{2}^{-}$ state to be. As the ETP will correspond to $\beta T_{1/2} C$ by multiplying the beam velocity by the expected target position the half life of the state is calculated. To find the correct energy of the state:

1. An approximate Doppler correction was performed.
2. The standard analysis was performed to get ETP and β.
3. Equation 5.2 was used to calculate a $T_{1/2}$ for the state.
4. The data was Doppler corrected again using an ETP corresponding to the calculated $T_{1/2}$.
5. The previous three steps were repeated until the inferred energy of the transition and $T_{1/2}$ of the state converge.

The $^{15}/_{2}^{-}$ state was found to have a half life of 25.6 ps and decay with an energy of 871(5) keV. However, as this method has not been tested on measured half lifes the reported number is that taken from a spectrum using a prompt Doppler correction of 862(5) keV.

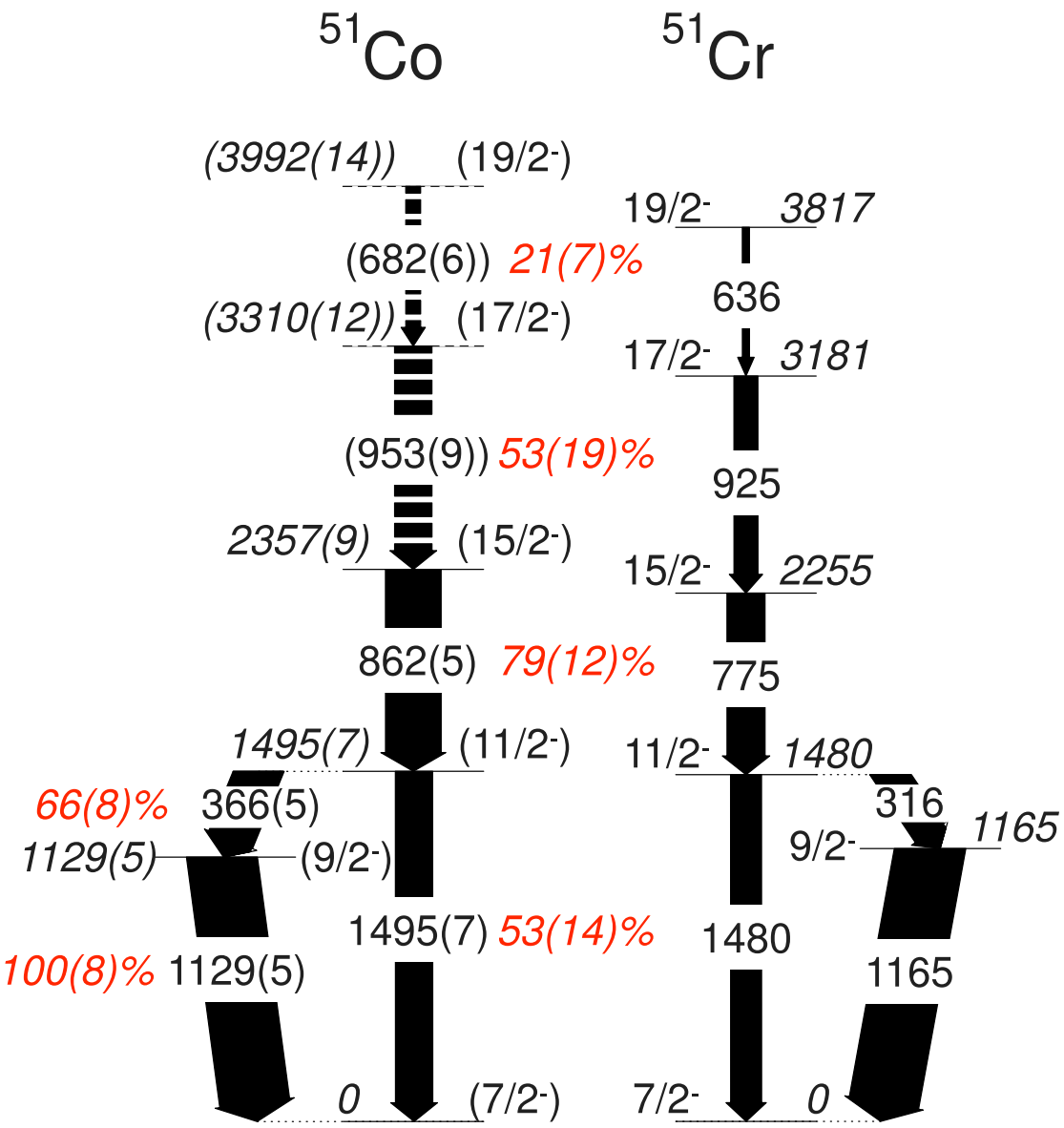

Figure 5.10: Level schemes of populated states in ^{51}Co and ^{51}Cr. The relative intensities are taken from the 2p1n reaction channel to ^{51}Cr and 2n channel to ^{51}Co. See text for details on the calculation of the relative intensity (in red). Gamma rays and states in ^{51}Cr are labelled with literature values, in ^{51}Co the values are taken from the presented analysis.

Chapter 6

GRETINA Analysis and Results

This Chapter concerns the analysis of data from GRETINA, in which nuclei in the $A = 62$ region were studied. The aim of this experiment was to use mirrored knockout and fragmentation reactions from an intermediate energy ($\sim$95MeV/u) ^{66}As beam to populate previously unknown excited states in low $|T_z|$, upper-fp shell nuclei. The primary beam of ^{78}Kr impinged on to a 650 $^{mg}/_{cm^2}$ ^{9}Be target. The A1900 was tuned to accept ^{66}As, however, isobaric contamination is always present in such a separator. In the case discussed here both ^{65}Ge and ^{64}Ga were present, and therefore the analysis of these nuclei is also presented. These secondary beams impinged on to a 96 $^{mg}/_{cm^2}$ ^{9}Be foil at the target position of the S800. An event-by-event identification of reaction products was performed using the S800 spectrometer. Gamma rays were detected by GRETINA.

The experiment was run over the course of a week, during which radiation damage due to the interaction of the beam and the scintillator caused a reduction in the scintillator's detection efficiency. Additionally, the damage caused the timing signals to drift. The solution to the loss in efficiency was to first place a shim underneath the scintillator to manually raster the scintillator surface with the scintillator being replaced once no unspoiled detection positions remained. The timing signals which had drifted were aligned in the analysis as the data were sorted. This was performed once as a rough correction gated on a secondary beam, then a further correction was time gated on a specific reaction in the S800.

6.1 Identification of secondary beam particles

A particle identification plot (PID) is presented in Figure 6.1. The primary nucleus of interest, ^{66}As, along with the isobaric contaminants of ^{65}Ge, ^{64}Ga and ^{63}Zn are highlighted. In addition, two key features, the resolution and charge state resolution, are also worth further discussion

Compared to the previous experiment investigating the structure of ^{51}Co, the resolution seen in the PID (Figure 5.1) is significantly worse. This is attributed to the thicker primary target and higher z of the beams selected in this experiment. The thicker primary target causes a larger spread in momentum of the secondary beam. The higher z introduces more momentum straggling each time the beam interacts with a component, compounding the effect of a thicker primary target. In

addition to the primary distribution representing the nuclei of interest, small localised distributions are observed. These are highlighted in Figure 6.1 with the letter e and correspond to the tail end of the momentum distribution of a different charge state. This is discussed in Appendix D. Gates were made to minimise contamination due to unwanted charge state distributions used in the analysis.

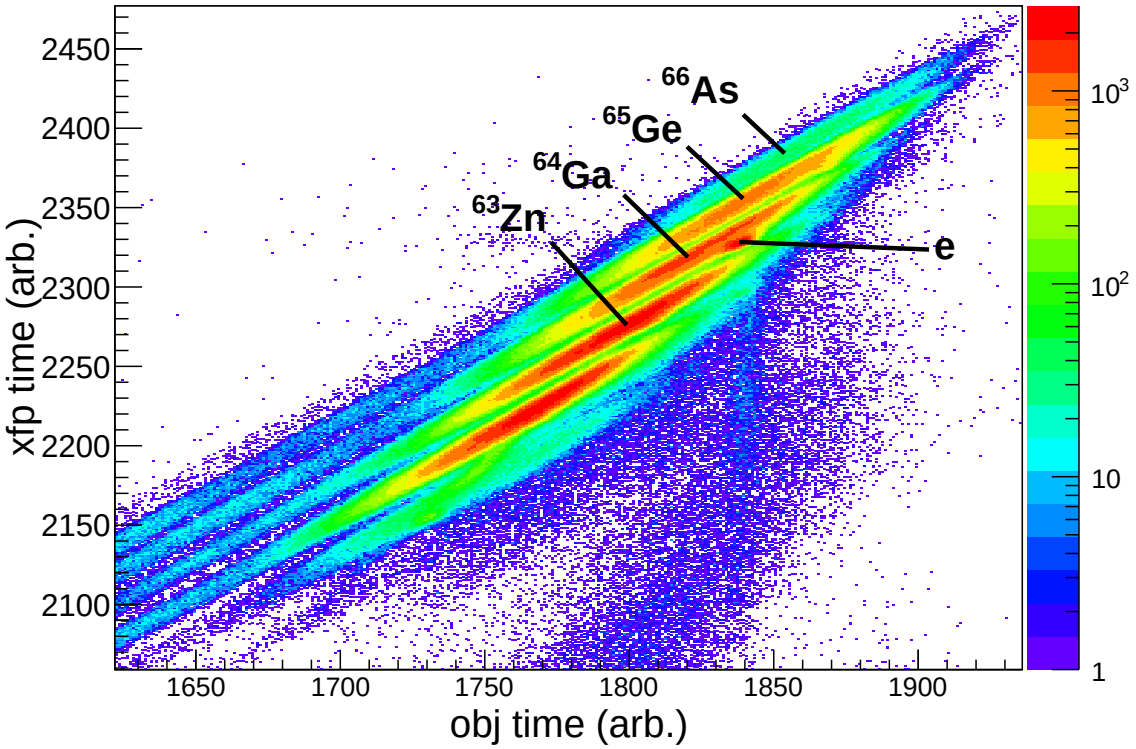

Figure 6.1: Particle identification of incoming beams; the time from the *xfp* and *obj* scintillator events, relative to the *E1* scintillator are plotted against each other. This plot represents around 1-2% of the total accumulated data.

6.2 S800 calibration

Once a secondary beam from the A1900 has been gated on, a plot of the S800 ion chamber energy vs time of flight should be able to identify all recoils from the reaction. Reaction products with the same A/Q and z enter the S800 at different angles and thus have different flight times and deposit different amounts of energy in the ion chamber (IC). The disparity in time and energy is caused by the total spread in momentum of the secondary beam and scattering angle at the target. The spread of energy and time is enough that without correcting for these effects an unambiguous particle identification (PID) cannot be achieved. Figure 6.2a is an example of an uncorrected PID.

To correct for the dispersive effects, angles and positions were measured by the CRDCs, as described in Chapter 3. Corrections have been found empirically and Equations 6.1 and 6.2 detail the corrections used in this thesis.

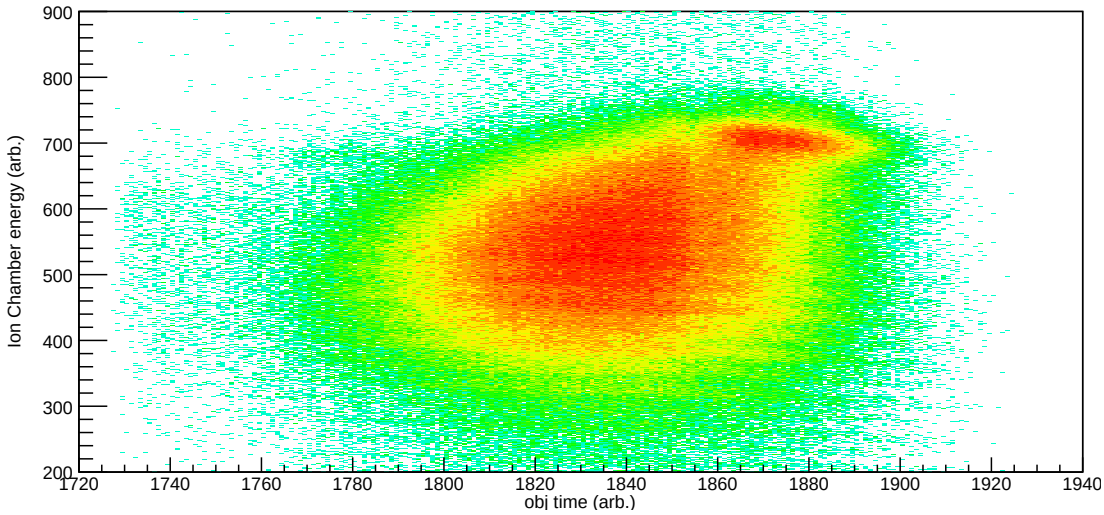

(a) Particle Identification in the S800 before the corrections detailed in Equations 6.1 and 6.2 have been applied, see text for details. This plot represents around 1-2% of the total accumulated data.

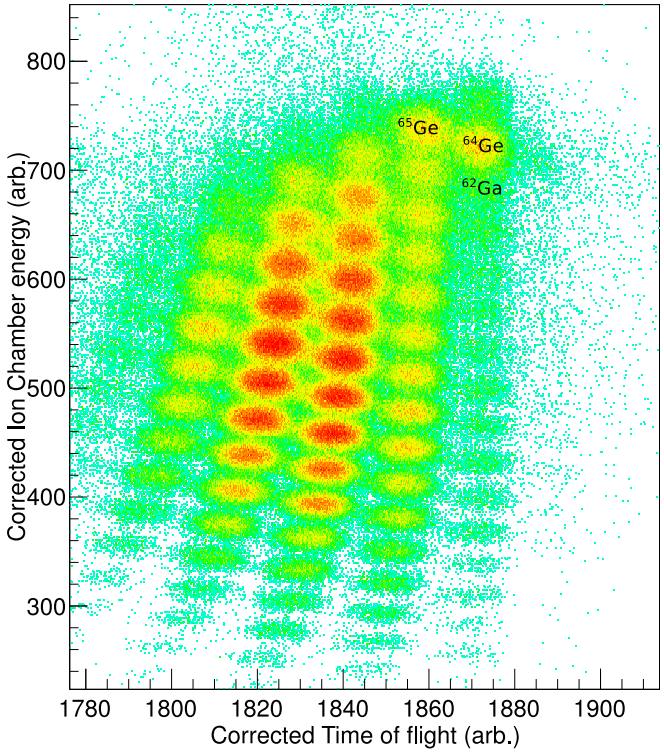

(b) S800 PID plot gated on a ^{66}As incoming beam. This plot represents around 1-2% of the total accumulated data.

Figure 6.2: S800 PID plots before and after correction using equations 6.1 and 6.2. These spectra were created by selecting the ^{66}As data from Figure 6.1

$$IC_{corr} = (IC_{sum} + -0.00001 \times IC_{sum} \times CRDC1_y) \times exp(0.00015 \times (100 - CRDC1_x)), \quad (6.1)$$

$$obj_{corr} = 0.7 \times A_{fp} \times 1000) + (0.07 \times CRDC1_x) + obj, \quad (6.2)$$

where IC_{corr} is the corrected ion chamber energy; IC_{sum} is the summed energy from all the ion chamber segments; $CRDC1_y$ is position of the recoil as measured by the CRDC in the non-dispersive plane of the S800 by the first CRDC; $CRDC1_x$ is the same but in the dispersive plane; $CRDC2_x$ is the position in the dispersive plane of the S800 measured by the second CRDC; obj_{corr} is the corrected obj time; and A_{fp} is the dispersive angle at the focal plane. A_{fp} is measured by taking the position in the dispersive plane from the two CRDCs $A_{fp} = \arctan\left((CRDC1_x - CRDC2_x)/1073\right)$.

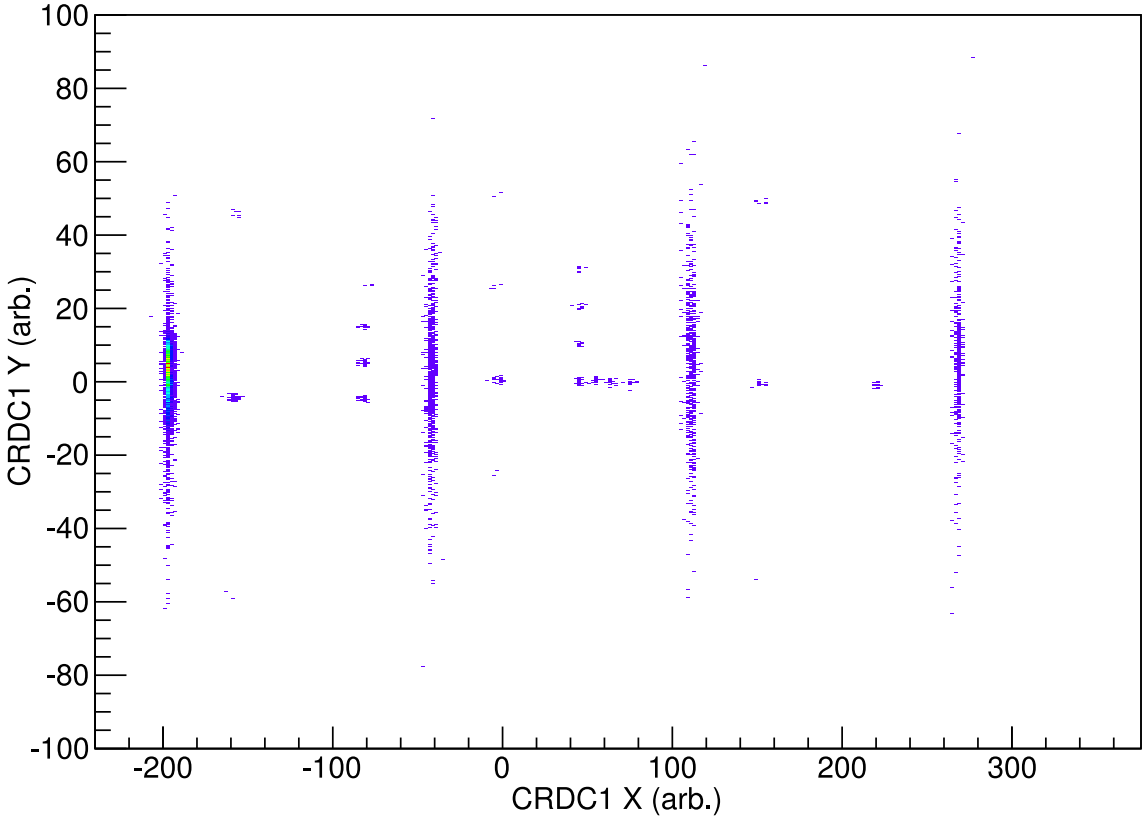

Figure 6.3: Deduced position of beam particles passing through a calibration mask in front of CRDC1. The holes in the mask are of known position which is used to calibrate position in the two CRDCs so that angles can be calculated.

In order to use the positions from the two CRDCs in tandem to calculate angles they must be calibrated. The calibration was performed by placing a metal mask in front of each CRDC. The masks have holes drilled into them at known positions. Figure 6.3 is an example of a run taken with the mask in front of CRDC1. Figure 6.4 shows an example of a fully corrected S800 PID

plot gated on a ^{66}As incoming beam. Particle identification plots from ^{65}Ge, and ^{64}Ga beams are shown in Figures 6.4 and 6.5, respectively.

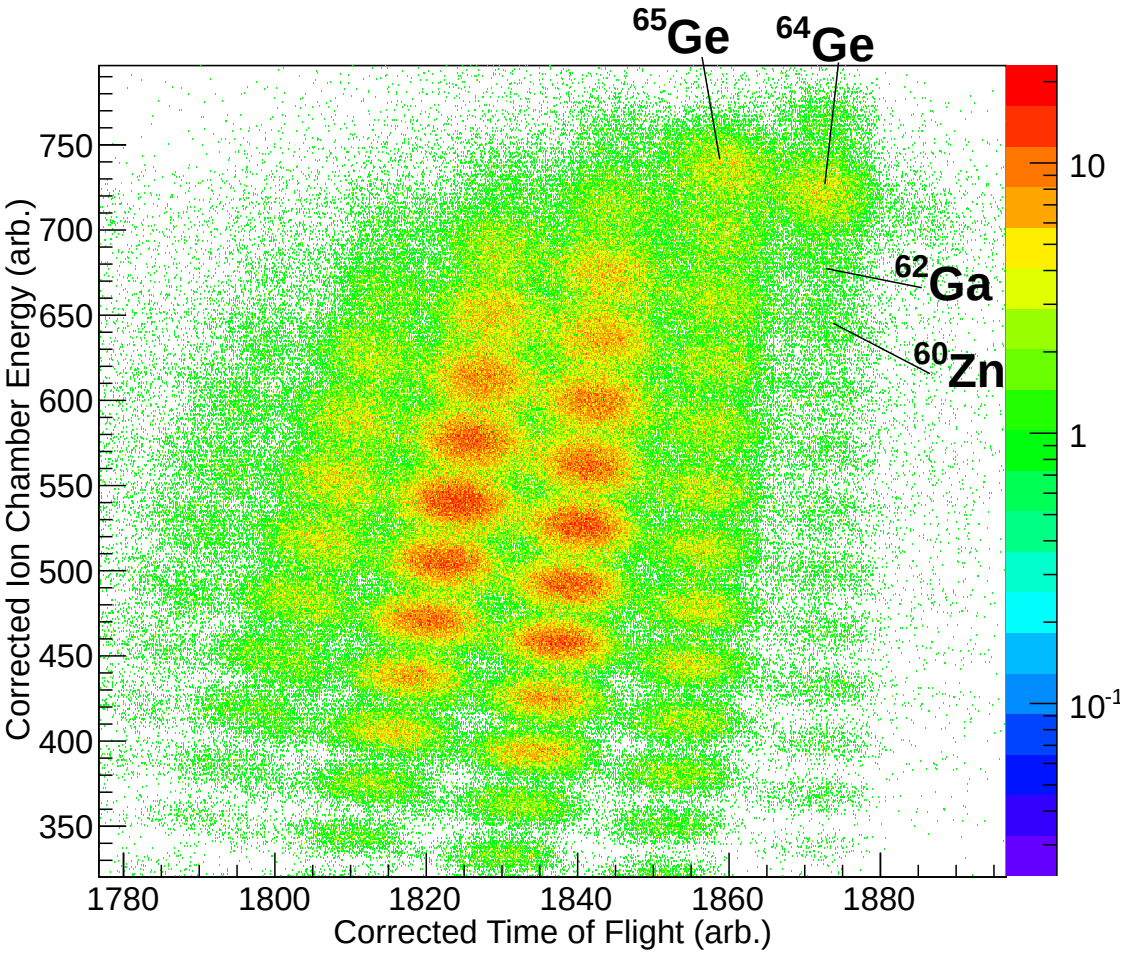

Figure 6.4: S800 PID plot produced by gated on a ^{65}Ge incoming beam from the A1900. This plot represents around 1-2% of the total accumulated data.

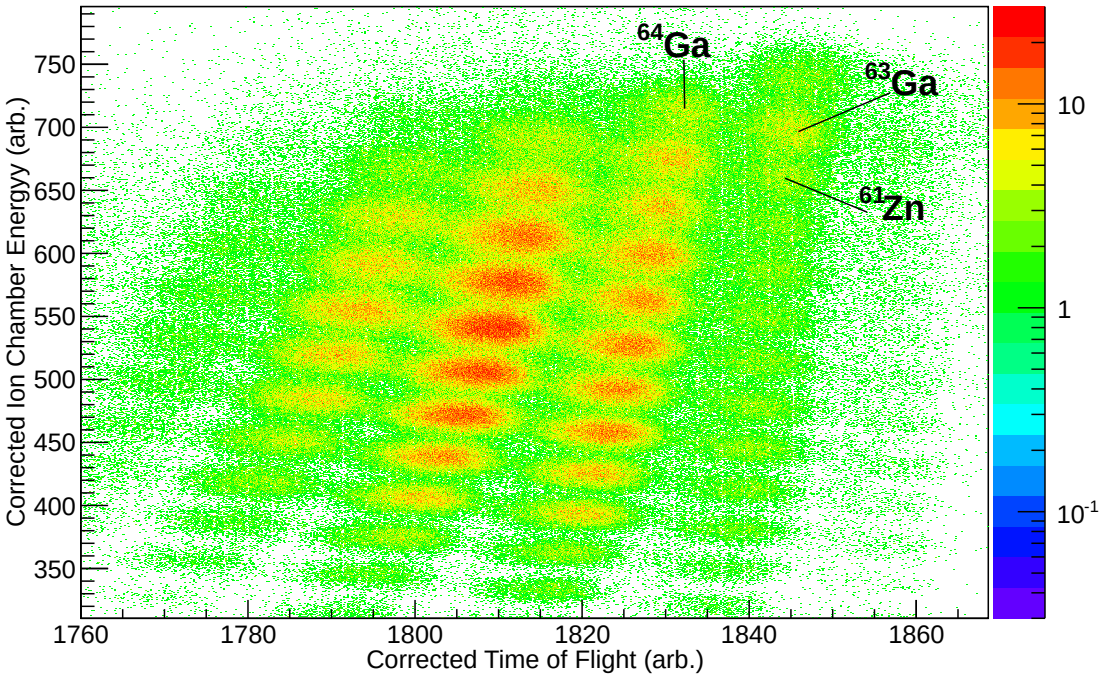

Figure 6.5: S800 PID plot produced by gated on a ^{64}Ga incoming beam from the A1900. This plot represents around 1-2% of the total accumulated data.

6.3 GRETINA time cut

Gamma ray data of interest arrives with in a well defined time window relative to the S800 scintillator (E1). This information was employed to apply a time condition, removing time random background events (e.g. natural radiation and radioactive build up within the target chamber). An example of such a time condition is presented in Figure 6.6a. The drift in time at low energy is the well known time walk caused by the poor timing quality of small signals in the Ge crystals induced by low energy gamma rays.

Figure 6.6a demonstrates the GRETINA time cut: the Y axis plots energy recorded by GRETINA without Doppler correction, the X axis plots the time of the GRETINA event relative to the time of the beam event in the E1 scintillator. The black contour describes a cut which is applied in Figure 6.6b. The blue spectrum has no FoM or time cut, the red spectrum has had the time from Figure 6.6a applied, and the black spectrum has both the time cut and the FoM cut applied. It is worth noting that the blue spectrum is clustered data, rather than just considering separate crystals. The process of clustering data (as described in Chapter 4) is particularly good for removing events that do not originate at the centre of GRETINA. When events originate from outside the centre of GRETINA the pattern of interaction points is likely to be so different they will not cluster properly. This property of the clustering is why the timing cut has such a small effect.

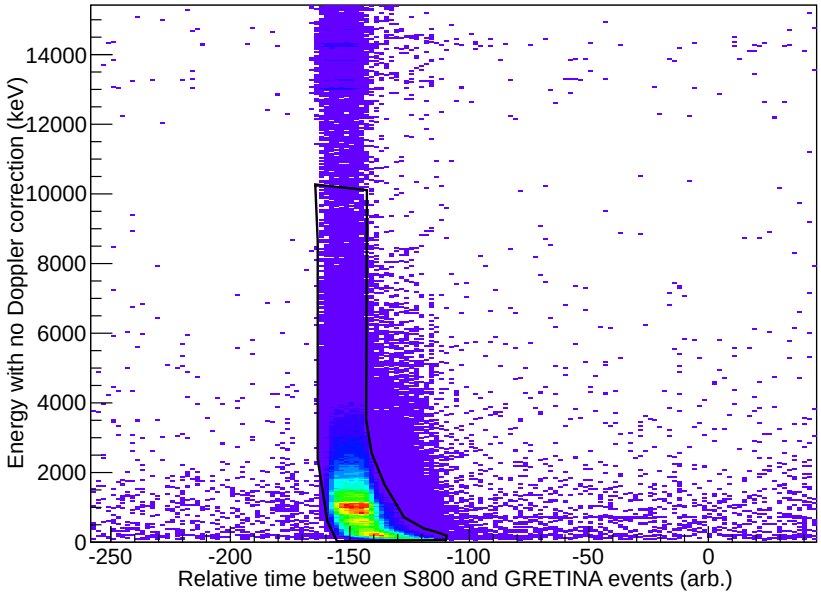

(a) Time vs energy spectrum gated ^{62}Zn recoils. The timing signal is the difference in time between the signal from GRETINA and in the *E1* scintillator; a FoM cut has also been applied to the data in this spectrum, as described in chapter 4. See text for details.

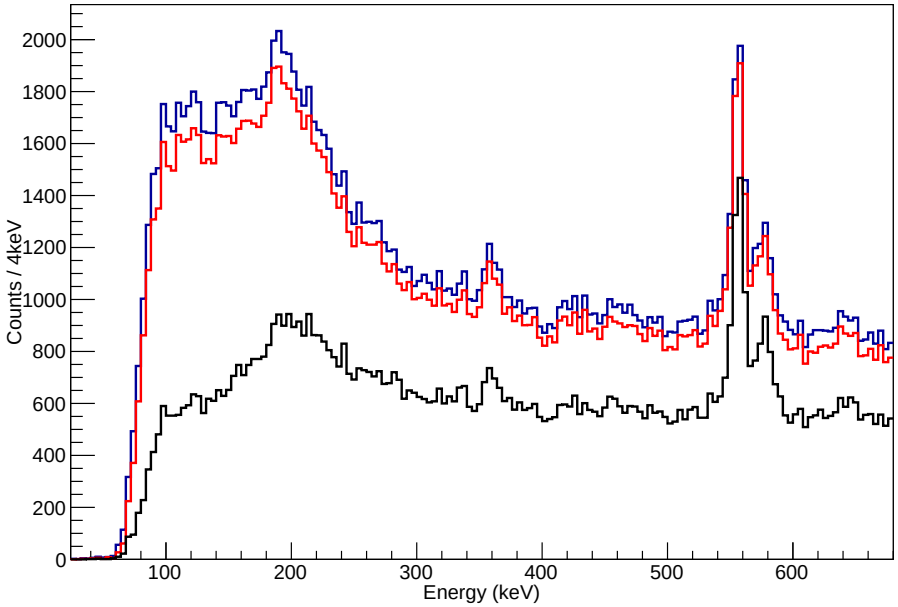

,

(b) Data from the ^{64}Ga pn-removal reaction to populate states in ^{62}Zn. The blue spectrum is gated on ^{62}Zn using particle detectors, additionally the red spectrum has a timing cut applied (see text for details), and the black spectrum has had both timing and FoM cuts applied.

Figure 6.6: GRETINA timing cut and the effect it has on gamma ray spectra compared to the FoM cut described in Chapter 4. These spectra were created by gating on ^{64}Ga beam in the A1900 and ^{62}Zn recoils in the S800.

6.4 Effective Target Position

The secondary beam of interest had a v/c ≈0.3. As a consequence of the beam velocity the gamma rays emitted in the centre of mass frame will be Doppler shifted, hence an event-by-event Doppler construction must be performed. To do this the Doppler correction formula must be employed, as was done previously in Section 3.5 described by Equations 3.6.

In order to perform a Doppler correction using Equation 3.6 the position and direction of the emitted gamma ray must be known. It is possible to determine the angle of the gamma ray from the primary interaction point in GRETINA and the position at which the reaction takes place. It is convenient to assume reactions occur at the centre of the target. However, this position relative to GRETINA is not well known. In addition, lifetime effects can cause gamma rays to be emitted down stream of the target position leading to incorrect determination of target position. An effective target position corresponding to the average decay position must be deduced in order to find the best possible Doppler correction. In Chapter 5 this was achieved by making use of the two distinct rings of SeGA. However, GRETINA has sub-segment resolution, meaning that in principle there are a continuum of angles between 40 and 120 degrees with no distinct angular rings. As a result, a different method was implemented to find the ideal Doppler correction.

To find the target position the additional peak width associated with an incorrect Doppler correction is utilized. The following method was used:

- A peak with a known half life is selected from a reaction channel where no evidence is found that it is fed by a more long lived state.
- This peak is Doppler corrected with a range of βs and many ETPs. For each correction the peak is fitted with a Gaussian peak and linear background, the peak width and centroid energy are recorded.
- The peak width is plotted on the Z axis of a graph against β and ETP for values where the centroid is within 1 keV of the known value. This graph is referred to as a peak width plot (PeWiP). An example of an ungated PeWiP is shown in Appendix C.

In a PeWiP with the correct centroid energy gate applied, the ideal ETP is immediately apparent (as shown in Figure 6.7b). Projecting the PeWiP along the ideal ETP one observes a shape that is approximately parabolic in β. This could be used to find the ideal β for Doppler correction. However, for ease in this analysis the β scan technique will be used in the following sections.

Data from ^{62}Zn was used to assess the ETP for prompt gamma rays. The populated states in ^{62}Zn from 1p1n removal from ^{64}Ga have been previously investigated and had lifetimes measured. Figure 6.7a shows a spectrum of ^{62}Zn with the strongly populated peaks have been labelled with spins and lifetimes. The only transition that meets the requirement of a sub-picosecond half life **and** not being fed by a half life greater than one picosecond is the 6_1^+ transition to the 4_1^+ state. Figure 6.7b shows the PeWiP for this transition, gated on the correct transition energy of 1521.5 keV ± 1 keV. The result from this PeWiP is an ETP of 0.15 mm. This ETP gives the best estimate for a physical position for the target, or the ETP that should be used for prompt data.

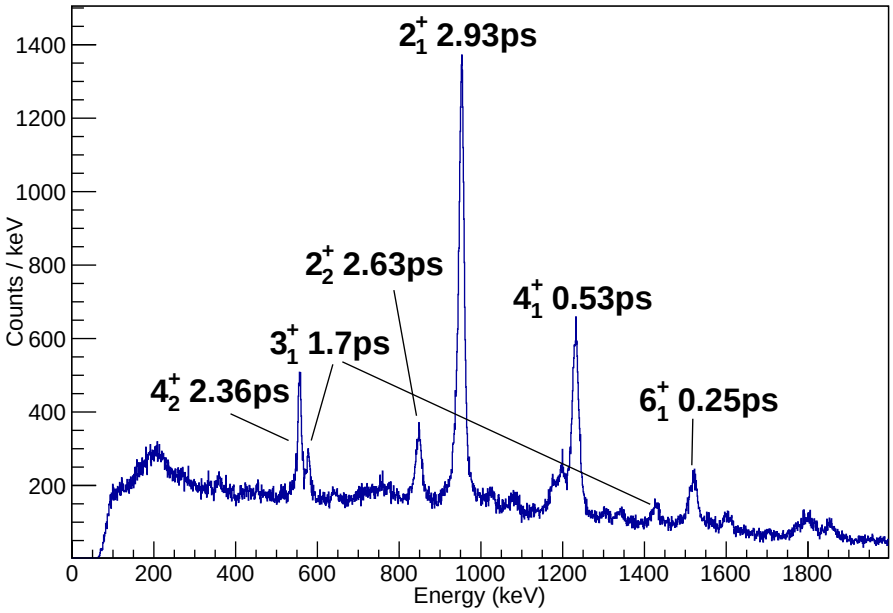

(a) Gamma ray spectrum from ^{62}Zn populated in 1n1p removal from ^{64}Ga The strongest peaks have been labelled along with half lifes taken from the ENSDF [59]. This spectrum was created by gating on ^{64}Ga data from the A1900 and ^{62}Zn data from the S800. A time cut has been applied such as that in Figure 6.6a and a FoM cut of 0.8 has been applied.

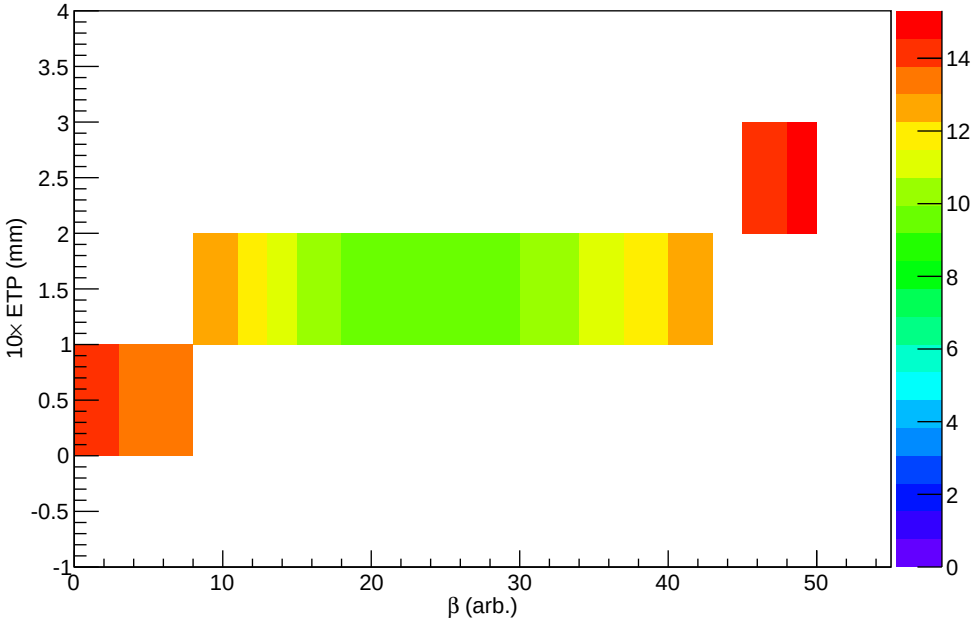

(b) Peak width plot for the 1521 keV transition in ^{62}Zn, for fits that give a centroid within 1 keV of the known value of 1521.5 keV. The Z axis (colour) shows the σ from the Gaussian fit equation in units of keV. This plot was created by iteratively Doppler correcting the ^{62}Zn spectrum from Figure 6.7a, and fitting Gaussian peaks with linear backgrounds

Figure 6.7: Labelled ^{62}Zn gamma ray spectrum and results from PeWiP method for the 1521 keV peak.

Unless otherwise stated the assumption has been made that the states of interest decay sufficiently promptly that the ETP for prompt data should be used. However, an ideal β still has to be chosen and for this β scans have been used. Figure 6.8 is an example of a β scan, which was produced by Doppler correcting a spectrum with the prompt ETP and a varying β. The counts per channel are described with colour. In Figure 6.8 it is most obvious for the 571 keV transition that there is an ideal β and that deviating from this causes the peak to spread out in energy. It is clear from Figure 6.8 that the ideal β in this case lies somewhere between 0.28 and 0.32. The ideal β occurs where the peak has the largest amplitude and smallest width. The Doppler correction error was estimated by looking around the extremes of where the ideal correction is thought to be. The error estimation was performed by Doppler correcting the spectrum to each each extreme and measuring the energy. It was found that an error of around 1 keV should be added to each peak for the ambiguity in finding the ideal β.

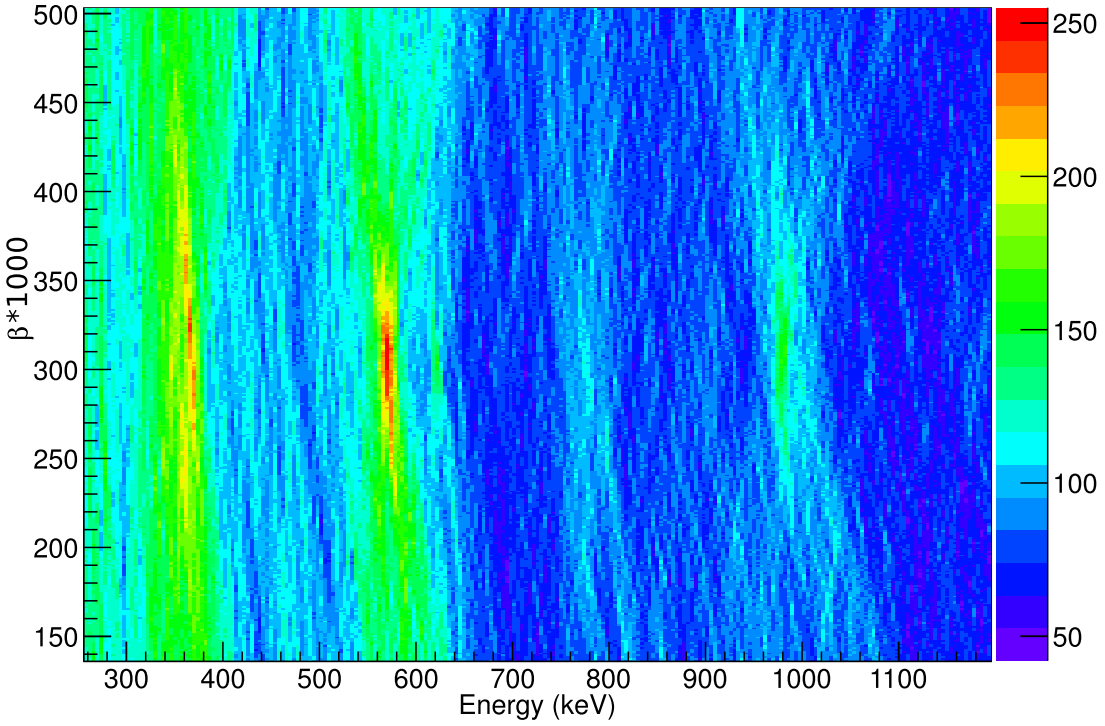

Figure 6.8: A β scan of ^{62}Ga populated in 1p2n removal from ^{65}Ge. This spectrum is a gamma ray spectrum where the Doppler correction has been performed iteratively with many values of β. The gamma ray spectrum is along the X axis, with the Z axis (intensity) shows the number of counts per 4 keV. The Y axis is β in units of .01 β. The ideal β from this scan was deduced to be 0.306.

6.5 Reactions to populate excited states in ^{62}Ga

The reactions ^{65}Ge(^{9}Be, 1p2n) and ^{64}Ga(^{9}Be, 2n) were both employed to populated the nucleus ^{62}Ga in this experiment. The latter reaction is treated as direct, so intensities of states populated are required for comparison to calculations later. The assumption of two-neutron knockout is good as the ground state of ^{63}Ga is 10 MeV more bound than the ground state of ^{62}Ga. Thus one neutron knockout followed by neutron emission or evaporation is not energetically favourable. In both of the presented reactions most of the states are known and are labelled with their spin assignment from previous experiment [60]. Previously unobserved peaks have been labelled with energy and error.

6.5.1 ^{62}Ga from ^{64}Ga

The ^{62}Ga gamma ray spectrum produced via two-neutron knockout reaction is shown in Figure 6.9a, with Figure 6.9b showing the intensity of the measured gamma rays. The intensities are measured using un-tracked data. The efficiency of GRETINA was calculated in Chapter 4 with tracked and untracked data. However, it is currently unclear whether bremsstrahlung or lifetime effects will affect the efficiency of GRETINA. Table 6.1 shows the tracked and untracked efficiency corrected area of these peaks along with measured energies.

Three previously known transitions are observed. They decay between, or into, the main low lying odd-J yrast structure [60,61]. They are the 571 keV transition from the 1^+ to the 0^+ ground state, the 376 keV transition from the 5^+ at 1193 keV to the 3^+ at 817 keV, and the 622 keV transition that also feeds the 3^+ state. The 3^+ state has a half life that was previously measured to be 3.4 ns. With the beam velocity of $\beta = 0.296$ it is not expected that the transition between the 3^+ and the 1^+ states will be observable. This lifetime corresponds to gamma decay occurring on average around 0.5 m outside the target. At this distance the angles relevant for Doppler correction cannot be determined.

The transition assigned as the 376-keV transition between the 5^+ and 3^+ states has a wide peak shape and is shifted to a lower energy. This is the expected behaviour of a transition from a state with a half life of a few hundred picoseconds. The low gamma ray energy of this $E2$ transition is indeed expected to result in the state being long lived. Shell-model predictions by Rudolf *et al.* [61] and Srivastava *et al.* [62] both predict half lifes of around 350 ps. The transitions observed in this experiment are shown in Figure 6.9b. The 246 keV transition is given a minimum intensity in the level scheme as it is not observed due to the lifetime of the 3^+ state. It is assumed that all the structure at around 360 keV in Figure 6.9a corresponds to the 376-keV transition. A new transition with an energy of 784(2) keV is observed in both spectra.

There is strong evidence that the ^{64}Ga beam is in the low lying 43 keV isomeric state. This is expanded upon in Section 6.6 where the one-neutron knockout channel is examined. In this reaction channel there is also evidence for a presence of the isomer in the beam: population of the 5^+ state is only possible from the ground state via removal of an $f_{\frac{7}{2}}$ neutron which is expected to be weak (considering that the $f_{\frac{7}{2}}$ orbital is not occupied by the last valence nucleons). The 5^+ being one of the strongest populated states supports the presence of the isomer in the beam. Additionally, reaction cross section calculations discussed in Chapter 7 show that the strong population of odd-spin states is evidence for a strong isomer presence.

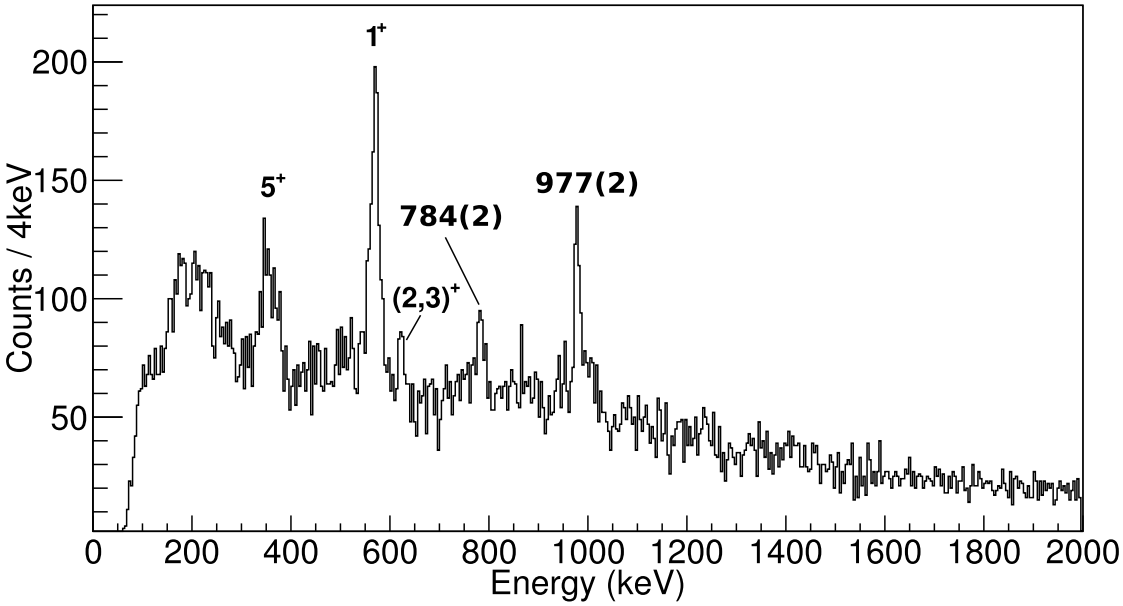

(a) Gamma ray spectrum from ^{62}Ga populated via two-neutron knockout from ^{64}Ga. The labelled 1^+ state has a measured energy of 570(2) keV and the labelled $(2,3)^+$ state has a measured energy of 623.7(10) keV. This spectrum was created by gating on ^{64}Ga data from the A1900 and ^{62}Ga data from the S800. A time cut has been applied such as that in Figure 6.6a and a FoM cut of 0.8 has been applied.

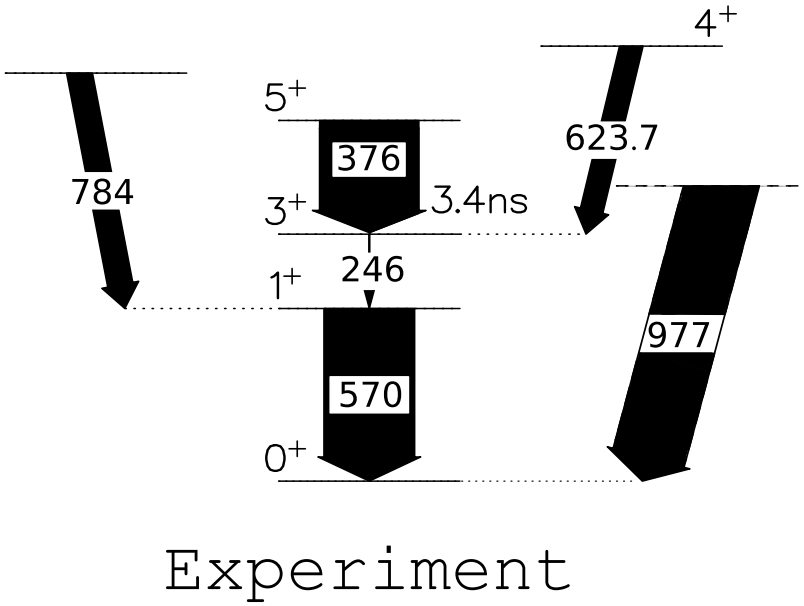

(b) Level scheme of the populated states in ^{62}Ga along with their intensity, calculated from the tracked spectrum. The gamma ray energy labels were taken from the data with the exception of decays from the 3^+ and 1^+ states due to the lifetime effects.

Figure 6.9: Gamma ray spectrum and level scheme from ^{62}Ga.

Energy (keV)	Tracked Intensity (arb.)	Untracked Intensity (arb.)
376 (Integrated)	126(13)	210(40)
570.0(7)	100(13)	100(7)
623.7(2)	25(6)	20(5)
783(1)	28(6)	44(7)
911(1)	81(9)	55(6)

Table 6.1: Efficiency corrected relative intensity of observed transitions in ^{62}Ga. Only the untracked intensity is used in arguments made due to assumptions made in the tracking routine, see Chapter 4 for details. It was not possible to extract an energy for the 376 keV peak as it decays from a long-lived state.

6.5.2 ^{62}Ga from ^{65}Ge

Figure 6.10a shows the S800 PID plot from the incoming ^{65}Ge beam. It is clear that the ^{62}Ga locus is not fully resolvable so an additional step was taken. It was discovered during the analysis that the ^{64}Ge component is wider at one side of the focal plane. To produce a ^{62}Ga spectrum first a cut was made on the $T_z = 0$ nuclei in the S800 PID. Then the data were projected into the focal plane as shown in Figure 6.10b, showing ion chamber energy and position from the CRDCs. A cut was then made on this to maximise the statistics from the ^{62}Ga channel.

The gamma ray spectrum for ^{62}Ga populated in 1p2n removal from ^{65}Ge is shown in Figure 6.11a. Below 1 MeV the same states are observed as in the two-neutron knockout case, except for what appears to be structure on the high side of the 977 keV peak. This structure can be fitted with a triple Gaussian and first order polynomial background (with peak energies of 977(1) keV, 997(2) keV, and 1012(3) keV), however, these peaks are not distinct and considering the β scan for this nucleus (shown in Figure 6.8) it is not immediately obvious how many peaks are observed. There is a known transition in ^{62}Ga with an energy of 1004 keV [60], however, this does not explain this distribution. Additional peaks are observed at higher energy which have not been observed in other reactions which are labelled in Figure 6.11a.

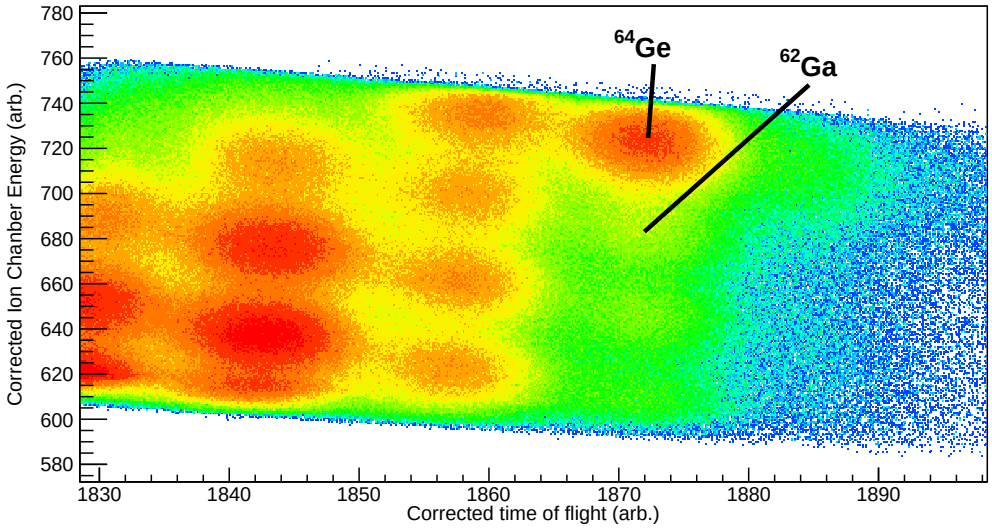

(a) S800 PID gated on a ^{65}Ge beam from the A1900. The ^{64}Ge loci is wider than the surrounding loci and cannot be completely resolved from the ^{62}Ga loci without further analysis.

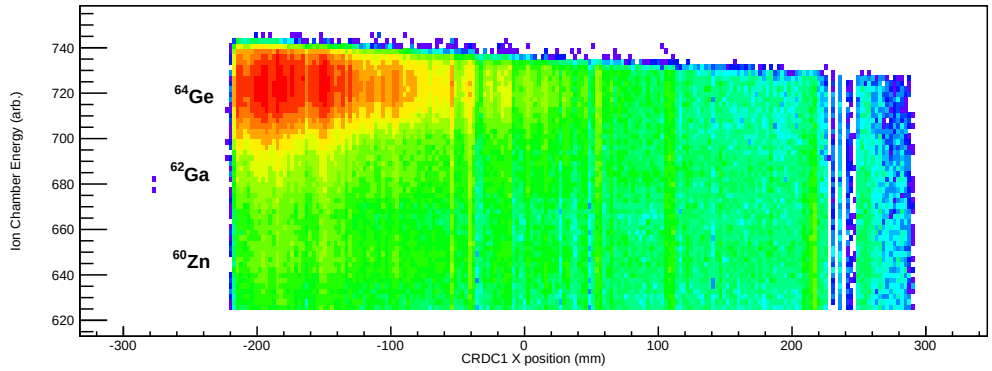

(b) Ion Chamber energy as a function of focal plane x position as measured by the first CRDC. This graph was produced with a gate on the $N = Z$ nuclei from Figure 6.10a to demonstrate the focal plane dependence of particle resolution.

Figure 6.10: S800 PID plots demonstrating that the resolution of Particle Identification around ^{65}Ge is dependent on focal plane position.

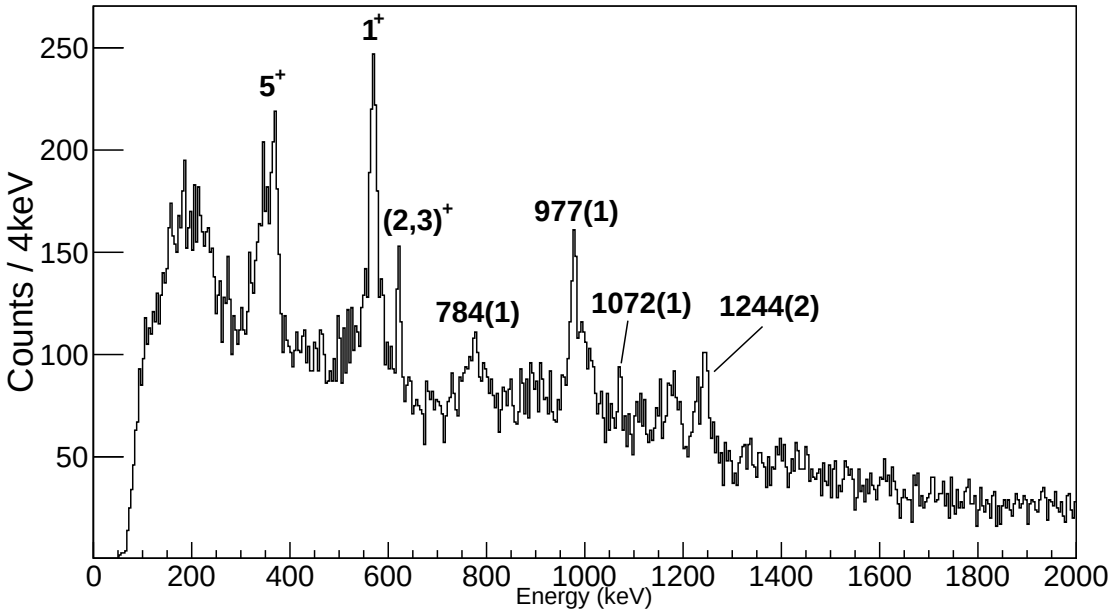

(a) Gamma ray spectrum of ^{62}Ga populated in 1p2n removal from ^{65}Ge using a cut on $N = Z$ nuclei in the S800 PID plot then gating on ^{62}Ga with the PID cut projected into the x position from CRDC1. The labelled 1^+ state has a measured energy of 570.0(7) keV and the labelled $(2,3)^+$ state has a measured energy of 623.7(2) keV. This spectrum was created by gating on ^{65}Ge data from the A1900 and ^{62}Ga data from the S800. A time cut has been applied such as that in Figure 6.6a and a FoM cut of 0.8 has been applied.

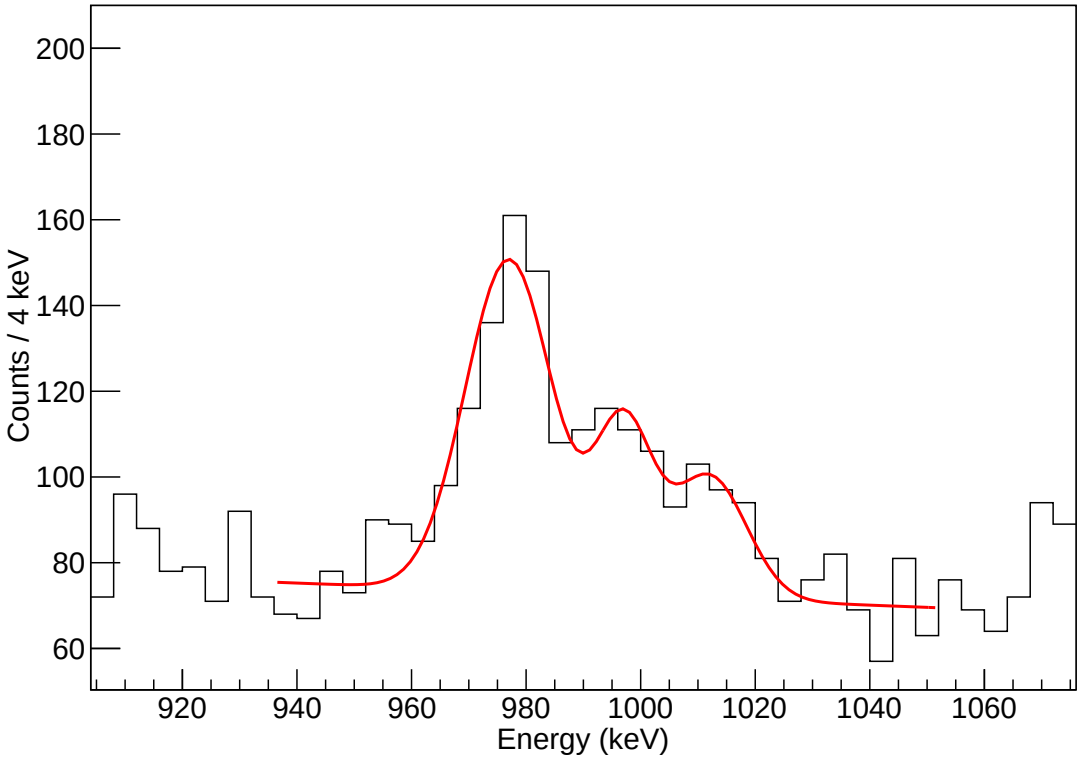

(b) An example of the fits used to ascertain energies from this analysis.

Figure 6.11: gamma ray spectrum of ^{62}Ga and fits used to ascertain energies.

6.5.3 ^{62}Ga gamma gamma analysis

Using the data from the ^{65}Ge 1p2n removal reaction, a gamma gamma analysis was performed to place previously unobserved transitions into the known level scheme. The analysis was performed by constructing a gamma gamma matrix of all coincident gamma ray events. Figure 6.12 shows an example of this matrix which has been constructed with the same particle gates as those used to construct the gamma ray spectrum in Figure 6.11a. The gamma gamma matrix was also constructed with less stringent gating conditions (i.e. wider S800 PID gate) to gain statistics while relying on the gamma coincidence gate to remove contamination. This approach yielded an identical result to the narrow gated approach.

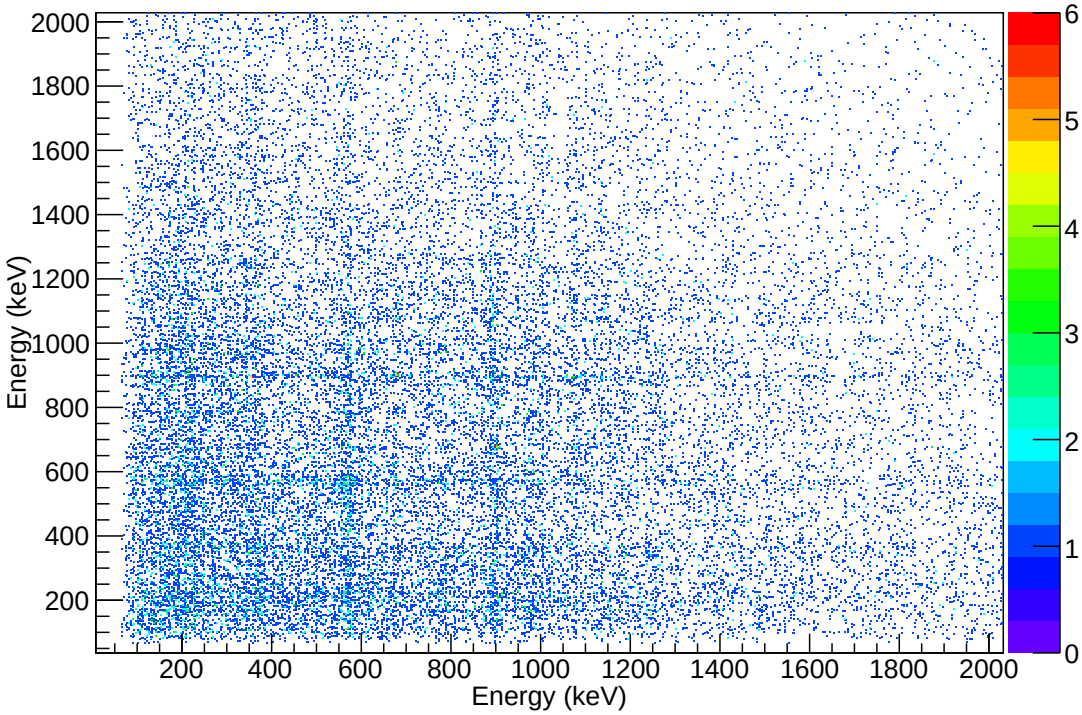

Figure 6.12: Gamma Gamma matrix for ^{62}Ga populated in 1p2n removal from ^{65}Ge. This spectrum was created by gating on ^{65}Ge data from the A1900 and ^{62}Ga data from the S800. A time cut has been applied such as that in Figure 6.6a and a FoM cut of 0.8 has been applied. The X and Y axis both show gamma ray energies for coincident events. The Z axis denotes the number of coincident events in units of coincidences per 4 keV per 4 keV. This matrix was constructed the same gates as those used to create the gamma ray spectrum in Figure 6.11a

The gamma gamma analysis was performed by projecting the gamma gamma matrix around the observe gamma ray peak in the gamma ray spectra. To remove random coincidence a local background subtraction was performed. The matrix was projected both above and below the transition of interest, with the resulting spectra subtracted from that created by the peak matrix projection. The results show that the 784-keV transition is in coincidence with the 571-keV transition from the 1^+ to the ground state, indicating a new state at 1355 keV. The 977 keV transition does not appear to be in coincidence with any peaks. Given that the 977 keV peak is much stronger

than the 784 keV peak which shows a clear coincidence it is assumed that this state decays to the ground state. The two coincidence spectra are shown in Figures 6.13a and 6.13b.

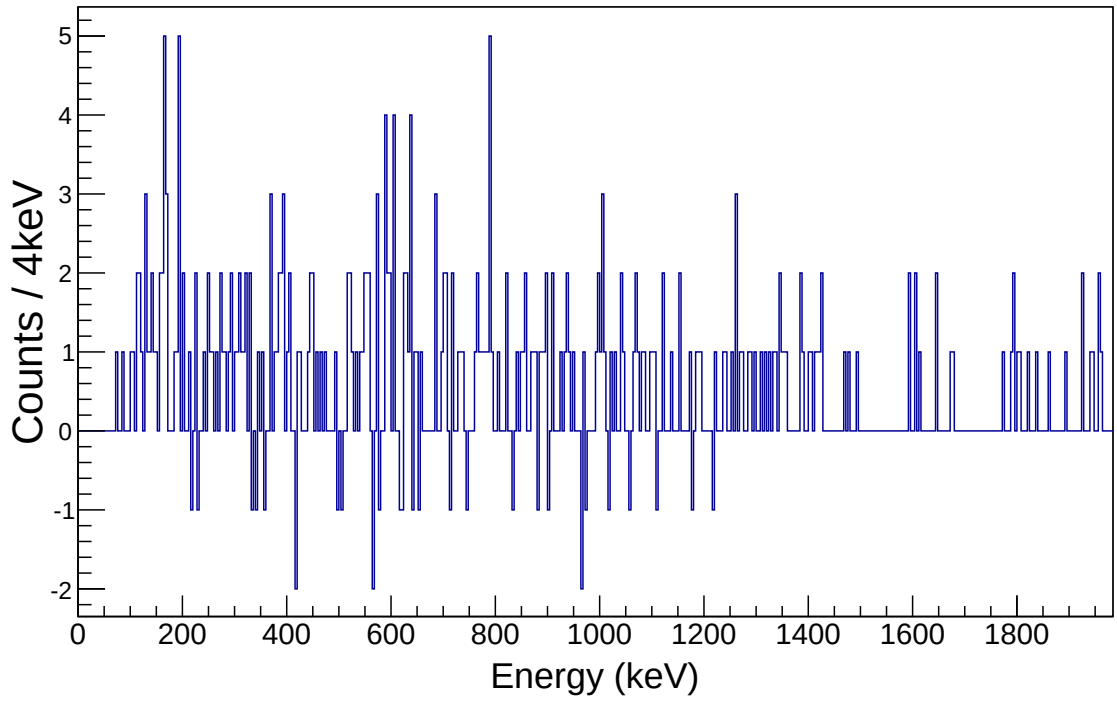

(a) A gamma gamma coincidence spectrum produced by projecting Figure 6.12 around the 977 keV peak and performing a local background subtraction above and below the peak.

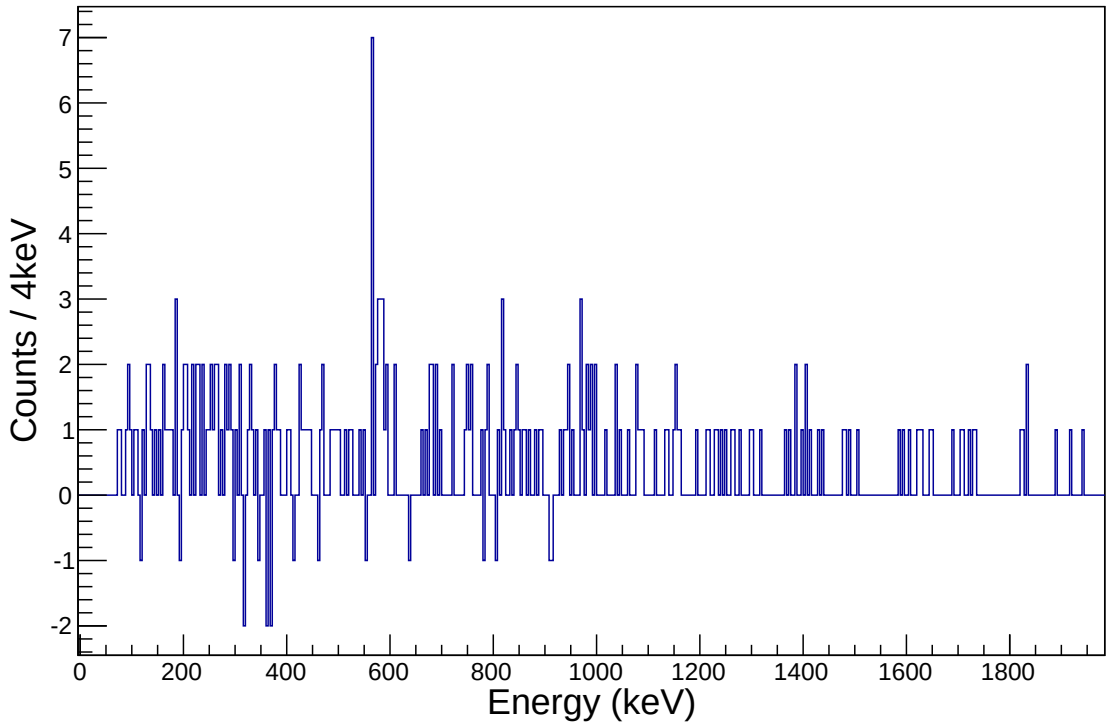

(b) A gamma gamma coincidence spectrum produced by projecting Figure 6.12 around the 784 keV peak and performing a local background subtraction above and below the peak.

Figure 6.13: gamma ray coincidence spectra populated in 1p2n removal from ^{65}Ge to ^{62}Ga.

6.6 Mirrored knockout to $A = 65$

Mirrored one-proton and one-neutron knockout reactions were studied from the ^{66}As beam to ^{65}As and ^{65}Ge. The states in ^{65}Ge are known well, however, only one state in ^{65}As has been previously observed, the first excited $\frac{5}{2}^-$ state. The observed gamma rays in this experiment represent the only known data from ^{65}As. To aid the discussion Figure 6.14 is a level scheme of ^{65}Ge, reproduced from Reference [63].

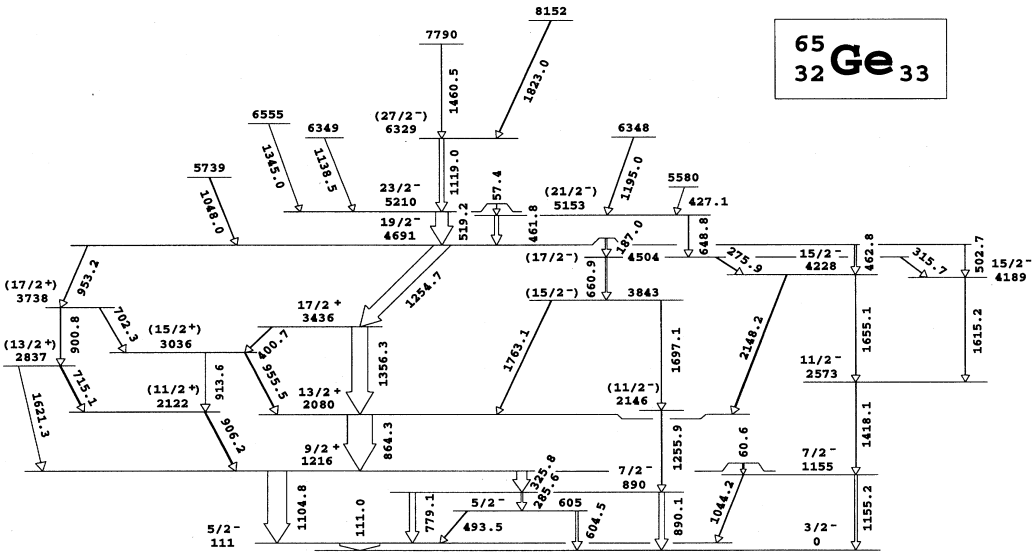

Figure 6.14: Energy level scheme of ^{65}Ge reproduced from Reference [63].

The mirror nuclei ^{65}Ge and ^{65}As were populated through mirrored 1p and 1n knockout reactions from the ^{66}As beam. The gamma ray spectrum for ^{65}Ge is shown in Figure 6.15a, the known [63,64] peaks populated have been labelled. Many of the known observed states decay to the $\frac{9}{2}^+$ state which has a 7 ns half life. This half life is sufficiently long that it is not possible to observe the decay from the state, or any subsequent feeding. It is possible to use this information to say that the $\frac{5}{2}^-$state is populated directly, as an indirect population would not show up in a peak at the correct energy due to poor Doppler correction. The $\frac{7}{2}^-$ state is labeled as tentative. From previous work [63] one would also expect a peak at 779.1 keV with the same intensity as a peak at 890.1 keV which is not observed. A spectrum of observed gamma rays from ^{65}As are shown in Figure 6.15b. The previously observed state [65] has been labelled, as has a 647 keV transition to highlight the questionable nature of the fit. All other peaks are labelled with their energies and error from Gaussian fits.

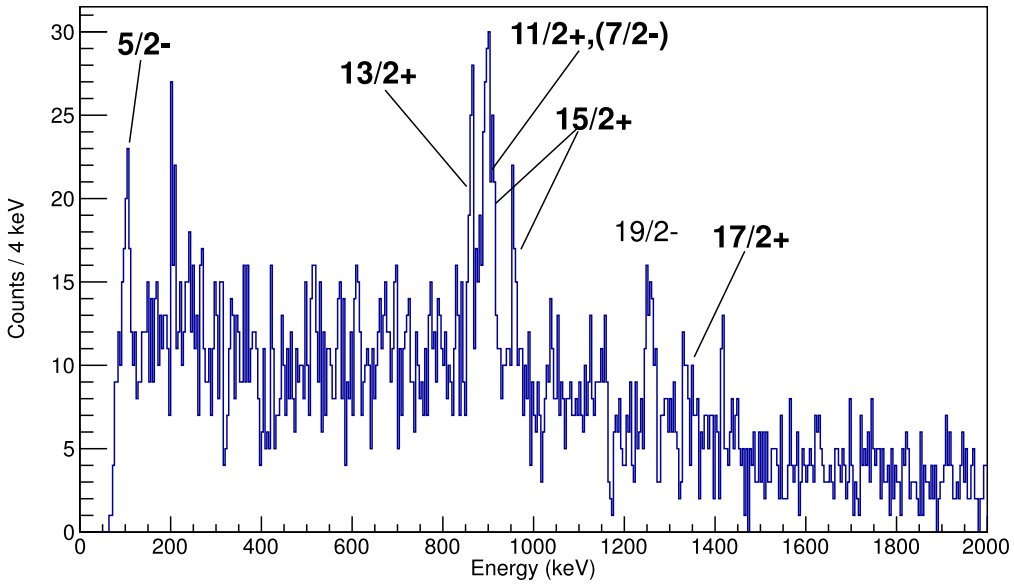

(a) Gamma rays from ^{65}Ge populated in one-proton knockout from ^{66}As. The previously observed states have been labelled [63].

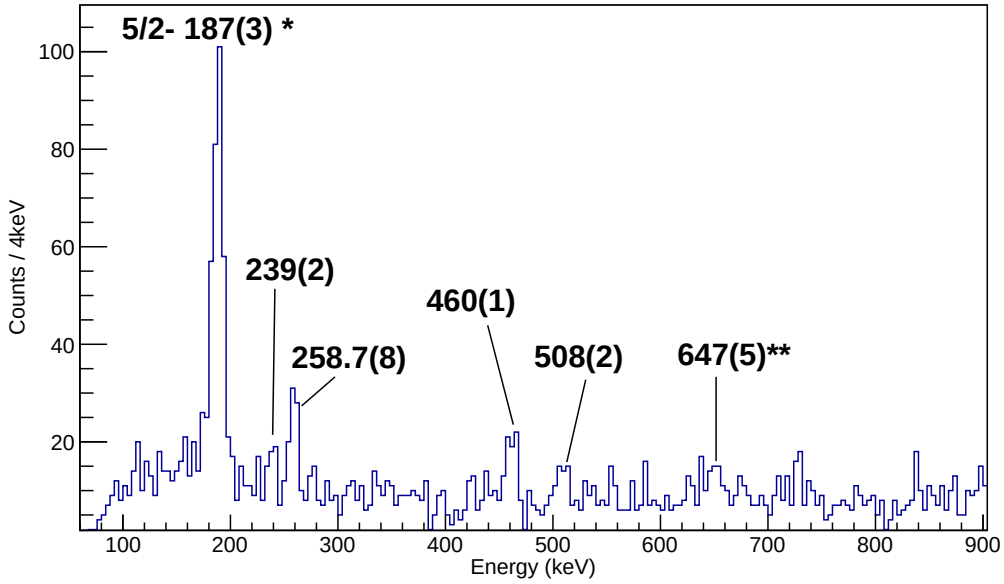

(b) Gamma rays from ^{65}As populated in one-neutron knockout from ^{66}As, the peaks that are new to this work have been labelled with the measured energy and statistical error from the fit. * The only previously observed gamma ray [65]. ** The fit to this peak was unsatisfactory due to the background, the resolution measured using the fit was 2.7%, higher than the 2.4% measured for the 460 keV and 508 keV peaks.

Figure 6.15: Gamma ray spectra from the $T_z = \frac{1}{2}$, $A = 65$ nuclei. These spectra were created by gating on ^{66}As data from the A1900 and ^{65}Ge/^{65}As data from the S800. A time cut has been applied such as that in Figure 6.6a and a FoM cut of 0.8 has been applied.

6.7 Reactions to populate ^{63}Ga and ^{63}Ge

The $T_z = \frac{1}{2}$, $A = 65$ mirror nuclei ^{63}Ge and ^{63}Ga were populated in a number of reactions: ^{65}Ge(^{9}Be,2n)^{63}Ge, ^{66}As(^{9}Be,1p2n)^{63}Ge, and ^{64}Ga(^{9}Be,1n)^{63}Ga. The data gathered on ^{63}Ge represents the only current data on the excited states of ^{63}Ge. The presented experiment is the only experiment to populate ^{63}Ga via knockout or fragmentation reactions and new states are observed. For reference during this analysis Figure 6.16 is the known low-lying level scheme (below 2.1 MeV) of ^{63}Ga. It is worth noting that all of the previously observed states above 2.0465 MeV decay to the 2.0465 MeV $\frac{9}{2}^+$ state. It is also worth noting that all previous experiments have been fusion evaporation experiments that have populated high spin states [66, 67]. Thus investigation of the level scheme below the 2.0465 MeV $\frac{9}{2}^+$ state has been dominated by the branching ratio of decays from it. The work presented in this thesis is the first to directly populate these states, which accounts for the large population of states such as that labelled "b" in Figure 6.17a, where previously there was not enough data to determine multipolarities.

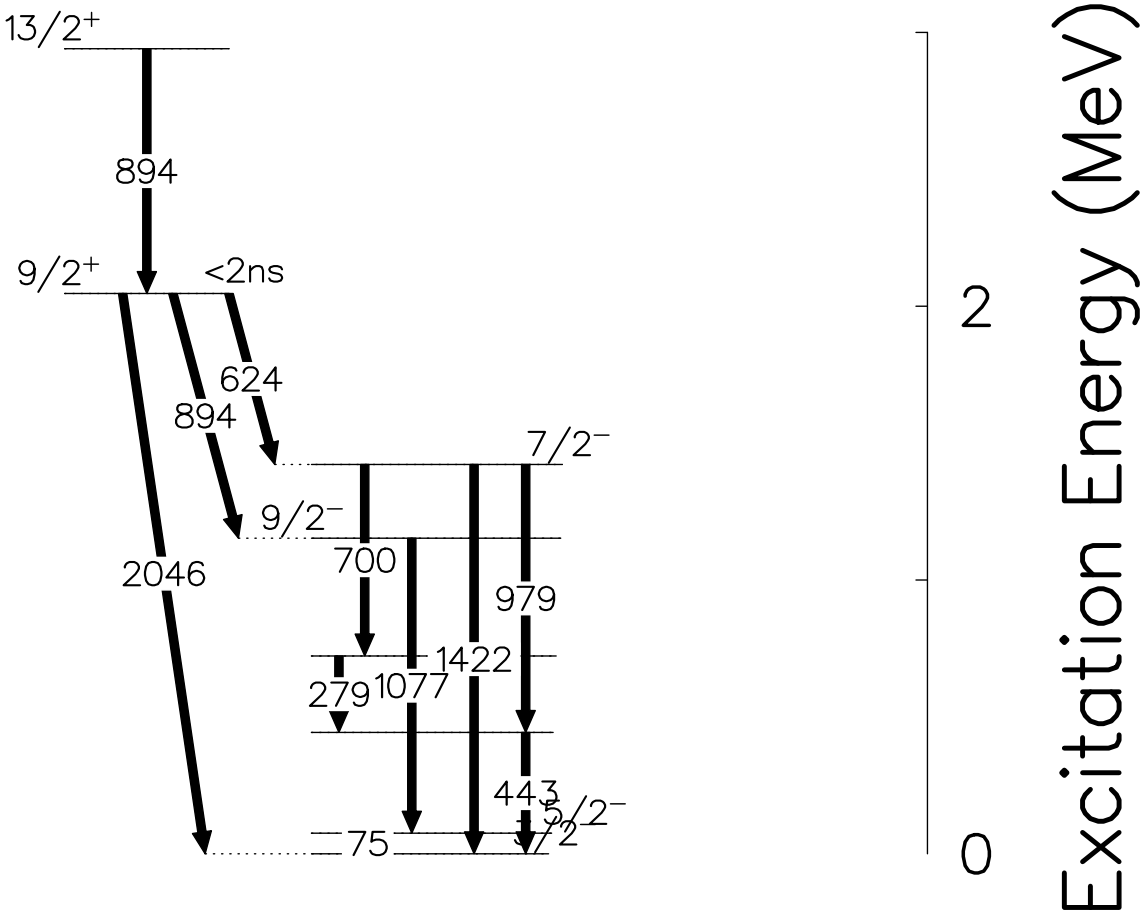

Figure 6.16: Energy level scheme of ^{63}Ga adapted from the National Nuclear Data Center (NNDC) [59].

Nucleon	Range of States
$f_{\frac{7}{2}}$	Negative parity states up to a maximum spin of $\frac{7}{2}$
$p_{\frac{3}{2}}$	Negative parity states up to a maximum spin of $\frac{3}{2}$
$f_{\frac{5}{2}}$	Negative parity states up to a maximum spin of $\frac{5}{2}$
$p_{\frac{1}{2}}$	Negative parity states up to a maximum spin of $\frac{1}{2}$
$g_{\frac{9}{2}}$	**Positive** parity states up to a maximum spin of $\frac{9}{2}$

Table 6.2: The range of states that can be populated in ^{63}Ga in one-neutron knockout from the ^{64}Ga ground state.

6.7.1 One neutron knockout from ^{64}Ga to ^{63}Ga

In one-neutron knockout from the 0^+ ground state of ^{64}Ga different states could be populated depending on which orbital the removed nucleon was in, Table 6.2 details these. Evidence for the ^{64}Ga beam being in an 2^+ isomeric state has already been presented in this Chapter, in which case population of higher spin states by two units of angular momentum) is expected. Table 6.2 shows that if there is a significant isomer ratio, population of states with spins up to $\frac{13}{2}^+$ is expected, if $g_{\frac{9}{2}}$ neutrons are removed.

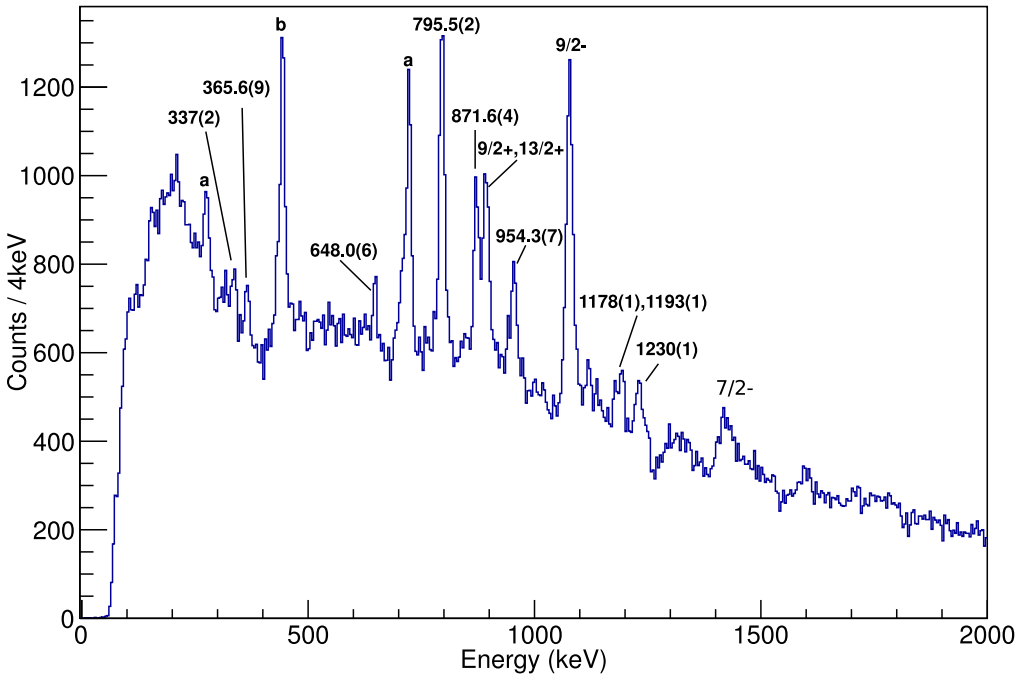

(a) Gamma ray spectrum of ^{63}Ga populated through one-neutron knockout, the gamma rays from known transitions have been labelled with the spin of the parent state, Table 6.3 lists the energies of gamma rays from this reaction.

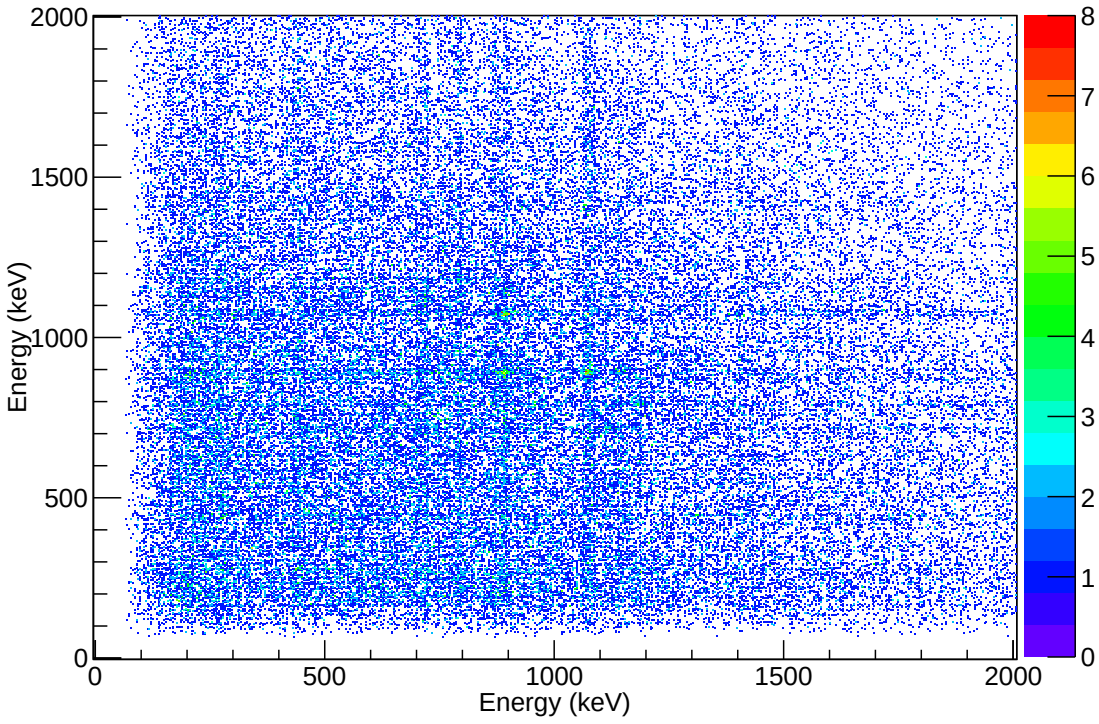

(b) A gamma gamma coincidence matrix for ^{63}Ga produced in one neutron knockout from ^{64}Ga.

Figure 6.17: ^{63}Ga gamma ray spectra by gating on ^{64}Ga data from the A1900 and ^{63}Ga data from the S800. A time cut has been applied such as that in Figure 6.6a and a FoM cut of 0.8 has been applied.

This high statistics channel has revealed previously unobserved states in ^{63}Ga. It is possible to tentatively assign some of these transitions to positions in the level scheme: the 365.6(9) keV transition has the correct energy to be the decay from the state labelled "b" in Figure 6.18 to the $\frac{5}{2}^-$ state (though it was not possible to place it with a gamma gamma analysis); the 795.5(2) keV and 871.6(4) keV transitions are (to within 1 keV) separated by the same energy as the $\frac{5}{2}^-$ state so it is proposed are decays from a new state at 871.6(4) keV to the ground state and $\frac{5}{2}^-$isomer. In the known level scheme (shown in Figure 6.16.) the gamma ray transitions from the $\frac{13}{2}^+$ and $\frac{9}{2}^+$ states are both at approximately 894 keV, closer in energy than can be resolved in this study. A gamma gamma analysis shows that both states are populated. Figures 6.18b, 6.18a show gamma gamma gated and background subtracted spectra gated on the 894 keV and 1078 keV peaks. The 1078 keV peak strongly returns the 894 keV peaks and the 894 keV peak is in self coincidence, i.e. gating on the 894 keV peak in the gamma gamma matrix returns a spectrum with an 894 keV peak. This self coincidence is the expected result from population of the $\frac{13}{2}^+$ state. Additionally, the 894 keV gate appears to return the 1140 keV transition from the $\frac{17}{2}$ state. This is highly suspect however, as it would not be possible from the reaction mechanism. The observed transitions are listed in Table 6.3 and shown in Figure 6.18.

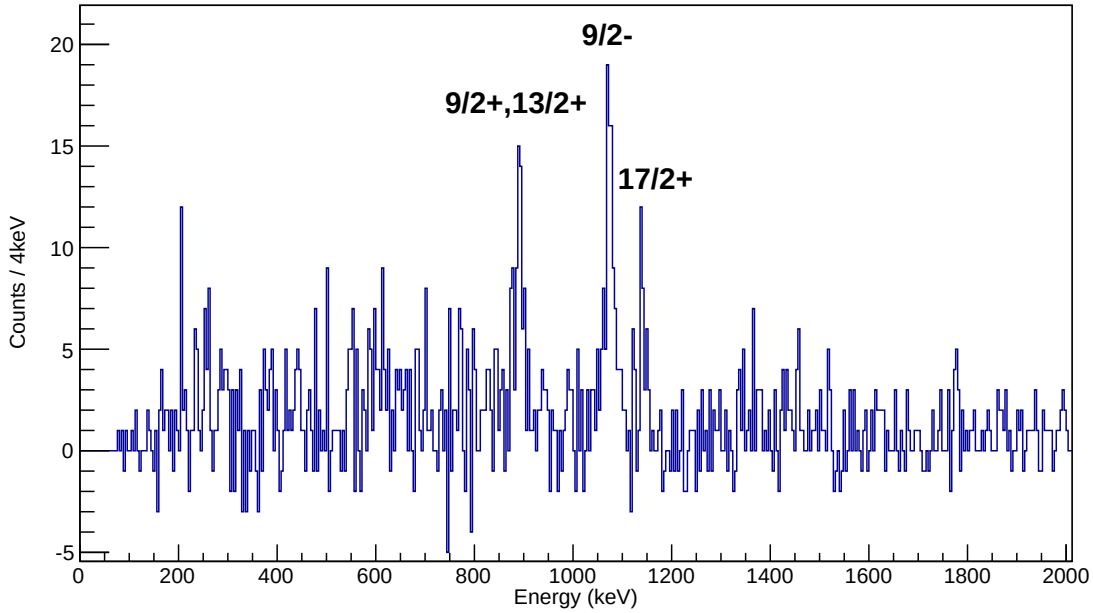

(a) A gamma gamma coincidence spectrum produced by projecting Figure 6.12 around the 894 keV peak and performing a local background subtraction above and below the peak.

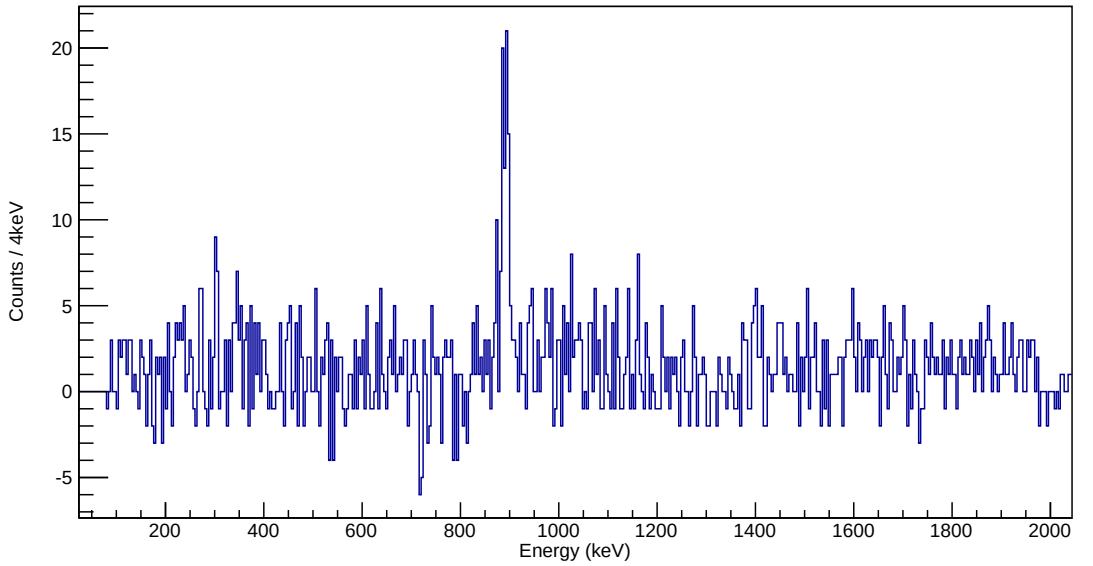

(b) A gamma gamma coincidence spectrum produced by projecting Figure 6.12 around the 1078 keV peak and performing a local background subtraction above and below the peak.

Energy (keV)	Error (keV)	Initial J^π	Final J^π
275.4	0.4	-	-
337	2	-	-
365.6	0.9	b	$(\frac{5}{2}^-)$
443.3	0.2	b	$\frac{3}{2}^-$
648.0	0.6	-	-
723.4	5	a	$\frac{3}{2}^-$
795.5	0.2	c	$\frac{5}{2}^-$
871.6	0.4	c	$(\frac{3}{2}^-)$
892.7	0.4	$\frac{13}{2}^+$	$\frac{9}{2}^+$
892.7	0.4	$\frac{9}{2}^+$	$\frac{9}{2}^-$
954.3	0.7	-	-
1077.7	0.2	$\frac{9}{2}^-$	$\frac{5}{2}^-$
1178	1	-	-
1193	1	-	-
1230	1	-	-

Table 6.3: Observed gamma rays from ^{63}Ga, where known initial and final spins and parities for the transitions are shown.

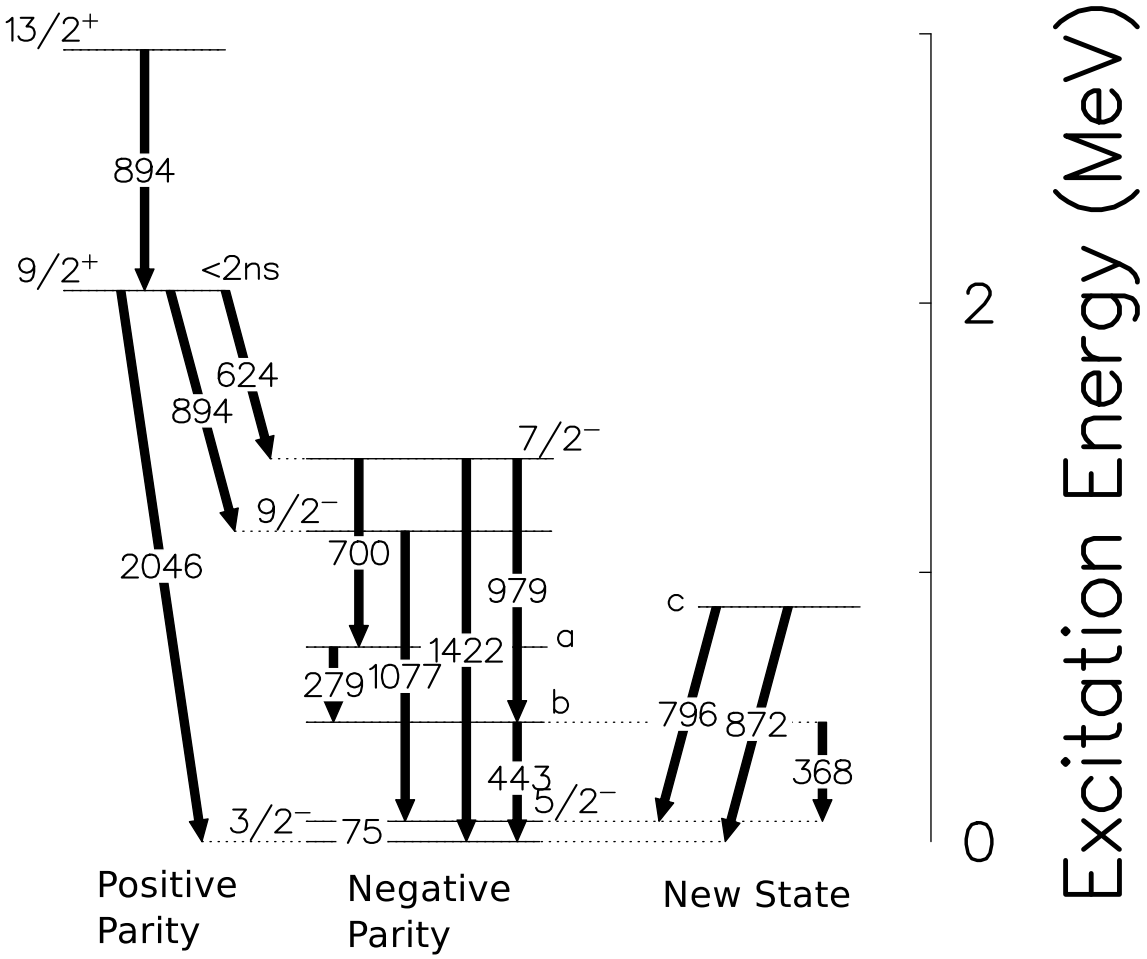

Figure 6.18: Energy level scheme of populated states in one neutron knockout from ^{64}Ga to ^{63}Ga.

6.7.2 ^{63}Ge Populated from ^{66}As

Unlike the $A = 65$ case the mirrored reactions here are not considered to be direct reactions, and as such the reaction to populate ^{63}Ga from ^{66}As is not utilised. Figure 6.19 shows the ^{63}Ge gamma ray spectrum, with the most prominent transitions being 416 keV and 1081 keV. These transitions are most likely the mirrors of the known 443.1 keV transition in ^{63}Ga shown in Figure 6.16, and the 1081 keV transition is likely the mirror of the $\frac{9}{2}^-$ to $\frac{5}{2}^-$ 1077.2 keV transition. Just considering the low-lying level scheme the only match (with an MED of less than 100 keV) for the 896 keV transition would be the 893.7 keV transition. The branching ratio from the $\frac{9}{2}^+$ state in ^{63}Ga is 15.1:57.5:0 to the 624, 893, 1971 keV transitions, which could account for not observing a candidate for the mirror of the 624 keV transition.

Unfortunately this analysis is not sufficient to perform an MED analysis as many of the observed transitions decay to the $\frac{5}{2}^-$ state, which is not observed due to the 25 ns lifetime [63]. A 25 ns lifetime corresponds to a decay over two metres past the centre of GRETINA. The only case where the energy of a state has been (tentatively) determined has unknown spin and parity.

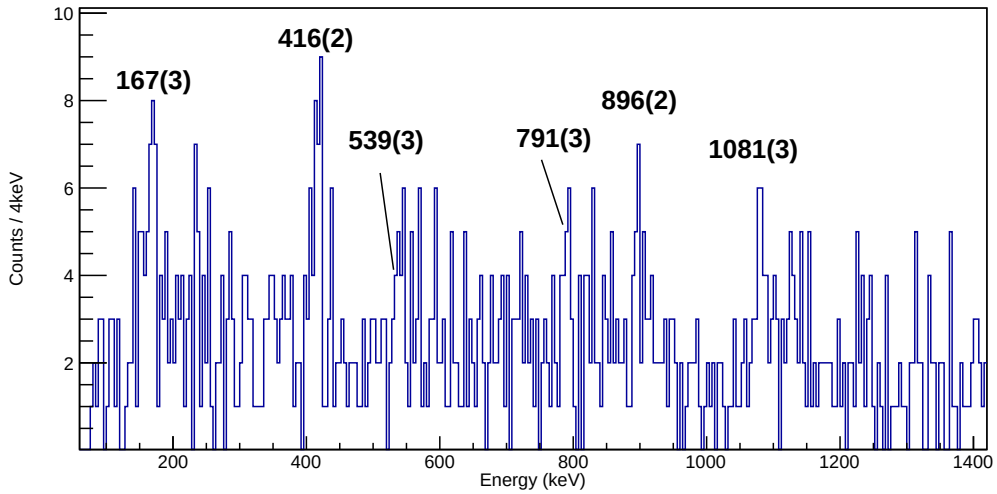

Figure 6.19: Gamma ray spectrum of ^{63}Ge created by gating on ^{66}As data from the A1900 and ^{63}Ge data from the S800. A time cut has been applied such as that in Figure 6.6a and a FoM cut of 0.8 has been applied. Gamma ray energies are based on χ^2 fits of Gaussian with a linear background, the errors are statistical from the fit and do not include any systemtatic error from the Doppler correction. $\beta = 0.301$

6.7.3 Two-neutron knockout from ^{65}Ge to ^{63}Ge

The ^{63}Ge spectrum is shown in Figure 6.20. Similarly to the ^{62}Ga case a section of the CRDC had to be gated away from in order to produce a clean spectrum. As in the case for population from ^{66}As the statistics are low, leading to a high error in the fits. In many cases the peak energies from the ^{66}As reaction channel differ to those from the ^{65}Ge reaction. This difference in peak energy likely stems from a systematic error in the Doppler correction which is more difficult to ascertain in the ^{66}As case due to the lower statistics. As such energy and error values from the ^{65}Ge are

used for the MED analysis later.

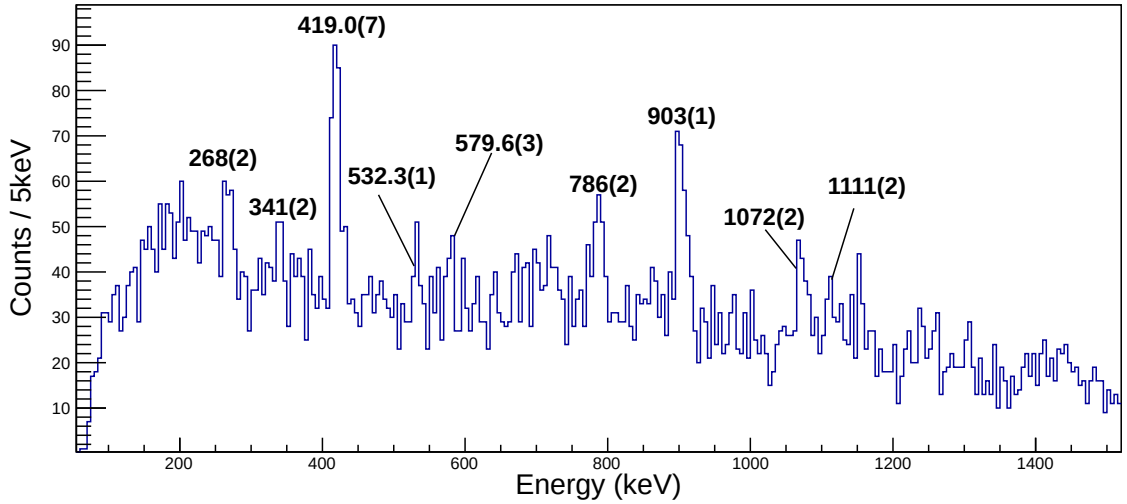

Figure 6.20: ^{63}Ge gamma ray spectrum populated by gating on ^{65}Ge data from the A1900 and ^{63}Ge data from the S800. A time cut has been applied such as that in Figure 6.6a and a FoM cut of 0.8 has been applied. A β of 0.306 was chosen to give the sharpest peaks.

In order to identify the energy of the $\frac{5}{2}^-_1$ state it is assumed that the 341(2) keV transition is the mirror of the observed 365.6(9) keV in ^{63}Ga and the 419.0(7) keV transition is the mirror of the 443.1 keV transition due to similar energies. This is a highly speculative result. This assignment is supported by the similar branching ratios of the 419 keV to 341 keV states in ^{63}Ge and 443 keV and 366 keV states in ^{63}Ga. However, the tentative nature of this assignment must be emphasised. Those transitions give the $\frac{5}{2}^-_1$ state an energy of 76(2) keV, which corresponds to an MED within error of 0 keV. Considering the 1072(2) keV transition as the mirror of the 1077.2 keV transition gives the $\frac{9}{2}^-_1$ state an energy of 1153(3) keV. The closest transition to the new 795.5(2) keV transition in ^{63}Ga is the 786(2) keV transition. However, a transition at 862(3) keV would also be expected and was not observed. The 268(2) keV peak has a similar energy to the observed 275.4(8) keV transition in the ^{63}Ga, however, this transition has not been associated with a state. None of the other transitions can be matched to a transition in the mirror nucleus, as any assignment leads to a missing transition that should be fed. Additionally, it has been impossible to identify the structure around 700 keV as a transition or series of transitions.

To construct an MED diagram the tentative assignment can be used: the $\frac{5}{2}^-_1$ state with an MED of 1(2) keV, and the $\frac{9}{2}^-_1$ state with an MED of -5(2) keV. Though the energy of the 419.0(7) keV state has also been assigned as it does not have a spin assignment it cannot be used for an MED. The experimental MED alongside theoretical predictions are shown in Figure 7.14

Chapter 7

Discussion

7.1 ^{51}Co

The level scheme for ^{51}Co is presented in Figure 5.10, alongside the analogue states in ^{51}Cr [59]. Negative parity yrast states are observed up to a spin of $\frac{19}{2}$. This is the expected result, as the knocked out neutrons can couple to a maximum spin of $J = 6$, and the g.s. of ^{53}Co has a spin of $\frac{7}{2}^-$. Cross section calculations presented in Figure 5.9 confirm these assumptions. The only real deviation is that high spins states, the $\frac{19}{2}^-$ and $\frac{17}{2}^-$ states, are populated more strongly than predicted. An isomer content to the incoming beam might explain the population of these states. Since the analysis presented in this thesis was performed, it was discovered that the beam was in an isomeric state (see Chapter 6, with the isomer ratio on the order of 40% [68]).

The strong presence of the isomer raises some issues concerning the states populated. Knockout from the ground state of ^{53}Co could populate states with a maximum spin of $\frac{19}{2}^-$, whereas knockout from the isomer can populate much higher-spin states which are not observed. The calculations presented in Chapter 6 only include knockout from the ground state and do not consider knockout from the isomer. These ground-state knockout calculations, which are presented only as a guide, predict that mostly yrast states should be populated. In considering the presence of the isomer one might expect stronger population of states close in spin to that of the isomer, $\frac{19}{2}^-$. Indeed, the higher-spin yrast states are populated with more strength than expected from the ground-state calculations. The ground-state knockout calculations suggest that some low-spin states should be populated at a similar strength to the $\frac{19}{2}^-$ state. This was not observed due to the significant isomeric content in the beam, since states with spin of lower than $\frac{7}{2}^-$ are impossible to populate from knockout from the isomer. Population of low spins via knockout from the isomer isn't possible as the $J = \frac{19}{2}$ state of the isomer must couple to the spin of the knocked out nucleons (which has a maximum of $J = 6$ for two $f_{\frac{7}{2}}$ nucleons). The lowest spin state it is possible to populate in the daughter nucleus via knockout from the isomer is $J = \frac{7}{2}$. The only remaining question then is why higher spin states have not been observed. The answer is that the remaining transitions in the yrast chain in ^{51}Cr have much larger energies (1894 keV and 1746 keV). Mirror transitions will have similar energies and would not be observed unless populated with significant strength.

The proton separation energy in ^{51}Co is 140 (80) keV [69] and the energies of the states of interest are all proton unbound, with energies between $1 - 4$ MeV. This represents a break in the

J^{Parent}	$E^{parent} - S_p$ (keV)	$J^{Daughter}$	$E^{Daughter}$ (keV)	Q-value of decay (keV)
$\frac{7}{2}$	-140	0	0	-140
$\frac{9}{2}$	989	2	746.9	242.1
$\frac{11}{2}$	1355	2	746.9	688.1
$\frac{15}{2}$	2217	4	1851.5	365.5
$\frac{17}{2}$	3170	6	3159.3	10.7
$\frac{19}{2}$	3852	6	3159.3	692.7

Table 7.1: Parent and possible daughter states that provide the largest Q-value for possible proton emission from ^{51}Co.

mirror symmetry: proton emission is energetically possible in the $T_z = -\frac{3}{2}$ nucleus; the mirrored decay (neutron emission) is not energetically possible in the $T_z = +\frac{3}{2}$ nucleus. Though proton emission is possible it will not necessarily happen and it would compete with gamma decay.

Assuming that proton decay proceeds to the lowest energy state allowed by conservation of angular momentum the partial half life for proton decay can be calculated. The approach taken is to use the tunnelling probability of a proton escaping a potential with a given Q-value. This approach does not take into account any overlap in the nuclear wavefunction between initial and final states. As such the results should be considered a minimum possible half life; the actual values are expected to be significantly higher. For this work the lowest energy state in ^{50}Fe [70] that can be populated from the decay of a particular state in ^{51}Co was used to calculate the maximum possible Q-value. Once a Q-value was known a simplistic code referred to as Barry was used to calculate the tunnelling probability. Barry uses an optical potential to fit to low-energy scattering on $A > 40$ nuclei [71]. Table 7.1 details the states and maximum possible Q-values from the known states in ^{50}Fe. Results from these calculations are shown in Figure 7.1.

Using the approach described the half life can be calculated from Figure 7.1 using the Q-values from Table 7.1. The shortest half life is around 4.5 ps, for the $\frac{19}{2}^-$ state. There is no indication of a long gamma decay half life in the $\frac{19}{2}^-$ state so proton emission may be a competing process. As the presented value is a minimum partial half life and the spectroscopic overlap is likely to be much less than 100% proton emission from this state is not considered. In this work no other states have half lifes that are sufficiently short so as to compete with gamma decay. The lower spin non-yrast states do have significant Q-value. They may well proton decay or decay to a state that undergoes proton decay. Specifically the $\frac{3}{2}^-_2$ and $\frac{5}{2}^-_2$ states are predicted to be populated by the calculations shown in Figure 5.9.

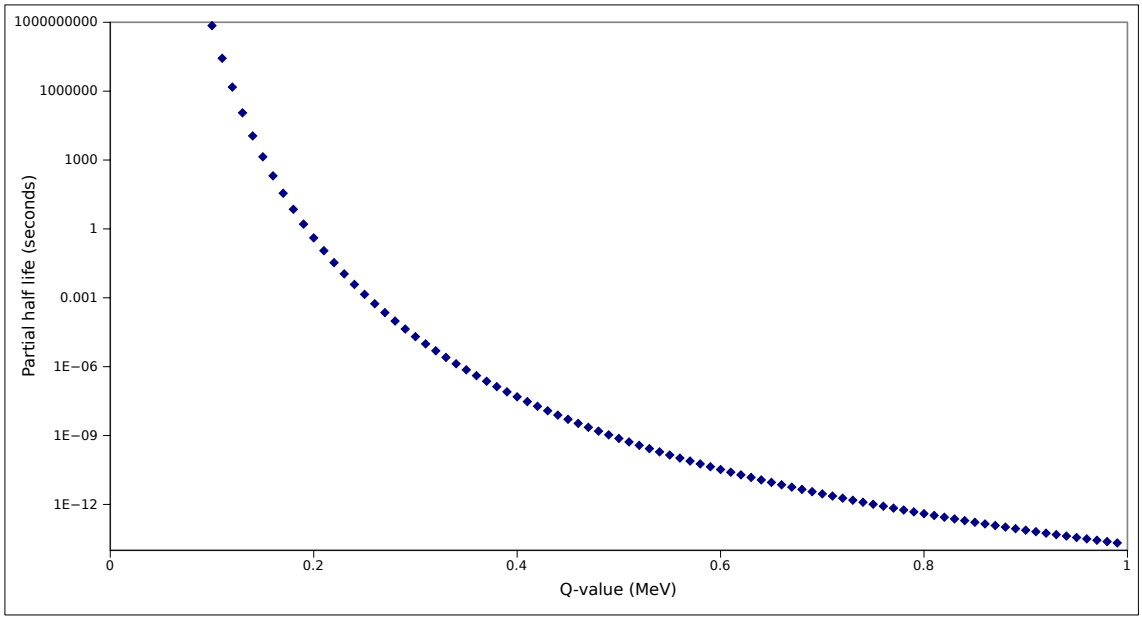

Figure 7.1: Partial half life for proton emission over a range of Q-values in ^{51}Co. These data were calculated using an optical potential fit to low energy scattering data and the code "Barry".

Figure 7.2 shows the experimental MED taken from the level scheme presented in Figure 5.10. The experimental data points are shown in red in the upper panel. These are compared to shell model calculations using the prescription put forward in Chapter 2 with the solid black line, the dashed black line represents this formalism without the V_b term. The lower panel shows a breakdown of the individual components to the calculations.

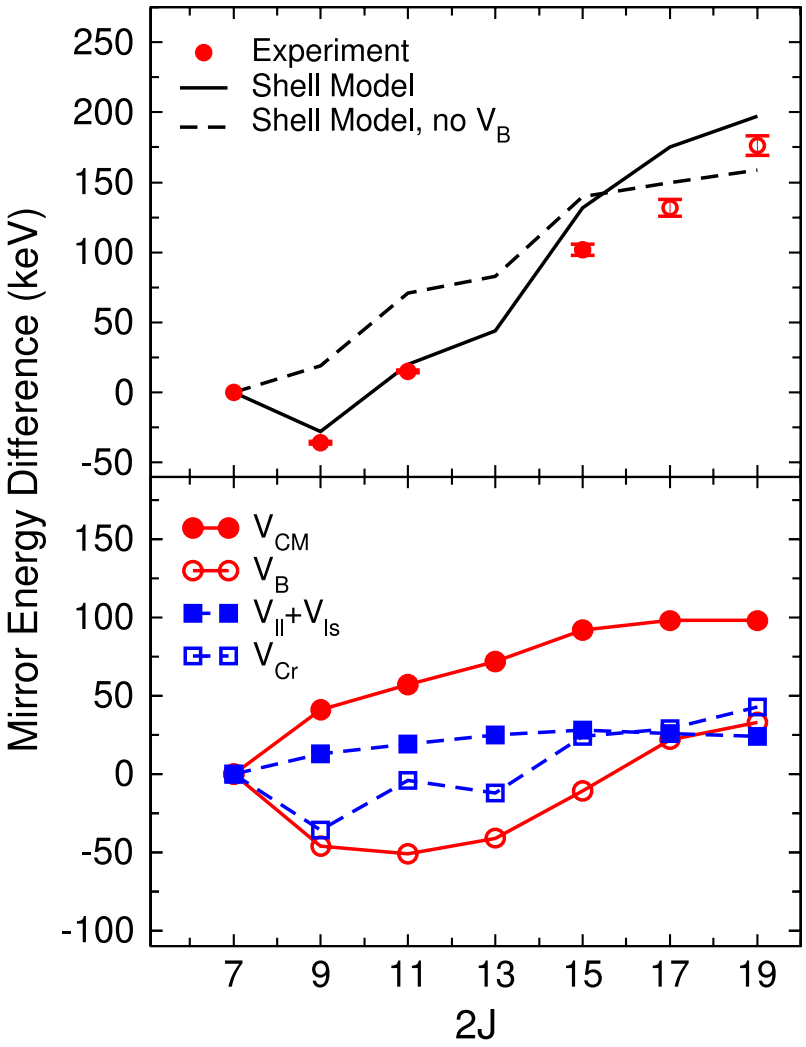

Figure 7.2: The experimental and theoretical mirror energy differences for the $A = 51$, $T_z = \frac{3}{2}$ system, adapted from Reference [55]. The upper panel compares the experimental data to the calculation with and without the V_b term. The lower panel shows the breakdown of the terms in the calculation. The open circles in the upper panel represent the tentatively assigned data. See text for details.

The calculations presented in Figure 7.2 were performed by Prof. M. A. Bentley using the code ANTOINE [30] and the KB3G interaction [31] in the full fp space. These calculations show exceptional agreement with the experimental data points when a V_b term is included. Without the V_b term the calculated Mirror Energy Difference (MED) is larger than the experimental MED over most of the range. The MED reduces to the expected value at the $\frac{19}{2}^-$ state. Both with and without the V_b term the general trend is correct, but the initial dip moving from the $\frac{7}{2}$ to the $\frac{9}{2}$ state in Figure 7.2 is only recreated with the inclusion of the V_b term. The V_b term only having a significant effect over higher spin states can be explained by considering the wavefunctions of these two states. The calculations predict that the dominant configuration to the wavefunction of the $\frac{7}{2}^-$ state, with around 50% of the total strength, has all of the particles in the $f_{\frac{7}{2}}$ shell (as shown in Figures 7.3b and 7.3a). This state in ^{51}Co then can be simplistically considered as two pairs of neutrons and one pair of proton holes all coupled to $J = 0$, with one spare $f_{\frac{7}{2}}$ proton with $J = \frac{7}{2}$. As the wavefunction of the $\frac{9}{2}^-$ state is 45% in the $f_{\frac{7}{2}}$ the $\frac{9}{2}^-$ is most likely created by a pair of $f_{\frac{7}{2}}$ particles recoupling to $J = 2$ from $J = 0$ (protons in the case of ^{51}Co and neutrons in the case of ^{51}Cr). It is the change in the number of $J = 2$ couplings that causes the V_b term to have such a dramatic effect on this coupling. The calculated occupations of the shells can be used to understand the remaining configurations.

Figure 7.3b and Figure 7.3a show the neutron and proton configurations of all of the states included in the MED diagram. This calculation was performed with an isoscalar interaction (i.e. treating protons and neutrons in an identical manner). The label proton is applied as though the nucleus of interest were ^{51}Co. Monopole terms in the calculations depend only on the occupancy of orbitals. As no significant change is seen to the occupancies as a function of spin the V_{lls} terms remain approximately constant. The V_{cr} term is linearly dependent on the sum of proton and neutron occupancy of the $p_{\frac{3}{2}}$ orbital. A factor of 200 keV is used to convert particle occupancy to the V_{cr} term, which makes the term very sensitive. While the proton $p_{\frac{3}{2}}$ occupancy remains very stable the neutron occupancy oscillates with spin. The neutron occupancy oscillation is what drives the oscillation observed in the V_{cr} term in Figure 7.2.

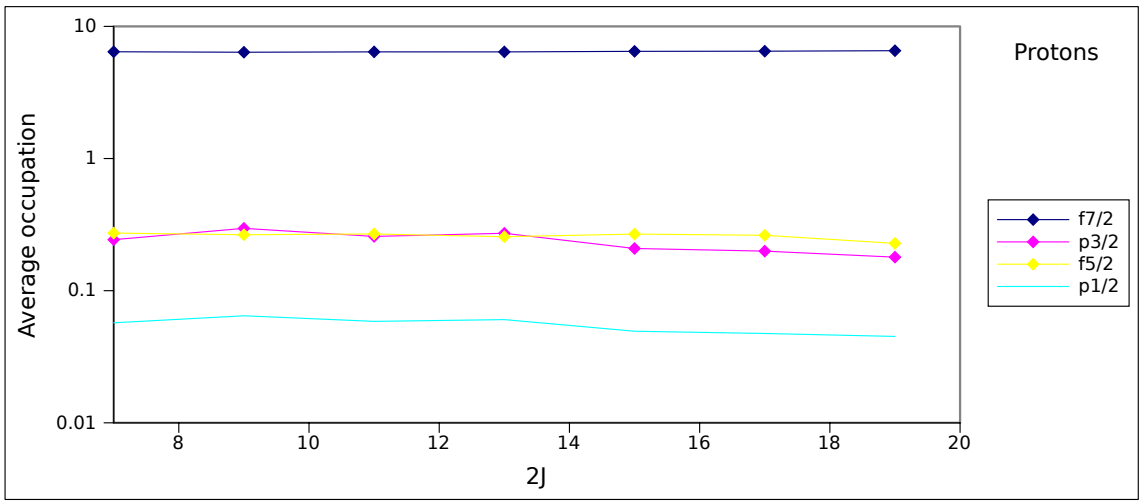

(a) Calculated average proton occupation in each of the fp shells for ^{51}Co.

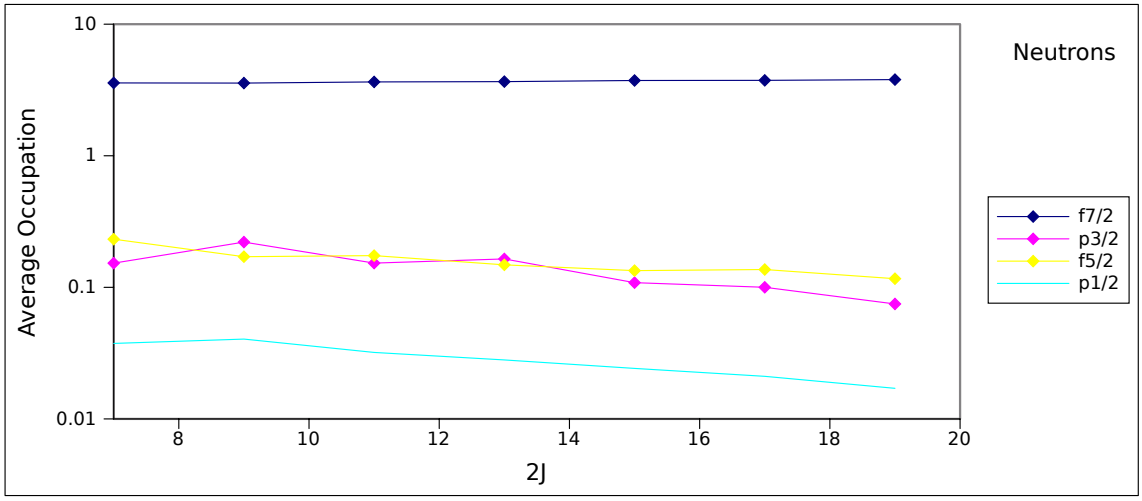

(b) Calculated average neutron occupation in each of the fp shells for ^{51}Co.

Figure 7.3: Calculated average proton and neutron fp-shell occupancies for states in ^{51}Co. Taken from shell-model calculations performed with ANTOINE and the kb3g interaction in the full fp shell space.

One of the concerns already expressed in this section is the possible breakdown of mirror symmetry in states above the proton separation energy. The shell-model approach employed has no capability to interpret any data that is influenced by weak binding energies. This may lead to a breakdown of isospin symmetry. If an effect not considered by the shell model were affecting the MED, the expectation is that the calculated MED would not match the experimental data. In this case agreement is seen between calculation and experiment. In conclusion, the $A = 51$, $T_Z = \frac{3}{2}$ mirror nuclei, the $J = 2$ anomaly is observed despite relevant states being above the proton separation energy.

7.1.1 $J = 0$ couplings

There is another possible analysis of the $A = 51$ MED: that of $J = 0$ vs $J = 2$ isospin non-conserving terms. The $J = 2$ anomaly is a positive isovector term that acts on $J = 2$ couplings, making $J = 2$ couplings more attractive (i.e. more bound) in protons compared to neutrons. The magnitude of the effect is such that $V_{pp} - V_{nn} = 100$ keV. It is also possible to apply a -100 keV term to $J = 0$ couplings. The $J = 0$ approach is taken by Kaneko *et al.*, who have performed a similar analysis using ground-state masses of nuclei across the fp-shell [72]. In the analysis presented in this thesis the isospin non-conserving components have been deduced using excitation energies.

If states are constructed entirely out of $J = 0$ and $J = 2$ coupled pairs of nuclei it should not make a difference whether a +100 keV $J = 2$ coupling or a -100 keV $J = 0$ coupling is used i.e. it is the J-dependence that matters not the absolute values. However, when states are populated with higher J couplings such as $J = 4$ or $J = 6$ in the $f_{\frac{7}{2}}$ shell (as might be expected for higher-spin states), the MED becomes dependent on the magnitude of the isovector nature of the higher-spin terms relative to the lower-spin terms which mostly make up the ground state. By performing calculations with $J = 0$ and $J = 2$ isospin non-conserving terms for higher-spin states, one can understand which term should be used, even though both may reproduce the trends at low spin. The MEDs, calculated in the same manner as presented in Figure 7.2, are presented in Table 7.2 and Figure 7.4. The experimental data show poor agreement at high spin with both $J = 0$ and $J = 2$ terms. At low spin this shows that it doesn't matter whether the negative $J = 0$ or positive $J = 2$ term is used. However, at high spin where there are more likely to be higher spin couplings ($J = 4$ or $J = 6$) it seems that this approach is insufficient.

Table 7.2: Experimental and theoretical $A = 51$ MED. The theoretical MED is presented with both $J = 0$ and $J = 2$ isospin non conserving terms. This data is graphed in Figure 7.4.

J	Theory$_{J=0}$ (keV)	Theory$_{J=2}$ (keV)	Experiment (keV)
7	0	0	0
9	-35	-28	-36
11	12	20	15
13	17	44	
15	79	132	102
17	95	175	129
19	110	197	175

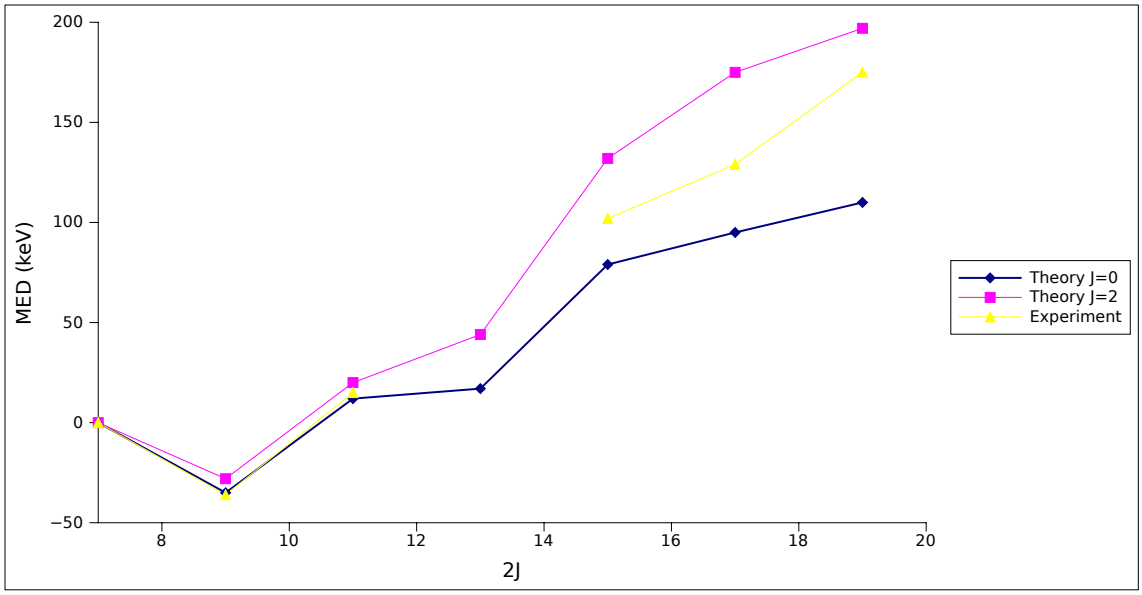

Figure 7.4: Experimental and theoretical MEDs for the $A = 51$ system. The calculations are presented with both $J = 0$ and $J = 2$ isospin non-conserving components. The experimental data are taken from this study (listed in Table 7.2), the calculations have been performed in a full fp space using ANTOINE and the kb3g interaction.

7.1.2 Further isospin non-conserving terms

Following the analysis presented in Section 7.1.1, Bentley *et al.* [73] performed an investigation using all available $f_{\frac{7}{2}}$ shell data. The MED shell model prescription was applied as described in Chapter 2, however initially no V_B term was applied. The difference between the experimental and calculated MED was fitted with a V_B term allowing J^2 isovector terms to vary freely. As a result $J = 0, 2, 4,$ and 6 terms were introduced as variables. It was found that the best terms to use are as described in Table 7.3. As can be seen, the best description is neither a pure $J = 0$ or $J = 2$ component, however the $J = 2$ component is always 100 keV larger than the $J = 0$. The fits show four distinct components acting on $J = 0, 2, 4,$ and 6. The calculated MEDs are not sensitive to the absolute scale of these interactions (so long as the interactions remain small enough to be treated as perturbations) but only on the relative differences. The key feature highlighted in the prior $J = 2$ and $J = 0$ work is the relative difference between $J = 0$ and $J = 2$ couplings. Speculatively, these calculations could be scaled such that the $J = 0$ term is the same as in the approach from Kaneko *et al.* which has been fitted to ground-state energies. To go beyond speculation, a full analysis of ground-state energies and MEDs would have to be undertaken.

7.2 ^{62}Ga

The work presented in this section has been published by T. W. Henry *et al.* [74]. Figures are reproduced with permission. The work in this section was motivated by the anomalous energy of the $T = 1$, $J^\pi = 2^+$ state in ^{62}Ga, when compared to states across $T = 1$ triplets with odd-odd $N = Z$ nuclei. The previous work was examined and data from two-neutron knockout from an

Table 7.3: Table of isospin non-consirving terms that have been deduced through a χ^2 fit to a variety of data ranges [73].

	$f_{\frac{7}{2}}$ V_B **matrix elements in (keV)**				RMS deviation	
Range	**J=0**	**J=2**	**J=4**	**J=6**	**fit**	**No VB**
	One-parameter fit					
A=42-54		68 (6)			32	41
A=42-54	-79 (6)				26	41
A=47-54		71 (5)			27	38
A=47-54	-83 (5)				22	38
A=51-54		61 (3)			28	40
A=51-54	-71 (3)				23	40
	Full fit					
A=42-54	-79(16)	25(13)	1(12)	-19(12)	23	41
A=47-54	-56(15)	46(11)	9(10)	2(11)	16	38
A=51-54	13(16)	82(10)	64(11)	39(11)	9	40
	Full fits: centroid-subtracted					
A=42-54	**-72(7)**	**32(6)**	**8(6)**	**-12(4)**	23	41
A=47-54	-66(7)	36(5)	-1(5)	-8(4)	17	38
A=51-54	-41(6)	28(3)	10(4)	-15(2)	18	40

isomer and ground state of ^{64}Ga is presented.

7.2.1 Previous observation of the $T = 1$, $J^\pi = 2^+$ state and the low lying level scheme of ^{62}Ga

Previous experiments to populate excited states in ^{62}Ga have been performed using fusion evaporation or β-decay. In Ref. [75] Vincent *et al.* used the ^{40}Ca(^{28}Si,αpn)^{62}Ga reaction to populate states up to 6.846 MeV, which were primarily yrast. These states were all assigned to be $T = 0$ as no observed states were obvious analogues to those in the $T_z = 1$ system (^{62}Zn). A further experiment was then performed by Rudolph *et al.* [61] using the ^{40}Ca(^{24}Mg,pn)^{62}Ga reaction at 55 MeV and 60 MeV to populate many non-yrast states. A gamma ray with an energy of 446 keV was observed in coincidence with the decay of the 571 keV 1^+ state to the $T = 1$, 0^+ ground state. The 446 keV transition was identified as a dipole transition, leading to the tentative assignment of a 2^+ state at 1017 keV. The first excited 2^+ state in ^{62}Zn (IAS to the $T = 1$, 2^+ state in ^{62}Ga) has an energy of 953.84 (9) keV. Rudoph *et al.* concluded that the 1017 keV state in ^{62}Ga was likely the $T = 1$, 2^+ state. Rudoph *et al.* did however comment that their shell model calculations (performed with the GXPF1a interaction) predicted the $T = 1$, 2^+ state to decay to the ground state via a quadrupole transition instead of to the first excited 1^+ state via a dipole transition. Two other works have since been published that populate the low lying structure of ^{62}Ga, the states populated are depicted in Figure 7.5.

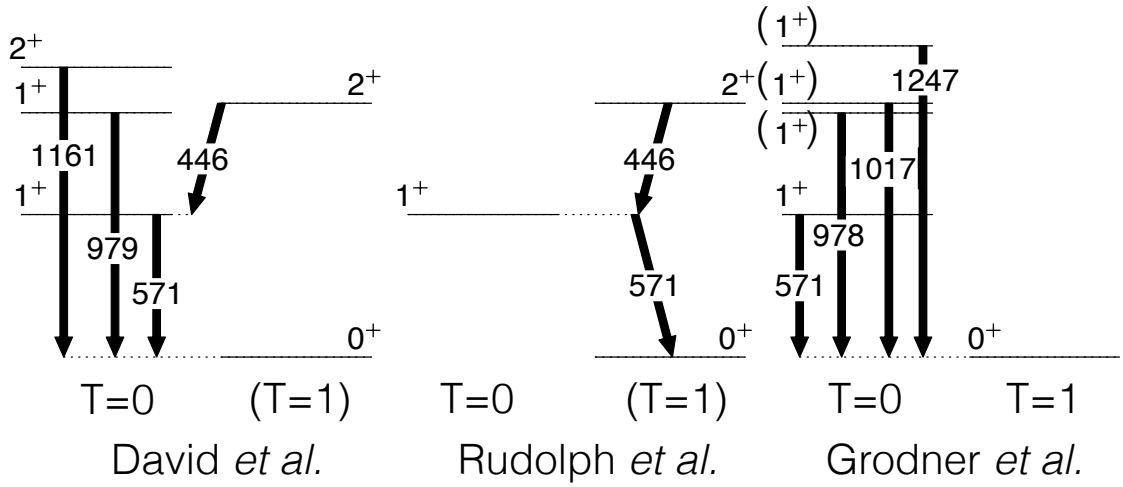

Figure 7.5: Energy level scheme and gamma ray transitions from Low lying 1^+ and 2^+ states in ^{62}Ga. The three schemes represent three previous experiments [43, 60, 75]. The $T = 1$ assignment of the 2^+ states is placed in parentheses here as it has been made on the basis of energy systematics.

David *et al.* used the ^{24}Mg(^{40}Ca,*pn*)^{62}Ga reaction at 103 MeV [60], with states in ^{62}Ga identified using a recoil-β-tagging method [76]. The spectrum of states reported below 1.5 MeV is the same as those of Rudolph *et al.*, with the addition of (presumed $T = 0$) states at 1161 keV and 979 keV, assigned as 2^+ and 1^+ respectively. It is noteworthy that the assignment of 1^+ from David *et al.* was made with an angular ratio of 0.77(25), where 1.15(3) would correspond to a 2^+, and 0.72(4) a 1^+ [60]. In both the work of Rudolph *et al.* and David *et al.* the authors suggest that the state at 1017 keV, decaying by a dipole transition to the first excited 1^+ state, is the $T = 1$ analog of the 2^+ states in the even-even neighbours ^{62}Ge and ^{62}Zn. In Ref. [43] Grodner *et al.* observed gamma ray transitions of 978 keV and 1017 keV in the β-decay of ^{62}Ge. These transitions were tentatively assigned as decays from (1^+) states to the 0^+ ground state. The authors suggest that this state is different from the 1017 keV state suggested to be the $T = 1$, 2^+ state. Thus, as summarised in Figure 7.5, there are tentative assignments of 1^+ and 2^+ for states at 1017 keV.

7.2.2 Systematics of $T = 1$, $J^\pi = 2^+$ state energies as a guide

An analysis of the energies of $T = 1$, 2^+ states provided an interesting description of the systematics of triplet energy differences and a possible guide to the energies of $T = 1$, 2^+ states. It is now possible to consider the systematics of $T = 1$ triplets across the fpg shell, considering $A = 4n + 2$ nuclei where n is any integer. $A = 4n + 2$ nuclei corresponds to those where the $T_z = 0$ nucleus is odd-odd. The pattern of excitation energies of such states is remarkably consistent, TED ($TED = Ex_{J,\pi}^{T_z=-1} + Ex_{J,\pi}^{T_z=1} - 2Ex_{J,\pi}^{T_z=0}$, which is discussed in full in Chapter 2) from across the fpg shell are shown in panel (B) of Figure 7.6. For comparison they have been divided by the average energy of the three $T = 1$, 2^+ in each triplet. This normalisation has been performed as the TED is generally proportional to the average energy of the states that comprise it. Taking advantage of this relationship to explore the TED while normalising out effects such as proximity to shell closures which have a significant effect on the energies of states.

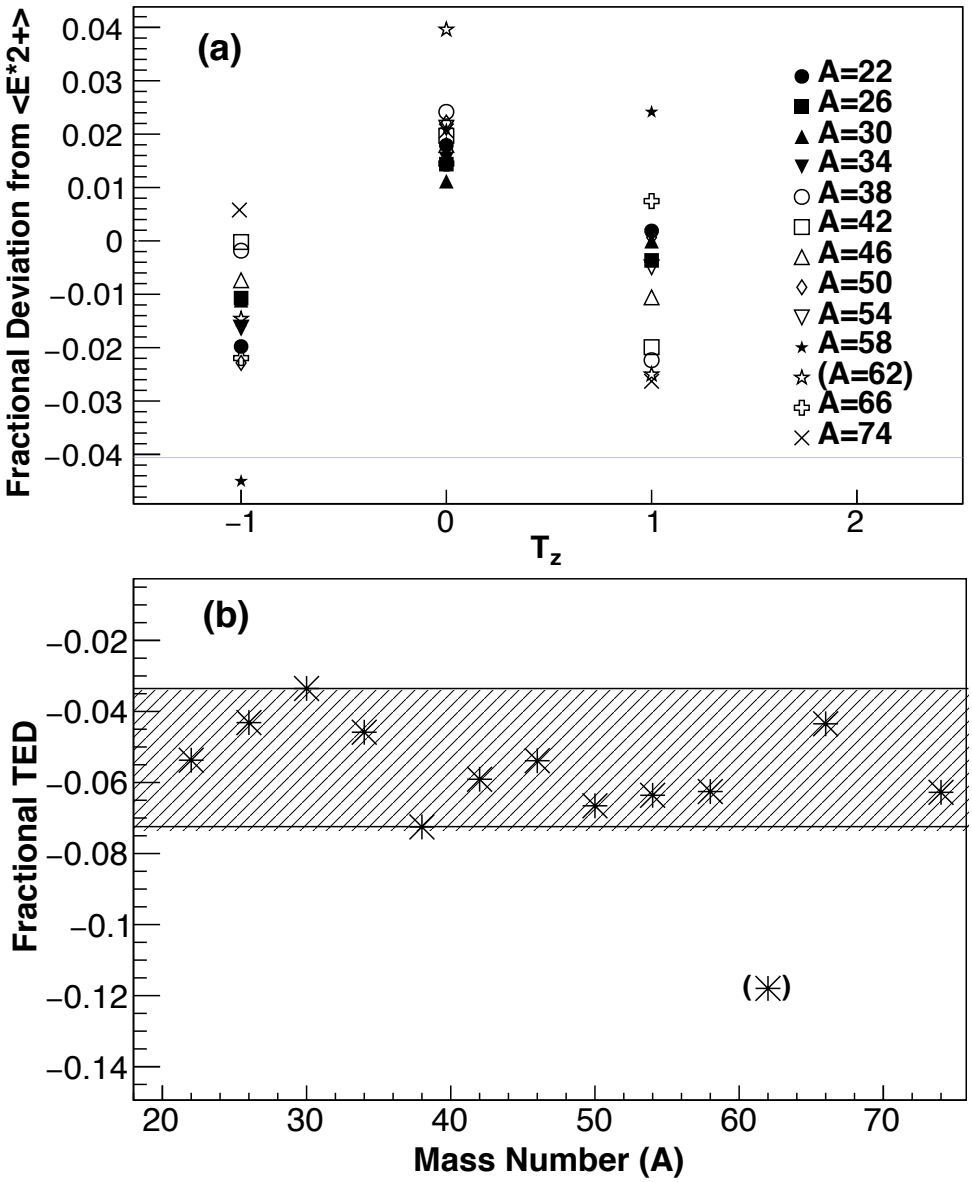

Figure 7.6: Panel (a) depicts energies of $T = 1$, 2^+ states for $A = 4n + 2$ systems (Where the $N = Z$ nucleus is odd-odd). The Fractional deviation is how the energy of each 2^+ state deviates from the average energy of the 2^+ states in that triplet (denoted by $< E * 2+ >$ in the Figure) for each triplet up to $A = 62$. Panel (b) shows the fractional TED, defined as the TED for the $T = 1$, 2^+ states divided by $< E^*_{2^+} >$ for that triplet. The shaded region covers the entire range of the data not including $A = 62$ and is used later in the analysis. The currently assigned datum for the $A = 62$ triplet is bracketed. The data for the *fpg* shell, which are generally the most recent, can be found in the following references: $A = 42$ [77],$A = 46$ [78, 79], $A = 50$ [70, 80], $A = 54$ [20], $A = 58$ [81, 82], $A = 62$ [61, 83] , $A = 66$ [84, 85], $A = 74$ [86, 87].

The trend clearly shows that the TED as a fraction of the average energy of the component IAS are within a narrow range with a clear outlier, the $A = 62$ data point. The $A = 62$ TED is calculated from the tentatively assigned $T = 1$, 2^+ states in ^{62}Ge and ^{62}Ga, at 964 keV and 1017 keV respectively [61, 88]. A further consideration is that the TED is twice as sensitive to

the energy of $T = 1$ state in the $N = Z$ nucleus compared to the energy of the $T = 1$ state in $N = Z+1$ nucleus. For the anomalous TED to be caused by incorrect assignment of the $T = 1$, 2^+ state in ^{62}Ge the actual state must have an energy of around 1026 keV. This energy would result in the MED for that state being on the order of 72.3 keV. As the ^{62}Ge data point being incorrect would cause a very large MED and as there are no further data for ^{62}Ge, it is assumed that the ^{62}Ga assignment is incorrect. A region has been shaded that encompasses all the data except the $A = 62$ data points, the boundaries of which will be used to guide the search for potential gamma ray transitions corresponding to the $T = 1$, 2^+ state in Figure 7.7.

7.2.3 Predicted population

In two-neutron knockout it is possible to use reaction models to predict what states will be populated. The calculations produce cross sections to individual states based on the wavefunction overlap between initial and final states. Here the relative cross sections are used to try and understand the spectrum of states observed. The methodology is discussed further in Chapter 2.

7.2.3.1 Reaction Model

Calculations are provided along the lines of those described in Chapter 2. The Eikonal reaction theory is used alongside spectroscopic factors from shell model calculations in order to predict the population of states in ^{62}Ga in two-neutron knockout from ^{64}Ga. The calculations were performed by E. C. Simpson [89]. The spectroscopic factors, or in the case of a two-neutron knockout reaction, two-nucleon amplitudes were calculated using the GXPF1a interaction in NUSHELLX using the fp valence space. The calculations allow three proton and three neutron excitations out of the (full) $f_{\frac{7}{2}}$ shell, while the three protons and three neutrons that fill the $p_{\frac{3}{2}}$ shell have no restrictions on which shells they can occupy (other than the $f_{\frac{7}{2}}$). The calculations are shown in Table 7.4 for knockout from both the 0^+ ground state and 2^+ isomer in ^{64}Ga, which has already been established as a significant proportion of the beam; further discussion on the isomer ratio is presented in Section 7.4.1. It is noteworthy that NUSHELLX does not label states by isospin. The isospin of states was identified by performing a calculation for the same nucleus, with the same truncation, and the same interaction in ANTOINE (which cannot produce two-nucleon amplitudes). ANTOINE does label the isospin of states. Once the comparable calculation was performed [57] energies and wavefunctions were compared to those from the NUSHELLX calculation in order to ascertain the isospin of states.

The cross sections shown are dependent on the wavefunctions of the states, thus it is of paramount importance to in some way assess the calculations. The low lying level scheme of ^{62}Ga is not accurately reproduced by the calculations, for example: the first excited 1^+ state is experimentally known to be at 571 keV, however the calculation predicts 283 keV. Using that as an indication and considering that the truncation used will affect the wavefunctions, a detailed numeric analysis of the calculations is not appropriate and the calculations are treated as a guide. The calculations suggest that the $T = 1$, 2^+ state in ^{62}Ga will be populated via knockout from both the ground state and 2^+ isomer in ^{64}Ga. From the ground state approximately 12% of the total cross section goes to the $T = 1$, 2^+ state in ^{62}Ga, with all other strongly populated states ($> 5\%$) having even J. From the isomeric state the population of the $T = 1$, 2^+ state in ^{62}Ga is

Table 7.4: Calculated relative cross sections for states in ^{62}Ga. Calculations are presented for knockout from both the ground state, $\sigma_{g.s.}$, and the isomer, σ_{iso}. The cross sections presented are relative cross sections in units of percentage of the total strength in the relevant channel. The $T = 1$ states are highlighted in yellow. See text for detail on the calculations.

Energy (keV)	J	π	$\sigma^{rel}_{g.s.}$	σ^{rel}_{iso}
0	0	+	3.6	3.4
0.283	1	+	1.9	3.1
0.428	3	+	1.3	7.6
0.572	1	+	4.7	6.2
0.626	3	+	2.8	10.0
0.683	2	+	27.2	5.7
0.794	5	+	0.0	4.5
0.924	1	+	0.6	3.0
1.017	2	+	11.7	16.7
1.068	2	+	8.3	8.0
1.245	3	+	3.1	4.0
1.303	4	+	8.6	1.2
1.411	4	+	1.0	4.8
1.973	4	+	2.1	9.6
2.038	6	+	0.1	2.3
2.093	0	+	20.7	0.3
2.183	5	+	0.2	1.2
2.21	0	+	0.3	0.8
2.219	5	+	0.8	4.0
2.301	7	+	0.0	0.3
2.483	6	+	0.2	0.9
3.217	6	+	0.8	0.3
3.244	7	+	0.0	0.6
3.42	7	+	0.0	0.5
3.552	8	+	0.0	0.2
4.276	8	+	0.0	0.1
4.628	8	+	0.0	0.6

larger, with approximately 17% of the total cross section. Knockout from the isomer also predicts strong population of odd-J states.

7.2.4 Experimentally observed states

Gamma ray spectra from ^{62}Ga were shown in Chapter 6. These were created in two-neutron knockout and one proton, two-neutron removal reactions. They are reproduced here in Figure 7.7 and further annotated as a guide. By re-arranging Equation 2.7 and using the relationship and limits depicted in Figure 7.6 it is possible to put limits on the expected energy of a $T = 1$, 2^+ state. This assumes the current tentative assignment in the literature is not correct. Regions are indicated in panels (a) and (b) of Figure 7.7: the lower energy region corresponds to the expected energy of a decay from the $T = 1$, 2^+ state to the $T = 0$, 1^+ state at 571 keV; the high energy region corresponds to the expected energy for the $E2$ decay of the $T = 1$, 2^+ state to the ground state assuming the $T = 1$, 2^+ state lies in the shaded area of Figure 7.6.

There are no peaks within the lower-energy region that is highlighted in panels (a) and (b) of Figure 7.7. There is one peak with an energy of 977(2) keV in the higher energy highlighted region, which has the right energy to correspond to the decay of the $T = 1$, 2^+ state to the ground state. If the 977 keV state is being directly populated and decaying to the ground state one would expect that no other peaks to be in coincidence with it. A coincidence analysis (see Chapter 6 for details) is shown in Figure 7.7, Panel (c) shows gamma gamma coincidence with the 784 keV peak which is much lower in intensity than the 977 keV peak. The coincidence spectrum gated on the 977 keV peak is shown in Figure 7.7, Panel (d), with no apparent coincidence peaks. As coincidence is seen when gating on the much smaller 784 keV peak, it is expected that it would be seen when gating on the much more intense 977 keV peak, if there is any significant coincidence. That there is no coincidence observed when gating on the 977 keV lends credence to the idea of the 977 keV state as the $T = 1$, 2^+ state, decaying to the ground state.

7.2.5 Predicted decay path of the $T = 1$,$J^\pi = 2^+$ state

Shell model calculations were performed by S. M. Lenzi *et al.* [34] to both compare to the energies of excited states in ^{62}Ga and also to compare with the decay path of the $T = 1$, 2^+ state. The calculations were performed using ANTOINE with the LNPS interaction [33]. The results of the calculations are shown in Figure 7.8. The calculations are in agreement with the experimentally observed states, though not all of the predicted states have been observed. These calculations are performed allowing for 5 excitations from the $f_{\frac{7}{2}}$ shell into other orbits, compared to the 6 (a maximum of three protons and three neutrons) that were allowed for the NUSHELLX calculations previously presented. It was not possible to either use the LNPS interaction with the NUSHELLX code, or extract two-nucleon amplitudes from ANTOINE. Consequently, the knockout calculations had to be performed using a different calculation.

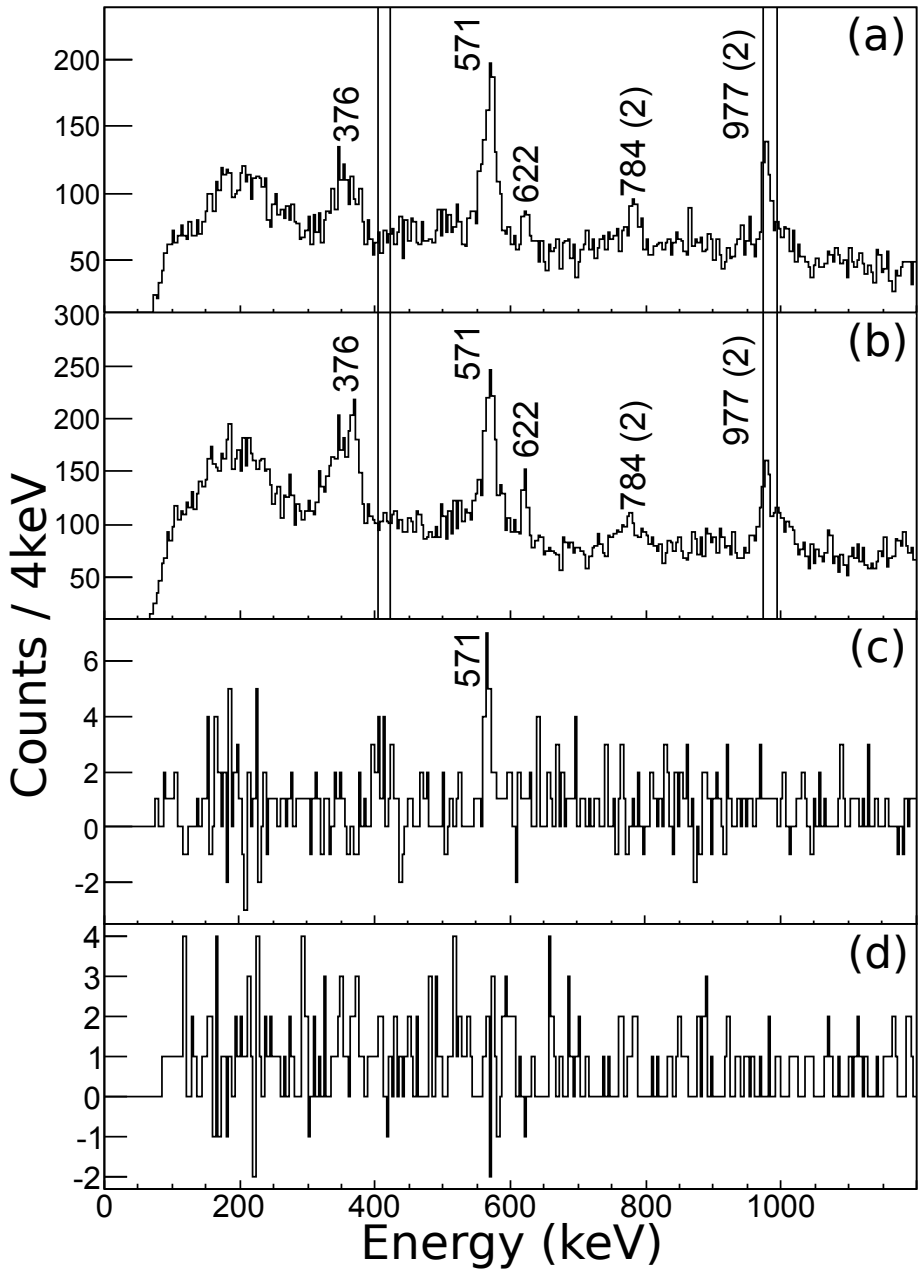

Figure 7.7: Panel (a) shows a Doppler-corrected gamma ray spectrum in coincidence with ^{62}Ga recoils populated by direct two-neutron knockout from ^{64}Ga. The vertical lines show the expected positions of the E2 and M1 decays from the $T = 1$, 2^+ state based on the systematics - see text for details. Panel (b) shows a gamma ray spectrum of ^{62}Ga created by 1p2n removal from ^{65}Ge. Panels (c) and (d) are from gamma gamma coincidence analysis in the 1p2n channel: panel (c) shows a (local-background-subtracted) spectrum of gamma rays in coincidence with the 784 keV peak, Panel (d) shows a (local-background-subtracted) spectrum of gamma rays in coincidence with the 977 keV peak. These spectra were created by gating on ^{65}Ge or ^{64}Ga data from the A1900 and ^{62}Ga data from the S800. Time cuts have been applied such as that in Figure 4 and a FoM cuts of 0.8 have been applied.

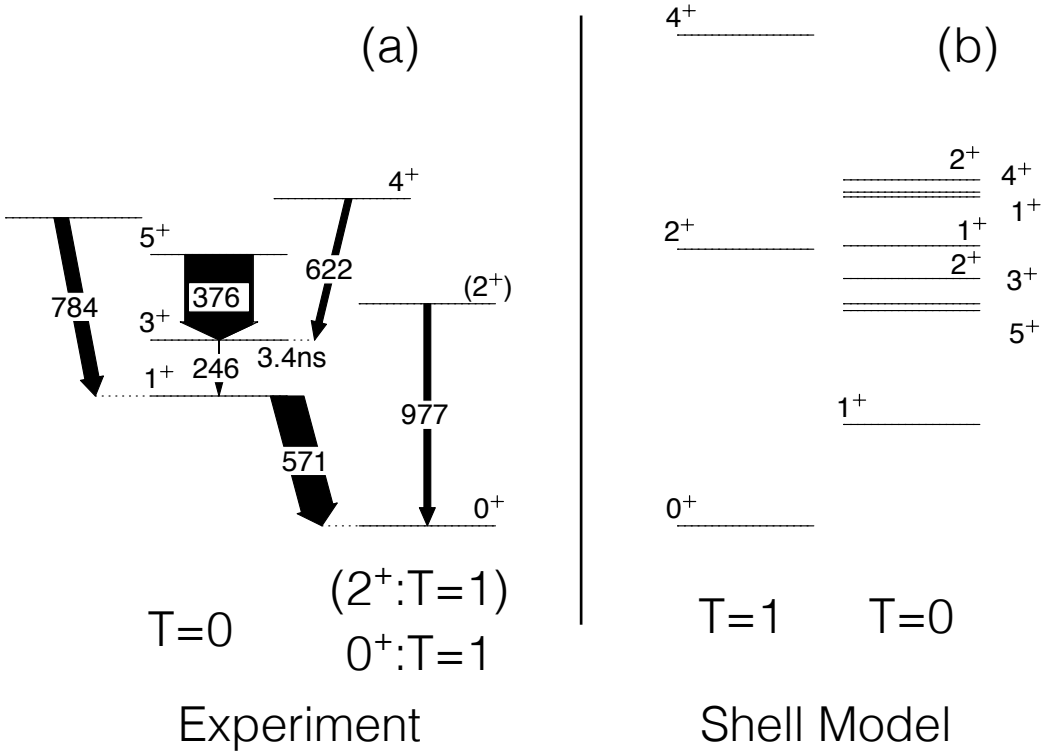

Figure 7.8: Panel (a), shows an energy level scheme depicting the gamma ray transitions observed in two-neutron knockout from ^{64}Ga to ^{62}Ga, using untracked efficiency see text for details. Panel (b) shows the predicted level scheme from shell model calculations, see text for details. The width of transitions is proportional to the efficiency corrected intensity of the state, which is given in table 6.1.

The presented LNPS shell model calculations have been used to calculate the B(M1) and B(E2) for the two possible decays of the 977 keV state (to the ground state and 571 keV state) under the assumption that this is the $T = 1,2^+$ state. The calculations predict that the decay from the $T = 1,2^+$ state will be around 7 times stronger to the ground state than to the $T = 0$, 1^+ state. This calculation is consistent with that of Rudolph *et al.* in suggesting that the dominant decay of the $T = 1$, 2^+ state is expected to be to the ground state and not to the $T = 0$, 1^+ state. This decay pattern is different from that found in odd-odd $N = Z$ nuclei in the $f_{\frac{7}{2}}$ shell, where strong M1 transitions have been observed to compete with the E2. This has been interpreted in a quasi-deuteron picture involving orbitals with $j = l + \frac{1}{2}$ [49, 50]. In the $f_{\frac{7}{2}}$ shell wavefunctions are dominated by this single $j = l + \frac{1}{2}$ orbital. Hence strong isovector M1 transitions are observed. However, all the calculations presented suggest that this simple picture does not apply in the mixed valence space around ^{62}Ga. In addition, Srivastava et al. [62] recently published shell model calculations in the full $f_{\frac{5}{2}}pg_{\frac{9}{2}}$ model space for ^{62}Ga and deformed shell-model calculations based on Hartree-Fock intrinsic states in the same model space. The spherical shell-model calculations show that the $T = 1$, 2^+ state E2 decay to the ground state is about a factor of four stronger than the M1 to the $T = 0$, 1^+ state, when calculated using experimental energies. The deformed

Table 7.5: Decay paths from the $T = 1$, 2^+ state in ^{62}Ga from literature.

Author	**B(E2)** e^2fm^4	**B(M1)** μ_N^2	**Branching Ratio of** $T_{\frac{1}{2}}$ **E2/M1**
Lenzi [74]	0.039	226	5.3
Srivastava [62]	0.005	51.6	4
Rudolph [61]	0.038		4.26

calculations show that the E2 decay completely dominates. The relevant B(E2) and B(M1) values are presented in Table 7.5.

7.2.6 Postulation on the $T = 1$, 2^+ state in ^{62}Ga

In the discussion presented in this section there is no firm conclusion on either the nature of the states observed in the presented data, or on the nature of the $T = 1$, 2^+ state. However, with the circumstantial evidence presented so far it is possible to define all the possible situations that would describe what has so far been experimentally observed, both in the literature and in data presented in this thesis. The evidence being used upon is summarised in the next few bullet points:

1. The systematic energies of all known $T = 1$, 2^+ states, which show an anomalous energy for ^{62}Ga, ^{62}Ge, or ^{62}Zn. As the states in ^{62}Ga and ^{62}Ge have only been tentatively identified this is taken as an argument that one has been misaligned. The argument that the ^{62}Ge $T = 1$, 2^+ state has been misaligned nullifies our argument, however as reasoned in Section 7.2.2 it is more likely that the state has been misaligned in ^{62}Ga.

2. Every presented shell model calculation (performed with a variety of valence spaces and interactions) predicts that the $T = 1$, 2^+ state in ^{62}Ga will decay more strongly via an E2 transition to the ground state, rather than an M1 transition to a 1^+ state as has been previously assigned.

3. Knockout cross section calculations clearly predict strong population of the $T = 1$, 2^+ state in ^{62}Ga in the reactions presented. Though it is not possible to fully assess the accuracy of such arguments the measured relative populations do match the predictions. This reaction mechanism is the most likely of those used to populate the $T = 1$, 2^+ state so it must be taken in to consideration.

4. In the presented data a state is observed at an energy consistent with the TED systematics for a $T = 1$, 2^+ state decaying to the ground state.

5. In the literature there are now both 1^+ and 2^+ states that have been observed with an energy of 1017 keV, and 1^+ states with energies of 979 keV and 978 keV.

The possible conclusions are as follows:
A) Despite the systematics from item 1 the $T = 1$, 2^+ state is at the energy previously identified (1017 keV). This implies that the 977 keV state populated in this study was a $T = 0$, 1^+ state, and that the cross section calculations from item 3 are incorrect, which is plausible due to their truncation. This conclusion would leave a question as to the deviation in the systematics.
B) The states previously observed at around 977 keV were the $T = 1$, 2^+ state, in which case the

data presented in this thesis is in agreement with the literature. However, this means the tentative assignment from Grodner *et al.* is incorrect. The work of David *et al.* suggests this is plausible due to the large error bar on the presented assignment.
C) There are degenerate $T = 1$ 2^+, and $T = 0$ 1^+ states at around 977 keV. This assumes that the previous assignment of the $T = 1$, 2^+ state is incorrect. This conclusion fits all the available data the best, but seems unlikely as despite the relatively large experimental error of the energy for the state (2 keV) this is not in keeping with the level density.

It is not possible to speculate more than the presented conclusions. The work and discussion in this thesis lends weight to conclusions B and C, and in the opinion of the Author option B is the most likely. Regardless of speculation, the possible deviation from the systematics does demonstrate a case for further experimental investigation of the low level structure of ^{62}Ga.

7.3 ^{65}As

The ground state of the $T_z = -\frac{1}{2}$ nucleus ^{65}As has a proton separation energy of $S_p = -90(80)\ keV$. As such, all excited states are expected to be proton unbound. One might expect deviation from the isospin symmetry as discussed in Section 7.1. The only published excited state in ^{65}As is a tentative $\frac{5}{2}^-$ state, proposed by Obertelli et al. [65].

The reactions used to populate ^{65}As and ^{65}Ge were one-neutron and one-proton knockout from the ^{66}As beam. In principle, mirrored knockout reactions should populate identical states in the mirrored reaction products. In Chapter 2 it was discussed that the relative cross section in knockout reactions is dominated by the spectroscopic factor between the initial state (in this case a state in ^{66}As) and the final populated state. From the principles of isospin symmetry it is expected that the wavefunctions of states in ^{66}As reveal identical behaviour for protons and neutrons (assuming any non isoscalar forces are small enough to be considered as perturbations, as has been the convention thus far). As previously stated, it is expected that a mirrored reaction to mirror nuclei will populate a very similar selection of states with similar strength, assuming the populated states in ^{65}As and ^{65}Ge are good IAS.

From conservation of angular momenta one can predict the states that could be populated in ^{65}Ge/^{65}As by knocking out $f_{\frac{7}{2}}$, $p_{\frac{3}{2}}$, $f_{\frac{5}{2}}$, $p_{\frac{1}{2}}$, or $g_{\frac{9}{2}}$ nucleons. In knockout from the ground state of ^{66}As it is possible to populate states with spins of $\frac{3}{2}^-$, $\frac{5}{2}^-$, $\frac{7}{2}^-$, and $\frac{9}{2}^+$; in knockout from the 5^+ isomer in ^{66}As (discussed further below in Section 7.3.1) it is possible to populate states of up to $\frac{15}{2}^-$ with negative parity and $\frac{19}{2}^+$ with positive parity; and from the 9^+ isomer (also discussed below in Section 7.3.1) it is possible to populate positive parity states up to $\frac{27}{2}^+$, and negative parity states up to $\frac{25}{2}^-$

In Chapter 6 Figures 6.15a and 6.15b show the Doppler corrected gamma ray spectra for ^{65}As and ^{65}Ge from the one-neutron and one-proton knockout reactions. The observed transitions in ^{65}Ge have been previously identified as the $\frac{5}{2}^-$, $\frac{7}{2}^-$, $\frac{11}{2}^+$, $\frac{13}{2}^+$, $\frac{15}{2}^+$, $\frac{17}{2}^+$, and $\frac{19}{2}^-$ states. The positive-parity states populated all decay through a $\frac{9}{2}^+$ state which has a 7 ns half life; as such the decay from this state is not observed in the Doppler corrected spectra. The observed gamma rays are shown in Figure 7.9

The populated states in ^{65}Ge bear little resemblance to those populated in ^{65}As. In the ^{65}As spectrum the previously observed $\frac{5}{2}^-$ state is very strongly populated, and then no other state

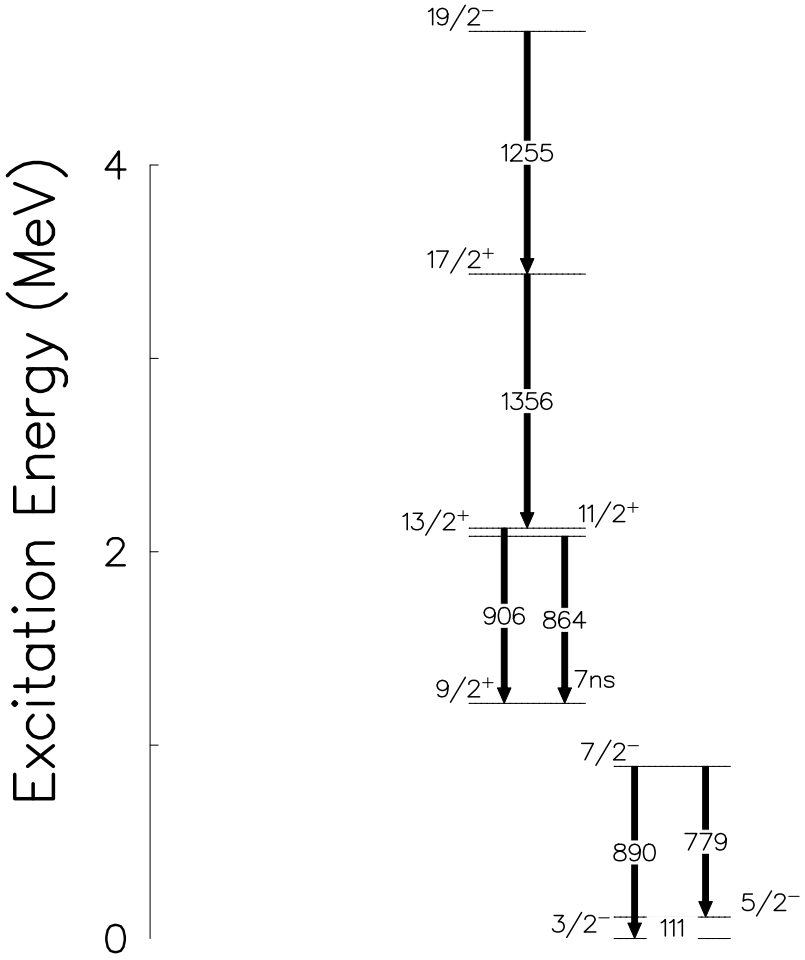

Figure 7.9: Energy Level scheme showing the gamma rays observed in one-proton knockout from ^{66}As to ^{65}Ge.

with an obvious mirror partner is observed. The $\frac{5}{2}^-$ state in the ^{65}As spectrum is the strongest feature. That no obvious analogues for the positive parity states in ^{65}Ge are observed is a significant deviation from the expected symmetry.

As there are no similar features in the ^{65}As and ^{65}Ge spectra, discussion in Sections 7.3.1 and 7.3.2 below detail the structure of relevant states in ^{65}Ge and ^{66}As to explain the observed disparity. Section 7.3.3 then considers which states are expected to be populated, and what the structure of those states means for observed strength.

7.3.1 Structure of initial states in ^{66}As

In one-neutron knockout from the 0^+ ground state of ^{66}As it would be possible to populate up to spins of $\frac{9}{2}^+$ in ^{65}Ge. As spins much higher than this are observed it is reasoned that the ^{66}As beam is in an isomeric state. There are two known isomers in ^{66}As [90], a 5^+ state with a half life of 1.1 μs, and a 9^+ state with a half life of 8.2 μs. Both of these half lifes are long enough that the ^{66}As beam could be in an isomeric state at the target position. Grzywacz *et al.* have described the structure of the 5^+ isomer as $\pi\nu f^2_{\frac{5}{2}}$, and the 9^+ isomer as $\pi\nu g^2_{\frac{9}{2}}$. Predominantly positive-parity

states are populated in ^{65}Ge, so knockout from the 9^+ isomer is considered. This isomer must have a strong $g_{\frac{9}{2}}$ component and to populate positive-parity states an even l nucleon must be knocked out.

One can additionally look at the structure of states that would be populated in this one-proton knockout reaction. If a $g_{\frac{9}{2}}$ proton is knocked out, then the populated state will likely have a large component with a $\nu g_{\frac{9}{2}}$ structure. With no other excitation expected and assuming that the ground states in ^{66}As and ^{64}Ge bear similarity one could expect the structure of the populated state to be $^{64}\mathrm{Ge}_{gs} \otimes \nu g_{\frac{9}{2}}$.

7.3.2 Structure of final states in ^{65}Ge

The structure of the relevant states in ^{65}Ge have been studied and interpreted by Hermkens *et al.* [63]. By comparing energies of states in ^{65}Ge to states in ^{64}Ge they deduce that the $\frac{9}{2}^+$ state and many states that decay to it, are states in ^{64}Ge coupled to a $g_{\frac{9}{2}}$ neutron. In particular the $\frac{9}{2}^+$ state is characterised by $^{64}\mathrm{Ge}_{gs} \otimes \nu g_{\frac{9}{2}}$. Hermkens *et al.* go on to explain that the chain of states observed in this work are the 2^+, 4^+, and 5^- states in ^{64}Ge coupled to $g_{\frac{9}{2}}$ neutrons. In particular the $\frac{19}{2}^-$ must be described by $^{64}\mathrm{Ge}_{5^-} \otimes \pi\nu(g_{\frac{9}{2}})^2$, as this is the only way to create a state of that spin/parity with the available nucleons and orbitals. Additionally the $\frac{5}{2}^-$ state is populated, which is likely described by an $f\frac{5}{2}$ neutron coupled to the ground state of ^{64}Ge.

7.3.3 Explanation for the observed spectroscopic strength

As has been borne out of the previous two sections, the one-proton knockout reaction from the 9^+ isomer in ^{66}As to ^{65}Ge is most likely to populate the states which are best described as single particle $g_{\frac{9}{2}}$ states. An implication of isospin symmetry and the mirrored knockout reaction used is that one can now predict the structure of the populated states in ^{65}As.

The states populated in ^{65}As in one-neutron knockout from the isomeric 9^+ state in ^{66}As are expected to have a structure broadly described by $^{64}\mathrm{Ge}_{gs} \otimes \pi g_{\frac{9}{2}}$. States described by $^{64}\mathrm{Ge}_{gs} \otimes \pi g_{\frac{9}{2}}$ will be populated when $g_{\frac{9}{2}}$ neutrons are removed from the isomer in ^{66}As. However, that may not be the case. If a $f_{\frac{5}{2}}$, $f_{\frac{7}{2}}$, or $p_{\frac{3}{2}}$ neutron is removed then the state populated will be described by $\nu(l)^{-1} \otimes \nu\pi(g_{\frac{9}{2}})^2$ (a neutron hole in ^{64}Ge coupled to an np $g_{\frac{9}{2}}$ pair.) This structure is identical to the described structure of the $\frac{19}{2}^-$ state in ^{65}Ge in the previous Section. Therefore strong population of the $\frac{19}{2}^-$ state is expected. In knockout from the ground state of ^{66}As one expects to see states that have a significant $f_{\frac{5}{2}}$ or $p_{\frac{3}{2}}$ component such as the first excited $\frac{5}{2}^-$ state.

In ^{65}Ge both positive and negative-parity states are observed. However, in ^{65}As only the negative-parity states are observed. Several smaller features are present in the ^{65}As spectrum which have not been identified. However, they are not nearly as strong as the negative parity states. To understand the disparity between the $A = 65$ spectra it may be simpler to consider the relative population of the positive and negative-parity states. While this cannot be calculated due to the low statistics it can be seen that ^{65}As is missing the strength to the positive-parity states. A possible explanation for the missing strength is proton emission from the $\frac{9}{2}^+$ state in ^{65}As. It is worth noting in the comparison between the $\frac{5}{2}^-$ state and positive-parity states in ^{65}Ge that the $\frac{5}{2}^-$ state is on the lowest edge of the spectrum. While a full peak appears to be observed it is not possible to tell if some strength has been cut off by the low energy discriminator.

All of the positive-parity states that are expected to be populated in ^{65}As are described by a single $g_{\frac{9}{2}}$ proton coupled to a state in ^{64}Ge. All of the states are also proton unbound compared to their equivalent state in ^{64}Ge by around 1.3 MeV. However the $\frac{9}{2}^+$ state is expected to gamma decay slowly (from the 7 ns half life of the IAS). It is this longer half life that makes us consider that proton emission now competes with the gamma decay. This situation is shown in Figure 7.10.

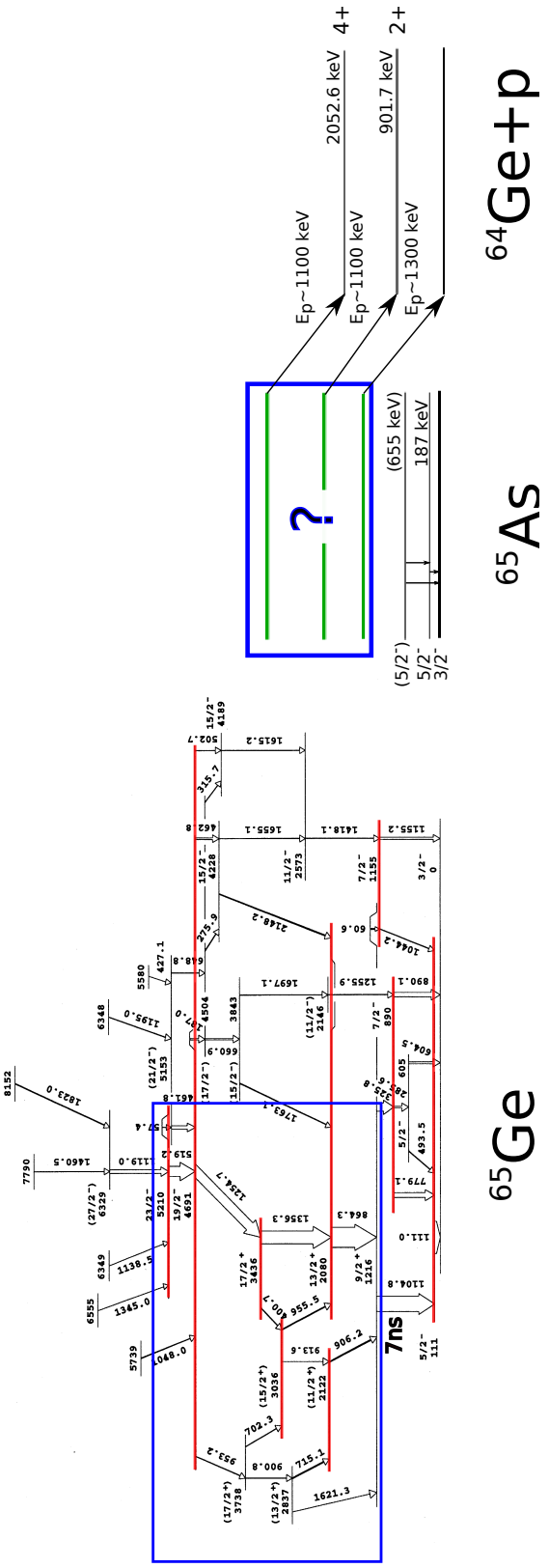

Figure 7.10: Schematic description of the postulated proton emission from states in ^{65}As also depicting the postulated daughter states in ^{64}Ge, these levels have been estimated using mirror symmetry. The ^{65}Ge IAS are also depicted. The states in ^{65}Ge that are expected to undergo proton decay are inside the blue box.

In the case of proton emission, it would likely happen shortly after the target position (to be competitive with gamma decay). The nuclei would decay to ^{64}Ge before arriving at the S800 focal plane, and thus the gamma rays are not observed. There is no trace of the ^{65}As gamma rays in the ^{64}Ge spectrum. This can be explained by the dramatic strength of ^{64}Ge population compared to ^{65}As, as can be seen in the S800 PID plots.

In conclusion, a discrepancy is observed between the ^{65}As and ^{65}Ge spectra in mirrored knockout. While identical spectra are expected instead there is no positive-parity strength in ^{65}As. This has been interpreted as proton emission of a state that all the observed positive-parity states in ^{65}Ge decay to. The state in ^{65}Ge has a 7 ns half life, thus allowing for proton emission to compete. Proton emission from ^{65}As is not an unexpected result. ^{65}As is part of a chain of $T_z = -\frac{1}{2}$ nuclei with unpaired protons where proton emission has been observed or used to describe spectroscopic strength. ^{61}Ga [91] and ^{58}Cu [92] are the first two in the chain, and the speculative result here fits with this trend. It is also possible that due to the comparatively weak binding of ^{65}As the wavefunctions are no longer similar and the mirrored knockout arguments no longer apply. However, there is currently no way to interpret this possibility.

7.4 ^{63}Ge and ^{63}Ga

Despite the measurement of never before observed gamma ray transitions in both ^{63}Ga and ^{63}Ge it has proven impossible to reach substantial conclusions. All of the discussion presented in this section is tentative with no firm conclusion.

The main issue has been a lack of knowledge of ^{63}Ga, which has been populated in the past with fusion-evaporation experiments. However, knockout experiments have never been performed. Thus the selection of states populated in ^{63}Ga had not all been previously observed. In this study it is not possible to draw conclusions on the spins and parities of newly populated states. So while it may be possible to draw comparisons between observed transitions in ^{63}Ge and ^{63}Ga it does not allow for the assignment of spins and parities or the construction of an MED with all of the newly observed states.

7.4.1 ^{63}Ga

The gamma rays observed from ^{63}Ga have a maximum spin of $\frac{13}{2}^+$. The ground state of ^{64}Ga is 0^+. Directly populating such high spins states in ^{63}Ga via knockout from a 0^+ state in ^{64}Ga is impossible as it would violate conservation of angular momentum. ^{64}Ga has a 2^+ isomer at 42.85 keV with a half life of 21.9μs [93]. If this isomer is populated in the primary fragmentation a large fraction of it would remain populated at the secondary target position as the beam velocity is in excess of $100\frac{m}{\mu s}$. This would allow for knockout reactions from the isomer in the beam. A further consequence of this mode of knockout is that to populate states with spins as high as $\frac{13}{2}^+$ a $g_{\frac{9}{2}}$ nucleon must be removed.

A consequence of observing the removal of a $g_{\frac{9}{2}}$ neutron from a 43 keV state is that there must be a significant $g_{\frac{9}{2}}$ component to that state. This $g_{\frac{9}{2}}$ component is an indication that around $A = 63$ the $g_{\frac{9}{2}}$ orbital has mixed with the fp orbitals. Such a result is unexpected as work performed by Nichols *et al.* around $A = 70$ concluded that the $g_{\frac{9}{2}}$ orbitals do not play a significant role at that

mass [94]. Nichols *et al.* used a recoil distance method experiment in inverse kinematics to extract lifetimes of states. The lifetimes were compared to shell model calculations performed with the Jun45 interaction (to include the $g_{\frac{9}{2}}$ orbital but no $f_{\frac{7}{2}}$ orbital), and GXPF1a to include the $f_{\frac{7}{2}}$ orbital and no $g_{\frac{9}{2}}$ orbital.

Many of the observed gamma rays from ^{63}Ga had not been previously observed and additionally some of the states they decay from do not have known spins and parities. As previously stated it is not possible, however, to measure spins and parities in this study. It may be possible to use the shell model to speculate on assignment of the observed states.

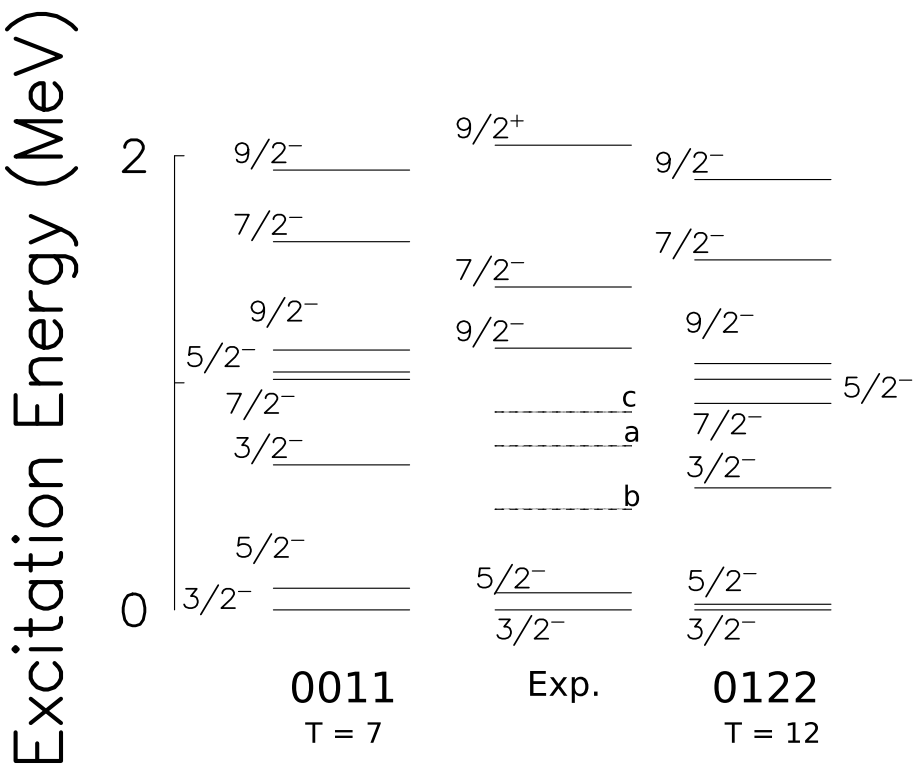

Figure 7.11: Experimental low-lying energy level scheme for ^{63}Ga (middle) alongside shell model predictions (either side). The shell model calculations have been performed in ANTOINE with the GXPF1a interaction but different truncations (See text for details).

To try to understand the spectrum of observed states shell-model calculations were performed using the GXPF1a interaction in the *fp* model space. The calculations are shown in Figure 7.11 alongside the low-lying level scheme from experiment. The calculations are labelled by their truncation, four numbers that represent the relative cost for moving a particle from one shell to another out of a defined limit. There is no limit on moving nucleons in a *0* shell to another *0* shell, or nucleons in a *1* shell to another a *1* shell, but moving nucleons from a *0* shell to a *1* shell has a cost of one and moving nucleons from a *0* shell to a *2* shell has a cost of two. Then a limit is defined with all configurations considered as long as the cost for each configuration is lower than the limit. Two truncations were investigated *0011* and *0122*. These were chosen as they only restrict the movement of nucleons from the filled shells to higher energy ones which should be less energetically favourable. In the case of *0122* there is some further restriction to make it more difficult for $f_{\frac{7}{2}}$ nucleons to be moved to higher shells than $p_{\frac{3}{2}}$ nucleons. The *0011* calculation allows particles to

freely move between the $f_{\frac{7}{2}}$ and $p_{\frac{3}{2}}$ shells, and costing one unit to move from that shell to the $f_{\frac{5}{2}}$ or $p_{\frac{1}{2}}$ shells. In this calculation a total of 7 units are available. For *0122* it is cheaper for $p_{\frac{3}{2}}$ nucleons to move to $f_{\frac{5}{2}}$ or $p_{\frac{1}{2}}$ shells, costing 1 unit, where as it costs $f_{\frac{7}{2}}$ nucleons 2 units, and one to move to the $p_{\frac{3}{2}}$. In the *0122* calculation 12 units are available. A good indication to which truncation provides a more realistic wavefunction is to consider the binding energies. The *0011* calculation has a ground state binding energy of -274.13 MeV, and the *0122* has a slightly lower ground state binding energy of -274.17 MeV. This small (40 keV) difference demonstrates that these calculations are comparable.

The same truncations used for the ^{63}Ga calculation were investigated for ^{63}Ge, a calculation which is in the same space with the same number of nucleons (albeit isospin inverted). The investigation should yield the same result as an investigation into the truncation performed on ^{63}Ga. A series of calculations were performed with both the *0011* and *0122* method gradually increasing the available number of excitations, the calculations predict the energy of the first two $\frac{3}{2}^-$, $\frac{5}{2}^-$, $\frac{7}{2}^-$, and $\frac{9}{2}^-$ states. The expectation is that once the number of excitations has been increased sufficiently high, regardless of the truncation method used, each calculation will show identical results. The identical results represent the best possible calculation with a given interaction in a given valence space. Figures 7.12 and 7.13 show these truncation schemes with the allowed number of excitations denoted by T. The results appear to show that the *0122* calculation is closer to an ideal result with only ≈10 keV difference between the energy of states in the final iterations, were as, for the *0011* calculation the difference is closer to ≈100 keV. The binding energies obey a similar trend. It should be noted that due to the larger number of states calculated it was not practical to calculate ^{63}Ga in the largest truncation presented in this analysis. It was performed with $T = 7$ in the *0011* method and $T = 12$ in the *0122* method. The ^{63}Ga calculations are thus provided with the caveat that the truncation is affecting the excitation energy of states. The energies should not be viewed as accurate to more than ≈100 keV. It should also be noted that the two different truncation methods will likely bias the calculated states however it is not possible to assess to what extent this has affected the calculations.

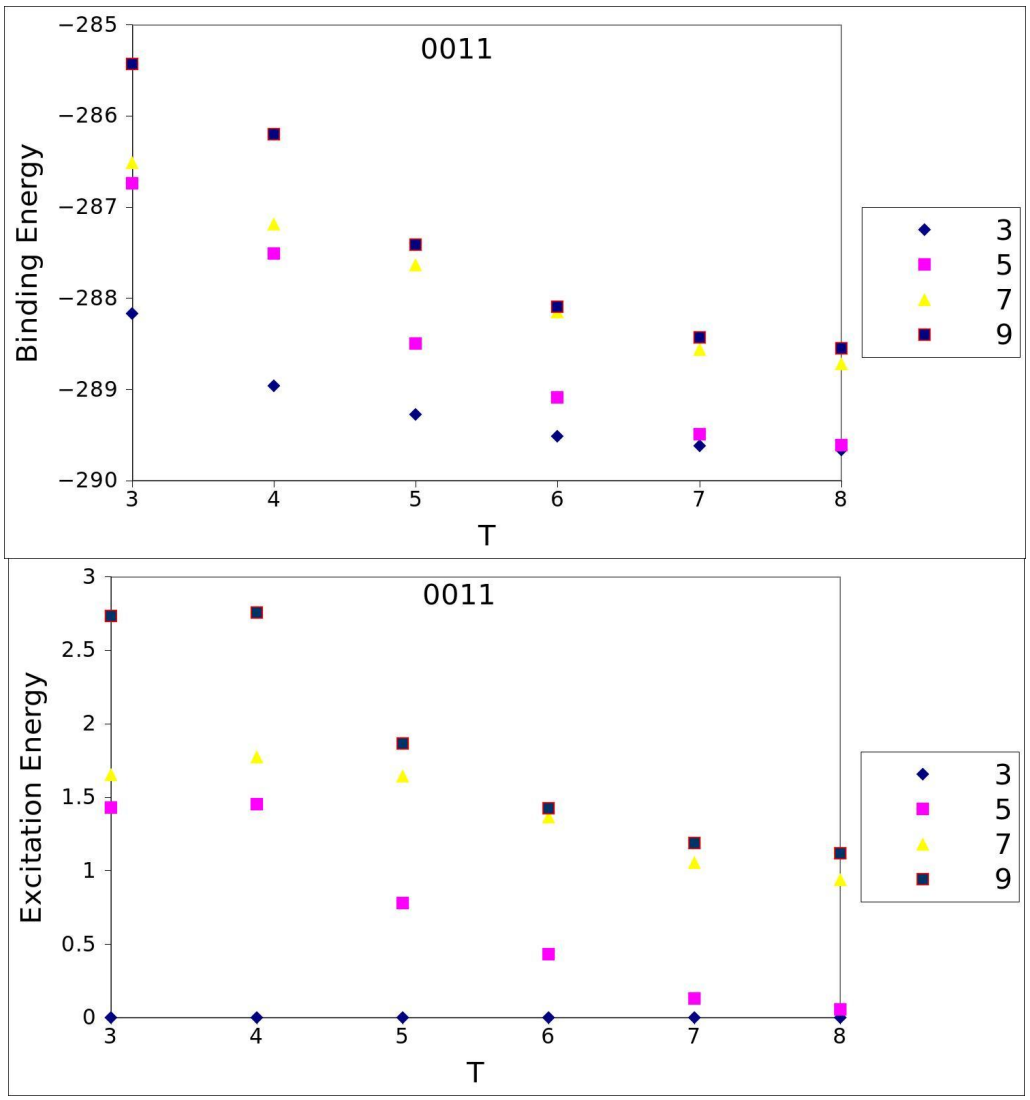

Figure 7.12: Results from shell model calculations performed in ANTOINE with the GXPF1a interaction. Binding energies and excitation energies are shown of the first $\frac{3}{2}^-$, $c = \frac{5}{2}^-$, $a = \frac{7}{2}^-$, and $\frac{9}{2}^-$ state in ^{63}Ge shown against the number of allowed excitations (denoted as T) in a *0011* truncation scheme.

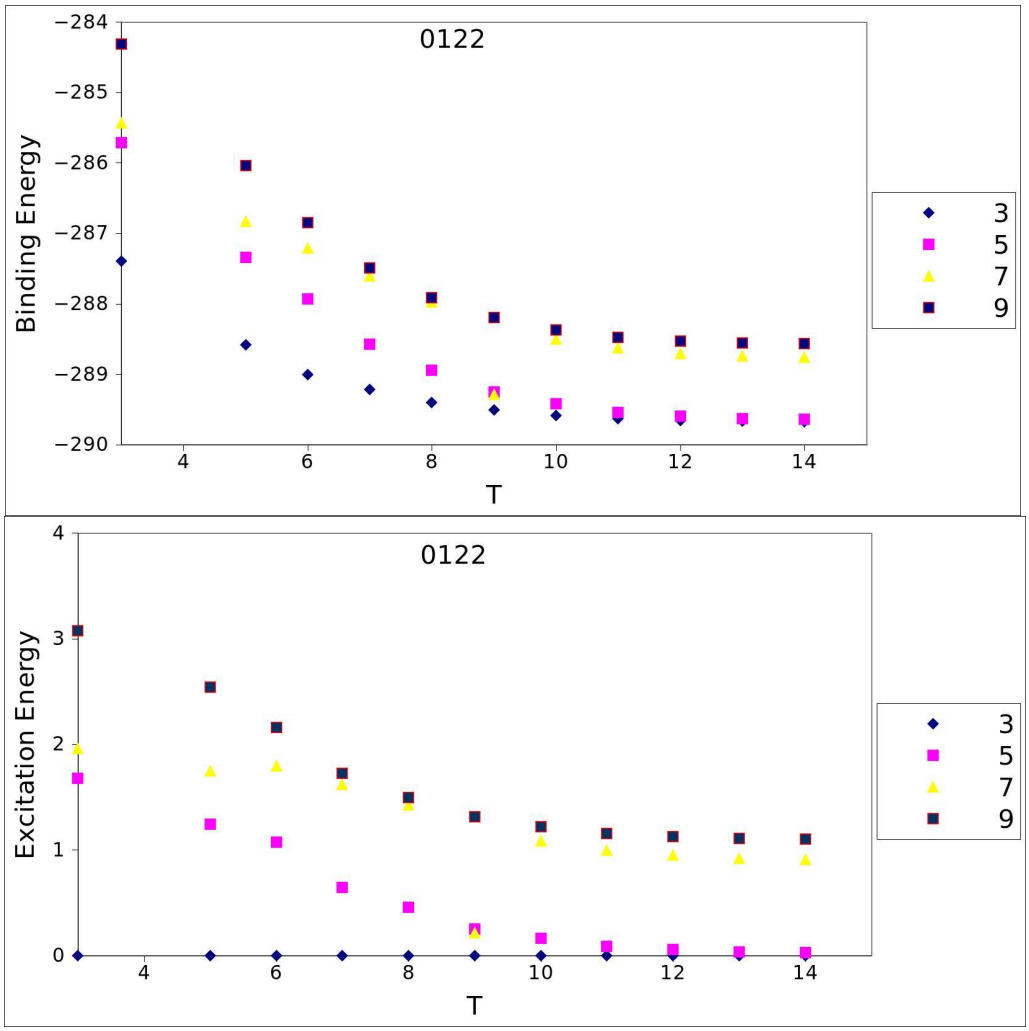

Figure 7.13: Results from shell model calculations performed in ANTOINE with the GXPF1a interaction. Binding energies and excitation energies are shown of the first $\frac{3}{2}^-$, $\frac{5}{2}^-$, $\frac{7}{2}^-$, and $\frac{9}{2}^-$ state in ^{63}Ge shown against the number of allowed excitations (denoted as T) in a *0122* truncation scheme.

The experimental data matches the theoretical ^{63}Ga calculations presented in Figure 7.11 very well. From the states observed via knockout, it has been surmised that there must be $g_{\frac{9}{2}}$ components to the relevant ^{64}Ga wavefunctions. As the ^{63}Ga calculation is performed only in the fp space, it suggests that the $g_{\frac{9}{2}}$ components must not be significant. Because all of the calculated states have roughly the same energy as their experimentally observed counterparts, the calculations can be used to infer spins an parities of unidentified states. Three theoretical states are within the region of three states that have been experimentally observed but do not have spin/parity assignments (a, b, and c). These states are therefore likely to be $b = \frac{3}{2}^-$, $c = \frac{5}{2}^-$, and $a = \frac{7}{2}^-$.

7.4.2 $A = 63$ MED

The $A = 63$ MED was calculated with the method described in Chapter 2. The GXPF1a interaction was used in the fp space with a *0011*, T=7 calculation. The calculations are compared to the data points in Figure 7.14 and a full description of the data used can be found in Chapter 6.

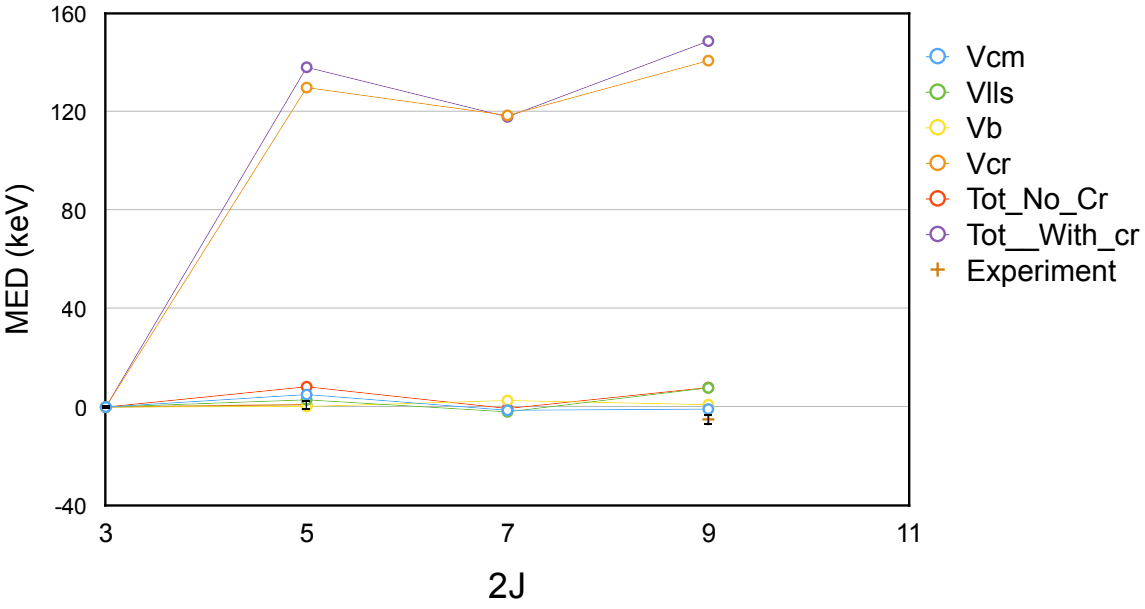

Figure 7.14: Calculated and experimental MED. The components of the calculated MED are shown, as is the sum of them both including and not including the V_{cr} term. The MED has been calculated in ANTOINE using the GXPF1a interaction with a *0011* $T = 7$ truncation, see text for details.

The theoretical MED shown in Figure 7.14 is calculated according to the methodology described in Chapter 2. The full MED, i.e. the sum of the terms, is shown both including and not including the V_{cr} term. The experimental MED data (though only two data points are available at $\frac{5}{2}^-$ and $\frac{9}{2}^-$) are very small, at 1(2) keV and -5(2) keV. It is clear that the V_{cr} term fails, the experimental data and all other theoretical terms have very low values. The V_{cr} term has values of above 100 keV for all of the states calculated; this is explained fully in the following text alongside the other MED terms.

The small MED values for the V_{lls} and V_{cm} terms can possibly be explained by the mixed valence space. The wavefunctions of states in the calculations contain contributions from many

configurations, not generally having one dominant configuration. With significant contributions from many shells and configurations it is not surprising that the terms would average to approximately zero. Since different configurations will have both positive and negative contributions to the MED, the more contributions the more likely they are to cancel out. In the presented calculations it is expected that the $J = 2$ terms have little impact. The V_b term has been applied as it was for work in the $f_{\frac{7}{2}}$ shell, with only $(f_{\frac{7}{2}})^2$, $J = 2$ couplings affected. As the valence nucleons are in the $p\frac{3}{2}$ shell it is expected that the $p_{\frac{3}{2}}$ orbital is where most of the recoupling happens, with minimal change in the $f\frac{7}{2}$ shell. It is not surprising that the $J = 2$ term has little effect.

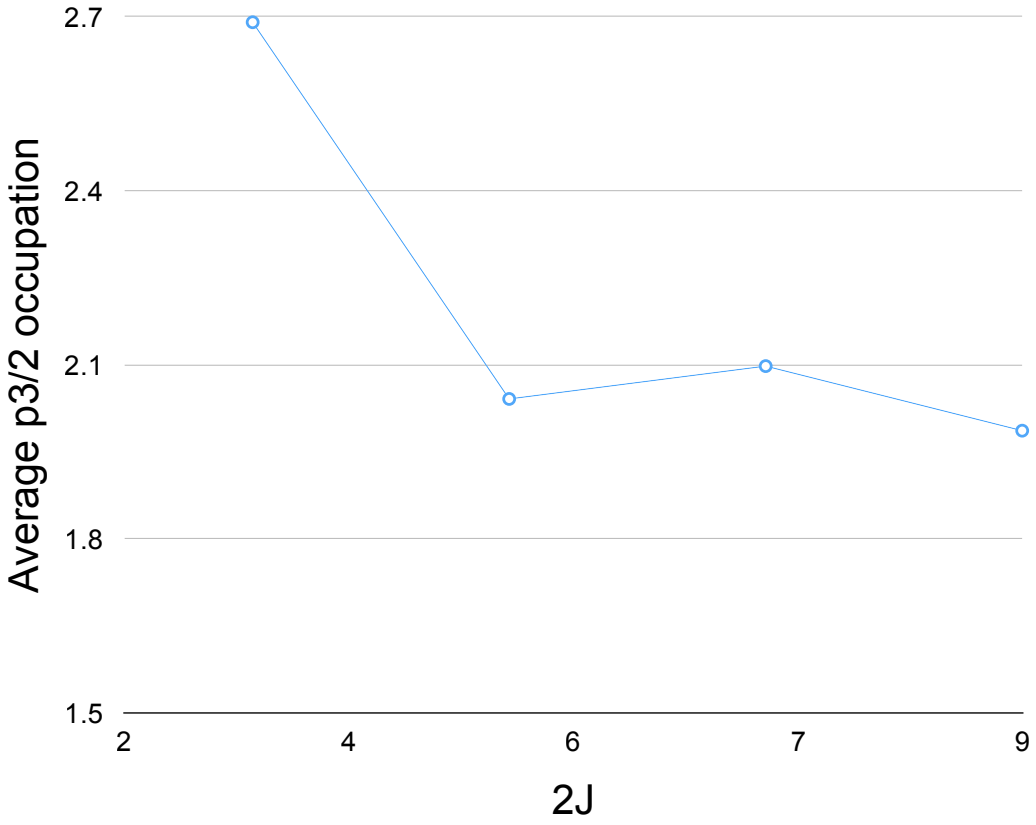

Figure 7.15: Calculated occupancy of the $p_{\frac{3}{2}}$ orbitals reproduced from an isoscalar interaction with the shell model. These occupations are from the calculations presented in Figure 7.14.

The V_{cr} term accounts for changing nuclear radii and deformation effects. This is the effect of bulk radius change of the nucleus. The full calculation for the V_{cr} term is explained in Chapter 2. The V_{cr} term is directly proportional to the $p_{\frac{3}{2}}$ occupancy relative to the ground state. Consequently an explanation for the large V_{cr} term can be found by plotting the average occupation of the $p_{\frac{3}{2}}$ orbital (for protons AND neutrons) in each state. It can be seen in Figure 7.15 that the ground state has a different average $p_{\frac{3}{2}}$ occupation compared to all of the calculated excited states, causing a large V_{cr} term. The V_{cr} term was tuned empirically in the $f_{\frac{7}{2}}$ shell where the average occupation of the $p_{\frac{3}{2}}$ orbital is low. The poor fit of the V_{cr} term to the $A = 63$ MED is a demonstration that this term does not function correctly when there are $p_{\frac{3}{2}}$ valence particles, as any excitation to different orbitals causes an unusually large V_{cr} contribution.

Ignoring the V_{cr} term the corresponding values for the theoretical calculation are very low,

summing to 8.2 keV and -0.6 keV respectively. This recreates both the general trend of the experimental data as well as values to within 10 keV. Despite the low number of data points this leads to one of two conclusions:

- A *0011* style calculation with $T = 7$ is not sufficient to accurately represent how the wavefunctions of low lying states in $A = 63$, $|T_z| = \frac{1}{2}$ nuclei recouple to different angular momenta, or;
- The V_{cr} term cannot be used without modification this close to the $p_{\frac{3}{2}}$ valence space.

Given that the V_{cr} term is fit to $A = 41$ data, and the assessment of the calculations used (presented in Figures 7.12 and 7.13), it seems likely that the truth lies between the two presented possibilities. Without fully trusting the presented calculations it is not possible to make firm conclusions. No evidence so far is seen for the need for a $J = 2$ term to reproduce the low spin $A = 63$ MEDs. It will be impossible to draw further conclusions until more experimental data can be found for the $A = 63$ and surrounding sets of mirror nuclei. In particular, higher spin states in the same band are needed, such that good comparisons can be made between states of similar wavefunctions with recoupled angular momenta.

Chapter 8

Conclusions and Future Work

Data has been presented from two experiments, both of which were performed at the NSCL facility with the A1900+S800 setup. The only significant difference in the equipment used (beyond specific settings) was the HPGe detector array. The first experiment used the SEgmented Germanium Array, SeGA; whereas the second experiment used the Gamma Ray Energy Tracking In-beam Nuclear Array, GRETINA.

The first experiment was performed using beams in the $f_{\frac{7}{2}}$ shell with the gamma ray analysis for ^{51}Co and ^{51}Cr presented in this thesis. The second experiment used beams in the upper-fp shell. The calibration and analysis of the A1900 and S800 data is presented in addition to the gamma ray analysis. The calibration of the A1900 and S800 data involved: the time alignment of signals from scintillation detectors; calibrating the position sensitive CRDCs using runs where masks were inserted in front of them; calibrating ion chamber segments; and optimising calibration coefficients to cleanly identify recoils. Additionally, the gamma ray analysis included an investigation of different coefficients and parameters to the tracking analysis such that ideal gamma ray spectra were produced.

The results from these experiments are presented within the context of four different physical topics:

- $T = 1$, 2^+ state in ^{62}Ga;
- $A = 63$ MED;
- $A = 51$ MED;
- proton emission from $A = 65$.

Despite the strength of the data, many of the results require assumptions about the physics involved in order to be interpreted. The results prove intriguing however, and have already been used to support proposals for further study. This Section will describe the conclusions of the present work and give descriptions of possible future experiments which may achieve quantitative conclusions.

8.1 Proton emission

8.1.1 ^{65}As

Data was presented for mirrored one-nucleon knockout from ^{66}As to ^{65}As and ^{65}Ge. Due to isospin symmetry in such reactions a very similar selection of states is expected to be populated in each of the resultant nuclei. However, the observed gamma ray spectra were notably different in both channels. The gamma rays observed from ^{65}Ge correspond to known transitions from either low lying $\frac{5}{2}^-$ states or states which have been previously described by a $g_{\frac{9}{2}}$ neutron coupled to states in ^{64}Ge [63]. In ^{65}As gamma rays from the previously observed $\frac{5}{2}^-$ state were observed. However, no obvious identification was made for the other (weakly populated) states. The large difference in observed strength can be explained by assuming that states in ^{65}As decay by proton emission, as they would be around 1.3 MeV proton unbound. A pure gamma decay of such states might have half lifes of the order of nano seconds.

8.1.2 Future experiments to identify proton emitting states in neutron deficient nuclei

In light of this work, and similar results from ^{57}Co and ^{61}Ga, a proposal was put forward to use a new setup to study all these nuclei at the Argonne Tandem Linear Accelerator System (ATLAS) facility at the Argonne National Lab. Experiment 1239 proposed by Dirk Rudolf was approved to study ^{57}Co with this method, and a subsequent proposal to study ^{61}Ga and ^{65}As was partially approved. The experimental method uses fusion evaporation to populate proton emitting states in the listed nuclei. A suite of detectors will be used to measure evaporated charged particles, evaporated neutrons, and protons emitted from the states of interest. It will be possible to identify the nucleus produced in the reaction by gating on the measured evaporated particles. Similarly, by producing gamma gamma proton coincidence it will be possible to identify all proton emitting states and place them in a level scheme. Figure 8.1, produced by D. Rudolf *et al.* for proposal 1239, details the new detector setup that will compliment Gammasphere [95], the neutron shell, and the FMA [96].

Thirty Gammasphere detectors in the forward hemisphere will be replaced with neutron detectors, while the Caesium Iodide (CsI) detectors of Microball, in combination with DSSDs will identify charged particles. Emitted protons have distinct energies which should be lower than that of evaporated protons, and thus will be stopped in the DSSDs and will not produce a signal in Microball. Finally, the Fragement Mass Analyser (FMA) will be used to provide an additional mass gate and ensure that clean spectra are obtained.

8.2 Mirror Energy Differences in the $f_{\frac{7}{2}}$ shell

8.2.1 $A = 51$ MED

The mirror nuclei ^{51}Cr and ^{51}Co were populated in fragmentation and knockout reactions in addition to mirrored 1p2n, and 2p1n removal. The states populated in ^{51}Cr are well known, however, none of the states populated in ^{51}Co have been previously observed. Mirror population

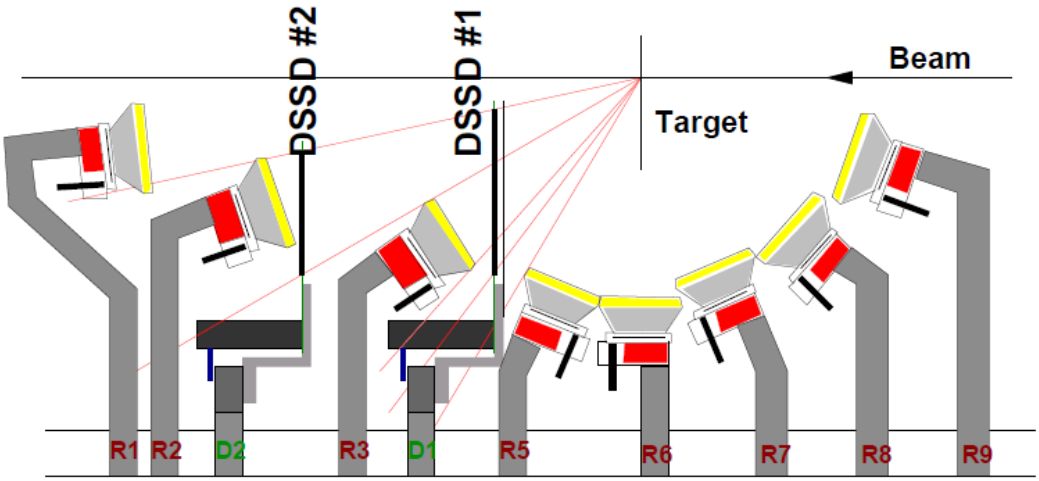

Figure 8.1: Setup proposed for experiment 1239 at the Argonne National Laboratory. The Microball [97] dector array, R1 to R9, will have the R4 ring of detectors removed. Replacing the R4 ring are two DSSDs, D1 and D2.

strengths and cross-section calculations were used to guide an analysis of the intensity of states in ^{51}Co and construct a level scheme.

Based on the scheme an MED was plotted and compared to calculations. The calculated MED did not fit well with the experimental data without an isospin non-conserving component. Both positive isovector $J = 2$ and negative isovector $J = 0$ isospin non-conserving terms were used, which accurately reproduces the data at low spin but deviate slightly at high spin. The latest work on the subject of isospin non-conserving forces was presented which demonstrates that a combination of $J = 0$, $J = 2$, $J = 4$, and $J = 6$ components are required.

8.2.2 Future work to elucidate isospin non-conserving effects

The approach to calculating an MED has been slowly constructed and the effects considered can be divided into monopole and multipole terms. Monopole terms are those that depend only on the number of nucleons occupying a shell, whereas multipole terms are those that depend on how pairs of nuclei couple to different spin. One of the monopole terms, V_{cr}, has been empirically fitted to the occupations of the $p_{\frac{3}{2}}$ orbitals.

With the advent of radioactive beam facilities it is now possible to measure the proton and neutron occupancies for states in ^{41}Ca and ^{41}Sc as required to validate the calculations used to determine the V_{cr} term. This validation would lend significant strength to the case that these isospin non-conserving terms are a real effect rather than a feature of the model.

The V_{cr} term is proportional to both neutron and proton occupancies. A check can be performed by calculating these occupancies for both pairs of a mirror doublet. As such, the four required reactions would be:

- Neutron adding from ^{40}Ca to ^{41}Ca
- Proton adding from ^{40}K to ^{41}Ca

- Proton adding from ^{40}Ca to ^{41}Sc
- Neutron adding from ^{40}Sc to ^{41}Sc

Such reactions could be achieved at the Argonne National Laboratory using Argonne In-flight Radioactive Ion Separator (AIRIS) radioactive beams [98] and the HELical Orbit Spectrometer (HELIOS) [99] spectrometer in a similar set up to reference [100].

8.3 Mirror Energy Differences in the upper-fp shell

8.3.1 $A = 63$ MED

^{63}Ga was populated in one-neutron knockout from ^{64}Ga. From the spins of populated states, using conservation of angular momentum, it was deduced that the beam is at least partially in an isomeric 2^+ state. A new state was observed in ^{63}Ga and a tentative assignment was made by comparing the observed states to shell model calculations performed with the GXPF1a interaction and two different truncations. An additional transition was also tentatively identified between the 443 keV state and the isomeric $\frac{5}{2}^-$ state. This transition is key for identifying states in the mirror nucleus, ^{63}Ge.

States in ^{63}Ge were populated in two-neutron knockout from ^{65}Ge, and in 1p2n removal from ^{66}As. At the time of writing the data gathered represents the only known data on ^{63}Ge. The 1p2n channel was compared to the mirrored channel, 2p1n removal to ^{63}Ga. Some comparisons were made between states in the reaction, enabling some mirrored transitions to be identified. By then examining the two-neutron knockout channel four states were tentatively assigned.

Unfortunately, two of the assigned states have no known spins or parities either in ^{63}Ge or the mirror nucleus ^{63}Ga. In this study it is not possible to measure spins and parities, and there is no option to assign via mirror symmetry. As a result, the MED constructed contained only two states. The MED was calculated using ANTOINE and the GXPF1a interaction, and compared to the experimental data. The comparison clearly shows that all contributions are having a minimal effect, most likely due to the mixed valence space. The exception to this is the V_{cr} term, with calculations showing that in this valence space the term fails significantly. As the ground state has a different average occupancy of the $p_{\frac{3}{2}}$ shell than the excited states (which are mostly based on excitations from the $p_{\frac{3}{2}}$ to the $f_{\frac{5}{2}}$) the magnitude of the term is artificially inflated. This study clearly shows that while the $p_{\frac{3}{2}}$ orbital is a valence orbital the V_{cr} term should not be applied.

As all of the terms calculated in the theoretical MED are very small in magnitude (except the V_{cr}), it is not possible to make a conclusion about the effect of the $J = 2$ anomaly or V_B term, as it is predicted to have a minimal effect in this case.

8.3.2 Further investigation of the ^{63}Ge level scheme

One of the issues identified in the study presented in this thesis is that ^{63}Ge was populated in a different way from all previous experiments that have populated excited states in the mirror nucleus, ^{63}Ga. This raises the issue that knockout has probed different states, making mirror symmetry assignments difficult.

A proposed experiment [34] at Grand Accélérateur National d'Ions Lourds (GANIL) would populate ^{63}Ge using the fusion evaporation reactions: ^{40}Ca(^{28}Si,αn) and ^{40}Ca(^{28}Si,αp) reactions at a bombarding energy of 120 MeV. The proposed detection method is to use the Advanced GAmma Tracking Array (AGATA) [101] to detect gamma rays, the Neutron Wall [102] to detect neutrons, and DIAMANT [103] to detect charged particles. DIAMANT and the N-Wall will be used to identify ^{63}Ge recoils, allowing for a clean gate on gamma rays from ^{63}Ge. It is proposed that 7 days of beam time with a 5 pnA beam will produce enough data to allow for construction of gamma gamma matrices and a coincidence analysis with high enough statistics to identify states.

8.4 The $T = 1$, 2^+ state in ^{62}Ga

The systematics of TED for the known $T = 1$, 2^+ states were presented. The systematics highlight the anomalous behaviour of the TED for the $A = 62$ triplet. Data was presented for ^{62}Ga from two-neutron knockout from a ^{64}Ga beam which was shown to be at least partially in an isomeric state. Reaction cross-section calculations using two-nucleon amplitudes indicate that this reaction should directly populate the $T = 1$, 2^+ state. Calculations also indicate population of other low-lying yrast states, from both the ground state and isomeric state in the beam. Gamma ray data from ^{62}Ga was also presented from an indirect 1p2n removal reaction from ^{65}Ge. The ^{65}Ge reaction channel contained the same peaks as the two-neutron knockout channel, but presented enough data that a coincidence analysis could be performed. Using the TED systematics as a guide a state has been identified as a candidate for the $T = 1$, 2^+ state. Furthermore, coincidence analysis shows it likely decays directly to the ground state, in line with all published calculations. However, an angular momentum/parity assignment could not be made for the state observed, and previous work has already identified a state at a very similar excitation energy as a $T = 0$, 1^+ state. It is possible there is doublet of transitions that cannot be experimentally resolved in this study. The question of the $A = 62$ TED then remains open until a definitive identification can be made for the $T = 1$, 2^+ states in ^{62}Ga.

8.4.1 Possible future experiments

Experiments have now been performed to populate states in ^{62}Ga using knockout, β decay, and fusion evaporation; none of these experiments was able to firmly identify the $T = 1$, 2^+ state. It is suggested that Coulomb excitation could be used to perform such an experiment. The primary obstacle to such an experiment being the ability to produce a ^{62}Ga beam with sufficient intensity.

8.5 Final Thoughts

Various nuclei have been studied in the fp shell through a combination of knockout and nucleon removal reactions. The main conclusions are that:

- Isospin symmetry appears to hold even when states in one nucleus are as much as 1.5 MeV unbound to proton emission, excepting the $J = 2$ anomaly.

- The $J = 2$ anomaly is a needed effect in the $f_{\frac{7}{2}}$ shell in order to reproduce data. However, recent in depth studies show that while the most significant required term is between the $J = 0$ and $J = 2$ couplings, in fact terms are required at $J = 0$, $J = 2$, $J = 4$, and $J = 6$.
- The implication from the presented data that states in ^{65}As undergo proton emission.
- A study of TED systematics is presented along side data from ^{62}Ga, to tentatively produce a new candidate for the anomalous $T = 1$, 2^+ state in ^{62}Ga.

Appendix A

Particle Identification plots from experiment 1

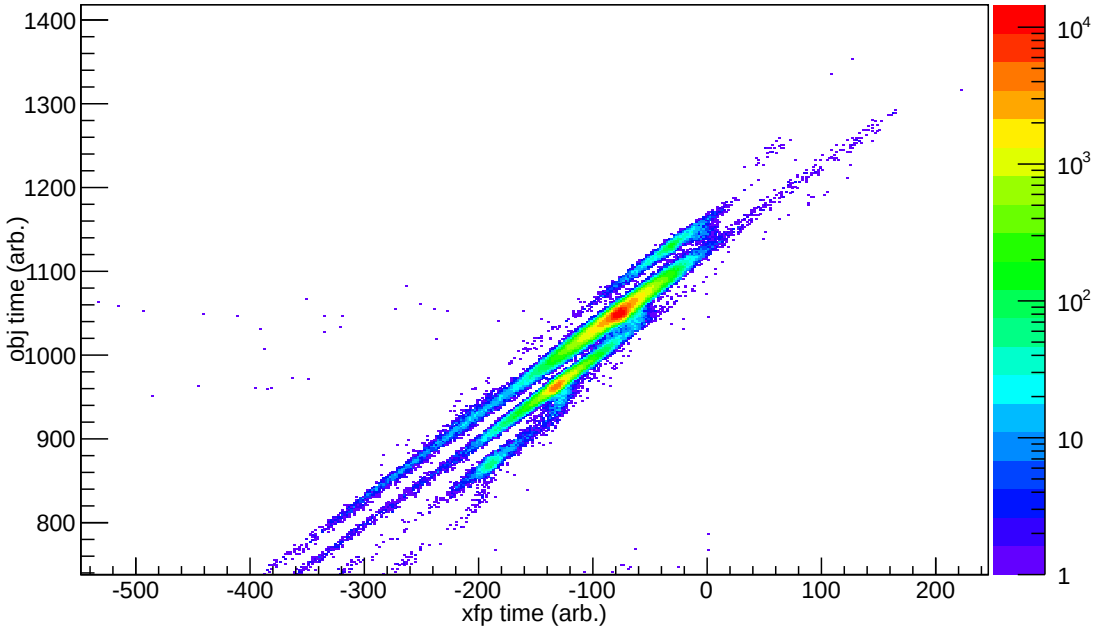

Figure A.1: The particle ID of incoming beams is shown with the A1900 tuned to produce ^{54}Fe. The highest intensity strip is ^{54}Fe.

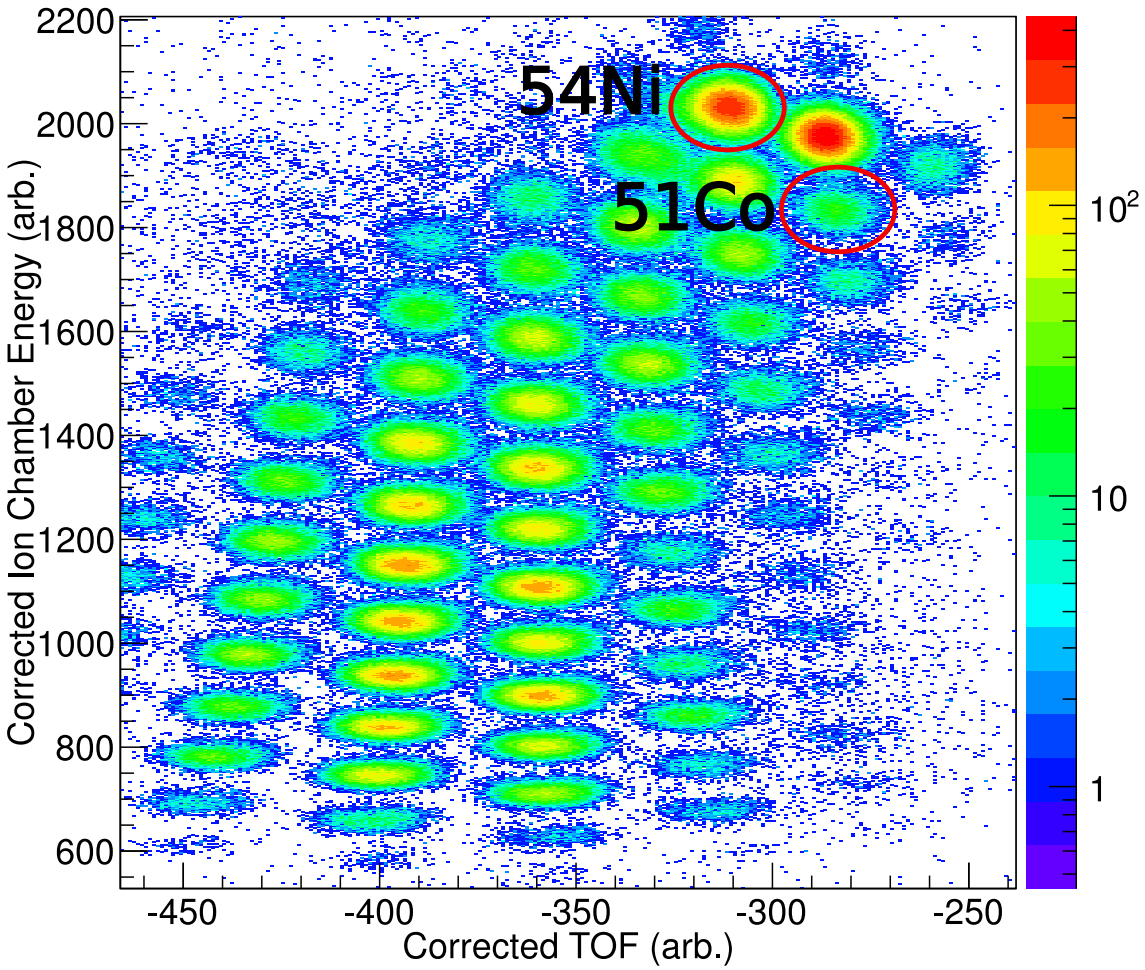

Figure A.2: The particle ID showing recoils from reactions with a ^{54}Ni beam. ^{54}Ni and the main nucleus of interest, ^{51}Co has been labelled.

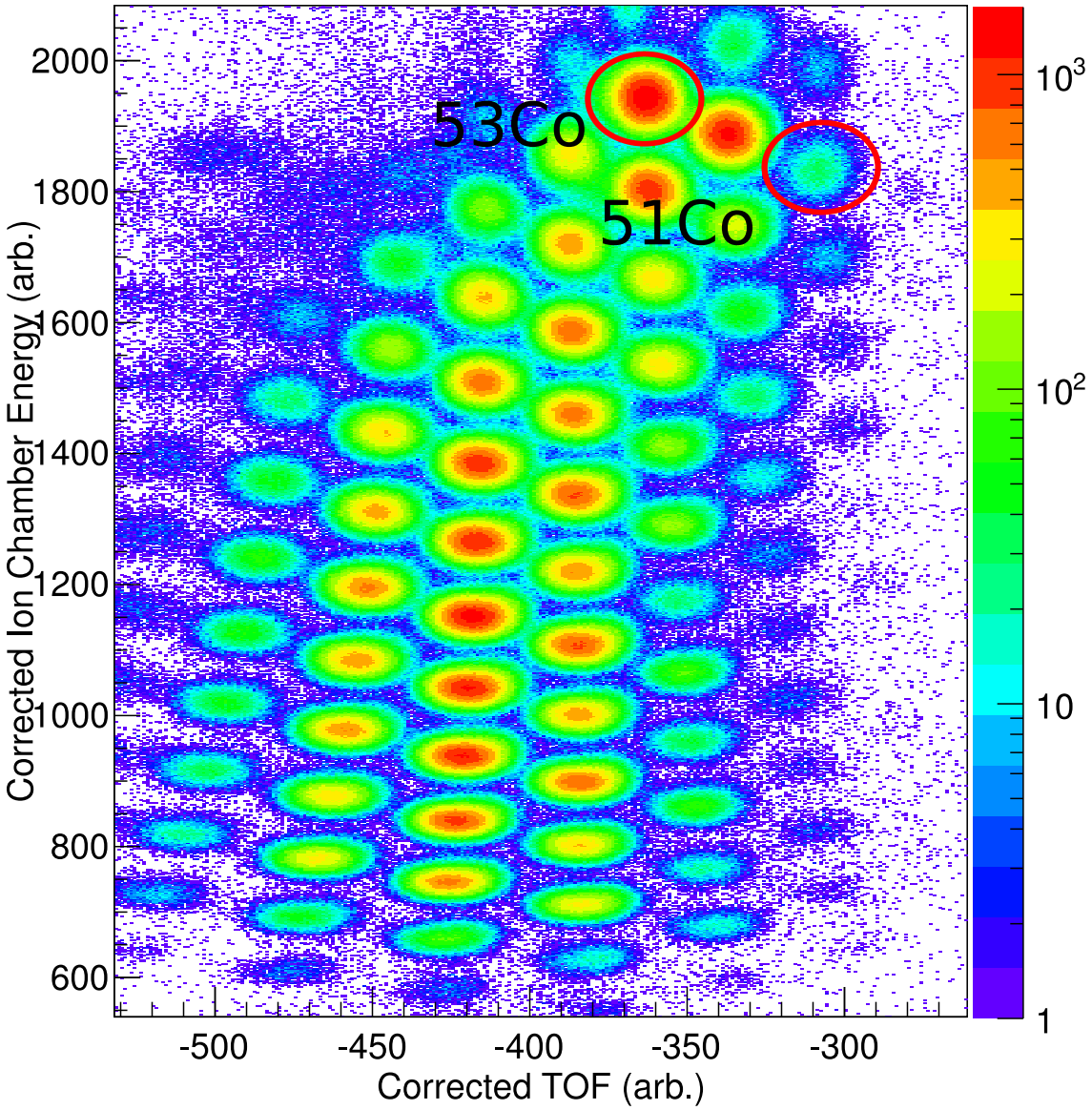

Figure A.3: The particle ID showing recoils from reactions with a ^{53}Co beam. ^{53}Co and the main nucleus of interest, ^{51}Co have been labelled.

Appendix B

FindBeta code

```
//calculate the appropriate beta for a gamma-ray that is not found at the same energy in
    both the 37 and 90 degree ring
//input the energy at 37 degrees, the energy at 90 degrees and the beta used to obtain
    these values

int FindBeta(double E_zero_37, double E_zero_90, double Beta_in){

       double E_gam_37 = E_zero_37 * TMath::Sqrt(1-Beta_in*Beta_in) / (1 - Beta_in*TMath::
           Cos(TMath::DegToRad()*37));
       double E_gam_90 = E_zero_90 * TMath::Sqrt(1-Beta_in*Beta_in) / (1 - Beta_in*TMath::
           Cos(TMath::DegToRad()*90));

       double Beta_new = Beta_in;
       double E_zero_37_new = E_zero_37;
       double E_zero_90_new = E_zero_90;
       cout << "Starting ratio of E_zero_37 to E_zero_90 : " << E_zero_37 / E_zero_90 <<
           endl;
       cout << endl;
       cout << "Beta_new" << "\t" << "E_0@37" << "\t\t" << "E_0@90" << "\t\t" << "E_0@37/
           E_0@90" << endl;
       while((E_zero_37_new / E_zero_90_new < 0.9999) || (E_zero_37_new / E_zero_90_new >
           1.0001)){

          E_zero_37_new = E_gam_37 * (1 - Beta_new*TMath::Cos(TMath::DegToRad()*37))
              / TMath::Sqrt(1-Beta_new*Beta_new);
          E_zero_90_new = E_gam_90 * (1 - Beta_new*TMath::Cos(TMath::DegToRad()*90))
              / TMath::Sqrt(1-Beta_new*Beta_new);
          if(E_zero_37 / E_zero_90 > 1.000001) Beta_new += Beta_in*0.0001;
          if(E_zero_37 / E_zero_90 < 0.999999) Beta_new -= Beta_in*0.0001;
          cout << Beta_new << "\t" << E_zero_37_new << "\t\t" << E_zero_90_new << "\t
              \t " << E_zero_37_new / E_zero_90_new << endl;
          if(Beta_new > 0.60){
```

```
                cout << "\n\nBeta greater than 60% c, there is a problem" << endl;
                return 0;
            }
            else if(Beta_new < 0.0){
                cout << "\n\nBeta less than 0% c, there is a problem" << endl;
                return 0;
            }
        }

        cout << endl;
        cout << "The correct Beta value is: " << Beta_new << endl;
        cout << "This gives a gamma-ray energy of: " << E_zero_90_new << endl;
        cout << "Determining the approprate Z and Beta for the Gamma of interest" << endl;
        cout << "Output is to histograms Beta_Z_E_diff and Beta_Z_E, and file tmp.dat" <<
            endl;
        FindZandBeta(E_zero_90_new, Beta_new);
        return 1;
}

//input is the experimentally measured energy of a gamma-ray and the beta at which the 37
    and 90 degree ring aligned for the inputed gamma-ray

int FindZandBeta(double E_exp, double Beta){

        int Z_00 = -250; // assume interaction is at the centre of the target
        double Z_0;
        double Beta_in = Beta;

        //Calculate the measured gamma-ray energy at 37 and 90 degrees
        double E_exp_37 = E_exp * TMath::Sqrt(1-Beta*Beta) / (1 - Beta*TMath::Cos(TMath::
            DegToRad()*37));
        double E_exp_90 = E_exp * TMath::Sqrt(1-Beta*Beta) / (1 - Beta*TMath::Cos(TMath::
            DegToRad()*90));

        //initialise some variables to be used later
        double Theta_corr_90 = 90.0*TMath::DegToRad();
        double Theta_corr_37 = 37.0*TMath::DegToRad();
        double a = 0.0;
        double E_corr_37 = 0.0;
        double E_corr_90 = 0.0;

        //initialise the constants
        double X_tg_sega = 2e2; // distance between target and sega in mm;

        //create spectra
        TH2F *Beta_Z_E_diff = new TH2F("Beta_Z_E_diff","Beta vs Z : Energy difference @ 37
            and 90",1000,0,1000,500,-250,250);
```

```
    TH2F *Beta_Z_E = new TH2F("Beta_Z_E","Beta vs Z : Energy @
        90",1000,0,1000,500,-250,250);

    //save data to tmp.dat
    ofstream data;
    data.open("tmp.dat");

//scan the range from -0.0500 below the calculated beta
Beta = Beta - 0.0500;

//scan the range to +0.0500 above the calculated beta
for(int i = 0 ; i < 1000 ; i++){
    //while(Beta < Beta_in + 0.0500){

            Z_00 = -250;
            data << "Z_0" << "\t" << "Beta" << "\t" << "Theta_corr_90*TMath::RadToDeg()
                " << "\t" << "Theta_corr_37*TMath::RadToDeg()" << "\t" << "E_corr_37"
                << "\t" << "E_corr_90" << endl;
            while(1){
                Z_00++;
                Z_0 = Z_00/10.0;

                if(Z_00 > 250){
                    //cout << "Beta = " << Beta << endl;
                           //cout << "reached end of target, no solution possible" <<
                               endl;
                           break;
                    }

                    //do the geometric manipulation
                    //assume the detectors at 20 cm from the target position, you will
                        need to validate this assumtion.
                    if(Z_0 == 0){
                           Theta_corr_90 == 90*TMath::DegToRad();
                           Theta_corr_37 == 37*TMath::DegToRad();
                    }
                    else if(Z_0 < 0){

                           Theta_corr_90 = -1 * TMath::ATan(X_tg_sega/Z_0);
                           a = TMath::Sqrt(X_tg_sega*X_tg_sega+Z_0*Z_0-2*Z_0*X_tg_sega*
                               TMath::Cos(37.0*TMath::DegToRad()));
                           Theta_corr_37 = TMath::Pi() - TMath::ACos((X_tg_sega*
                               X_tg_sega-a*a-Z_0*Z_0)/(-2*a*Z_0));
                    }
                    else{

                           Theta_corr_90 = TMath::Pi() - TMath::ATan(X_tg_sega/Z_0);
```

```
                        a = TMath::Sqrt(X_tg_sega*X_tg_sega+Z_0*Z_0-2*Z_0*X_tg_sega*
                            TMath::Cos(37.0*TMath::DegToRad()));
                        Theta_corr_37 = TMath::Pi() - TMath::ACos((X_tg_sega*
                            X_tg_sega-a*a-Z_0*Z_0)/(-2*a*Z_0));
                    }
                    //calculate the new energies

                    E_corr_37 = E_exp_37 * (1 - Beta*TMath::Cos(Theta_corr_37)) / TMath
                        ::Sqrt(1-Beta*Beta);
                    E_corr_90 = E_exp_90 * (1 - Beta*TMath::Cos(Theta_corr_90)) / TMath
                        ::Sqrt(1-Beta*Beta);

                    data << Z_0 << "\t" << Beta << "\t" << Theta_corr_90*TMath::RadToDeg
                        () << "\t" << Theta_corr_37*TMath::RadToDeg() << "\t" <<
                        E_corr_37 << "\t" << E_corr_90 << endl;

                    if((E_corr_90-E_corr_37) > 0.0) Beta_Z_E_diff->Fill(i,Z_0,E_corr_90-
                        E_corr_37);
                    if((E_corr_90-E_corr_37) < 0.0) Beta_Z_E_diff->Fill(i,Z_0,E_corr_37-
                        E_corr_90);
                    if((E_corr_90-E_corr_37) < 0.1 && (E_corr_90-E_corr_37) > -0.1)
                        Beta_Z_E->Fill(i,Z_0,E_corr_90);
                }

                Beta+=0.0001;
                data << "-----------------------------------------" << endl;
                data << endl;

        }
        data.close();
        return 1;
}
```

Appendix C

Particle Identification plots and spectra from experiment 2

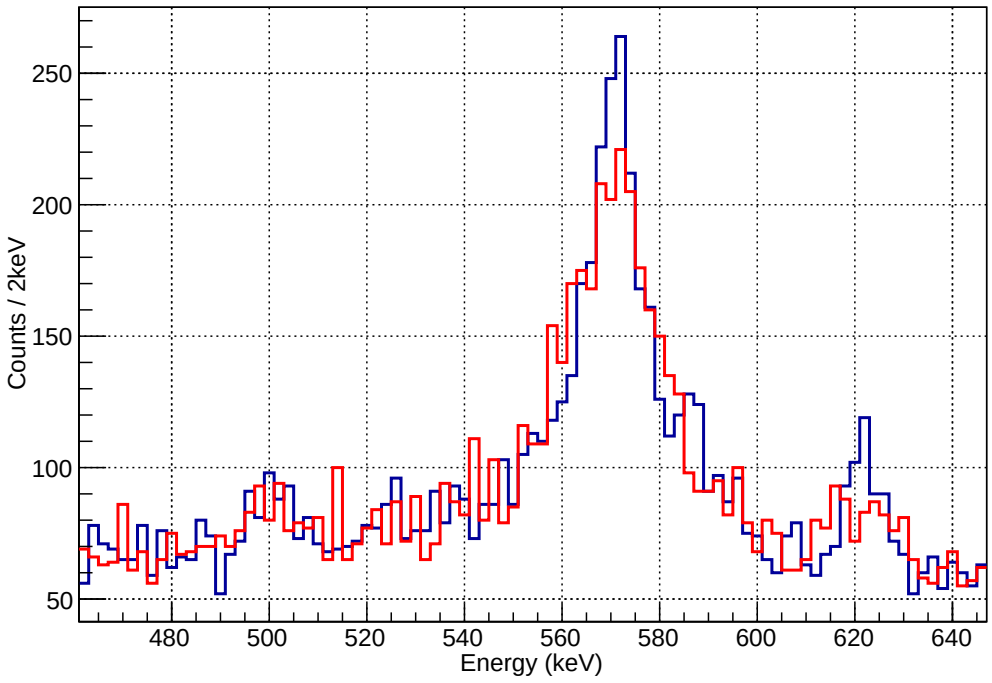

Figure C.1: Spectrum taken from 1p2n removal from ^{65}Ge to populate states in ^{62}Ga. The blue spectrum has a correct Doppler correction, the β used to Doppler correct the red spectrum is not correct.

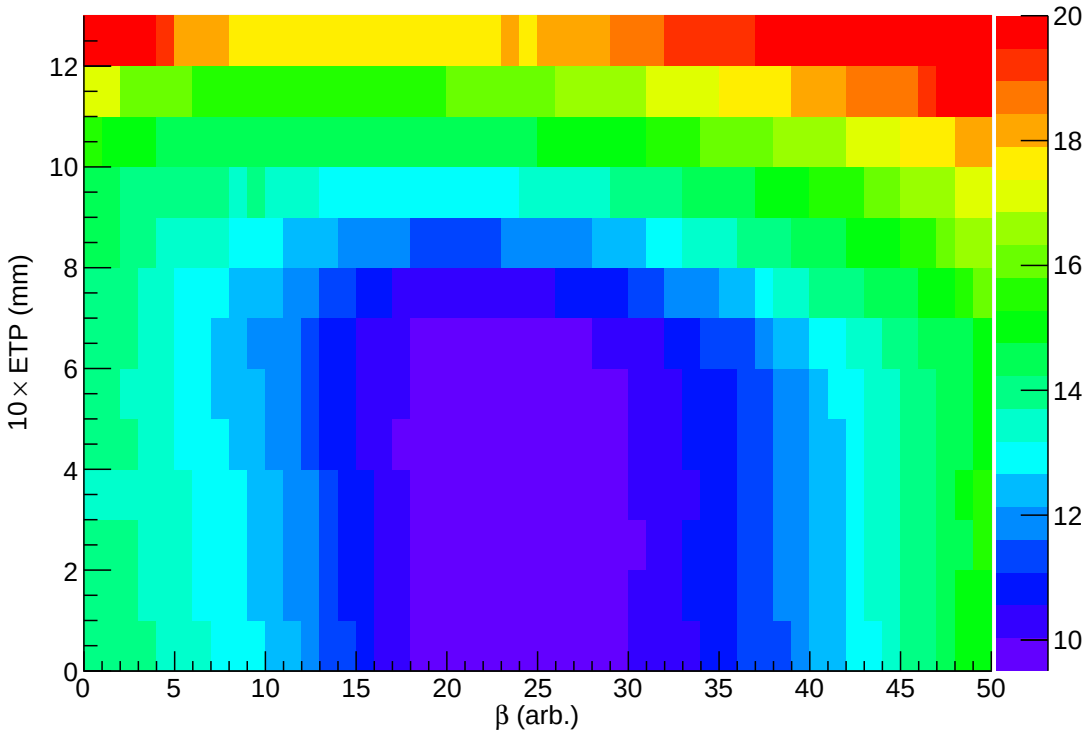

Figure C.2: Peak width plot for the 1521 keV transition in ^{62}Zn, for all data. The Z axis (colour) shows the σ from the gaussian fit equation in units of keV.

Appendix D

Possible evidence for the radiative electron capture

During the analysis of data from the second experiment presented in this thesis it was noticed that there are unknown distributions in both A1900 and S800 PID spectra. In the main analysis gates are created to avoid thesis data such that they are irrelevant. In this appendix we provide evidence that these are radiative electron capture.

Figure D.1 demonstrates the A1900 PID plot, the REC distribution is highlighted by a 2D gate. A projection from this gate is shown in Figure D.2. This plot varies from those seen in the main analysis: the pattern of repeating loci, coresponding to different nuclei is faded; the majority of the data lies in one intense distribution.

The gamma ray spectrum gated on this distribution is shown in Figure D.3. In the case of radiative electron capture a gamma ray is expected at an energy of $E_{REC} = E_{Kin} + E_{Bind}$ where E_{Bind} is the binding energy of a k-electron and E_{Kin} is the kinetic energy of an electron travelling at the beam velocity. At these beam velocities $E_{Kin} \approx 25$ keV. The binding energy for Gallium is 10.367 keV. These figures do not match the spectrum shown in Figure D.3, however, to have made it through the S800 this data must correspond to the edge of a momentum distribution, and a different β may apply.

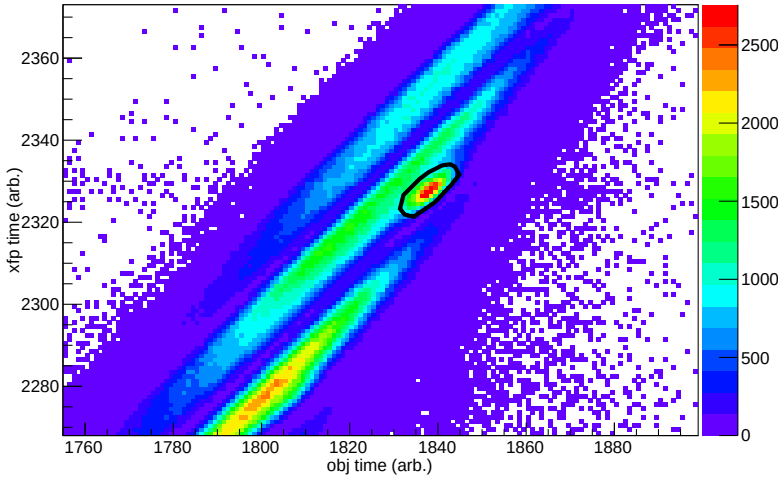

Figure D.1: A1900 PID plot from the Second experiment. The REC distribution is highlighted by a 2d gate.

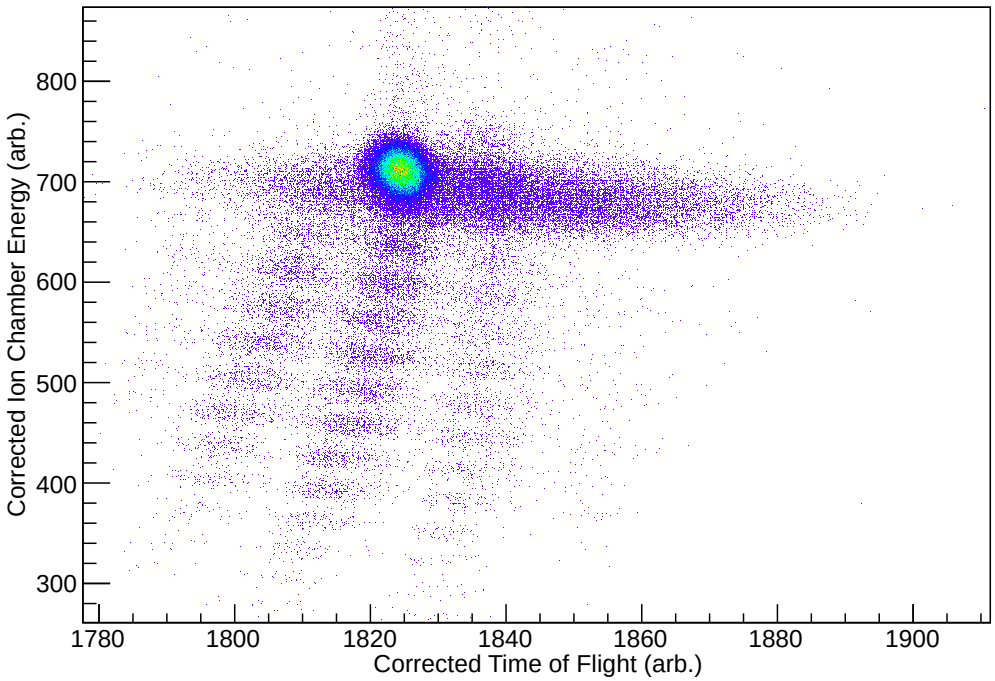

Figure D.2: S800 PID plot gated on the gate shown in Figure D.1.

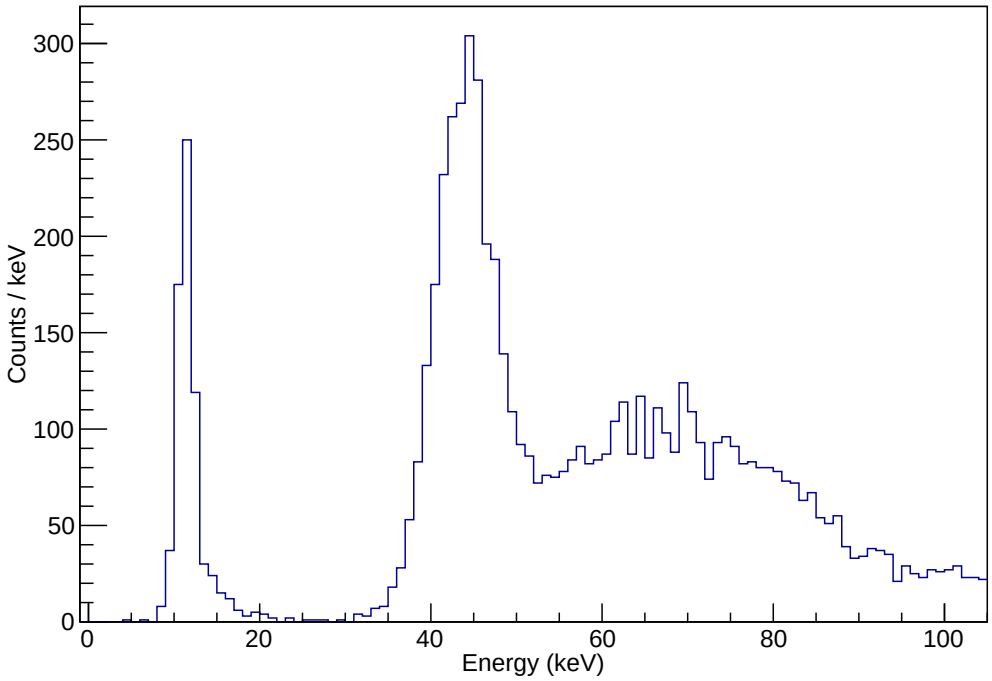

Figure D.3: Doppler corrected gamma ray spectrum gated on the highlighted distribution in Figure D.1

Bibliography

[1] R. Machleidt and H. Muther, "Charge symmetry breaking of the nucleon-nucleon interaction:$\rho - \omega$ mixing versus nucleon mass splitting," *Phys. Rev. C*, vol. 63, p. 034005, 2002.

[2] D. E. González Trotter, F. Salinas, Q. Chen, A. S. Crowell, W. Glöckle, C. R. Howell, C. D. Roper, D. Schmidt, I. Šlaus, H. Tang, W. Tornow, R. L. Walter, H. Witała, and Z. Zhou, "New measurement of the $^1S_0$ neutron-neutron scattering length using the neutron-proton scattering length as a standard," *Phys. Rev. Lett.*, vol. 83, pp. 3788–3791, Nov 1999.

[3] H. A. Bethe, "Coulomb energy of light nuclei," *Phys. Rev.*, vol. 54, p. 436, 1938.

[4] J. A. Nolen and J. P. Schiffer, "Coulomb energies," *Annual Review of Nuclear Science*, vol. 19, no. 1, pp. 471–526, 1969.

[5] J. Cameron, M. Bentley, A. Bruce, R. Cunningham, W. Gelletly, H. Price, J. Simpson, D. Warner, and A. James, "High-spin states in the mirror nuclei ^{49}Cr and ^{49}Mn," *Phys. Lett. B*, vol. 235, no. 34, pp. 239 – 244, 1990.

[6] J. Sheikh, P. V. Isacker, D. Warner, and J. Cameron, "Coulomb displacement energies and bandcrossing phenomena," *Physics Letters B*, vol. 252, no. 3, pp. 314 – 318, 1990.

[7] M. Bentley, C. OLeary, *et al.*, "Erratum," *Physics Letters B*, vol. 451, no. 34, pp. 445 – 446, 1999.

[8] A. P. Zuker, S. M. Lenzi, G. Martínez-Pinedo, and A. Poves, "Isobaric multiplet yrast energies and isospin nonconserving forces," *Phys. Rev. Lett.*, vol. 89, p. 142502, Sep 2002.

[9] S. J. Williams, M. A. Bentley, D. D. Warner, A. M. Bruce, J. A. Cameron, M. P. Carpenter, P. Fallon, L. Frankland, W. Gelletly, R. V. F. Janssens, D. T. Joss, C. D. O'Leary, C. J. Lister, A. Poves, P. H. Regan, P. Reiter, B. Rubio, D. Seweryniak, C. E. Svensson, and S. M. Vincent, "Anomalous coulomb matrix elements in the $f_{7/2}$ shell," *Phys. Rev. C*, vol. 68, p. 011301, Jul 2003.

[10] M. Bentley and S. Lenzi, "Coulomb energy differences between high-spin states in isobaric multiplets," *Progress in Particle and Nuclear Physics*, vol. 59, no. 2, pp. 497 – 561, 2007.

[11] F. Marti *et al.*, "Commissioning of the coupled cyclotron system at NSCL," *American Institute of Physics*, vol. 600, 2001.

[12] D. Bazin, J. Caggiano, B. Sherrill, J. Yurkon, and A. Zeller, "The spectrograph," *Nuclear Instruments and Methods in Physics Research Section B: Beam Interactions with Materials and Atoms*, vol. 204, no. 0, pp. 629 – 633, 2003. 14th International Conference on Electromagnetic Isotope Separators and Techniques Related to their Applications.

[13] D. Morrissey, B. Sherrill, M. Steiner, A. Stolz, and I. Wiedenhoever, "Commissioning the a1900 projectile fragment separator," *Nuclear Instruments and Methods in Physics Research Section B: Beam Interactions with Materials and Atoms*, vol. 204, no. 0, pp. 90 – 96, 2003. 14th International Conference on Electromagnetic Isotope Separators and Techniques Related to their Applications.

[14] S. Paschalis, I. Lee, A. Macchiavelli, C. Campbell, M. Cromaz, S. Gros, J. Pavan, J. Qian, R. Clark, H. Crawford, D. Doering, P. Fallon, C. Lionberger, T. Loew, M. Petri, T. Stezelberger, S. Zimmermann, D. Radford, K. Lagergren, D. Weisshaar, R. Winkler, T. Glasmacher, J. Anderson, and C. Beausang, "The performance of the gamma-ray energy tracking in-beam nuclear array {GRETINA}," *Nuclear Instruments and Methods in Physics Research Section A: Accelerators, Spectrometers, Detectors and Associated Equipment*, vol. 709, no. 0, pp. 44 – 55, 2013.

[15] R. R. C. Clement, *A New Method for the Nuclear Structure Measurement of Neutron Deficient Nuclei,*. PhD thesis, Michigan State University, 2003.

[16] W. Heisenberg, "Uber den bau der atomkerne. i.," *Z. Phys.*, vol. 77, no. 1, 1932.

[17] E. Wigner, "On the consequences of the symmetry of the nuclear hamiltonian on the spectroscopy of nuclei," *Phys. Rev.*, vol. 51, pp. 106–119, Jan 1937.

[18] M. Bentley, "Private communications," 2013.

[19] M. A. B. D. D. Warner and P. V. Isacker, "The role of isospin symmetry in collective nuclear structure," *Nature Physics*, vol. 2, pp. 311–318, 2006.

[20] A. Gadea, S. M. Lenzi, S. Lunardi, N. Mărginean, A. P. Zuker, G. de Angelis, M. Axiotis, T. Martínez-Pinedo, D. R. Napoli, E. Farnea, R. Menegazzo, P. Pavan, C. A. Ur, D. Bazzacco, R. Venturelli, P. Kleinheinz, P. Bednarczyk, D. Curien, O. Dorvaux, J. Nyberg, H. Grawe, M. Górska, M. Palacz, K. Lagergren, L. Milechina, J. Ekman, D. Rudolph, C. Andreoiu, M. A. Bentley, W. Gelletly, B. Rubio, A. Algora, E. Nacher, L. Caballero, M. Trotta, and M. Moszyóski, "Observation of ^{54}Ni: Cross-conjugate symmetry in f7/2 mirror energy differences," *Phys. Rev. Lett.*, vol. 97, p. 152501, Oct 2006.

[21] A. Bohr, B. R. Mottelson, and D. Pines, "Possible analogy between the excitation spectra of nuclei and those of the superconducting metallic state," *Phys. Rev.*, vol. 110, pp. 936–938, May 1958.

[22] A. O. Macchiavelli, P. Fallon, R. M. Clark, M. Cromaz, M. A. Deleplanque, R. M. Diamond, G. J. Lane, I. Y. Lee, F. S. Stephens, C. E. Svensson, K. Vetter, and D. Ward, "Is there np pairing in N=Z nuclei?," *Phys. Rev. C*, vol. 61, p. 041303, Mar 2000.

[23] J. Dobe, "How to count nucleon pairs?," *Physics Letters B*, vol. 413, no. 34, pp. 239 – 245, 1997.

[24] J. Engel, K. Langanke, and P. Vogel, "Isovector pairing in odd-a proton-rich nuclei," *Physics Letters B*, vol. 429, no. 34, pp. 215 – 221, 1998.

[25] C. Lanczos *Journal of Research of the National Bureau of Standards*, vol. 45, p. 2133, 1950.

[26] R. Roth and P. Navrátil, "*Ab Initio* study of ^{40}Ca with an importance-truncated no-core shell model," *Phys. Rev. Lett.*, vol. 99, p. 092501, Aug 2007.

[27] B. A. Brown and B. H. Wildentha, "Status of the nuclear shell model," *Annual Review of Nuclear and Particle Science*, vol. 38, pp. 29–66, Dec 1988.

[28] P. Navrátil and W. E. Ormand, "*Ab Initio* shell model calculations with three-body effective interactions for *p*-shell nuclei," *Phys. Rev. Lett.*, vol. 88, p. 152502, Apr 2002.

[29] M. Horoi, B. A. Brown, and V. Zelevinsky, "Exponential convergence method: Nonyrast states, occupation numbers, and a shell-model description of the superdeformed band in ^{56}Ni," *Phys. Rev. C*, vol. 67, p. 034303, Mar 2003.

[30] E. Caurier, G. Martínez-Pinedo, F. Nowacki, A. Poves, and A. P. Zuker, "The shell model as a unified view of nuclear structure," *Rev. Mod. Phys.*, vol. 77, pp. 427–488, Jun 2005.

[31] A. Poves, J. Sánchez-Solano, E. Caurier, and F. Nowacki, "Shell model study of the isobaric chains A=50, A=51 and A=52," *Nuclear Physics A*, vol. 694, no. 1–2, pp. 157 – 198, 2001.

[32] M. Honma, T. Otsuka, B. A. Brown, and T. Mizusaki, "New effective interaction for *p*-shell nuclei and its implications for the stability of the $N = 28$ closed core," *Phys. Rev. C*, vol. 69, p. 034335, Mar 2004.

[33] S. M. Lenzi, F. Nowacki, A. Poves, and K. Sieja, "Island of inversion around ^{64}Cr," *Phys. Rev. C*, vol. 82, p. 054301, Nov 2010.

[34] S. M. Lenzi. Private communication, 2014.

[35] D. R. Inglis, "Spin-orbit coupling in nuclei," *Phys. Rev.*, vol. 50, pp. 783–783, Oct 1936.

[36] D. R. Inglis, "Spin-orbit coupling in ^{7}Li and ^{7}Be," *Phys. Rev.*, vol. 82, pp. 181–189, Apr 1951.

[37] J. Duflo and A. P. Zuker, "Mirror displacement energies and neutron skins," *Phys. Rev. C*, vol. 66, p. 051304, Nov 2002.

[38] A. Obertelli, A. Gade, D. Bazin, C. M. Campbell, J. M. Cook, P. D. Cottle, A. D. Davies, D.-C. Dinca, T. Glasmacher, P. G. Hansen, T. Hoagland, K. W. Kemper, J.-L. Lecouey, W. F. Mueller, R. R. Reynolds, B. T. Roeder, J. R. Terry, J. A. Tostevin, K. Yoneda, and H. Zwahlen, "Population of bound excited states in intermediate-energy fragmentation reactions," *Phys. Rev. C*, vol. 73, p. 044605, Apr 2006.

[39] E. C. Simpson and J. A. Tostevin, "One- and two-neutron removal from the neutron-rich carbon isotopes," *Phys. Rev. C*, vol. 79, p. 024616, Feb 2009.

[40] M. H. Macfarlane and J. B. French, "Stripping reactions and the structure of light and intermediate nuclei," *Rev. Mod. Phys.*, vol. 32, pp. 567–691, Jul 1960.

[41] E. C. Simpson, J. A. Tostevin, D. Bazin, B. A. Brown, and A. Gade, "Two-nucleon knockout spectroscopy at the limits of nuclear stability," *Phys. Rev. Lett.*, vol. 102, p. 132502, Apr 2009.

[42] J. A. Tostevin and B. A. Brown, "Diffraction dissociation contributions to two-nucleon knockout reactions and the suppression of shell-model strength," *Phys. Rev. C*, vol. 74, p. 064604, Dec 2006.

[43] E. Grodner, A. Gadea, P. Sarriguren, S. M. Lenzi, J. Grębosz, J. J. Valiente-Dobón, A. Algora, M. Górska, P. H. Regan, D. Rudolph, G. de Angelis, J. Agramunt, N. Alkhomashi, L. Amon Susam, D. Bazzacco, J. Benlliure, G. Benzoni, P. Boutachkov, A. Bracco, L. Caceres, R. B. Cakirli, F. C. L. Crespi, C. Domingo-Pardo, M. Doncel, Z. Dombrádi, P. Doornenbal, E. Farnea, E. Ganioğlu, W. Gelletly, J. Gerl, A. Gottardo, T. Hüyük, N. Kurz, S. Leoni, D. Mengoni, F. Molina, A. I. Morales, R. Orlandi, Y. Oktem, R. D. Page, D. Perez, S. Pietri, Z. Podolyák, A. Poves, B. Quintana, S. Rinta-Antila, B. Rubio, B. S. Nara Singh, A. N. Steer, S. Verma, R. Wadsworth, O. Wieland, and H. J. Wollersheim, "Hindered gamow-teller decay to the odd-odd $N = Z$ ^{62}Ga: Absence of proton-neutron $t = 0$ condensate in $a = 62$," *Phys. Rev. Lett.*, vol. 113, p. 092501, Aug 2014.

[44] J. Yurkon, D. Bazin, W. Benenson, D. Morrissey, B. Sherrill, D. Swan, and R. Swanson, "Focal plane detector for the {S800} high-resolution spectrometer," *Nuclear Instruments and Methods in Physics Research Section A: Accelerators, Spectrometers, Detectors and Associated Equipment*, vol. 422, no. 13, pp. 291 – 295, 1999.

[45] M. Berz, K. Joh, J. A. Nolen, B. M. Sherrill, and A. F. Zeller, "Reconstructive correction of aberrations in nuclear particle spectrographs," *Phys. Rev. C*, vol. 47, pp. 537–544, Feb 1993.

[46] K. Makino and M. Berz *Nucl. Instrum. and Methods A*, vol. 427, pp. 338–343, 2007.

[47] M. Deleplanque, I. Lee, K. Vetter, G. Schmid, F. Stephens, R. Clark, R. Diamond, P. Fallon, and A. Macchiavelli, "Greta: utilizing new concepts in γ-ray detection," *Nuclear Instruments and Methods in Physics Research Section A: Accelerators, Spectrometers, Detectors and Associated Equipment*, vol. 430, no. 23, pp. 292 – 310, 1999.

[48] M. Hubbell, J. Seltzer, S. Chang, J. Coursey, J. Sukumar, R. Zucker, D. Olsen, and K. Berger, "Xcom: Photon cross section database (version 1.5)," 2010.

[49] F. Mueller, J. Church, T. Glasmacher, D. Gutknecht, G. Hackman, P. Hansen, Z. Hu, K. Miller, and P. Quirin, "Thirty-two-fold segmented germanium detectors to identify î-rays from intermediate-energy exotic beams," *Nuclear Instruments and Methods in Physics Research Section A: Accelerators, Spectrometers, Detectors and Associated Equipment*, vol. 466, no. 3, pp. 492 – 498, 2001.

[50] W. Mueller, D. Bazin, C. Campbell, J. Church, D. Dinca, A. Gade, T. Glasmacher, P. Hansen, K. Yurkewicz, H. Olliver, B. Sherrill, and J. Terry, "In-beam -ray spectroscopy of fast beams at the {NSCL}," *Nuclear Physics A*, vol. 734, no. 0, pp. 418 – 424, 2004. Proceedings of the Eighth International Conference On Nucleus-Nucleus Collisions.

[51] K. Vetter, A. Kuhn, I. Lee, R. Clark, M. Cromaz, M. Deleplanque, R. Diamond, P. Fallon, G. Lane, A. Macchiavelli, M. Maier, F. Stephens, C. Svensson, and H. Yaver, "Performance of the {GRETA} prototype detectors," *Nuclear Instruments and Methods in Physics Research Section A: Accelerators, Spectrometers, Detectors and Associated Equipment*, vol. 452, no. 12, pp. 105 – 114, 2000.

[52] I.-Y. Lee, "The gammasphere," *Progress in Particle and Nuclear Physics*, vol. 28, no. 0, pp. 473 – 485, 1992.

[53] K. Vetter, A. Kuhn, M. Deleplanque, I. Lee, F. Stephens, G. Schmid, D. Beckedahl, J. Blair, R. Clark, M. Cromaz, R. Diamond, P. Fallon, G. Lane, J. Kammeraad, A. Macchiavelli, and C. Svensson, "Three-dimensional position sensitivity in two-dimensionally segmented hp-ge detectors," *Nuclear Instruments and Methods in Physics Research Section A: Accelerators, Spectrometers, Detectors and Associated Equipment*, vol. 452, no. 12, pp. 223 – 238, 2000.

[54] G. Schmid, M. Deleplanque, I. Lee, F. Stephens, K. Vetter, R. Clark, R. Diamond, P. Fallon, A. Macchiavelli, and R. MacLeod, "A -ray tracking algorithm for the {GRETA} spectrometer," *Nuclear Instruments and Methods in Physics Research Section A: Accelerators, Spectrometers, Detectors and Associated Equipment*, vol. 430, no. 1, pp. 69 – 83, 1999.

[55] P. Davies, M. Bentley, T. Henry, E. Simpson, A. Gade, S. Lenzi, T. Baugher, D. Bazin, J. Berryman, A. Bruce, C. Diget, H. Iwasaki, A. Lemasson, S. McDaniel, D. Napoli, A. Ratkiewicz, L. Scruton, A. Shore, R. Stroberg, J. Tostevin, D. Weisshaar, K. Wimmer, and R. Winkler, "Mirror energy differences at large isospin studied through direct two-nucleon knockout," *Phys. Rev. Lett.*, vol. 111, p. 072501, Aug 2013.

[56] K. Wimmer, "Grroot software," 2011.

[57] M. Bentley, "Private communications," 2015.

[58] J. R. Brown, *Gamma-ray Spectroscopy of Tz=3/2 Mirror Nuclei in the f7/2 Shell: Isospin Breaking Effects at LargeProton Excess.* PhD thesis, The University of York, Heslington, York, YO10 5DD, UK, 9 2009.

[59] "Evaluated nuclear structure data." www.nndc.bnl.gov/ensdf. Accessed: 1st September 2015.

[60] H. David, P. Woods, G. Lotay, D. Seweryniak, M. Albers, M. Alcorta, M. Carpenter, C. Chiara, T. Davinson, D. Doherty, C. Hoffman, R. Janssens, T. Lauritsen, A. Rogers, and S. Zhu, "Low-lying states in the oddodd nucleus 62ga," *Physics Letters B*, vol. 726, no. 45, pp. 665 – 669, 2013.

[61] D. Rudolph, C. Andreoiu, J. Ekman, C. Fahlander, M. N. Mineva, S. M. Lenzi, E. Farnea, C. Rossi-Alvarez, C. A. Ur, M. Axiotis, G. de Angelis, A. Gadea, T. Kröll, N. Mărginean,

T. Martinez, and F. Nowacki, "Nonyrast states in the odd-odd $N = Z$ nucleus ^{62}Ga," *Phys. Rev. C*, vol. 69, p. 034309, Mar 2004.

[62] P. Srivastava, R. Sahu, and V. Kota, "Shell model and deformed shell model spectroscopy of 62ga," *The European Physical Journal A*, vol. 51, no. 1, 2015.

[63] U. Hermkens, F. Becker, T. Burkardt, J. Eberth, S. Freund, T. Mylaeus, S. Skoda, W. Teichert, H. G. Thomas, and A. v. d. Werth, "Search for enhanced octupole correlations in ^{65}Ge," *Phys. Rev. C*, vol. 52, pp. 1783–1791, Oct 1995.

[64] D. Sohler, Z. Dombrdi, S. Brant, J. Cederkll, M. Lipoglavek, M. Palacz, V. Paar, J. Persson, A. Atac, C. Fahlander, H. Grawe, A. Johnson, A. Kerek, W. Klamra, J. Kownacki, A. Likar, L. Norlin, J. Nyberg, R. Schubart, D. Seweryniak, G. de Angelis, P. Bednarczyk, D. Foltescu, M. Fayez-Hassan, D. Jerrestam, S. Juutinen, E. Mkel, B. Nyak, M. de Poli, H. Roth, T. Shizuma, . Skeppstedt, G. Sletten, and S. Trmnen, "Spectroscopy of neutron deficient 65ge," *Zeitschrift fr Physik A Hadrons and Nuclei*, vol. 357, no. 3, pp. 239–240, 1997.

[65] A. Obertelli, T. Baugher, D. Bazin, S. Boissinot, J.-P. Delaroche, A. Dijon, F. Flavigny, A. Gade, M. Girod, T. Glasmacher, G. Grinyer, W. Korten, J. Ljungvall, S. McDaniel, A. Ratkiewicz, B. Sulignano, P. V. Isacker, and D. Weisshaar, "First spectroscopy of 66se and 65as: Investigating shape coexistence beyond the line," *Physics Letters B*, vol. 701, no. 4, pp. 417 – 421, 2011.

[66] D. P. Balamuth, U. J. Hüttmeier, T. Chapuran, D. G. Popescu, and J. W. Arrison, "In-beam γ-ray spectroscopy of the $N = Z + 1$ nucleus ^{63}Ga," *Phys. Rev. C*, vol. 43, pp. 2082–2097, May 1991.

[67] M. Weiszflog, G. de Angelis, A. Axelsson, D. Bazzacco, F. Becker, M. De Poli, J. Eberth, C. Fahlander, A. Gadea, S. Lunardi, D. Napoli, J. Nyberg, C. Rossi Alvarez, B. Rubio, D. Rudolph, S. Skoda, H. Thomas, and R. Wyss, "High-spin spectroscopy of 63 31ga32 and 65 31ga34," *The European Physical Journal A - Hadrons and Nuclei*, vol. 11, no. 1, pp. 25–38, 2001.

[68] S. Milne. Private communication, 2015.

[69] M. Wang, G. Audi, A. H. Wapstra, F. G. Kondev, M. MacCormick, X. Xu, and B. Pfeiffer, "The ame2012 atomic mass evaluation (ii). tables, graphs and references," *Chin.Phys.C*, vol. 36, p. 1603, 2012.

[70] S. M. Lenzi, N. Mărginean, D. R. Napoli, C. A. Ur, A. P. Zuker, G. de Angelis, A. Algora, M. Axiotis, D. Bazzacco, N. Belcari, M. A. Bentley, P. G. Bizzeti, A. Bizzeti-Sona, F. Brandolini, P. von Brentano, D. Bucurescu, J. A. Cameron, C. Chandler, M. De Poli, A. Dewald, H. Eberth, E. Farnea, A. Gadea, J. Garces-Narro, W. Gelletly, H. Grawe, R. Isocrate, D. T. Joss, C. A. Kalfas, T. Klug, T. Lampman, S. Lunardi, T. Martínez, G. Martínez-Pinedo, R. Menegazzo, J. Nyberg, Z. Podolyak, A. Poves, R. V. Ribas, C. Rossi Alvarez, B. Rubio, J. Sánchez-Solano, P. Spolaore, T. Steinhardt, O. Thelen, D. Tonev, A. Vitturi, W. von

Oertzen, and M. Weiszflog, "Coulomb energy differences in $T = 1$ mirror rotational bands in ^{50}Fe and ^{50}Cr," *Phys. Rev. Lett.*, vol. 87, p. 122501, Aug 2001.

[71] F. D. Becchetti and G. W. Greenlees, "Nucleon-nucleus optical-model parameters, $a >; 40$, $e < 50$ mev," *Phys. Rev.*, vol. 182, pp. 1190–1209, Jun 1969.

[72] K. Kaneko, Y. Sun, T. Mizusaki, and S. Tazaki, "Variation in displacement energies due to isospin-nonconserving forces," *Phys. Rev. Lett.*, vol. 110, p. 172505, Apr 2013.

[73] M. A. Bentley, S. M. Lenzi, S. A. Simpson, and C. A. Diget, "Isospin-breaking interactions studied through mirror energy differences," *Phys. Rev. C*, vol. 92, p. 024310, Aug 2015.

[74] T. W. Henry, M. A. Bentley, R. M. Clark, P. J. Davies, V. M. Bader, T. Baugher, D. Bazin, C. W. Beausang, J. S. Berryman, A. M. Bruce, C. M. Campbell, H. L. Crawford, M. Cromaz, P. Fallon, A. Gade, J. Henderson, H. Iwasaki, D. G. Jenkins, I. Y. Lee, A. Lemasson, S. M. Lenzi, A. O. Macchiavelli, D. R. Napoli, A. J. Nichols, S. Paschalis, M. Petri, F. Recchia, J. Rissanen, E. C. Simpson, S. R. Stroberg, R. Wadsworth, D. Weisshaar, A. Wiens, and C. Walz, "Triplet energy differences and the low lying structure of ^{62}Ga," *Phys. Rev. C*, vol. 92, p. 024315, Aug 2015.

[75] S. Vincent, P. Regan, D. Warner, R. Bark, D. Blumenthal, M. Carpenter, C. Davids, W. Gelletly, R. Janssens, C. O'Leary, C. Lister, J. Simpson, D. Seweryniak, T. Saitoh, J. Schwartz, S. Trmnen, O. Juillet, F. Nowacki, and P. V. Isacker, "Competing t=0 and t=1 structures in the N=Z nucleus ^{62}Ga," *Physics Letters B*, vol. 437, no. 34, pp. 264 – 272, 1998.

[76] A. Steer, D. Jenkins, R. Glover, B. N. Singh, N. Pattabiraman, R. Wadsworth, S. Eeckhaudt, T. Grahn, P. Greenlees, P. Jones, R. Julin, S. Juutinen, M. Leino, M. Nyman, J. Pakarinen, P. Rahkila, J. Sarn, C. Scholey, J. Sorri, J. Uusitalo, P. Butler, I. Darby, R.-D. Herzberg, D. Joss, R. Page, J. Thomson, R. Lemmon, J. Simpson, and B. Blank, "Recoil-beta tagging: A novel technique for studying proton-drip-line nuclei," *Nuclear Instruments and Methods in Physics Research Section A: Accelerators, Spectrometers, Detectors and Associated Equipment*, vol. 565, no. 2, pp. 630 – 636, 2006.

[77] B. Singh and J. A. Cameron, "Nuclear data sheets for a = 42," *Nuclear Data Sheets*, vol. 92, no. 1, pp. 1 – 146, 2001.

[78] S. M. Lenzi, D. R. Napoli, C. A. Ur, D. Bazzacco, F. Brandolini, J. A. Cameron, E. Caurier, G. de Angelis, M. De Poli, E. Farnea, A. Gadea, S. Hankonen, S. Lunardi, G. Martínez-Pinedo, Z. Podolyak, A. Poves, C. Rossi Alvarez, J. Sánchez-Solano, and H. Somacal, "Band termination in the $N = Z$ odd-odd nucleus ^{46}V," *Phys. Rev. C*, vol. 60, p. 021303, Jul 1999.

[79] P. E. Garrett, W. E. Ormand, D. Appelbe, R. W. Bauer, J. A. Becker, L. A. Bernstein, J. A. Cameron, M. P. Carpenter, R. V. F. Janssens, C. J. Lister, D. Seweryniak, E. Tavukcu, and D. D. Warner, "Observation of ^{46}cr and testing the isobaric multiplet mass equation at high spin," *Phys. Rev. Lett.*, vol. 87, p. 132502, Sep 2001.

[80] C. E. Svensson, S. M. Lenzi, D. R. Napoli, A. Poves, C. A. Ur, D. Bazzacco, F. Brandolini, J. A. Cameron, G. de Angelis, A. Gadea, D. S. Haslip, S. Lunardi, E. E. Maqueda,

G. Martínez-Pinedo, M. A. Nagarajan, C. R. Alvarez, A. Vitturi, and J. C. Waddington, "High-spin states in the odd-odd $N = Z$ nucleus ^{50}Mn," *Phys. Rev. C*, vol. 58, pp. R2621–R2625, Nov 1998.

[81] C. Langer, F. Montes, A. Aprahamian, D. W. Bardayan, D. Bazin, B. A. Brown, J. Browne, H. Crawford, R. H. Cyburt, C. Domingo-Pardo, A. Gade, S. George, P. Hosmer, L. Keek, A. Kontos, I.-Y. Lee, A. Lemasson, E. Lunderberg, Y. Maeda, M. Matos, Z. Meisel, S. Noji, F. M. Nunes, A. Nystrom, G. Perdikakis, J. Pereira, S. J. Quinn, F. Recchia, H. Schatz, M. Scott, K. Siegl, A. Simon, M. Smith, A. Spyrou, J. Stevens, S. R. Stroberg, D. Weisshaar, J. Wheeler, K. Wimmer, and R. G. T. Zegers, "Determining the *rp*-process flow through ^{56}Ni: Resonances in ^{57}Cu$(p,\gamma)^{58}$Zn identified with gretina," *Phys. Rev. Lett.*, vol. 113, p. 032502, Jul 2014.

[82] A. F. Lisetskiy, N. Pietralla, M. Honma, A. Schmidt, I. Schneider, A. Gade, P. von Brentano, T. Otsuka, T. Mizusaki, and B. A. Brown, "Experimental evidence for ^{56}Ni-core breaking from the low-spin structure of the $N = Z$ nucleus $^{58}_{29}$cu$_{29}$," *Phys. Rev. C*, vol. 68, p. 034316, Sep 2003.

[83] D. Rudolph, E. Johansson, L.-L. Andersson, J. Ekman, C. Fahlander, and R. du Rietz, "Exotic decay modes in rotating nuclei," *Nuclear Physics A*, vol. 752, pp. 241 – 250, 2005. Proceedings of the 22nd International Nuclear Physics Conference (Part 2).

[84] R. Grzywacz, C. Yu, Z. Janas, S. Paul, J. Batchelder, C. Bingham, T. Ginter, C. Gross, J. McConnell, M. Lipoglavek, A. Piechaczek, D. Radford, J. Ressler, K. Rykaczewski, J. Shergur, W. Walters, E. Zganjar, C. Baktash, M. Carpenter, R. Janssens, C. Svensson, J. Waddington, D. Ward, and E. Dragulescu, "In-beam study of the N=Z nucleus $^{66}_{33}As_{33}$ using the decay tagging technique," *Nuclear Physics A*, vol. 682, no. 14, pp. 41 – 47, 2001.

[85] P. Ruotsalainen, D. G. Jenkins, M. A. Bentley, R. Wadsworth, C. Scholey, K. Auranen, P. J. Davies, T. Grahn, P. T. Greenlees, J. Henderson, A. Herzáň, U. Jakobsson, P. Joshi, R. Julin, S. Juutinen, J. Konki, M. Leino, G. Lotay, A. J. Nichols, A. Obertelli, J. Pakarinen, J. Partanen, P. Peura, P. Rahkila, M. Sandzelius, J. Sarén, J. Sorri, S. Stolze, and J. Uusitalo, "Spectroscopy of proton-rich ^{66}se up to $j^\pi = 6^+$: Isospin-breaking effect in the $a = 66$ isobaric triplet," *Phys. Rev. C*, vol. 88, p. 041308, Oct 2013.

[86] D. Rudolph, C. J. Gross, J. A. Sheikh, D. D. Warner, I. G. Bearden, R. A. Cunningham, D. Foltescu, W. Gelletly, F. Hannachi, A. Harder, T. D. Johnson, A. Jungclaus, M. K. Kabadiyski, D. Kast, K. P. Lieb, H. A. Roth, T. Shizuma, J. Simpson, O. Skeppstedt, B. J. Varley, and M. Weiszflog, "Identification of $t = 0$ and $t = 1$ bands in the $N = Z$ nucleus ^{74}rb," *Phys. Rev. Lett.*, vol. 76, pp. 376–379, Jan 1996.

[87] J. Henderson, D. G. Jenkins, K. Kaneko, P. Ruotsalainen, P. Sarriguren, K. Auranen, M. A. Bentley, P. J. Davies, A. Görgen, T. Grahn, P. T. Greenlees, A. Hay, T. W. Henry, A. Herzáň, U. Jakobsson, R. Julin, S. Juutinen, J. Konki, M. Leino, C. McPeake, S. Milne, A. J. Nichols, J. Pakarinen, P. Papadakis, J. Partanen, P. Peura, P. Rahkila, E. Sahin, M. Sandzelius, J. Sarén, C. Scholey, M. Siciliano, L. Sinclair, J. Sorri, S. Stolze, J. Uusitalo, R. Wadsworth,

and M. Zielińska, "Spectroscopy on the proton drip-line: Probing the structure dependence of isospin nonconserving interactions," *Phys. Rev. C*, vol. 90, p. 051303, Nov 2014.

[88] B. C. Hyman, V. E. Iacob, A. Azhari, C. A. Gagliardi, J. C. Hardy, V. E. Mayes, R. G. Neilson, M. Sanchez-Vega, X. Tang, L. Trache, and R. E. Tribble, "Beta decay of ^{62}Ga," *Phys. Rev. C*, vol. 68, p. 015501, Jul 2003.

[89] E. Simpson. Private communication, 2014.

[90] R. Grzywacz, S. Andriamonje, B. Blank, F. Bou, S. Czajkowski, F. Davi, R. D. Moral, C. Donzaud, J. Dufour, A. Fleury, H. Grawe, A. Grewe, A. Heinz, Z. Janas, A. Junghans, M. Karny, M. Lewitowicz, A. Musqure, M. Pftzner, M.-G. Porquet, M. Pravikoff, J.-E. Sauvestre, and K. Smmerer, "Isomeric states in 66as," *Physics Letters B*, vol. 429, no. 34, pp. 247 – 253, 1998.

[91] L.-L. Andersson, E. K. Johansson, J. Ekman, D. Rudolph, R. du Rietz, C. Fahlander, C. J. Gross, P. A. Hausladen, D. C. Radford, and G. Hammond, "Identification of excited states in $^{31}_{61}\mathrm{Ga}_{30}$: Mirror nuclei in the upper *fp* shell," *Phys. Rev. C*, vol. 71, p. 011303, Jan 2005.

[92] D. Rudolph, C. Baktash, J. Dobaczewski, W. Nazarewicz, W. Satuła, M. J. Brinkman, M. Devlin, H.-Q. Jin, D. R. LaFosse, L. L. Riedinger, D. G. Sarantites, and C.-H. Yu, "Prompt proton decay of a well-deformed rotational band in ^{58}Cu," *Phys. Rev. Lett.*, vol. 80, pp. 3018–3021, Apr 1998.

[93] R. G. H. Robertson and S. M. Austin, "Neutron-deficient isotopes ^{64}Ge and ^{65}Ge," *Phys. Rev. C*, vol. 9, pp. 1801–1812, May 1974.

[94] A. Nichols, R. Wadsworth, H. Iwasaki, K. Kaneko, A. Lemasson, G. de Angelis, V. Bader, T. Baugher, D. Bazin, M. Bentley, J. Berryman, T. Braunroth, P. Davies, A. Dewald, C. Fransen, A. Gade, M. Hackstein, J. Henderson, D. Jenkins, D. Miller, C. Morse, I. Paterson, E. Simpson, S. Stroberg, D. Weisshaar, K. Whitmore, and K. Wimmer, "Collectivity in a 70 nuclei studied via lifetime measurements in 70br and 68,70se," *Physics Letters B*, vol. 733, no. 0, pp. 52 – 57, 2014.

[95] I.-Y. Lee, "Nuclear structure in the nineties the gammasphere," *Nuclear Physics A*, vol. 520, pp. c641 – c655, 1990.

[96] C. Davids, B. Back, K. Bindra, D. Henderson, W. Kutschera, T. Lauritsen, Y. Nagame, P. Sugathan, A. Ramayya, and W. Walters, "Startup of the fragment mass analyzer at {ATLAS}," *Nuclear Instruments and Methods in Physics Research Section B: Beam Interactions with Materials and Atoms*, vol. 70, no. 14, pp. 358 – 365, 1992.

[97] D. Sarantites, P.-F. Hua, M. Devlin, L. Sobotka, J. Elson, J. Hood, D. LaFosse, J. Sarantites, and M. Maier, "the microball design, instrumentation and response characteristics of a 4-multidetector exit channel-selection device for spectroscopic and reaction mechanism studies with gammasphere," *Nuclear Instruments and Methods in Physics Research Section A: Accelerators, Spectrometers, Detectors and Associated Equipment*, vol. 381, no. 23, pp. 418 – 432, 1996.

[98] S. e. a. Manikonda, "Argonne in-flight radioactive ion separator," in *Heavy Ion Accelerator Technology*, 2012.

[99] J. Lighthall, B. Back, S. Baker, S. Freeman, H. Lee, B. Kay, S. Marley, K. Rehm, J. Rohrer, J. Schiffer, D. Shetty, A. Vann, J. Winkelbauer, and A. Wuosmaa, "Commissioning of the {HELIOS} spectrometer," *Nuclear Instruments and Methods in Physics Research Section A: Accelerators, Spectrometers, Detectors and Associated Equipment*, vol. 622, no. 1, pp. 97 – 106, 2010.

[100] B. B. Back, S. I. Baker, B. A. Brown, C. M. Deibel, S. J. Freeman, B. J. DiGiovine, C. R. Hoffman, B. P. Kay, H. Y. Lee, J. C. Lighthall, S. T. Marley, R. C. Pardo, K. E. Rehm, J. P. Schiffer, D. V. Shetty, A. W. Vann, J. Winkelbauer, and A. H. Wuosmaa, "First experiment with helios: The structure of ^{13}**B**," *Phys. Rev. Lett.*, vol. 104, p. 132501, Mar 2010.

[101] S. Akkoyun, A. Algora, B. Alikhani, F. Ameil, G. de Angelis, L. Arnold, A. Astier, A. Ata, Y. Aubert, C. Aufranc, A. Austin, S. Aydin, F. Azaiez, S. Badoer, D. Balabanski, D. Barrientos, G. Baulieu, R. Baumann, D. Bazzacco, F. Beck, T. Beck, P. Bednarczyk, M. Bellato, M. Bentley, G. Benzoni, R. Berthier, L. Berti, R. Beunard, G. L. Bianco, B. Birkenbach, P. Bizzeti, A. Bizzeti-Sona, F. L. Blanc, J. Blasco, N. Blasi, D. Bloor, C. Boiano, M. Borsato, D. Bortolato, A. Boston, H. Boston, P. Bourgault, P. Boutachkov, A. Bouty, A. Bracco, S. Brambilla, I. Brawn, A. Brondi, S. Broussard, B. Bruyneel, D. Bucurescu, I. Burrows, A. Brger, S. Cabaret, B. Cahan, E. Calore, F. Camera, A. Capsoni, F. Carri, G. Casati, M. Castoldi, B. Cederwall, J.-L. Cercus, V. Chambert, M. E. Chambit, R. Chapman, L. Charles, J. Chavas, E. Clment, P. Cocconi, S. Coelli, P. Coleman-Smith, A. Colombo, S. Colosimo, C. Commeaux, D. Conventi, R. Cooper, A. Corsi, A. Cortesi, L. Costa, F. Crespi, J. Cresswell, D. Cullen, D. Curien, A. Czermak, D. Delbourg, R. Depalo, T. Descombes, P. Dsesquelles, P. Detistov, C. Diarra, F. Didierjean, M. Dimmock, Q. Doan, C. Domingo-Pardo, M. Doncel, F. Dorangeville, N. Dosme, Y. Drouen, G. Duchne, B. Dulny, J. Eberth, P. Edelbruck, J. Egea, T. Engert, M. Erduran, S. Ertrk, C. Fanin, S. Fantinel, E. Farnea, T. Faul, M. Filliger, F. Filmer, C. Finck, G. de France, A. Gadea, W. Gast, A. Geraci, J. Gerl, R. Gernhuser, A. Giannatiempo, A. Giaz, L. Gibelin, A. Givechev, N. Goel, V. Gonzlez, A. Gottardo, X. Grave, J. Grebosz, R. Griffiths, A. Grint, P. Gros, L. Guevara, M. Gulmini, A. Grgen, H. Ha, T. Habermann, L. Harkness, H. Harroch, K. Hauschild, C. He, A. Hernndez-Prieto, B. Hervieu, H. Hess, T. Hyk, E. Ince, R. Isocrate, G. Jaworski, A. Johnson, J. Jolie, P. Jones, B. Jonson, P. Joshi, D. Judson, A. Jungclaus, M. Kaci, N. Karkour, M. Karolak, A. Kaka, M. Kebbiri, R. Kempley, A. Khaplanov, S. Klupp, M. Kogimtzis, I. Kojouharov, A. Korichi, W. Korten, T. Krll, R. Krcken, N. Kurz, B. Ky, M. Labiche, X. Lafay, L. Lavergne, I. Lazarus, S. Leboutelier, F. Lefebvre, E. Legay, L. Legeard, F. Lelli, S. Lenzi, S. Leoni, A. Lermitage, D. Lersch, J. Leske, S. Letts, S. Lhenoret, R. Lieder, D. Linget, J. Ljungvall, A. Lopez-Martens, A. Lotod, S. Lunardi, A. Maj, J. van der Marel, Y. Mariette, N. Marginean, R. Marginean, G. Maron, A. Mather, W. Meczyski, V. Mendz, P. Medina, B. Melon, R. Menegazzo, D. Mengoni, E. Merchan, L. Mihailescu, C. Michelagnoli, J. Mierzejewski, L. Milechina, B. Million, K. Mitev, P. Molini, D. Montanari, S. Moon, F. Morbiducci, R. Moro, P. Morrall, O. Mller, A. Nannini, D. Napoli,

L. Nelson, M. Nespolo, V. Ngo, M. Nicoletto, R. Nicolini, Y. L. Noa, P. Nolan, M. Norman, J. Nyberg, A. Obertelli, A. Olariu, R. Orlandi, D. Oxley, C. zben, M. Ozille, C. Oziol, E. Pachoud, M. Palacz, J. Palin, J. Pancin, C. Parisel, P. Pariset, G. Pascovici, R. Peghin, L. Pellegri, A. Perego, S. Perrier, M. Petcu, P. Petkov, C. Petrache, E. Pierre, N. Pietralla, S. Pietri, M. Pignanelli, I. Piqueras, Z. Podolyak, P. L. Pouhalec, J. Pouthas, D. Pugnre, V. Pucknell, A. Pullia, B. Quintana, R. Raine, G. Rainovski, L. Ramina, G. Rampazzo, G. L. Rana, M. Rebeschini, F. Recchia, N. Redon, M. Reese, P. Reiter, P. Regan, S. Riboldi, M. Richer, M. Rigato, S. Rigby, G. Ripamonti, A. Robinson, J. Robin, J. Roccaz, J.-A. Ropert, B. Ross, C. R. Alvarez, D. Rosso, B. Rubio, D. Rudolph, F. Saillant, E. ahin, F. Salomon, M.-D. Salsac, J. Salt, G. Salvato, J. Sampson, E. Sanchis, C. Santos, H. Schaffner, M. Schlarb, D. Scraggs, D. Seddon, M. enyiit, M.-H. Sigward, G. Simpson, J. Simpson, M. Slee, J. Smith, P. Sona, B. Sowicki, P. Spolaore, C. Stahl, T. Stanios, E. Stefanova, O. Stzowski, J. Strachan, G. Suliman, P.-A. Sderstrm, J. Tain, S. Tanguy, S. Tashenov, C. Theisen, J. Thornhill, F. Tomasi, N. Toniolo, R. Touzery, B. Travers, A. Triossi, M. Tripon, K. Tun-Lano, M. Turcato, C. Unsworth, C. Ur, J. Valiente-Dobon, V. Vandone, E. Vardaci, R. Venturelli, F. Veronese, C. Veyssiere, E. Viscione, R. Wadsworth, P. Walker, N. Warr, C. Weber, D. Weisshaar, D. Wells, O. Wieland, A. Wiens, G. Wittwer, H. Wollersheim, F. Zocca, N. Zamfir, M. Ziebliski, and A. Zucchiatti, "Agataadvanced {GAmma} tracking array," *Nuclear Instruments and Methods in Physics Research Section A: Accelerators, Spectrometers, Detectors and Associated Equipment*, vol. 668, pp. 26 – 58, 2012.

[102] . Skeppstedt, H. Roth, L. Lindstrm, R. Wadsworth, I. Hibbert, N. Kelsall, D. Jenkins, H. Grawe, M. Grska, M. Moszyski, Z. Sujkowski, D. Wolski, M. Kapusta, M. Hellstrm, S. Kalogeropoulos, D. Oner, A. Johnson, J. Cederkll, W. Klamra, J. Nyberg, M. Weiszflog, J. Kay, R. Griffiths, J. G. Narro, C. Pearson, and J. Eberth, "The {EUROBALL} neutron wall design and performance tests of neutron detectors," *Nuclear Instruments and Methods in Physics Research Section A: Accelerators, Spectrometers, Detectors and Associated Equipment*, vol. 421, no. 3, pp. 531 – 541, 1999.

[103] J. Scheurer, M. Aiche, M. Aleonard, G. Barreau, F. Bourgine, D. Boivin, D. Cabaussel, J. Chemin, T. Doan, J. Goudour, M. Harston, A. Brondi, G. L. Rana, R. Moro, E. Vardaci, and D. Curien, "Improvements in the in-beam -ray spectroscopy provided by an ancillary detector coupled to a ge -spectrometer: the diamant-eurogam {II} example," *Nuclear Instruments and Methods in Physics Research Section A: Accelerators, Spectrometers, Detectors and Associated Equipment*, vol. 385, no. 3, pp. 501 – 510, 1997.